frontiers | Research Topics

Women in cancer imaging and image-directed interventions: 2021, 2nd Edition

Edited by
Samata Kakkad, Pilar López-Larrubia, Ellen Ackerstaff and Marie-France Penet

Published in
Frontiers in Oncology

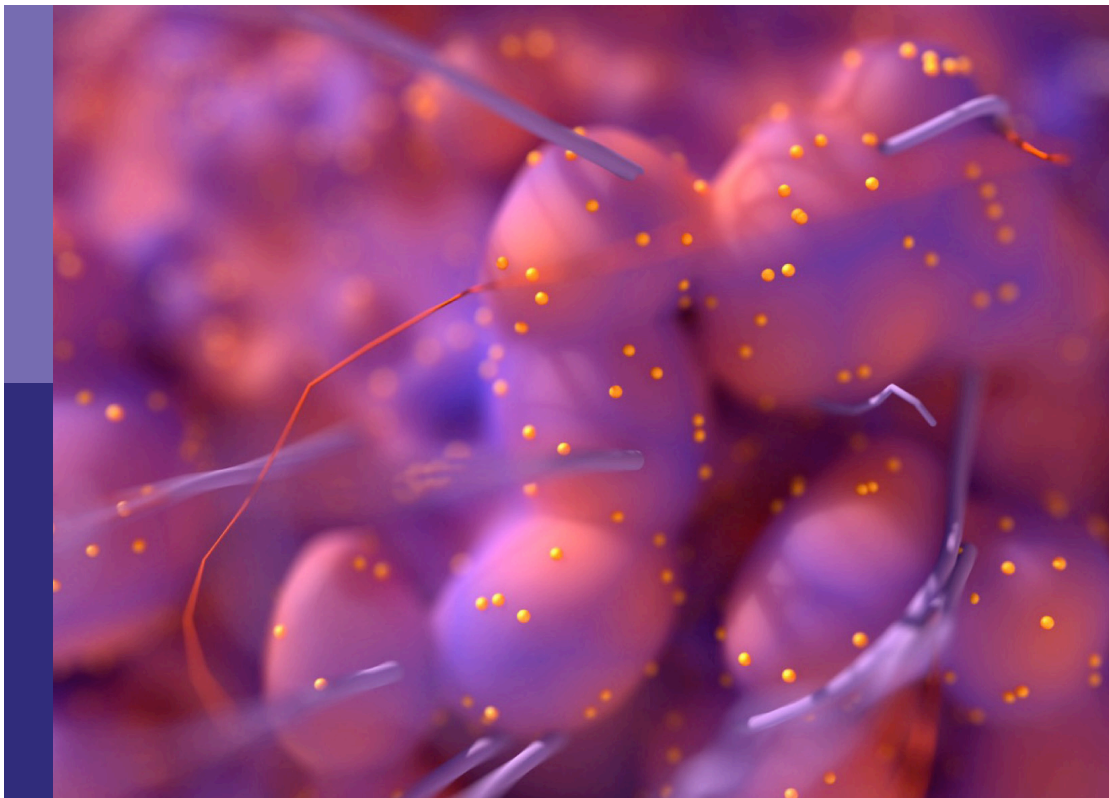

ISSN 1664-8714
ISBN 978-2-8325-4250-7
DOI 10.3389/978-2-8325-4250-7

About Frontiers

Frontiers is more than just an open access publisher of scholarly articles: it is a pioneering approach to the world of academia, radically improving the way scholarly research is managed. The grand vision of Frontiers is a world where all people have an equal opportunity to seek, share and generate knowledge. Frontiers provides immediate and permanent online open access to all its publications, but this alone is not enough to realize our grand goals.

Frontiers journal series

The Frontiers journal series is a multi-tier and interdisciplinary set of open-access, online journals, promising a paradigm shift from the current review, selection and dissemination processes in academic publishing. All Frontiers journals are driven by researchers for researchers; therefore, they constitute a service to the scholarly community. At the same time, the *Frontiers journal series* operates on a revolutionary invention, the tiered publishing system, initially addressing specific communities of scholars, and gradually climbing up to broader public understanding, thus serving the interests of the lay society, too.

Dedication to quality

Each Frontiers article is a landmark of the highest quality, thanks to genuinely collaborative interactions between authors and review editors, who include some of the world's best academicians. Research must be certified by peers before entering a stream of knowledge that may eventually reach the public - and shape society; therefore, Frontiers only applies the most rigorous and unbiased reviews. Frontiers revolutionizes research publishing by freely delivering the most outstanding research, evaluated with no bias from both the academic and social point of view. By applying the most advanced information technologies, Frontiers is catapulting scholarly publishing into a new generation.

What are Frontiers Research Topics?

Frontiers Research Topics are very popular trademarks of the *Frontiers journals series*: they are collections of at least ten articles, all centered on a particular subject. With their unique mix of varied contributions from Original Research to Review Articles, Frontiers Research Topics unify the most influential researchers, the latest key findings and historical advances in a hot research area.

Find out more on how to host your own Frontiers Research Topic or contribute to one as an author by contacting the Frontiers editorial office: frontiersin.org/about/contact

Women in cancer imaging and image-directed interventions: 2021, 2nd Edition

Topic editors

Samata Kakkad — Merck, United States

Pilar López-Larrubia — Spanish National Research Council (CSIC), Spain

Ellen Ackerstaff — Memorial Sloan Kettering Cancer Center, United States

Marie-France Penet — School of Medicine, Johns Hopkins Medicine, United States

Citation

Kakkad, S., López-Larrubia, P., Ackerstaff, E., Penet, M.-F., eds. (2023). *Women in cancer imaging and image-directed interventions: 2021, 2nd Edition*. Lausanne: Frontiers Media SA. doi: 10.3389/978-2-8325-4250-7

Publisher's note: This is a 2nd edition due to an article retraction from this Research Topic.

Table of contents

frontiers in Oncology

ORIGINAL RESEARCH
published: 09 November 2021
doi: 10.3389/fonc.2021.779612

Added Value of a New Strain Elastography Technique in Conventional Ultrasound for the Diagnosis of Breast Masses: A Prospective Multicenter Study

Qi Wei[1†], Yu-Jing Yan[1†], Ge-Ge Wu[1], Xi-Rong Ye[2], Fan Jiang[3], Jie Liu[4], Gang Wang[5], Yi Wang[6], Yu Wang[7], Zhi-Ping Pan[8], Jin-Hua Hu[9], Juan Song[7], Christoph F. Dietrich[10] and Xin-Wu Cui[1]*

[1] Sino-German Tongji-Caritas Research Center of Ultrasound in Medicine, Department of Medical Ultrasound, Tongji Hospital, Tongji Medical College, Huazhong University of Science and Technology, Wuhan, China, [2] Department of Medical Ultrasound, The Central Hospital of EDong Healthcare, Huangshi, China, [3] Department of Medical Ultrasound, The Second Hospital of Anhui Medical University, Hefei, China, [4] Department of Medical Ultrasound, Yichang General Hospital, Renmin Hospital of Three Gorges University, Yichang, China, [5] Department of Medical Ultrasound, Taizhou Hospital of Zhejiang Province, Linhai, China, [6] Department of Medical Ultrasound, Macheng People's Hospital, Macheng, China, [7] Department of Medical Ultrasound, Xiangyang No. 1 People's Hospital, Affiliated Hospital of Hubei University of Medicine, Xiangyang, China, [8] Department of Medical Ultrasound, Yixing Traditional Chinese Medicine Hospital, Yixing, China, [9] Department of Medical Ultrasound, Anqing First People's Hospital of Anhui Medical University, Anqing, China, [10] Department of Internal Medicine, Hirslanden Clinic, Bern, Switzerland

Objective: This study aimed to explore the value of elasticity score (ES) and strain ratio (SR) combined with conventional ultrasound in distinguishing benign and malignant breast masses and reducing biopsy of BI-RADS (Breast Imaging Reporting and Data System) 4a lesions.

Methods: This prospective, multicenter study included 910 patients from nine different hospitals. The acquisition and analysis of conventional ultrasound and strain elastography (SE) were obtained by radiologists with more than 5 years of experience in breast ultrasound imaging. The diagnostic sensitivity, specificity, positive predictive value (PPV), negative predictive value (NPV), and area under curve (AUC) of conventional ultrasound alone and combined tests with ES and/or SR were calculated and compared.

Results: The optimal cutoff value of SR for differentiating benign from malignant masses was 2.27, with a sensitivity of 60.2% and a specificity of 84.8%. When combined with ES and SR, the AUC of the new BI-RADS classification increased from 0.733 to 0.824 ($p < 0.001$); the specificity increased from 48.1% to 68.5% ($p < 0.001$) without a decrease in the sensitivity (98.5% *vs*. 96.4%, $p = 0.065$); and the PPV increased from 52.2% to 63.7% ($p < 0.001$) without a loss in the NPV (98.2% *vs*. 97.1%, $p = 0.327$). All three combinations of conventional ultrasound, ES, and SR could reduce the biopsy rate of category 4a lesions without reducing the malignant rate of biopsy (from 100% to 68.3%, 34.9%, and 50.4%, respectively, all $p < 0.001$).

OPEN ACCESS

Edited by:
Pilar López-Larrubia, Consejo Superior de Investigaciones Científicas (CSIC), Spain

Reviewed by:
Eduardo Fleury, Instituto Brasileiro de Controle do Câncer, Brazil
Jianhua Zhou, Sun Yat-sen University Cancer Center (SYSUCC), China

***Correspondence:**
Xin-Wu Cui
cuixinwu@live.cn

[†]These authors have contributed equally to this work

Specialty section:
This article was submitted to Cancer Imaging and Image-directed Interventions, a section of the journal Frontiers in Oncology

Received: *19 September 2021*
Accepted: *18 October 2021*
Published: *09 November 2021*

Citation:
Wei Q, Yan Y-J, Wu G-G, Ye X-R, Jiang F, Liu J, Wang G, Wang Y, Wang Y, Pan Z-P, Hu J-H, Song J, Dietrich CF and Cui X-W (2021) Added Value of a New Strain Elastography Technique in Conventional Ultrasound for the Diagnosis of Breast Masses: A Prospective Multicenter Study. Front. Oncol. 11:779612. doi: 10.3389/fonc.2021.779612

Conclusions: SE can be used as a useful and non-invasive additional method to improve the diagnostic performance of conventional ultrasound by increasing AUC and specificity and reducing the unnecessary biopsy of BI-RADS 4a lesions.

Keywords: strain elastography, elasticity score, strain ratio, ultrasound, breast masses

INTRODUCTION

The morbidity of breast cancer is the highest in the world, and the mortality ranks fifth among all cancers but first in female cancers (1). Early detection and timely diagnosis of breast cancer are closely related to the prognosis of patients. Ultrasound is widely used in the examination of patients with breast abnormalities. However, the lack of specificity of B-mode ultrasound in the diagnosis of breast masses leads to unnecessary biopsy (2), which leads to negative effects such as pain, anxiety, and complications (3).

Strain elastography (SE) is easily performed and provides elastic images with a high spatial resolution by evaluating tissue deformation (4). In general, malignant breast tissue is harder than normal breast tissue and produces less strain (5). Differentiating benign and malignant breast masses and upgrading or downgrading the Breast Imaging Reporting and Data System (BI-RADS) classification to avoid unnecessary biopsy are clinical indications for elastography according to the WFUMB guidelines and recommendations for clinical use of ultrasound elastography to breast (6). Ultrasound elastography technique may improve the specificity of B-mode ultrasound in the differential diagnosis of breast masses by measuring tissue stiffness (2, 7), even for breast masses smaller than 1 cm in diameter (8). Elasticity assessment has been incorporated into the fifth edition of BI-RADS lexicon to further describe the characteristics of breast masses (9). The combination of conventional ultrasound and SE can reduce unnecessary biopsy of breast masses by down-staging the BI-RADS classification (10). SE was strongly recommended as a supplementary diagnostic tool for conventional ultrasound by the latest EFSUMB (European Federation of Societies for Ultrasound in Medicine and Biology) guidelines and recommendations for the clinical practice of elastography for non-hepatic applications released in 2018 (11). Three diagnostic methods of SE including elasticity score (ES), strain ratio (SR), and strain size ratio (EI/B ratio) were mainly used to classify breast lesions in clinic (6).

Most previous studies explored the value of SE in breast masses using Hitachi ultrasound equipment (5, 12, 13). However, the SE in different brands of ultrasound systems has different reference standards for clinical use. Recently, a new SE technique, with the function of measuring ES and SR, has been equipped in Samsung ultrasound systems. At present, only one single study has explored the diagnostic performance of SE of this system in differentiating benign and malignant breast masses (14). More studies are needed to explore the added value of ES and SR in the differential diagnosis of breast masses.

The prospective multicenter study aimed to determine the cutoff value of SR and to explore the value of ES and SR in combination with conventional ultrasound in distinguishing benign and malignant breast masses and reducing biopsy of BI-RADS 4a lesions.

MATERIALS AND METHODS

This prospective multicenter study enrolled patients from nine institutions in different regions of China between April 2019 and November 2020. It was approved by the ethics committee of Tongji Medical College of Huazhong University of Science and Technology and registered in ClinicalTrials.gov (NCT 03887598). The informed consent of all participants was obtained in this study.

Participants

The inclusion criteria of participants were as follows: (i) patients had definite pathological results after ultrasound examination, and (ii) patients were at least 18 years old. The exclusion criteria were as follows: (i) patients who received radiotherapy or chemotherapy before the examination; (ii) patients who did not have reliable SE images or SR analyses; and (iii) patients who were lactating or pregnant.

Image Acquisition: B-Mode Ultrasound and SE

Conventional ultrasound imaging and SE technique were performed with the Samsung RS80A ultrasound system (Samsung Madison Co., Ltd., Seoul, South Korea) in all patients. The acquisition of ultrasound images and the analysis of SE images were performed by nine radiologists with more than 5 years of experience in breast ultrasound imaging. The standard data acquisition process was established, and all operators received rigorous training before the enrollment of patients. The study was conducted only after five qualified test cases were uploaded from every single center and checked by the principle investigator.

Breast B-mode ultrasound was performed in the supine position in all patients using a 3–12 MHz linear transducer. B-mode videos of the lesions were documented in both the long axis and short axis. SE imaging was performed using the same 3–12 MHz linear transducer based on WFUMB guidelines (6). The SE images were obtained by manually applying slight vibration with the probe perpendicular to the skin under the guidance of the quality indicator. After the elastic image was stabilized, SR and ES were acquired on a representative static image by the same operator. Strain A was obtained by placing the ROI in the target mass, and strain B was obtained by placing the ROI in the subcutaneous fibroglandular tissue at the same depth as the mass (**Figure 1**). The SR (the ratio of strain B to strain A)

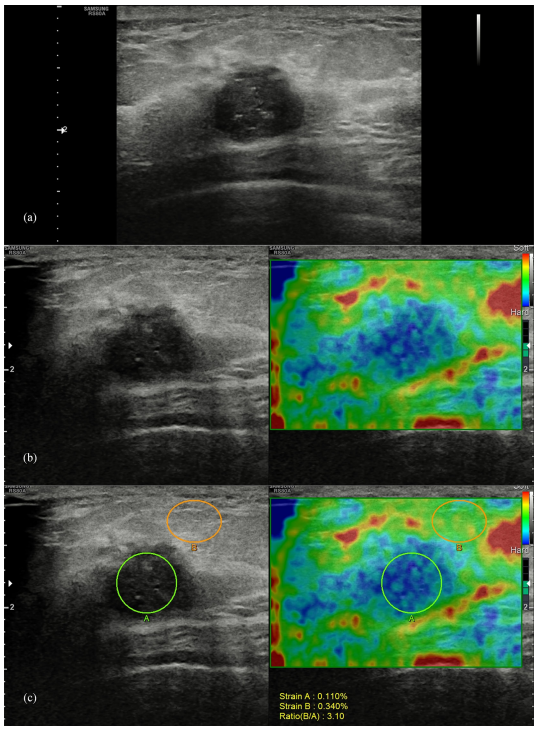

FIGURE 1 | Pathologically confirmed breast invasive ductal carcinoma in a 44-year-old female patient. Ultrasound images of the long-axis section of the breast mass were evaluated as BI-RADS 4c **(A)**, with an elasticity score of 4 **(B)**, and a strain ratio of 3.1 **(C)**.

calculated by the system was recorded. SE videos of the lesions were documented in both the long axis and short axis.

Image Analysis

Conventional ultrasound features of breast masses were analyzed by two experienced radiologists (more than 5 years of experience in breast ultrasound imaging) who were blinded to the pathological results according to BI-RADS classification (12) and finally evaluated as category 2, 3, 4a, 4b, 4c, and 5. The final assessments would be given after a discussion of two radiologists when there was a disagreement. Category 4a was considered as the cutoff value: benign, category 2 or 3; malignant, category 4a, 4b, 4c, or 5.

The elastic scoring criteria of breast masses are shown in **Table 1** (8). Scores 1 to 3 were considered benign, while scores 4 and 5 were considered malignant. The optimum cutoff value of SR was determined by receiver operating characteristic (ROC) analysis. A breast mass was considered malignant when the SR value was higher than the cutoff value. Otherwise, it was considered benign.

Combination Criteria of B-Mode Ultrasound and ES and/or SR

The combined analysis of B-mode ultrasound, ES, and SR of all images was based on the long-axis section of the breast mass. The BI-RADS classification of the breast mass was reassessed when combined with the ES and SR. Only BI-RADS categories 3 and 4a were upgraded or downgraded in this study. When conventional ultrasound was combined with ES or SR, BI-RADS category 3 was upgraded to category 4a if the result was malignant; BI-RADS category 4a would be downgraded to category 3 if benign was recommended. When conventional ultrasound was combined with ES and SR, category 3 was upgraded to category 4a if both ES and SR results are malignant; category 4a would be downgraded to category 3 if both were recommended as benign; otherwise, the BI-RADS classification of the mass would be unchanged.

Statistical Analysis

The histopathological results were considered the reference standard for this study. The diagnostic sensitivity, specificity, positive predictive value (PPV), negative predictive value (NPV), area under the curve (AUC) value, and positive and negative diagnostic likelihood ratios (LR+, LR-) of ES and SR on two different sections (long axis and short axis) were calculated and compared. The diagnostic value of the combination of conventional ultrasound and ES and/or SR in differentiating benign and malignant breast masses and reducing biopsy of BI-RADS 4a lesions were analyzed and compared: conventional ultrasound and ES, conventional ultrasound and SR, and conventional ultrasound and ES and SR.

Quantitative data such as patient age and tumor size were expressed as means and standard deviations, and compared using *t* test or Mann–Whitney *U* test. The chi-square test and Fisher's test were used to compare categorical variables. The comparison between AUC values was performed by the DeLong method (15). The SPSS (version 22, IBM Corp.) and MedCalc software (V.19.0.7, MedCalc Software, Ostend, Belgium) were used for all statistical analyses. *p*-values less than 0.05 were assumed to be statistically significant.

RESULTS

Clinical Characteristics

A total of 910 patients (mean age, 45.3 ± 10.9 years) were finally included in this study after the exclusion criteria were performed (**Figure 2**). Invasive ductal carcinoma was the most common of 332 (36.5%) malignant breast masses, accounting for 83.4% (277/332). Among 578 (63.5%) cases of benign breast masses, proliferative disease (61.2%, 354/578) and fibroadenoma

TABLE 1 | The elastic scoring criteria of breast masses.

Elasticity score	Description
Score 1	Homogeneous green within the mass
Score 2	Most of the area is light green, with some blue around and/or in the center of the mass
Score 3	Half of the area is blue and half is green in the mass
Score 4	Homogeneously blue with or without a little green within the mass
Score 5	Homogeneously blue with or without a little green throughout the entire mass and its surrounding area

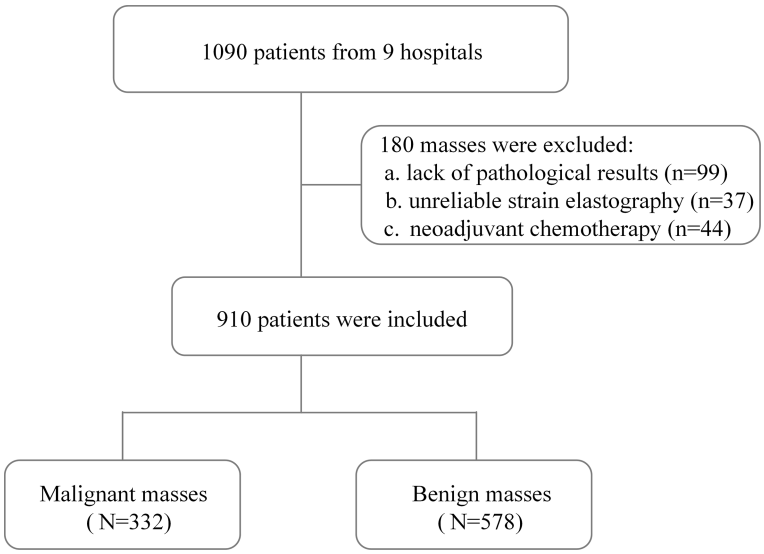

FIGURE 2 | Flowchart of patient selection in the study.

(31.0%, 179/578) were the main ones. The characteristics of patients and masses are summarized in **Table 2**. Patients with benign breast masses are significantly younger than those with malignant masses (42.3 ± 9.9 *vs.* 50.4 ± 10.5, $p < 0.001$). The diameter (22.5 ± 10.4 *vs.* 14.6 ± 7.3, $p < 0.001$) and SR (2.8 ± 1.6 *vs.* 1.6 ± 0.8, $p < 0.001$) of the breast mass with histopathological findings of malignancy were significantly higher than those of the benign mass. In addition, there were significant statistical differences in the distribution of malignant and benign breast masses in the ES and BI-RADS classification (all $p < 0.001$).

SR in BI-RADS Classification

SR values of different BI-RADS categories are shown in **Table 3**. For masses classified as BI-RADS category 5, the SR value was significantly higher than that of category 4 (median value, 2.520 *vs.* 1.770, $p < 0.001$), and the SR value for category 4 masses was significantly higher than that of category 3 (median value, 1.770 vs. 1.330, $p < 0.001$, **Table 3** and **Figure 3A**). The median value of SR increased with the increase of BI-RADS classification. When BI-RADS 4 were sub-categorized as 4a, 4b, and 4c, the SR value of category 5 was higher than category 4c (median value, 2.520 *vs.* 2.150, $p = 0.048$), category 4b was higher than category 4a (median value, 1.910 *vs.* 1.595, $p = 0.007$), and category 4a was higher than category 3 (median value, 1.595 vs. 1.330, $p < 0.001$). However, there was no statistical difference in the SR value between category 4b and 4c (median value, 2.150 *vs.* 1.910, $p = 0.054$, **Table 3** and **Figure 3B**).

TABLE 2 | The characteristics of patients and breast masses.

Characteristics	All masses	Malignant	Benign	*p*
Mean age, years	45.3 ± 10.9	50.4 ± 10.5	42.3 ± 9.9	<0.001
Mean tumor size, mm*	17.5 ± 9.3	22.5 ± 10.4	14.6 ± 7.3	<0.001
Size <20 mm	617	148	469	
Size ≥20 mm	293	184	109	
Strain ratio*	2.1 ± 1.3	2.8 ± 1.6	1.6 ± 0.8	<0.001
Elasticity score (ES) *				<0.001
ES 1	19	0	19	
ES 2	343	28	315	
ES 3	66	8	58	
ES 4	459	273	186	
ES 5	23	23	0	
BI-RADS classification*				<0.001
Category 3	283	5	278	
Category 4a	252	29	223	
Category 4b	89	37	52	
Category 4c	99	82	17	
Category 5	187	179	8	

**Data obtained based on the long-axis section of the mass.*

TABLE 3 | The strain ratio in different BI-RADS classifications.

Strain Ratio	BI-RADS 3	BI-RADS 4				BI-RADS 5
		All	BI-RADS 4a	BI-RADS 4b	BI-RADS 4c	
Median value	1.330	1.770	1.595	1.910	2.150	2.520
Interquartile range	(1.020, 1.790)	(1.250, 2.568)	(1.210, 2.108)	(1.185, 2.915)	(1.600, 3.250)	(1.860, 3.280)

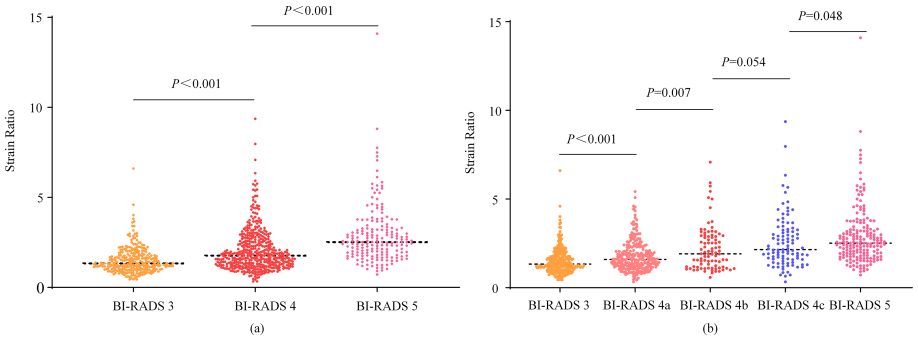

FIGURE 3 | Scatter plots of strain ratios in different BI-RADS classifications. The Mann-Whitney U test was used to compare the difference in strain ratio between different BI-RADS classifications.

Diagnostic Performance of ES and SR

The optimal cutoff values of SR in the long-axis and short-axis sections were determined by the Youden index. In the long-axis section of the breast mass, 2.27 was the optimal cutoff value of SR, with a sensitivity of 60.2% and a specificity of 84.8%. In the short-axis section, 2.12 was the optimal cutoff value of SR, with a sensitivity of 63.6% and a specificity of 82.5% (**Table 4**). The AUC of SR on the long-axis and short-axis sections was 0.787 and 0.786, respectively. The AUC of ES on the long-axis and short-axis sections was 0.829 and 0.817, respectively. There was no statistical difference in the diagnostic performance of SR in different sections of breast masses, with the p values all greater than 0.05. Similarly, the diagnostic performance of ES was not affected by different planes of breast masses (all $p > 0.05$, **Table 4**).

Compared with SR, ES showed higher AUC (0.829 *vs.* 0.787, $p = 0.003$; 0.817 *vs.* 0.786, $p = 0.028$), sensitivity (89.2% *vs.* 60.2%, $p < 0.001$; 88.9% *vs.* 63.6%, $p < 0.001$), and NPV (91.6% *vs.* 78.8%, $p < 0.001$; 90.9% vs. 79.8%, $p < 0.001$), and lower specificity (67.8% *vs.* 84.8%, $p < 0.001$; 64.0% *vs.* 82.5%, $p < 0.001$) and PPV (61.4% *vs.* 69.4%, $p = 0.024$; 58.6% *vs.* 67.6%, $p = 0.010$) in different planes (**Table 4**). The comparison of ROC curves between ES and SR is shown in **Figure 4**.

TABLE 4 | Comparison of the diagnostic performance of elasticity score and strain ratio.

Parameter	SR			ES			Long axis	Short axis
	Long axis	Short axis	*p*	Long axis	Short axis	*p*	*p* (SR *vs.* ES)	*p* (SR *vs.* ES)
Cutoffs	2.27	2.12						
AUC	0.787 (0.759, 0.814)	0.786 (0.758, 0.812)	0.928	0.829 (0.803, 0.853)	0.817 (0.790, 0.841)	0.229	0.003	0.028
Sensitivity, %	60.2 (54.8, 65.5)	63.6 (58.1, 68.7)	0.278	89.2 (85.3, 92.3)	88.9 (85.0, 92.0)	>0.999	<0.001	<0.001
Specificity, %	84.8 (81.6, 87.6)	82.5 (79.2, 85.5)	0.223	67.8 (63.8, 71.6)	64.0 (60.0, 67.9)	0.053	<0.001	<0.001
PPV, %	69.4 (64.8, 73.7)	67.6 (63.2, 71.7)	0.632	61.4 (58.4, 64.3)	58.6 (55.8, 61.4)	0.376	0.024	0.010
NPV, %	78.8 (76.4, 81.0)	79.8 (77.3, 82.0)	0.671	91.6 (88.8, 93.7)	90.9 (88.0, 93.2)	0.728	<0.001	<0.001
LR+	4.0 (3.2, 4.9)	3.6 (3.0, 4.4)		2.8 (2.4, 3.1)	2.5 (2.2, 2.8)			
LR-	0.5 (0.4, 0.5)	0.4 (0.4, 0.5)		0.2 (0.1, 0.2)	0.2 (0.1, 0.2)			

SR, strain ratio; ES, elasticity score; AUC, the area under curve; PPV, positive predictive value; NPV, predictive value.
LR+, positive diagnostic likelihood ratios; LR-, negative diagnostic likelihood ratios.
95% confidence interval in parentheses.

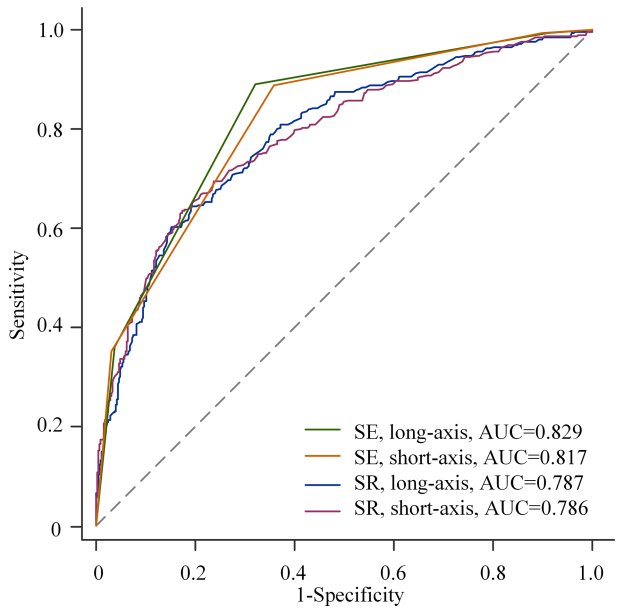

FIGURE 4 | Receiver operating characteristic (ROC) curves for elasticity score (ES) and strain ratio (SR) in different planes.

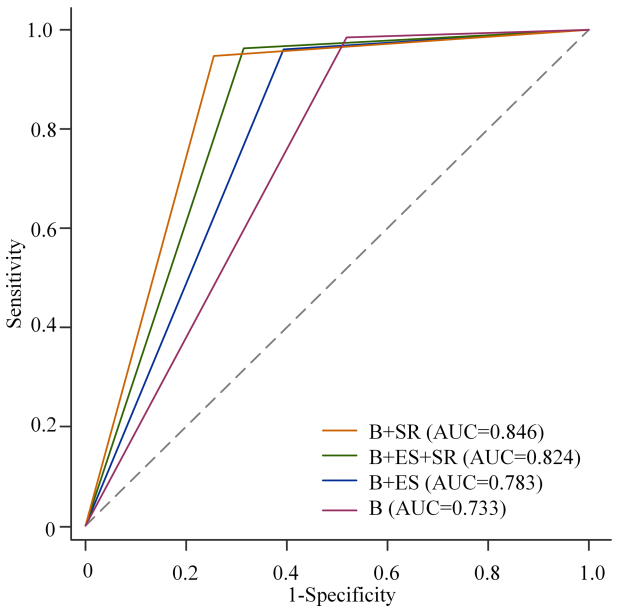

FIGURE 5 | Receiver operating characteristic (ROC) curves for B-mode ultrasound (B) alone, B-mode ultrasound combined with elasticity score (ES), and/or strain ratio (SR). Among the three combinations, the AUC of BI-RADS classification combined with SR was the highest, and that of BI-RADS classification combined with SE was the lowest (0.846 *vs*. 0.824, $p = 0.001$; 0.846 vs. 0.783, $p < 0.001$; 0.824 *vs*. 0.783, $p < 0.001$).

Diagnostic Value of BI-RADS Combined ES and SR

When combined with ES and SR, the diagnostic performance of the re-assessed BI-RADS classification was as follows: the AUC increased from 0.733 to 0.824 ($p < 0.001$); the specificity increased from 48.1% to 68.5% ($p < 0.001$) without a decrease in the sensitivity (98.5% *vs*. 96.4%, $p = 0.065$), and the PPV increased from 52.2% to 63.7% ($p < 0.001$) without a loss in the NPV (98.2% *vs*. 97.1%, $p = 0.327$, **Table 5**).

The AUC, specificity, and PPV were higher than those of BI-RADS classification alone by the addition of ES or SR to the BI-RADS classification (all $p < 0.05$). However, the sensitivity decreased from 98.5% to 96.1% (BI-RADS combined with ES, $p = 0.039$) and 94.9% (BI-RADS combined with SR, $p = 0.004$), respectively. There was no statistically significant difference in NPV, with all $p > 0.05$ (**Table 5**). The comparison of the AUC of the three combination methods is shown in **Figure 5**.

The Value of ES and SR in Reducing Unnecessary Biopsy

The value of ES and SR in reducing biopsy of BI-RADS 4a lesions is summarized in **Table 6**. When BI-RADS was combined with ES, biopsy was avoided in 80 masses, and the biopsy rate decreased from 100% to 68.3% ($p < 0.001$). When combined with SR, 164 masses avoided biopsy, with a lower biopsy rate

TABLE 5 | Diagnostic value of BI-RADS and combined tests with strain ratio and/or elasticity score.

Parameter	BI-RADS	B+ES		B+SR		B+ES+SR	
		Combined	p*	Combined	p*	Combined	p*
AUC	0.733 (0.703, 0.761)	0.783 (0.755, 0.810)	<0.001	0.846 (0.821, 0.869)	<0.001	0.824 (0.798, 0.849)	<0.001
Sensitivity, %	98.5 (96.5, 99.5)	96.1 (93.4, 97.9)	0.039	94.9 (91.9, 97.0)	0.004	96.4 (93.8, 98.1)	0.065
Specificity, %	48.1 (44.0, 52.3)	60.6 (56.4, 64.6)	<0.001	74.4 (70.6, 77.9)	<0.001	68.5 (64.6, 72.3)	<0.001
PPV, %	52.2 (50.2, 54.1)	58.3 (55.8, 60.8)	0.034	68.0 (64.9, 71.0)	<0.001	63.7 (60.9, 66.5)	<0.001
NPV, %	98.2 (95.9, 99.3)	96.4 (94.0, 97.9)	0.164	96.2 (94.1, 97.6)	0.117	97.1 (95.0, 98.3)	0.327
LR+	1.9 (1.8, 2.1)	2.4 (2.2, 2.7)	NA	3.7 (3.2, 4.3)	NA	3.1 (2.7, 3.5)	NA
LR-	0.03 (0.01, 0.08)	0.07 (0.04, 0.1)	NA	0.07 (0.04, 0.1)	NA	0.05 (0.03, 0.09)	NA

B, BI-RADS; ES, elasticity score; SR, strain ratio; AUC, the area under curve.
PPV, positive predictive value; NPV, negative predictive value.
LR+, positive diagnostic likelihood ratios; LR-, negative diagnostic likelihood ratios; NA, not applicable.
**Compared with BI-RADS classification alone. 95% confidence interval in parentheses.*

TABLE 6 | The value of ES and SR in reducing biopsy of BI-RADS 4a lesions.

Parameter	BI-RADS	B+ES		B+SR		B+ES+SR	
		Combined	p*	Combined	p*	Combined	p*
Number of 4a lesions	252	172		88		127	
Number of 3 to 4a		80		29		23	
Number of 4a to 3		160		193		148	
Masses avoid biopsy	0	80		164		125	
Biopsy rate, %	100 (252/252)	68.3 (172/252)	<0.001	34.9 (88/252)	<0.001	50.4 (127/252)	<0.001
Malignant rate of biopsy, %	11.5 (29/252)	12.2 (21/172)	0.826	19.3 (17/88)	0.065	17.3 (22/127)	0.117

B, BI-RADS; ES, elasticity score; SR, strain ratio.
**Compared with BI-RADS classification alone.*

(34.9% vs. 100%, $p < 0.001$). When combined with both ES and SR, biopsy of 125 masses was avoided and the biopsy rate decreased to 50.4% ($p < 0.001$). There was no statistical difference in the malignant rate of biopsy regardless of the combination of BI-RADS and SE (all $p > 0.05$).

DISCUSSION

This prospective multicenter study explored the auxiliary value of two SE diagnostic methods, ES and SR, in the assessment of B-mode ultrasound breast lesions. Our results indicate that ES has a higher AUC, sensitivity, and NPV, but lower specificity and PPV in differentiating benign from malignant breast masses compared with SR. The AUC, specificity, and PPV of BI-RADS combined with ES and SR were higher than those of BI-RADS alone, without the loss of sensitivity and NPV. In addition, BI-RADS combined with ES or/and SR can significantly reduce the biopsy rate of BI-RADS 4a lesions without affecting the malignant rate of biopsy.

Recently, a new SE technique equipped in Samsung ultrasound system has been more and more widely used, and a multicenter study to explore how to make better use of its strain technique is necessary. Studies have shown that the ES and SR of SE techniques show good diagnostic accuracy in distinguishing benign from malignant breast masses (16, 17). These are consistent with our result that both ES and SR have statistical differences in the differentiation between benign and malignant breast masses. However, 3.5 (10), 4.2 (16), 2.3 (17), and 4.5 (18) were used as cutoff values of SR to distinguish benign and malignant breast masses. The difference in the cutoff value of SR may be caused by the difference in strain calculation methods of various equipment vendors (17). In addition, the measurement of SR is greatly affected by the initial shear modulus and elastic nonlinearity of the lesion, as well as the pre-compression during image acquisition (19). In the previous single-center study, the cutoff value of SR was 1.765, and the sensitivity and specificity were 76% and 75%, respectively. In our multicenter study, 2.27 was the optimal cutoff value of SR, with a sensitivity of 60.2% and a specificity of 84.8%. The data for this study come from nine different hospitals, and the cutoff value of SR may be more objective.

The influence of different planes of breast masses on elastography imaging was discussed in this study. The results showed that there were no statistical differences in the diagnostic performance of both ES and SR in the long-axis and short-axis sections, which reflected the stability of SE. With respect to the diagnostic performance of ES and SR in the diagnosis of breast lesions, our study showed that ES was superior to SR, with a higher AUC (0.829 *vs.* 0.787, $p < 0.001$). A previous study showed that ES was the most useful in the identification of benign and malignant breast masses among the four diagnostic methods (ES, SR, distance ratio, and area ratio) of SE (20), which was consistent with our result. However, some studies showed that there was no significant statistical difference in the diagnostic value of ES and SR in distinguishing benign and malignant breast masses (10, 16). The operator dependence of elastography may be one of the reasons.

Elastography was considered to be helpful to improve the specificity of conventional ultrasound (11). In this study, the combination of BI-RADS and SE was in the following three forms: BI-RADS combined with ES, BI-RADS combined with SR, and BI-RADS combined with both ES and SR. Our results indicated that the combination of ES and/or SR could significantly improve the AUC and specificity of BI-RADS, which was consistent with the guidelines. Therefore, SE can be used as a useful additional method for a conventional ultrasound. Among the three combinations, the AUC of BI-RADS classification combined with SR was the highest, followed by that of BI-RADS classification combined with both ES and SR, and that of BI-RADS classification combined with SE was the lowest (0.846 *vs.* 0.824, $p = 0.001$; 0.846 *vs.* 0.783, $p < 0.001$; 0.824 *vs.* 0.783, $p < 0.001$). However, the combination of BI-RADS classification and ES or SR decreased the sensitivity compared to the BI-RADS evaluation alone (98.5% *vs.* 96.1%, $p = 0.039$; 98.5% *vs.* 94.9%, $p = 0.004$). When combined with both ES and SR, the sensitivity of the BI-RADS classification decreased from 98.5% to 96.4% with no statistical difference ($p = 0.065$). Therefore, BI-RADS classification combined with both ES and SR performed best to improve specificity without the loss of sensitivity.

The study showed that SR can be used as a valuable method for the evaluation of breast lesions in categories 3 and 4a, but not in categories 4b and 4c (21). Similarly, our results showed that the SR value for category 4a lesions was significantly higher than that for category 3 lesions, but there was no significant difference between category 4b and 4c lesions. For breast lesions that were highly suspected for malignancy by conventional ultrasound, the stiffness of the tissue had little effect on the patient's clinical

decision-making (21). Elastography may play a role in improving the selection of biopsy for patients with low suspicion lesions (20). BI-RADS category 3 or 4a lesions were upgraded or downgraded based on the results of ES and SR. This multicenter study showed that all three combined methods could reduce the biopsy rate of category 4a lesions without reducing the malignant rate of biopsy, and BI-RADS classification combined with SR was found to be the most useful. Therefore, elastography imaging can be used as a non-invasive auxiliary method to reduce unnecessary biopsy of BI-RADS 4a lesions, thus avoiding negative emotions of patients and complications of tissue biopsy.

The main limitation of our study was the uneven distribution of the patient population and histopathological results. In addition, the repeatability of the breast SE technique with the Samsung ultrasound system was not explored in this study. The repeatability of elastography is mainly manifested in the variability of data acquisition and interpretation (22). Our prospective studies followed very strict procedural protocols to minimize differences among radiologists in data acquisition and interpretation. Lastly, some patients were unable to be included in this study because they did not get a reliable SE assessment. On the one hand, breast masses do not meet the requirements of elastic quality indicators. On the other hand, the breast mass is too large and occupies the whole elastic frame, so it is impossible to evaluate the elasticity.

In summary, the optimal cutoff value of SR for differentiating benign from malignant masses was 2.27, with a sensitivity of 60.2% and a specificity of 84.8%. In addition, SE can be used as a useful and non-invasive additional method to improve the diagnostic performance of conventional ultrasound by increasing AUC and specificity and reducing unnecessary biopsy of BI-RADS 4a lesions.

DATA AVAILABILITY STATEMENT

The raw data supporting the conclusions of this article will be made available from the corresponding author upon reasonable request.

ETHICS STATEMENT

The studies involving human participants were reviewed and approved by the Institutional Review Board of Tongji Medical College of Huazhong University of Science & Technology. The patients/participants provided their written informed consent to participate in this study.

AUTHOR CONTRIBUTIONS

Conception and design of the study: X-WC and CD. Acquisition of data: QW, Y-JY, X-RY, FJ, JL, GW, YiW, YuW, Z-PP, and J-HH. Analysis and interpretation of data: QW, G-GW, JS, and X-WC. Drafting the article: QW, Y-JY, and X-WC. Revising it critically for important intellectual content: all authors. All authors contributed to the article and approved the submitted version.

FUNDING

This research was supported by the National Natural Science Foundation of China (Grant No. 82071953), Key R&D Projects of Science and Technology of Hubei Province in 2020 (Grant No. 2020BCB022), and Tongji Hospital (HUST) Foundation for Excellent Young Scientist (Grant No. 2020YQ01).

REFERENCES

1. Sung H, Ferlay J, Siegel RL, Laversanne M, Soerjomataram I, Jemal A, et al. Global Cancer Statistics 2020: GLOBOCAN Estimates of Incidence and Mortality Worldwide for 36 Cancers in 185 Countries. *CA Cancer J Clin* (2021) 71(3):209–49. doi: 10.3322/caac.21660
2. Hooley RJ, Scoutt LM, Philpotts LE. Breast Ultrasonography: State of the Art. *Radiology* (2013) 268(3):642–59. doi: 10.1148/radiol.13121606
3. Ji T, Gao S, Liu Z, Xing H, Zhao G, Ma Q. 99mtc-Glu-C(RGDyK)-Bombesin SPECT Can Reduce Unnecessary Biopsy of Masses That Are BI-RADS Category 4 on Ultrasonography. *J Nucl Med* (2016) 57(8):1196–200. doi: 10.2967/jnumed.115.168773
4. Shiina T, Nightingale KR, Palmeri ML, Hall TJ, Bamber JC, Barr RG, et al. WFUMB Guidelines and Recommendations for Clinical Use of Ultrasound Elastography: Part 1: Basic Principles and Terminology. *Ultrasound Med Biol* (2015) 41(5):1126–47. doi: 10.1016/j.ultrasmedbio.2015.03.009
5. Itoh A, Ueno E, Tohno E, Kamma H, Takahashi H, Shiina T, et al. Breast Disease: Clinical Application of US Elastography for Diagnosis. *Radiology* (2006) 239(2):341–50. doi: 10.1148/radiol.2391041676
6. Barr RG, Nakashima K, Amy D, Cosgrove D, Farrokh A, Schafer F, et al. WFUMB Guidelines and Recommendations for Clinical Use of Ultrasound Elastography: Part 2: Breast. *Ultrasound Med Biol* (2015) 41(5):1148–60. doi: 10.1016/j.ultrasmedbio.2015.03.008
7. Yi A, Cho N, Chang JM, Koo HR, La Yun B, Moon WK. Sonoelastography for 1,786 Non-Palpable Breast Masses: Diagnostic Value in the Decision to Biopsy. *Eur Radiol* (2012) 22(5):1033–40. doi: 10.1007/s00330-011-2341-x
8. Xiao X, Jiang Q, Wu H, Guan X, Qin W, Luo B. Diagnosis of Sub-Centimetre Breast Lesions: Combining BI-RADS-US With Strain Elastography and Contrast-Enhanced Ultrasound-a Preliminary Study in China. *Eur Radiol* (2017) 27(6):2443–50. doi: 10.1007/s00330-016-4628-4
9. D'Orsi C, Sickles E, Mendelson E, Morris E. *ACR BI-RADS® Atlas, Breast Imaging Reporting and Data System. 5th ed.* Reston, VA: American College of Radiology (2013).
10. Bojanic K, Katavic N, Smolic M, Peric M, Kralik K, Sikora M, et al. Implementation of Elastography Score and Strain Ratio in Combination With B-Mode Ultrasound Avoids Unnecessary Biopsies of Breast Lesions. *Ultrasound Med Biol* (2017) 43(4):804–16. doi: 10.1016/j.ultrasmedbio.2016.11.019
11. Săftoiu A, Gilja OH, Sidhu PS, Dietrich CF, Cantisani V, Amy D, et al. The EFSUMB Guidelines and Recommendations for the Clinical Practice of Elastography in Non-Hepatic Applications: Update 2018. *Ultraschall Med* (2019) 40(4):425–53. doi: 10.1055/a-0838-9937
12. Lee SH, Chung J, Choi HY, Choi SH, Ryu EB, Ko KH, et al. Evaluation of Screening US-Detected Breast Masses by Combined Use of Elastography and Color Doppler US With B-Mode US in Women With Dense Breasts: A Multicenter Prospective Study. *Radiology* (2017) 285(2):660–9. doi: 10.1148/radiol.2017162424
13. Hatzung G, Grunwald S, Zygmunt M, Geaid AA, Behrndt PO, Isermann R, et al. Sonoelastography in the Diagnosis of Malignant and Benign Breast

Lesions: Initial Clinical Experiences. *Ultraschall Med* (2010) 31(6):596–603. doi: 10.1055/s-0029-1245526
14. Di Segni M, de Soccio V, Cantisani V, Bonito G, Rubini A, Di Segni G, et al. Automated Classification of Focal Breast Lesions According to S-Detect: Validation and Role as a Clinical and Teaching Tool. *J Ultrasound* (2018) 21(2):105–18. doi: 10.1007/s40477-018-0297-2
15. DeLong ER, DeLong DM, Clarke-Pearson DL. Comparing the Areas Under Two or More Correlated Receiver Operating Characteristic Curves: A Nonparametric Approach. *Biometrics* (1988) 44(3):837–45. doi: 10.2307/2531595
16. Mutala TM, Ndaiga P, Aywak A. Comparison of Qualitative and Semiquantitative Strain Elastography in Breast Lesions for Diagnostic Accuracy. *Cancer Imaging* (2016) 16(1):12. doi: 10.1186/s40644-016-0070-8
17. Cantisani V, David E, Barr RG, Radzina M, de Soccio V, Elia D, et al. US-Elastography for Breast Lesion Characterization: Prospective Comparison of US BIRADS, Strain Elastography and Shear Wave Elastography. *Ultraschall Med* (2020) 42(5):533–40. doi: 10.1055/a-1134-4937
18. Balçık A, Polat AV, Bayrak İK, Polat AK. Efficacy of Sonoelastography in Distinguishing Benign From Malignant Breast Masses. *J Breast Health* (2016) 12(1):37–43. doi: 10.5152/tjbh.2015.2843
19. Rosen D, Jiang J. Modeling Uncertainty of Strain Ratio Measurements in Ultrasound Breast Strain Elastography: A Factorial Experiment. *IEEE Trans Ultrason Ferroelectr Freq Control* (2020) 67(2):258–68. doi: 10.1109/tuffc.2019.2942821
20. Menezes R, Sardessai S, Furtado R, Sardessai M. Correlation of Strain Elastography With Conventional Sonography and FNAC/Biopsy. *J Clin Diagn Res* (2016) 10(7):Tc05–10. doi: 10.7860/jcdr/2016/20239.8177
21. Zhao XB, Yao JY, Zhou XC, Hao SY, Mu WJ, Li LJ, et al. Strain Elastography: A Valuable Additional Method to BI-RADS? *Ultraschall Med* (2018) 39 (5):526–34. doi: 10.1055/s-0043-115108
22. Regner DM, Hesley GK, Hangiandreou NJ, Morton MJ, Nordland MR, Meixner DD, et al. Breast Lesions: Evaluation With US Strain Imaging–Clinical Experience of Multiple Observers. *Radiology* (2006) 238(2):425–37. doi: 10.1148/radiol.2381041336

Conflict of Interest: Author CD was employed by company Hirslanden Clinic.

The remaining authors declare that the research was conducted in the absence of any commercial or financial relationships that could be construed as a potential conflict of interest.

Publisher's Note: All claims expressed in this article are solely those of the authors and do not necessarily represent those of their affiliated organizations, or those of the publisher, the editors and the reviewers. Any product that may be evaluated in this article, or claim that may be made by its manufacturer, is not guaranteed or endorsed by the publisher.

frontiers in Oncology

ORIGINAL RESEARCH
published: 10 November 2021
doi: 10.3389/fonc.2021.745242

The Potential Value of Texture Analysis Based on Dynamic Contrast-Enhanced MR Images in the Grading of Breast Phyllode Tumors

Xiaoguang Li[1†], Hong Guo[1†], Chao Cong[1], Huan Liu[2], Chunlai Zhang[1], Xiangguo Luo[1], Peng Zhong[3], Hang Shi[4], Jingqin Fang[1] and Yi Wang[1*]*

[1] Department of Radiology, Daping Hospital, Army Medical University, Chongqing, China, [2] GE Healthcare, Shanghai, China, [3] Department of Pathology, Daping Hospital, Army Medical University, Chongqing, China, [4] Department of Information, Daping Hospital, Army Medical University, Chongqing, China

Purpose: To explore the value of texture analysis (TA) based on dynamic contrast-enhanced MR (DCE-MR) images in the differential diagnosis of benign phyllode tumors (BPTs) and borderline/malignant phyllode tumors (BMPTs).

Methods: A total of 47 patients with histologically proven phyllode tumors (PTs) from November 2012 to March 2020, including 26 benign BPTs and 21 BMPTs, were enrolled in this retrospective study. The whole-tumor texture features based on DCE-MR images were calculated, and conventional imaging findings were evaluated according to the Breast Imaging Reporting and Data System (BI-RADS). The differences in the texture features and imaging findings between BPTs and BMPTs were compared; the variates with statistical significance were entered into logistic regression analysis. The receiver operating characteristic (ROC) curve was used to assess the diagnostic performance of models from image-based analysis, TA, and the combination of these two approaches.

Results: Regarding texture features, three features of the histogram, two features of the gray-level co-occurrence matrix (GLCM), and three features of the run-length matrix (RLM) showed significant differences between the two groups (all $p < 0.05$). Regarding imaging findings, however, only cystic wall morphology showed significant differences between the two groups ($p = 0.014$). The areas under the ROC curve (AUCs) of image-based analysis, TA, and the combination of these two approaches were 0.687 (95% CI, 0.518–0.825, $p = 0.014$), 0.886 (95% CI, 0.760–0.960, $p < 0.0001$), and 0.894 (95% CI, 0.754–0.970, $p < 0.0001$), respectively.

Conclusion: TA based on DCE-MR images has potential in differentiating BPTs and BMPTs.

Keywords: breast, phyllodes tumors, magnetic resonance imaging, texture analysis, differential diagnosis

OPEN ACCESS

Edited by:
Pilar López-Larrubia, Consejo Superior de Investigaciones Científicas (CSIC), Spain

Reviewed by:
Stefano Marrone, University of Naples Federico II, Italy
Sarah Boughdad, Centre Hospitalier Universitaire Vaudois (CHUV), Switzerland
Peter Gibbs, Memorial Hospital, United States

***Correspondence:**
Jingqin Fang
jingqin0405@163.com
Yi Wang
ywhxl@qq.com

†These authors have contributed equally to this work

Specialty section:
This article was submitted to Cancer Imaging and Image-directed Interventions, a section of the journal Frontiers in Oncology

Received: *21 July 2021*
Accepted: *18 October 2021*
Published: *10 November 2021*

Citation:
Li X, Guo H, Cong C, Liu H, Zhang C, Luo X, Zhong P, Shi H, Fang J and Wang Y (2021) The Potential Value of Texture Analysis Based on Dynamic Contrast-Enhanced MR Images in the Grading of Breast Phyllode Tumors. Front. Oncol. 11:745242. doi: 10.3389/fonc.2021.745242

INTRODUCTION

Phyllodes tumors (PTs) of the breast are rare fibroepithelial neoplasms, accounting for 0.3% to 1% of all primary breast tumors. PTs are classified as benign, borderline, and malignant, according to the latest edition of the World Health Organization (WHO) classification of the breast, which is based on the semiquantitative evaluation of key histological features, such as stromal cellularity, stromal atypia, stromal mitosis, stromal overgrowth, and tumor margin. Surgery is an essential means to treat PTs, and different surgical methods are commonly selected according to histologic grade. Generally, local excision is applied for BPTs, and wide excision or mastectomy is used for BMPTs (1). Therefore, the preoperative differentiation between benign and malignant PTs would be significant for surgery planning. Although a fine-needle biopsy is sometimes helpful in determining the preoperative diagnosis of PTs, it is insufficient for PT grading because of potential inadequate cytologic samples resulting from the heterogeneous nature of PTs (2).

Magnetic resonance imaging (MRI) is a well-established method in breast imaging, with various clinical applications, including the noninvasive differentiation between benign and malignant breast lesions, preoperative staging, detection of recurrence, and the evaluation of prognosis (3, 4). At present, dynamic contrast-enhanced MRI (DCE-MRI) is the most sensitive imaging technique for breast cancer diagnosis and provides excellent morphological and, to some extent, also functional information (4). However, breast MRI still has limitations in the differentiation between benign and malignant PTs to date. Firstly, MRI morphology alone does not differentiate benign from malignant PTs (5). Secondly, many studies have reported that noncontrast MRI has little significance in the differentiation of benign and malignant PTs (5, 6). Even functional imaging parameters, such as the ADC value, still have contradictions in different studies (7, 8). Finally, PTs could demonstrate significant enhancement on DCE-MRI, regardless of histological type, which may be related to angiogenesis factors that promote the growth of matrix and epithelial components (9). Therefore, it would be valuable to find a new way to improve the diagnostic performance of MR images in differentiating BPTs from BMPTs.

Recently, with the rapid development of digital image processing, texture analysis (TA) has become an important quantitative method for medical image analysis. Compared with the overall or qualitative reports of tumor appearance, TA can provide an accurate local description of tumor complexity, heterogeneity, and dynamic behavior on medical images (10). Many previous studies have shown that TA of DCE-MRI can provide an opportunity to promote clinical decision-making in terms of low-cost and noninvasive evaluation of tumors, such as in histopathologic and molecular subtype classification of breast cancer (11), tumor prognosis (12), and treatment response prediction (13, 14). However, few studies have shown the role of texture features based on DCE-MR images in PT grading (15). The purpose of this study, therefore, was to explore the value of TA based on DCE-MR images in distinguishing BPTs from BMPTs.

Abbreviations: BPTs, benign phyllodes tumors; BMPTs, borderline/malignant phyllodes tumors; AUC, area under the receiver operating characteristic curve; HIS, gray-level histogram; GLCM, gray-level co-occurrence matrix; RLM, run-length matrix; ROC, receiver operating characteristic; VOI, volume of interest; GLevNonU, gray-level non-uniformity; TA, texture analysis.

MATERIALS AND METHODS

Patients

This study was approved by the institutional ethics committee of our hospital [Ratification NO: 2019(160)]. The need for informed consent was waived by the institutional review board (IRB) due to the nature of this retrospective study. The DCE-MRI data of 55 patients with histopathological confirmed PTs from November 2012 to March 2021 were reviewed, and 47 eligible patients were enrolled in this study finally. The exclusion criteria included the following: 1) low-quality images cannot be used for subsequent analysis (n = 3); 2) a history of breast implants in one or both sides (n = 2); and 3) MRI scanning after surgery, chemotherapy, or radiotherapy (n = 3). All the patients were female and between the ages of 16 and 71 years (mean 44.30 ± 10.26 years). Each patient had only 1 lesion in the unilateral breast, 20 lesions in the left, and 27 lesions in the right. Of the 47 PT cases, 26 were benign, 18 were borderline, and 3 were malignant.

Imaging Protocol

MRI was performed using a 1.5-T scanner (MAGNETOM Aera, Siemens Healthcare, Erlangen, Germany) with a dedicated eight-channel breast coil. The MRI protocol included axial turbo inversion recovery magnitude (TIRM) T2WI with fat saturation ($T2WI_{FS}$), axial FL3D-T1WI with nonfat saturation, DWI, and DCE-MRI based on the FL3D sequence. The detailed scan parameters were as follows: $T2WI_{FS}$ (TR 5,600 ms, TE 57 ms, FOV 340 mm×340 mm); T1-FL3D (TR 8.6 ms, TE 4.7 ms, FOV 360 mm×360 mm; DWI (TR 6,300 ms, TE 68 ms, FOV 340 mm × 340 mm b=0, 50, 600, 1000 s/mm^2); and DCE-MRI (TR 4.62 ms, TE 1.75 ms, FOV 360 mm×360 mm). After a 90-s scan, the dynamic contrast-enhanced scan was performed. The contrast agent Gd-DTPA (Magnevist, Bayer Healthcare, Berlin, Germany) was injected into the elbow vein by a high-pressure syringe at a dose of 0.1 mmol/kg and a flow rate of 2.0 ml/s. Subsequently, seven phases were continuously collected without intervals. Each scanning duration was approximately 60.01 s, the layer thickness was 3 mm, and the total time was 7 min. After contrast agent injection, 15 ml of normal saline was injected at the same flow rate.

Imaging Analysis

MR images of all patients were independently reviewed by two senior radiologists (CZ and X-Luo with 10 and 15 years of experience in breast imaging, respectively) blinded to the histopathological results, and the imaging findings were evaluated according to the BI-RADS MRI (16). The following descriptors were recorded: the maximum diameter, shape

(round, oval, or irregular), margin (circumscribed or irregular), $T2WI_{FS}$ signal, hyperintense on $T2WI_{FS}$, hyperintense on T1WI, lobulation (absence or presence), cystic component (absence or presence), and if present, the wall of the cystic component (regular or irregular), internal enhancement characteristics (heterogeneous or homogeneous), and time signal intensity curve (TIC) patterns (type I, persistent pattern, the signal intensity rose continuously during the dynamic observation; type II, plateau pattern, the signal intensity was gradually increased at an early stage and then maintained at a platform level; type III, washout pattern, the signal intensity was increased rapidly at an early stage and then decreased rapidly) (17). All imaging findings were determined by consensus.

Texture Analysis

MaZda software (version 4.7, The Technical University of Lodz, Institute of Electronics, http://www.eletel.p.lodz.pl/mazda/) was used for the TA. Based on our previous study (18), DCE-MR images at phase VII were selected for texture analysis, which showed the best contrast enhancement of PTs. To obtain the reproducible and dependable results for signal intensity measurement, the VOI (volume of interest) of each tumor, which encompassed the whole lesion on each consecutive slice, was manually delineated respectively by the above radiologists. For every VOI, gray-level normalization was performed using the limitation of dynamics $\mu \pm 3\sigma$ (μ is the gray-level mean; σ is the gray-level standard deviation) to minimize the influence of contrast and brightness variations (19). Texture features derived from the gray-level histogram (HIS), the gray-level co-occurrence matrix (GLCM), the gradient matrix (GrM), and the run-length matrix (RLM) were calculated for the VOIs. The numbers of calculated features per feature class are as follows: HIS, n=9; GLCM, n=275; RLM, n=25; GRM n=5; (total number of features per lesion, n= 314). HIS features are calculated based on pixel intensity, regardless of the spatial relationships between pixels in the image (20). GLCM features are calculated based on how often pairs of pixels/voxels with specific values, which could provide information on lesion heterogeneity (21). GrM features are calculated for direction changes in gray-level intensity and represent the image intensity distribution (20). RLM features are calculated for five directions (Z-axis, horizontal, vertical, 45 degrees, and 135 degrees) and represent the number of times there is a run of pixels having a certain gray level (22, 23). The categories of the texture features are listed in **Table 1**. They can be accessed at (http://www.eletel.p.lodz.pl/programy/mazda/download/mazda_manual.pdf).

Statistical Analysis

Statistical analysis was performed using IBM SPSS version 21.0 (IBM Corporation, New York). With regard to the reproducibility of volumetric and texture analysis, interobserver reliability was assessed by intraclass correlation coefficient (ICC) test (0.000–0.200, poor; 0.201–0.400, fair; 0.401–0.600, moderate; 0.601–0.800, good; and 0.801–1.000, excellent). The Kolmogorov–Smirnov and Levene tests were used to determine the normality and homogeneity of the variance, respectively, for all measurement data. Intergroup comparisons were performed with independent sample t-tests and Mann–Whitney U tests for data with normal and abnormal distribution, respectively (24). Quantitative data with a normal distribution are expressed as the means ± standard deviations (SDs), while quantitative data with a skewed distribution are presented as median (quartile 1, quartile 3). Categorical data were shown as a percentage and were analyzed using the chi-square test or Fisher's exact test. To evaluate the effect of conventional MRI findings on tumor classification, we include variables with a value of $p < 0.20$ for multivariate logistic regression. A p-value < 0.05 was considered to be statistically significant. In terms of feature selection, we applied the Institute of Precision Medicine Statistics (IPMs, version 2.0, GE Healthcare). Before feature selection, all parameters are processed by the standardization function of IPMs software to reduce differences in dimensions. The specific steps of feature selection and model establishment are as follows: Firstly, the variance threshold method was used to reduce the redundant features. The threshold value was 0.8; thus, the eigenvalues of the variance smaller than 0.8 were removed (25). Secondly, the univariate analysis was adopted to obtain features with statistically significant differences ($p < 0.05$) between BPT and BMPT groups. Thirdly, the univariate logistic regression analysis was used to retain the variables with statistical differences ($p < 0.05$). Finally, the promising features were fed into multivariate logistic regression analysis with a backward stepwise selection procedure

TABLE 1 | List of texture features in the MaZda software.

Category	Features
Histogram (n = 9)	Mean (histogram's mean); variance (histogram's variance); skewness (histogram's skewness); kurtosis (histogram's kurtosis); Perc.01% (1% percentile); Perc.10% (10% percentile); Perc.50% (50% percentile); Perc.90% (90% percentile); Perc.99% (99% percentile)
Gray-level co-occurrence matrix (n = 275)	AngScMom, Contrast, Correlat, SumOfSqs, InvDfMom, SumAverg, SumVarnc, SumEntrp, Entropy, DifVarnc, DifEntrp. Features are computed for five between-pixels distances (1, 2, 3, 4, 5) and for four various directions (horizontal, vertical, 45 degrees, 135 degrees)
Run-length matrix (n = 25)	RLNonUni, GLevNonU, LngREmph, ShrtREmp, Fraction. Features are computed for 5 various directions (Z-axis, horizontal, vertical, 45 degrees, 135 degrees)
Absolute gradient (n = 5)	GrMean, GrVariance, GrSkewness, GrKurtosis, GrNonZeros (percentage of pixels with non-zero gradient)

AngScMom, angular second moment; Correlat, correlation; DifEntrp, difference entropy; DifVarnc, difference variance; GLevNonU, gray-level non-uniformity; GrKurtosis, absolute gradient kurtosis; GrMean, absolute gradient mean; GrNonZeros, percentage of pixels with nonzero gradient; GrSkewness, absolute gradient skewness; GrVariance, absolute gradient variance; InvDfMom, inverse difference moment; LngREmph, long run emphasis; n = total number of texture features of each category extracted from MaZda; RLNonUni, run length non-uniformity; ShrtREmp, short run emphasis; SumAverg, sum average; SumEntrp, sum entropy; SumOfSqs, sum of squares; SumVarnc, sum variance.

for tumor classification. A combined model integrating promising imaging findings and texture features was also established. The goodness-of-fit of the logistic regression model was evaluated using the Hosmer–Lemeshow test (26). The diagnostic efficacy of these models based on image-based analysis, TA, and the combination of the two approaches was measured by the area under the curve (AUC) of ROC curves. The Delong test was adopted to compare AUCs. A p-value < 0.05 was considered to be statistically significant. A workflow chart of this study is illustrated in **Figure 1**.

RESULTS

Comparison of Texture Features Between BPTs and BMPTs

The interobserver reproducibility of texture features extraction was good, with ICC values ranging from 0.71 to 0.98. In this study, 314 texture features were extracted from the DCE-MR images of each lesion (**Table 1**). A total of 263 nonsignificant features were first eliminated using variance analysis with the threshold value of 0.8 (**Figure 2A**). After removing the redundant features using univariate analysis (**Figure 2B**), a total of 11 significant features remained. Through univariate logistic regression analysis (**Figure 2C**), eight features with statistical differences were retained for further multivariate logistic regression analysis. For the HIS features, the Perc.90% (percentile 90%), mean, and variance in BMPTs were significantly lower than those in BPTs (p = 0.001, 0.003, and 0.004, respectively). For the GLCM features, the S(0,0,1) AngScMom and S(1,0,0)AngScMom in BMPTs were significantly lower than those in BPTs (p = 0.019 and 0.029, respectively). However, for the RLM features, the Z_GLevNonU, 45dgr_GLevNonU, and 135dr_GLevNonU (gray-level nonuniformity in Z-axis, 45, and 135 degree directions, respectively) in BMPTs were significantly higher (p = 0.039, 0.037, and 0.037, respectively) (**Table 2**).

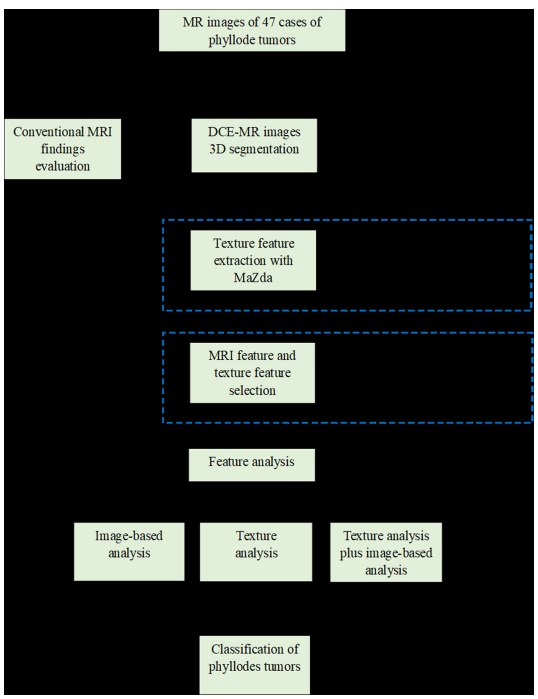

FIGURE 1 | The workflow chart of this study.

The definition and formula of the above features were as follows:

HIS Parameter 1: Perc.90%. A percentile represents the value below which a percentage of observations is calculated.

HIS Parameter 2: Mean. Mean measures the average gray-level intensity within the VOI.

$$\text{Formula}: \Sigma k \frac{k^* g(k)}{\Sigma k g^k}$$

HIS Parameter 3: Variance. Variance is the mean of the squared distances of each intensity value from the mean value. This is a measure of the spread of the distribution about the mean. By definition, variance=σ^2.

$$\text{Formula}: \frac{1}{N_p} \Sigma_{i=1}^{N_p} (X(i) - \bar{X})^2$$

GLCM Parameter: S(0,0,1)AngScMom and S(1,0,0) AngScMom. AngScMom is a measure of image homogeneity. This feature obtains a high value when a gray-level distribution in the image is either constant or periodic.

$$\text{Formula}: \Sigma_{i,j} f(i,j)^2$$

RLM Parameter: Z_GLevNonU, 45dgr_GLevNonU, and 135dr_GLevNonU. GLevNonU measures the similarity of gray-level intensity values in the image, where a lower GLevNonU value correlates with a greater similarity in intensity values.

$$\text{Formula}: \frac{\Sigma_{i=1}^{N_g} \left(\Sigma_{j=1}^{N_r} \quad p(i,j|\theta) \right)^2}{N_r(\theta)}$$

Comparison of Conventional MRI Findings Between BPTs and BMPTs

The conventional MRI findings of BPTs and BMPTs are summarized in **Table 3**. Between the two groups, except the cystic wall morphology, all the conventional MRI findings including tumor shape, cystic component, lobulation, margin, $T2WI_{FS}$ signal, hyperintense on $T2WI_{FS}$, hyperintense on T1WI, dark internal septation, enhancement signal, and TIC pattern showed no significant differences. The irregular cyst wall was more commonly seen in BMPTs (11/18, 61.1%) than in BPTs (5/22, 22.7%) (p = 0.014) (**Figures 3**, **4**).

ROC Analysis and Diagnostic Performance

In the comparison of conventional MRI findings between BPTs and BMPTs, three parameters with p < 0.20 were obtained: they were the max diameter (p = 0.159), enhancement signal (p = 0.137), and cystic wall morphology (p = 0.014). Further

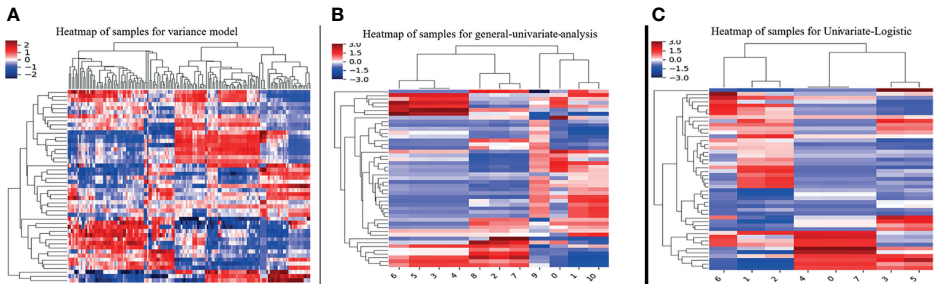

FIGURE 2 | The steps of texture features reduction and selection by the method of **(A)** variance, **(B)** univariate analysis, and **(C)** univariate logistic regression.

TABLE 2 | Comparisons of texture features from DCE-MR images between BPT and BMPT groups.

Variable	BPT (n = 26)	BMPT (n = 21)	F-value	p value
RLM				
Z_GLevNonU	370.02 (206.79, 1059.87)	1204.56 (489.95, 3072.55)	-2.054	0.039
135dr_GLevNonU	367.10 (207.28, 1061.48)	1236.88 (486.62, 3166.87)	-2.076	0.037
45dgr_GLevNonU	370.81 (203.73, 1066.45)	1224.05 (487.62, 3176.61)	-2.054	0.037
GLCM				
S (0,0,1) AngScMom	36.68 (25.39, 57.51)	24.99 (19.28, 42.06)	-2.054	0.019
S (1,0,0) AngScMom	42.01 (26.17, 60.59)	29.41 (22.36, 43.30)	-1.883	0.029
Histogram				
Perc.90%	43.17 (37.80, 52.05)	25.00 (15.70, 40.00)	3.338	0.001
Variance	39.53 (12.31, 60.36)	9.74 (5.91, 25.99)	2.889	0.004
Mean	36.40 (27.20, 45.44)	21.60 (12.73, 33.77)	3.295	0.003

Data are expressed as median (quartile 1, quartile 3), and intergroup comparison was performed with Mann–Whitney U test.
BPT, Benign phyllode tumor; BMPT, borderline/malignant phyllode tumor; RLM, run-length matrix; GLCM, gray-level co-occurrence matrix; Z_GLevNonU, 135dr_GLevNonU, and 45dgr_GLevNonU, gray-level non-uniformity calculated for Z-axis, 135-, and 45-degree directions, respectively; AngScMom, angular second moment; Perc.90%, percentile 90%.

multivariable logistic regression analysis found that the cystic wall morphology differed significantly between the two groups (p = 0.020) and was thus regarded as an independent variable. The final regression model achieved an AUC of 0.687 (sensitivity 61.1%, specificity 76.2%, and 95%CI, 0.518-0.825) (p = 0.014). Multivariate logistic regression analysis of eight texture features found that Z_GLevNonU, S(0,0,1)AngScMom, Perc.90%, variance, and mean differed significantly between the two groups (p = 0.029, 0.031, 0.004, 0.001, and 0.003, respectively) and were thus regarded as independent variables. The following equation was obtained: Logit(p) = 0.067×S(0,0,1)AngScMom + 0.001×Z_GLevNonU +1.944×Perc.90%−0.301×Variance−1.994×Mean−4.552. The model exhibited an AUC of 0.886 (95%CI, 0.760–0.960) (p < 0.0001), with a sensitivity of 85.7% and a specificity of 80.8%. The combined model showed an AUC of 0.894 (95%CI, 0.754–0.970) (p < 0.0001), with a sensitivity of 94.4% and a specificity of 76.2%. The Hosmer–Lemeshow test showed a good model fit for these models from image-based analysis, TA, and the combination of the two approaches (p = 1.000, 0.788, and 0.588, respectively) (**Table 4** and **Figure 5**). The Delong test showed that both the AUC of TA and the combined model were significantly higher than that of image-based analysis (p=0.010 and 0.003, respectively). However, no significant difference was found between TA and the combined model (p=0.893).

DISCUSSION

The latest frontiers in medical image analysis have highlighted the implementation of computer vision principles and analytical techniques for quantifying and describing medical images. TA is a statistical method that can be used to characterize the gray-level signal intensity and its spatial variation within an image, capturing image patterns usually unrecognizable or indistinguishable to the human eye (10). Compared with conventional imaging methods, TA can provide objective and additional quantitative image information on lesions independent of the subjective judgment and experience of clinicians or radiologists, adding potential clinical value (18). Recently, TA has been widely used to evaluate tumor heterogeneity. Many studies also indicate that texture features are good predictors of breast tumor classification (10, 11, 19). In the present study, we attempted to evaluate the role of TA based on DCE-MR images in grading PTs. Our results suggested that TA based on DCE-MR images has potential in differentiating BPTs and BMPTs. We found that three histogram features, two GLCM features, and three RLM features were significantly different between BPTs and BMPTs. Moreover, TA or combined with imaging findings exhibited better diagnostic performance in differentiating BPTs and BMPTs than that from imaging analysis alone.

TABLE 3 | Conventional MRI findings between BPT and BMPT groups.

MRI findings	BPT (n = 26)	BMPT (n = 21)	p-value
Max diameter	4.58 ± 2.38	5.55 ± 2.18	0.159[a]
Shape			0.495[b]
Round	10 (38.5%)	7 (33.3%)	
Oval	9 (34.6%)	5 (23.8%)	
Irregular	7 (26.9%)	9 (42.9%)	
$T2WI_{FS}$ signal			0.851[b]
Homogeneous	8 (30.8%)	7 (33.3%)	
Heterogeneous	18 (69.2%)	14 (66.7%)	
Hyperintense on $T2WI_{FS}$			0.472[b]
Absent	3 (11.5%)	4 (19.0%)	
Present	23 (88.5%)	17 (81.0%)	
Hyperintense on T1WI			0.466[b]
Absent	22 (84.6%)	16 (76.2%)	
Present	4 (15.4%)	5 (23.8%)	
Cystic component			0.916[b]
Absent	4 (15.4%)	3 (14.3%)	
Present	22 (84.6%)	18 (85.7%)	0.014[b]
Regular wall	17 (77.3%)	7 (38.9%)	
Irregular wall	5 (22.7%)	11 (61.1%)	
Lobulation			0.933[b]
Absent	9 (34.6%)	7 (33.3%)	
Present	17 (65.4%)	14 (66.7%)	
Margin			0.774[b]
Regular	15 (57.7%)	11 (52.4%)	
Circumscribed	11 (42.3%)	10 (47.6%)	
Dark internal septation			0.900[b]
Absent	19 (73.1%)	15 (71.4%)	
Present	7 (26.9%)	6 (28.6%)	
Enhancement signal			0.137[b]
Homogeneous	14 (53.8%)	6 (28.6%)	
Heterogeneous	12 (46.2%)	15 (71.4%)	
TIC pattern			0.691[b]
Type I	8 (30.8%)	7 (33.3%)	
Type II	17 (65.4%)	12 (57.1%)	
Type III	1 (3.8%)	2 (9.5%)	

Quantitative variables are expressed as mean ± standard deviation. Qualitative variables are expressed as proportions. [a]Data were performed with independent t-test. [b]Data were performed with chi-square test. The level of significance for intergroup differences was set at $p < 0.05$.
BPT, benign phyllode tumor; BMPT, borderline/malignant phyllode tumor; $T2WI_{FS}$, T2 weighted imaging with fat saturation; T1WI, T1 weighted imaging; TIC, time-intensity curve.

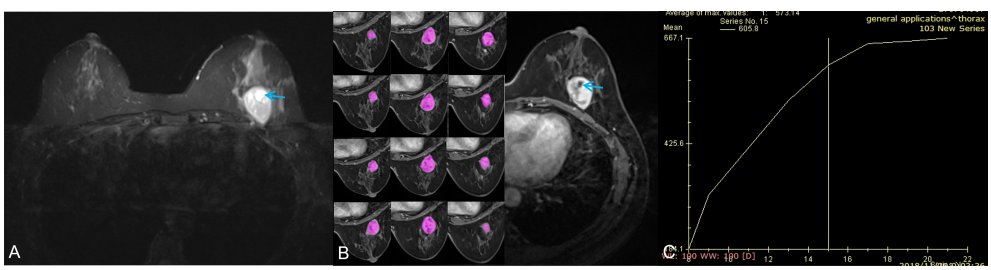

FIGURE 3 | A 42-year-old woman with a benign phyllodes tumor. **(A)** Axial T2WI showed a heterogeneous mass in the left breast, with a regular wall of cystic area (red arrow). **(B)** Axial DCE-MRI showed the mass with heterogeneous enhancement and non-enhancement cystic area; the segmentation of VOI was shown on the left series images. **(C)** The time-intensity curve was type II (plateau pattern).

As a first-order texture, gray-level histogram analysis can be used to describe the distribution of pixel intensities within an image without considering the neighboring pixels. The mean value reflects the central trend and average level of grayscale, while the percentile provides the highest gray-level value that contains a given percentage of the pixels in the VOI. It has been suggested that the whole-lesion analysis of breast tumors instead of the single slice measurement may better depict the tissue heterogeneity (27). In this study, the mean gray value of BPTs was significantly greater than that of BMPTs, indicating that the

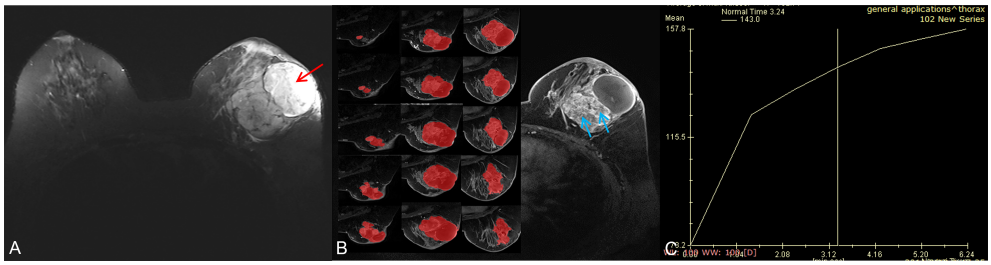

FIGURE 4 | A 56-year-old woman with a borderline/malignant phyllodes tumor. **(A)** Axial T2WI showed a heterogeneous mass with a huge cystic cavity (red arrow) in the left breast. **(B)** Axial DCE-MRI showed the mass with heterogeneous enhancement and large numbers of unenhanced areas with irregular walls (blue arrow); the segmentation of VOI was shown on the left series images. **(C)** The time-intensity curve was type I (persistent pattern).

TABLE 4 | ROC analysis of image-based analysis, texture analysis, and the combination analysis.

Logistic regression model	AUC	95% CI	Sensitivity	Specificity
Image-based analysis	0.687	0.518-0.825	0.611	0.762
Texture analysis	0.886	0.760-0.960	0.857	0.808
Combination analysis	0.894	0.754-0.970	0.944	0.762

ROC, receiver operating characteristic; AUC, area under receiver operator characteristic curve; CI, confidence interval.

average signal intensity of BPTs was higher than that of BMPTs on DCE-MR images. This result was consistent with our previous study (18), which showed that the average gray value obtained from a single slice was higher in BPTs than in BMPTs, though there was no intergroup difference. Additionally, we found that the variance and 90th percentile gray values in BPTs were also higher than those in BMPTs. Variance reflects the degree of dispersion between the gray values of an image, and the 90th percentile represents the pixels close to the highest gray values. The increased frequency indicates that the proportion of high signal pixels in the enhanced images of BPTs was higher than that in BMPTs. This indicates that there are more areas of higher brightness, or significant enhancement, in BPTs than in BMPTs. Therefore, the histogram analysis of the whole tumor has advantages in PT grading over that of a single slice.

The GLCM features are the most commonly extracted second-order texture features for MRI quantification, which were used to reflect the spatial relationship of pixel or voxel gray-level values in the image. The GLCM feature angular second moment (AngScMom) reflects the uniformity of the gray-level distribution, where a higher AngScMom value indicates a more homogenous image (10). Ma et al. (15) showed that the texture parameter SumAverage from DCE-MR images was significantly different in BPTs and BMPTs, which was identified as one of three significant predictors (Compactness, SumAverage, and Correlation) for PT grading. In our study, we also found that the values of S(0,0,1)AngScMom and S(1,0,0)AngScMom were significantly higher in BPTs than in BMPTs, which indicated that BPTs had a relatively homogeneous gray level and regular textures compared with BMPTs. RLM reflects the comprehensive information of the image grayscale concerning direction, adjacent interval, and variation amplitude. The RLM feature GLevNonU measures the similarity of gray-level intensity values in the image. The smaller the GLevNonU value is, the more times a certain gray level appears, and the more uniform the gray level of the corresponding image is. Many texture features are unstable in different reconstruction algorithms, while GLevNonU is one of the most repetitive radiomics features showing good stability. The GLevNonU value increases with the tumor heterogeneity, which is related to tumor invasion, treatment response, and prognosis (28). In this study, we found that the Z_GLevNonU, 45dgr_GLevNonU, and 135dr_GLevNonU values of the BMPTs were statistically larger than those of the BPTs, indicating that the gray-level distribution was more heterogeneous in BMPTs on DCE-MR images, compared with BPTs. Thus, combined with the pathological basis, we hypothesized that the significantly higher value of GLevNonU might be related to the greater heterogeneity caused by the more stromal atypia and cellular necrosis in BMPTs (29). This finding was similar to the results of a previous study of triple-negative breast cancer (TNBC) (30). By ultrasound (US) TA, patients with TNBC have a higher GLevNonU value than that in patients with non-TNBC, indicating that TNCB has higher heterogeneity and malignancy.

The BI-RADS lexicon has been widely used for more clear and concise communication of physicians and radiologists based on imaging findings to evaluate the classification and gradation of breast diseases (16). A previous study has described cysts and hemorrhage as typical signs of phyllodes breast tumors (8); however, our results showed that there was no difference between BPTs and BMPTs in the signal changes representing bleeding and cysts on T1W or $T2W_{FS}$ images. According to the BI-RADS diagnostic criteria of breast MRI (16), one of the descriptions of the nature of a mass lesion is the internal

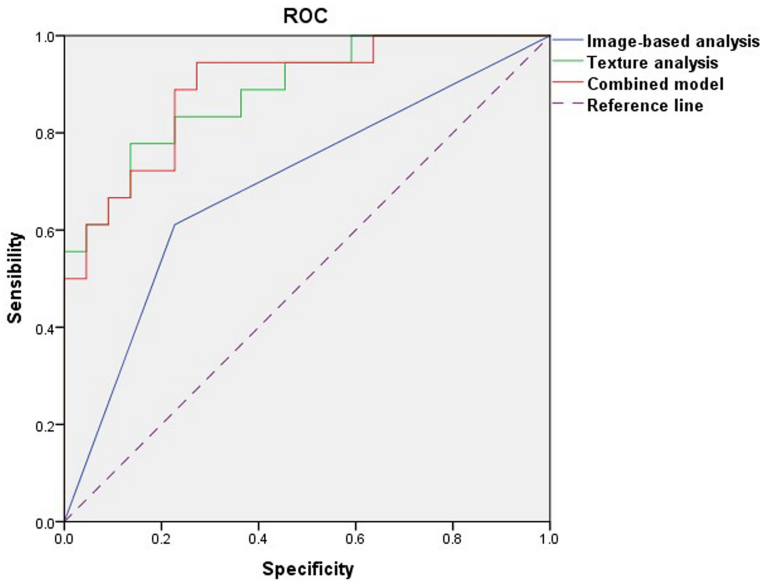

FIGURE 5 | Receiver operating characteristic curves of image-based analysis, TA, and the combined model.

enhancement characteristics, which can be divided into homogeneous, heterogeneous, rim enhancement, etc. In this study, the irregular heterogeneous enhancement was more common in BMPTs; however, consistent with previous studies (6, 8), there were no significant differences in the enhancement type and the TIC type between BPTs and BMPTs. Tumor size was considered to be an important factor for PTs' biological behavior (6). Our results showed that the malignancy rate increased with increasing tumor size. This finding reflects the high proliferative activity of BMPTs, though there was no significant difference among the PTs. Well-defined margins with a round or lobulated shape and a septate inner structure have been described as characteristic morphologic signs of PTs (15). However, our study showed no significant difference among BPTs and BMPTs in terms of lesion shape. The cystic component was found in 22 cases of BPTs (84.6%) and 18 cases of BMPTs (85.7%), with no intergroup difference. Interestingly, however, we found that the irregular cyst wall was more commonly seen in BMPTs (11/18, 61.1%) than in BPTs (5/22, 22.7%), with a significant intergroup difference. Multivariable logistic regression analysis further showed that irregular cystic walls could be an independent factor for differentiating BPTs from BMPTs. Therefore, in this study, the irregular cystic wall could be used as a valuable imaging label for differentiating BPTs from BMPTs.

In this study, ROC analysis was adopted to evaluate the diagnostic efficacy for the models from image-based analysis, TA, and a combination of the two approaches in differentiating BPTs from BMPTs. The results indicated that the diagnostic performance of the TA model or the combination model was greater than that achieved with image-based analysis alone (AUC: 0.894 vs 0.886 vs 0.687), even though there was no difference between the TA model and the combination model. Therefore, compared with conventional imaging findings based on human visual analysis, TA or combined with imaging findings has the potential in improving the differential diagnosis ability between BPTs and BMPTs, which is consistent with the result of a previous study by Cui et al. (31), who found that combining mammography findings and texture features can provide optimal predictions in the classification of PTs in mammography.

We acknowledge the following limitations in our study. Firstly, as a retrospective study, the limited number of samples, especially for the malignant PTs, may lead to inherent variations and selected bias and therefore impact the accuracy of the result. Secondly, as a single-center retrospective study, the results needed to be externally validated through a multicenter study. Thirdly, texture features are only obtained from the DCE-MR image; however, it is not ruled out that more meaningful quantitative features derived from other sequences, such as T2WI, DWI, will produce more diagnostic performance. Fourthly, manual VOI segmentation led to inevitable measurement errors; thus, the next step is to resort to semiautomatic or artificial intelligence tools that can accurately recognize these lesions. Finally, although the texture features provided a quantitative method of classifying breast lesions, we have to admit that the direct biological interpretation of texture features remains largely uncertain.

CONCLUSIONS

Our results suggest that the TA based on DCE-MR images has the potential to differentiate BPTs and BMPTs. Compared with traditional imaging analysis, TA or combined with imaging findings yielded better diagnosis performance for PT grading. Considering that it is a relatively small sample size and

single-center study, future validation studies with multiple centers are needed to verify its clinical feasibility.

DATA AVAILABILITY STATEMENT

The data analyzed in this study are subject to the following licenses/restrictions: the data supporting the conclusions of this study are available upon request for researchers who met the criteria for access to confidential data. Requests to access these datasets should be directed to X-Li, (18225023834@163.com).

ETHICS STATEMENT

This study was approved by the institutional ethics committee of Da-ping Hospital of Army Medical University [Ratification NO: 2019(160)]. The ethics committee waived the requirement of written informed consent for participation.

AUTHOR CONTRIBUTIONS

JF and X-Li conceived and designed the study. HS collected the MRI data. CZ and X-Luo analyzed MRI data. PZ provided pathology results. CC performed figure and table preparation. HL performed statistics. X-Li and HG wrote the manuscript. JF and YW edited the manuscript. All authors revised the manuscript, read, and approved the submitted version.

FUNDING

This work was supported by the Fund of National Natural Science Foundation of China (81671943), Chongqing Health Commission Fund (2022WSJK029), Chongqing Clinical Research Centre of Imaging and Nuclear Medicine (CSTC2015YFPT-gcjsyjzx0175), and Central government guide of the development of local science and technology special fund (YDZX20175000004270).

REFERENCES

1. Tan BY, Acs G, Apple SK, Badve S, Bleiweiss IJ, Brogi E. Phyllodes Tumours of the Breast: A Consensus Review. *Histopathology* (2016) 68:5–21. doi: 10.1111/his.12876
2. Li J, Tsang JY, Chen C, Chan SK, Cheung SY, Wu C. Predicting Outcome in Mammary Phyllodes Tumors: Relevance of Clinicopathological Features. *Ann Surg Oncol* (2019) 26:2747–58. doi: 10.1245/s10434-019-07445-1
3. Mann RM, Balleyguier C, Baltzer PA, Bick U, Colin C, Cornford E. Breast MRI: EUSOBI Recommendations for Women's Information. *Eur Radiol* (2015) 25:3669–78. doi: 10.1007/s00330-015-3807-z
4. Leithner D, Wengert GJ, Helbich TH, Thakur S, Ochoa-Albiztegui RE, Morris EA. Clinical Role of Breast MRI Now and Going Forward. *Clin Radiol* (2018) 73:700–14. doi: 10.1016/j.crad.2017.10.021
5. Plaza MJ, Swintelski C, Yaziji H, Torres-Salichs M, Esserman LE. Phyllodes Tumor: Review of Key Imaging Characteristics. *Breast Dis* (2015) 35:79–86. doi: 10.3233/BD-150399
6. Tan H, Zhang S, Liu H, Peng W, Li R, Gu Y. Imaging Findings in Phyllodes Tumors of the Breast. *Eur J Radiol* (2012) 81:e62–9. doi: 10.1016/j.ejrad.2011.01.085
7. Kawashima H, Miyati T, Ohno N, Ohno M, Inokuchi M, Ikeda H. Differentiation Between Phyllodes Tumours and Fibroadenomas Using Intravoxel Incoherent Motion Magnetic Resonance Imaging: Comparison With Conventional Diffusion-Weighted Imaging. *Br J Radiol* (2018) 91:20170687. doi: 10.1259/bjr.20170687
8. Yabuuchi H, Soeda H, Matsuo Y, Okafuji T, Eguchi T, Sakai S. Phyllodes Tumor of the Breast: Correlation Between MR Findings and Histologic Grade. *Radiology* (2006) 241:702–9. doi: 10.1148/radiol.2413051470
9. Shen X, Jan HN, Peng WJ, Li RM, Gu YJ, Huang D. MRI Findings and Correlation With Pathological Features in Breast Phyllodes Tumor. *Chin J Radiol* (2011) 45:1108–12. doi: 10.3760/cma.j.issn.1005-1201.2011.12.007
10. Chitalia RD, Kontos D. Role of Texture Analysis in Breast MRI as a Cancer Biomarker: A Review. *J Magn Reson Imaging* (2019) 49:927–38. doi: 10.1002/jmri.26556
11. Waugh SA, Purdie CA, Jordan LB, Vinnicombe S, Lerski RA, Martin P. Magnetic Resonance Imaging Texture Analysis Classification of Primary Breast Cancer. *Eur Radiol* (2016) 26:322–30. doi: 10.1007/s00330-015-3845-6
12. Park H, Lim Y, Cho H, Lee J, Han B, Ko ES. Radiomics Signature on Magnetic Resonance Imaging: Association With Disease-Free Survival in Patients With Invasive Breast Cancer. *Clin Cancer Res* (2018) 24:2017–3783. doi: 10.1158/1078-0432.CCR-17-3783
13. Golden D, Rubin D, Lipson J, Telli M, Ford J. Dynamic Contrast-Enhanced MRI-Based Biomarkers of Therapeutic Response in Triple-Negative Breast Cancer. *J Am Med Inf Assoc: JAMIA* (2013) 20:1059–66. doi: 10.1136/amiajnl-2012-001460
14. Thibault G, Tudorica A, Afzal A, Chui S, Naik A, Troxell M. DCE-MRI Texture Features for Early Prediction of Breast Cancer Therapy Response. *Tomogr: J Imaging Res* (2017) 3:23–32. doi: 10.18383/j.tom.2016.00241
15. Ma W, Guo X, Liu L, Qi L, Liu P, Zhu Y. Magnetic Resonance Imaging Semantic and Quantitative Features Analyses: An Additional Diagnostic Tool for Breast Phyllodes Tumors. *Am J Transl Res* (2020) 12:2083–92. doi: 10.1186/s13058-019-1187-z
16. Rao AA, Feneis J, Lalonde C. Ojeda-Fournier H. A Pictorial Review of Changes in the BI-RADS Fifth Edition. *Radiographics* (2016) 36:623–39. doi: 10.1148/rg.2016150178
17. Yin J, Yang J, Jiang Z. Discrimination Between Malignant and Benign Mass-Like Lesions From Breast Dynamic Contrast Enhanced MRI: Semi-Automatic vs. Manual Analysis of the Signal Time-Intensity Curves. *J Cancer* (2018) 9:834–40. doi: 10.7150/jca.23283
18. Li X, Jiang N, Zhang C, Luo X, Fang J. Value of Conventional Magnetic Resonance Imaging Texture Analysis in the Differential Diagnosis of Benign and Borderline/Malignant Phyllodes Tumors of the Breast. *Cancer Imaging: Off Publ Int Cancer Imaging Soc* (2021) 21:29. doi: 10.1186/s40644-021-00398-3
19. Holli-Helenius K, Salminen A, Rinta-Kiikka I, Koskivuo I, Brück N, Boström P. MRI Texture Analysis in Differentiating Luminal A and Luminal B Breast Cancer Molecular Subtypes - A Feasibility Study. *BMC Med Imaging* (2017) 17:69. doi: 10.1186/s12880-017-0239-z
20. Szczypiński PM, Strzelecki M, Materka A, Klepaczko A. MaZda–a Software Package for Image Texture Analysis. *Comput Meth Prog Bio* (2009) 94:66–76. doi: 10.1016/j.cmpb.2008.08.005
21. Chen PC, Pavlidis T. Segmentation by Texture Using a Co-Occurrence Matrix and a Split-and-Merge Algorithm. *Comput Graphics Image Process* (1979) 10:172–82. doi: 10.1016/0146-664X(79)90049-2
22. Leithner D, Horvat JV, Marino MA, Bernard-Davila B, Jochelson MS, Ochoa-Albiztegui RE. Radiomic Signatures With Contrast-Enhanced Magnetic Resonance Imaging for the Assessment of Breast Cancer Receptor Status and Molecular Subtypes: Initial Results. *Breast Cancer Res: BCR* (2019) 21:106. doi: 10.1186/s13058-019-1187-z
23. Tang X. Texture Information in Run-Length Matrices. *IEEE Trans Image Process* (1998) 7:1602–9. doi: 10.1109/83.725367
24. Henderson S, Purdie C, Michie C, Evans A, Lerski R, Johnston M. Interim Heterogeneity Changes Measured Using Entropy Texture Features on T2-Weighted MRI at 3.0 T Are Associated With Pathological Response to Neoadjuvant Chemotherapy in Primary Breast Cancer. *Eur Radiol* (2017) 27:4602–11. doi: 10.1007/s00330-017-4850-8

25. Lin F, Wang Z, Zhang K, Yang P, Ma H, Shi Y. Contrast-Enhanced Spectral Mammography-Based Radiomics Nomogram for Identifying Benign and Malignant Breast Lesions of Sub-1 cm. *Front Oncol* (2020) 10:573630. doi: 10.3389/fonc.2020.573630
26. Xu X, Zhu H, Li R, Lin H, Grimm R, Fu C. Whole-Liver Histogram and Texture Analysis on T1 Maps Improves the Risk Stratification of Advanced Fibrosis in NAFLD. *Eur Radiol* (2021) 31:1748–59. doi: 10.1007/s00330-020-07235-4
27. Bougias H, Ghiatas A, Priovolos D, Veliou K, Christou A. Whole-Lesion Histogram Analysis Metrics of the Apparent Diffusion Coefficient as a Marker of Breast Lesions Characterization at 1.5 T. *Radiography* (2017) 23:e41–6. doi: 10.1016/j.radi.2017.02.002
28. Li Y, Yu M, Wang G, Yang L, Ma C, Wang M. Contrast-Enhanced CT-Based Radiomics Analysis in Predicting Lymphovascular Invasion in Esophageal Squamous Cell Carcinoma. *Front Oncol* (2021) 11:644165. doi: 10.3389/fonc.2021.644165
29. Zhang Y, Kleer CG. Phyllodes Tumor of the Breast: Histopathologic Features, Differential Diagnosis, and Molecular/Genetic Updates. *Arch Pathol Lab Med* (2016) 140:665–71. doi: 10.5858/arpa.2016-0042-RA
30. Chen Q, Xia J, Zhang J. Identify the Triple-Negative and Non-Triple-Negative Breast Cancer by Using Texture Features of Medicale Ultrasonic Image: A STROBE-Compliant Study. *Medicine* (2021) 100:e25878. doi: 10.1097/MD.0000000000025878
31. Cui WJ, Wang C, Jia L, Ren S, Duan SF, Cui C. Differentiation Between G1 and G2/G3 Phyllodes Tumors of Breast Using Mammography and Mammographic Texture Analysis. *Front Oncol* (2019) 9:433. doi: 10.3389/fonc.2019.00433

Conflict of Interest: Author HL was employed by GE Healthcare.

The remaining authors declare that the research was conducted in the absence of any commercial or financial relationships that could be construed as a potential conflict of interest.

frontiers in Oncology

ORIGINAL RESEARCH
published: 01 December 2021
doi: 10.3389/fonc.2021.724656

Using Ultrasound-Based Multilayer Perceptron to Differentiate Early Breast Mucinous Cancer and its Subtypes From Fibroadenoma

Ting Liang[1,2†], Junhui Shen[3†], Shumei Zhang[4†], Shuzhen Cong[1], Juanjuan Liu[1], Shufang Pei[1], Shiyao Shang[1] and Chunwang Huang[1]*

[1] Department of Ultrasound, Guangdong Provincial People's Hospital, Guangdong Academy of Medical Sciences, Guangzhou, China, [2] Department of Ultrasound, Affiliated Hospital of Guangdong Medical University, Zhanjiang, China, [3] Department of Rehabilitation Medicine, Guangdong Provincial People's Hospital, Guangdong Academy of Medical Sciences, Guangzhou, China, [4] Department of Ultrasound, Guangzhou Eighth People's Hospital, Guangzhou Medical University, Guangzhou, China

OPEN ACCESS

Edited by:
Ellen Ackerstaff, Memorial Sloan Kettering Cancer Center, United States

Reviewed by:
Celine Taglang, University of California, San Francisco, United States
Jie Yuan, Nanjing University, China

***Correspondence:**
Chunwang Huang
huangchunwang@126.com

[†]These authors have contributed equally to this work

Specialty section:
This article was submitted to Cancer Imaging and Image-directed Interventions, a section of the journal Frontiers in Oncology

Received: *14 June 2021*
Accepted: *09 November 2021*
Published: *01 December 2021*

Citation:
Liang T, Shen J, Zhang S, Cong S, Liu J, Pei S, Shang S and Huang C (2021) Using Ultrasound-Based Multilayer Perceptron to Differentiate Early Breast Mucinous Cancer and its Subtypes From Fibroadenoma. Front. Oncol. 11:724656. doi: 10.3389/fonc.2021.724656

Objectives: Mucinous breast cancer (MBC), particularly pure MBC (pMBC), often tend to be confused with fibroadenoma (FA) due to their similar images and firm masses, so some MBC cases are misdiagnosed to be FA, which may cause poor prognosis. We analyzed the ultrasonic features and aimed to identify the ability of multilayer perceptron (MLP) to classify early MBC and its subtypes and FA.

Materials and Methods: The study consisted of 193 patients diagnosed with pMBC, mMBC, or FA. The area under curve (AUC) was calculated to assess the effectiveness of age and 10 ultrasound features in differentiating MBC from FA. We used the pairwise comparison to examine the differences among MBC subtypes (pure and mixed types) and FA. We utilized the MLP to differentiate MBC and its subtypes from FA.

Results: The nine features with AUCs over 0.5 were as follows: age, echo pattern, shape, orientation, margin, echo rim, vascularity distribution, vascularity grade, and tumor size. In subtype analysis, the significant differences were obtained in 10 variables (p-value range, 0.000–0.037) among pMBC, mMBC, and FA, except posterior feature. Through MLP, the AUCs of predicting MBC and FA were both 0.919; the AUCs of predicting pMBC, mMBC, and FA were 0.875, 0.767, and 0.927, respectively.

Conclusion: Our study found that the MLP models based on ultrasonic characteristics and age can well distinguish MBC and its subtypes from FA. It may provide a critical insight into MBC preoperative clinical management.

Keywords: ultrasound, mucinous breast carcinoma, fibroadenoma, multilayer perceptron, machine learning

Abbreviations: MBC, mucinous breast cancer; pMBC, pure mucinous breast cancer; mMBC, mixed mucinous breast cancer; FA, fibroadenoma; MRI, magnetic resonance imaging; US, ultrasound; ROC, receiver operating characteristic curve; AUC, area under curve; MLP, multilayer perceptron.

INTRODUCTION

Mucinous breast cancer (MBC) accounts for about 2% of all invasive breast carcinomas (1), whose prevalence is reported to be 1%–6% of all breast cancers (2). According to WHO classification, MBCs are classified as pure (pMBCs) and mixed MBCs (mMBCs) based on the lesions' mucin production. The pMBC consists exclusively of tumor tissue with a mucinous component above 90%, while mMBC with mucinous areas covers more than 50% but <90% of the total area and admixes usually with an infiltrating ductal epithelial component (2, 3). For MBC, metastatic disease rate ranges were reported from 12% to 14% in the case series (4). pMBC has a better overall survival than mMBC (3). Clinically, MBCs are palpable and firm masses and often tend to be confused with fibroadenomas (FAs). Some of them were misdiagnosed as FAs, delaying treatment, resulting in axillary node metastasis, chemotherapy, and shortened disease-free survival. Thus, it is essential to precisely differentiate early MBCs and their subtypes from FAs through radiological methods.

Mammography, magnetic resonance imaging (MRI), and ultrasound (US) are the main imaging techniques for discovering breast masses and preliminarily judging their histological properties. The efficiency of mammographic mass detection is low in dense breast tissues and in MBCs (5, 6). MRI is very expensive and has been associated with high false-positive rate for breast cancers (7). In contrast, US is inexpensive, non-radioactive, and widely available, and is therefore the preferred radiological means for diagnosing breast masses, especially in dense breast tissues (8).

Currently, the American College of Radiology Breast Imaging Reporting and Data System's (ACR BI-RADS) lexicon is the most commonly implemented evaluating system for breast lesions. In practice, some MBCs and FAs have the similar images. Based on the lexicon, some MRI studies focused on differentiating MBCs and FAs (9, 10). Despite the fact that one of such studies has selected optimal characteristics related with MBCs, it has not analyzed the association with the subtypes (10). Regrettably, previous US studies have just presented the features of each MBC subtype (11–13). They failed to predict MBCs, subtypes, and FAs based on a single clinical or ultrasonic feature. Therefore, we should conduct the integrated approach, such as machine learnings.

As one of machine learnings, multilayer perceptron (MLP) performs very well on nonlinear data (14), has high fault tolerance, and can solve complex problems (15, 16). Previous ultrasonic studies have performed the classification well for malignant tumors using MLP (17, 18). To our best knowledge, there is no ultrasonic study that analyzes the ultrasonic characteristics to distinguish MBC and its subtypes from FA using MLP. In this study, we analyzed the ultrasonic features of MBC subtypes and FA using MLP and identified whether MLP can perform the classification well to improve the diagnostic performance for early MBC subtypes and FA.

MATERIALS AND METHODS

Participants and Study Design

Ethical approval was approved by Research Ethics Committee of Guangdong Provincial People's Hospital for this retrospective study, and the informed consent requirement was waived due to the retrospective study. The histological characteristics of the included breast masses were gathered from pathology reports. From January 1, 2013 to December 30, 2019, 61 pMBCs and 31 mMBCs patients were enrolled in this retrospective study. Then, from January 1, 2019 to May 31, 2019, 101 consecutive FAs were enrolled in this retrospective study because FAs were the most common. All patients' age range was 15–82 years old, and mean age was 43.64 ± 14.40 years old.

The inclusion criteria were the following: (1) breast masses identified as pMBCs, mMBCs, or FAs through histological examination; (2) patients with single mass; and (3) patients of MBC without axillary node and distant metastasis.

The exclusion criteria were the following: (1) lesions that were metastatic tumors; (2) patients exposed to systemic hormone therapy or adjuvant chemotherapy; (3) lesions larger than 6 cm.

Ultrasonic Image Acquisition and Interpretation

Ultrasonic image acquisition was captured using a 14-MHz linear transducer (Toshiba Aplio 500, Canon Medical Systems Corp., Tokyo, Japan). Images of the masses were collected in a standard manner, containing at least two orthogonal planes (the radial and antiradial planes or transverse and longitudinal planes), by two breast radiologists (reader 1 with 10 and reader 2 with 5 years' experience, respectively) following the ACR BI-RADS fifth edition classification scheme. As directed by the guide and previous article (19), the two radiologists kept a strict record of US features. Both were blind to the histological outcome but not to ages. The ultrasonic characteristics comprised of 10 items: nodulous echo pattern, shape, orientation, margin, posterior features, tumor size, calcifications, echogenic rim, vascularity distribution, and vascularity grade. Detailed feature descriptions are presented in the data supplement (**Appendix 1**).

For the records of each ultrasonic feature, any disagreements between the two readers were resolved by final consensus following discussion.

Statistical Analysis

Statistical analysis was conducted with the SPSS software (Version 22.0, IBM Corp., Armonk, NY, USA). The statistical significance levels were two-sided, and $p < 0.05$ was deemed to be statistically significant.

Comparison of the MBC and FA Groups and Multiple Comparisons of pMBC, mMBC, and FA

Depending on ultrasonic features and age, the differences between MBC and FA were evaluated. Continuous variables were compared using the Mann–Whitney U test or t-test. Categorical variables were compared using the chi-square test or Fisher's exact test.

With respect to ultrasonic features and age, the multiple comparisons among pMBC, mMBC, and FA were assessed. Hereby, continuous variables were compared using the least significance difference (LSD), whereas categorical variables were compared using the Kruskal–Wallis test.

Predicting MBC and FA

For all ultrasonic features and age, the receiver operating characteristic curves (ROCs) were plotted using ROC in SPSS

Statistics. According to the curves, the respective area under curves (AUCs), sensitivity, and specificity were calculated and given automatic in SPSS Statistics. Youden index is equal to sensitivity plus specificity minus one. The sensitivity, specificity, and Youden index of those features, whose AUCs were over 0.5, were presented.

In addition, for distinguishing MBC from FA, the Multilayer Perceptron in SPSS Statistics was used to complete MLP analysis. After completing the process, the AUC of MLP and the importance of features were given automatic in SPSS Statistics.

Predicting MBC Subtypes and FA

MLP was used to distinguish MBC subtypes from FA, and the corresponding methods are shown in the previous paragraph. The AUC of MLP and the importance of features were provided.

Clinical Use

The two models of MLP can be saved in the XML file. When there are new data, you can directly call this file in the SPSS software to calculate the probability of the type of MBC or FA in the data supplement (**Appendix 2**).

RESULTS

Comparison of MBC and FA and Multiple Comparisons of pMBC, mMBC, and FA

Patients' ages and 10 detailed ultrasonic characteristics are revealed in **Table 1**. The prevalence of FA, MBC, pMBC, and mMBC were 52% (101/193), 48% (92/193), 32% (61/193), and 16% (31/193), respectively.

TABLE 1 | Patients' age and ultrasonic characteristics in FA, MBC, and subtypes.

	MBC				P_1	P_2	P_3	P_4
	pMBC (n = 61)	mMBC (n = 31)	(pMBC + mMBC) (n = 92)	FA (n = 101)				
Age (year)					0.000	0.000	0.143	0.000
Mean ± SD	52.85 ± 13.02	48.87 ± 13.51	51.51 ± 13.25	36.47 ± 11.38				
Echo pattern					0.036	0.334	0.000	0.000
Hyperechoic	0 (0)	0 (0)	0 (0)	1 (1%)				
Complex cystic and solid	1 (2%)	1 (3%)	2 (2)	0 (0)				
Hypoechoic	30 (49%)	19 (61%)	49 (53%)	84 (83%)				
Isoechoic	28 (46%)	6 (19%)	34 (37%)	12 (12%)				
Heterogeneous	2 (3%)	5 (16%)	7 (8%)	4 (4%)				
Shape					0.000	0.315	0.001	0.000
Oval	7 (11%)	1 (3%)	8 (9%)	36 (36%)				
Round	3 (5%)	1 (3%)	4 (4%)	3 (3%)				
Irregular	51 (84%)	29 (94%)	80 (87%)	62 (61%)				
Margin					0.000	0.294	0.001	0.000
Circumstance	8 (13%)	1 (3%)	9 (10%)	36 (36%)				
Not circumstance	53 (87%)	30 (97%)	83 (90%)	65 (64%)				
Orientation					0.057	0.885	0.027	0.010
Parallel	46 (76%)	23 (74%)	69 (75%)	88 (87%)				
Not parallel	15 (24%)	8 (26%)	23 (25%)	13 (13%)				
Posterior feature					/	/	/	0.561
No posterior feature	30 (49%)	18 (58%)	48 (52%)	54 (53%)				
Enhancement sound	28 (46%)	12 (39%)	40 (43%)	31 (31%)				
Shadowing	3 (5%)	1 (3%)	4 (4%)	14 (14%)				
Combined pattern	0 (0)	0 (0)	0 (0)	2 (2%)				
Calcification					0.000	0.065	0.030	0.001
In a mass	22 (36%)	16 (52%)	38 (41%)	20 (20%)				
None	39 (64%)	15 (48%)	54 (59%)	81 (80%)				
Echogenic rim					0.351	0.129	0.001	0.004
None	47 (77%)	28 (90%)	75 (82%)	97 (96%)				
Enhanced	14 (23%)	3 (10%)	17 (18%)	4 (4%)				
Vascularity distribution					0.028	0.847	0.012	0.003
Absent	24 (39%)	12 (39%)	36 (39%)	62 (61%)				
Vessels in rim	2 (3%)	2 (6%)	4 (4%)	34 (34%)				
Internal	35 (57%)	17 (55%)	52 (57%)	4 (4%)				
Vascularity grade					0.011	0.455	0.028	0.004
Grade I	23 (38%)	11 (35%)	34 (37%)	62 (61%)				
Grade II	16 (26%)	6 (19%)	22 (24%)	13 (13%)				
Grade III	17 (29%)	8 (26%)	35 (38%)	19 (19%)				
Grade IV	5 (8%)	6 (19%)	11 (12%)	7 (7%)				
Size (cm)					0.000	0.007	0.280	0.000
Mean ± SD	2.71 ± 1.31	2.47 ± 1.06	2.63 ± 1.23	1.91 ± 0.74				

P_1, pMBC vs. FA; P_2, mMBC vs. FA; P_3, pMBC vs. mMBC; P_4, MBC vs. FA; pMBC, pure mucinous breast cancer; mMBC, mixed mucinous breast cancer; MBC, mucinous breast cancer; FA, fibroadenoma.

There were significant differences in 10 variables (p-value range, 0.000–0.004) between MBC and FA, except posterior feature (**Table 1**).

In subtype analysis, one-way ANOVA analysis found that there were statistically significant differences in 10 variables (p-value range, 0.000–0.037) between pMBC, mMBC, and FA groups as a whole, except posterior feature (p-value, 0.630). Furthermore, the multiple comparisons of the 10 variables with statistically significant differences are outlined in **Table 1**.

Predicting MBC and FA

The AUCs of all the 11 variables for MBC and FA were calculated. The nine AUCs over 0.5 were as follows: age, echo pattern, shape, orientation, margin, echo rim, vascularity distribution, vascularity grade, and size. Their corresponding AUCs and sensitivity, specificity, and Youden index of the above predictors for differentiating MBC from FA are displayed in **Table 2**. The AUCs of posterior feature and calcification were below 0.5, indicating that these two variables could not distinguish between MBC and FA.

For predicting MBC and FA, the AUCs of MLP were calculated, and the ROCs of MLP are plotted in **Figure 1**. According to ROCs, AUCs were both 0.919. The importance of the features is depicted in **Figure 2**.

Predicting MBC Subtypes and FA

The AUCs of MLP for predicting pMBC, mMBC, and FA were calculated (AUCs, 0.875, 0.767, and 0.927), and the ROCs of MLP are plotted in **Figure 3**. The importance of the features is plotted in **Figure 4**.

Clinical Use

The two models of MLP can be saved in the XML format for analysis of new data (data supplement), and the illustrations of their application are shown in data supplement (**Appendix 2**).

DISCUSSION

In our study, we analyzed the differences between MBC and FA, and the pairwise comparison of MBC subtypes and FA. For differentiating MBC and FA, our study observed that the sensitivity, specificity, and Youden index of age were highest, and the other eight variables exhibited modest values. Subsequently, we used the MLP to predict MBC and its subtypes and FA. Our study showed that the MLP models based on ultrasonic characteristics and age can well predict MBC and its subtypes and FA.

Our study is distinct from previous studies. Previous studies focused on reporting the correlation between ultrasonic imaging features and histological signs (12, 13). Additionally, one study proposed automated breast volume scanning and ultrasound elastography as means of predicting breast cancer, but MBC was just one of the several subtypes of breast cancer that had to be studied (20). Obviously, these studies did not investigate the differences between MBC subtypes and FA in sufficient depth.

Our study found that age and ultrasonic features, except for posterior feature and calcification, could differentiate MBC and FA based on AUCs, but the effectiveness of the ultrasonic features was moderate or poor. Obviously, the above AUCs for predicting MBC were not applicable to predict each subtype and FA. The multiple comparisons among pMBC, mMBC, and FA pointed out that there were differences in 10 variables (**Table 1**), but there was no feature that can predict MBC subtypes and FA. Therefore, single feature could not predict MBC and its subtypes and FA well. We need a more efficient tool to accomplish this task.

Before using MLP, we tried to use multinomial regression analysis, a traditional statistical method used in a similar study (21). However, the results were not satisfactory. The pseudo R^2 of Cox and Snell was 0.495, and the p-value of Pearson test for goodness-of-fit was 0.000. The closer the R^2 and p-value to 1, the better the fit of the model, which indicated that the fit of our model was poor and the model was meaningless.

Our study showed that the combination of ultrasonic characteristics with age by MLP can predict MBC and its subtype and FA well using MLP. Then, the two MLP maps of importance demonstrated that the importance of features was different. The top 5 features were age, size, margin, posterior features, and echo rim (**Figures 2** and **4**). As far as we know, there is no study assessing the importance of ultrasonic features for MBC and its subtypes.

Age and tumor size were the strongest predictor of MBC and its subtype and FA. The older the patients are, the more likely the patients are to develop breast cancer (22, 23). Tumor size remains the important risk factor for predicting MBC, especially for pMBC. According to the biological behavior of the tumor, the more rapidly that tumor size increases, the greater the likelihood of malignancy. The size of benign tumor can remain stable for many years or increase slowly. Not circumstanced margin and calcification within masses were more positively correlated with mMBC, which is mixed with less mucin content and more no-special-type content. According to **Table 2**, the AUC of posterior features was lower than 0.5, and it cannot differentiate MBC from FA alone. However, posterior feature was one of the top 5 features in MLP. Enhanced posterior feature was the most common in pMBC because pMBC contains

TABLE 2 | Sensitivity, specificity, and Youden index of nine features for differentiating MBC from FA.

	Sensitivity	Specificity	Youden Index	AUC
Age	76.10%	81.20%	0.57%	0.817
Echo pattern	44.60%	84.20%	0.288	0.635
Shape	87%	38.60%	0.256	0.634
Orientation	25%	81.10%	0.061	0.571
Margin	90.20%	36.60%	0.268	0.648
Echogenic rim	16.30%	96%	0.123	0.571
Vascularity Distribution	60.90%	61.40%	0.223	0.608
Vascularity grade	63%	60.40%	0.234	0.611
Size	70.70%	63.40%	0.341	0.683

The AUCs (area under curve) of the nine features were over 0.5.

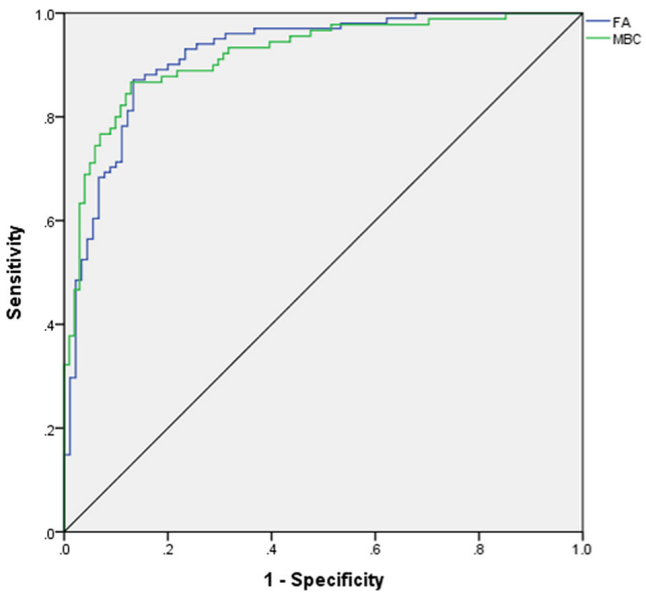

FIGURE 1 | ROC for differentiating mucinous breast carcinoma from fibroadenoma. ROC, receiver operating characteristic curve; AUC, area under curve; FA, fibroadenoma; MBC, mucinous breast carcinoma.

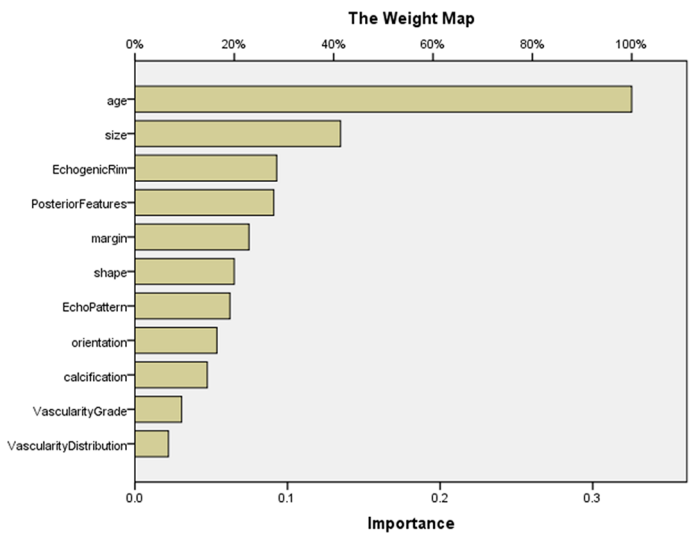

FIGURE 2 | The importance of features in MLP for predicting MBC and FA. The map could present the importance of each feature. The longer the bar represented by this feature, the greater its weight. According to the map, the top 5 features were age, size, echogenic rim, posterior features, and margin. MLP, multilayer perceptron.

more extracellular mucin and has a better sound transmission ability than mMBC and FA. The presence of enhanced echogenic rim is more common in pMBC and less common in FA. In previous studies, the perifocal hyperechoic zone was associated with malignancy due to histological lymphatic invasion of the surrounding breast tissue (24, 25).

In our study, although a single feature could not predict MBC well, a strong predictive ability can be obtained by combining all features through MLP, especially in predicting FA and MBC (AUC, 0.919). Therefore, MLP was identified to be a fine classifier for the complex issue, like the previous study (15).

Our study has several limitations. First, our study's sample size was relatively small; prospective studies with large datasets are indispensable to validate our study's result. Second, the features did not contain clinical risk factors due to the incomplete nature of retrospective study data. Prospective

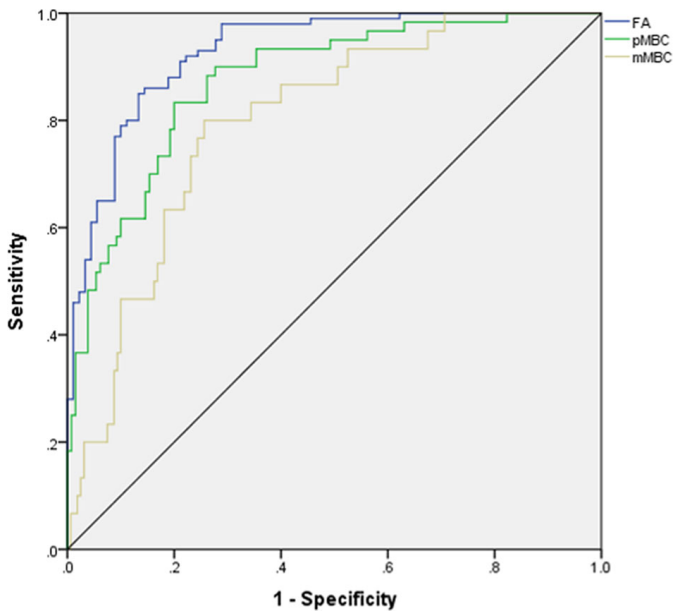

FIGURE 3 | ROC for differentiating mucinous breast carcinoma or subtypes from fibroadenoma. ROC, receiver operating characteristic curve; AUC, area under curve; FA, fibroadenoma; MBC, mucinous breast carcinoma; pMBC, pure mucinous breast carcinoma; mMBC, mixed mucinous breast carcinoma.

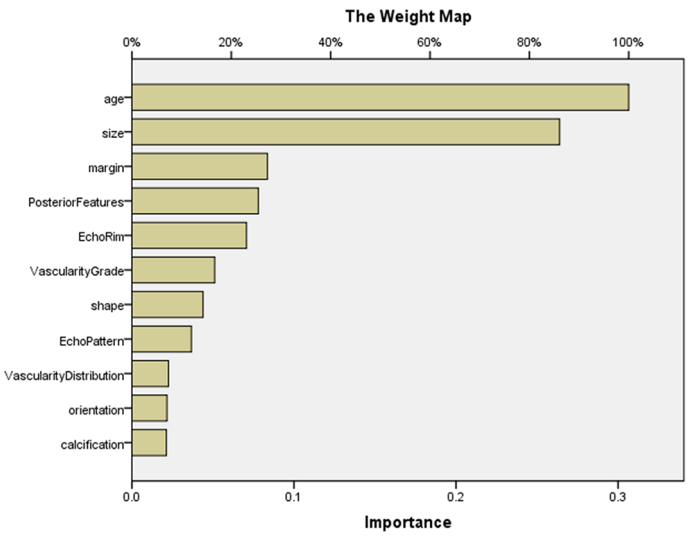

FIGURE 4 | The importance of features in MLP for predicting MBC subtypes and FA. The map could present the importance of each feature. The longer the yellow bar represented by this feature, the greater its weight. According to the map, the top 5 features were age, size, margin, posterior features, and echo rim. MLP, multilayer perceptron.

studies necessitating complete datasets (BMI, serological examination) should be conducted. Third, our feature estimation was highly dependent on a subjective analysis with inevitable bias. Objective parameters' studies need to be conducted (ultrasonic radiomics, contrast enhancement). Finally, the MLP can solve the complex classification and has the strong practicality, but the interpretability of each feature is poor. We can try other machine learnings to deal with this classification in future.

In summary, ultrasound characteristics of MBC, particularly pMBC, tend to be similar with FA. Our study found that combination of ultrasound characteristics and age by MLP can predict MBC and its subtypes and FA well. It may provide a critical insight into MBC preoperative clinical management.

DATA AVAILABILITY STATEMENT

The raw data supporting the conclusions of this article will be made available by the authors, without undue reservation.

ETHICS STATEMENT

The studies involving human participants were reviewed and approved by the Guangdong Provincial People's Hospital. Written informed consent to participate in this study was provided by the participants' legal guardian/next of kin.

AUTHOR CONTRIBUTIONS

TL, JS, and CH conceived and designed the study. TL, SZ, and SC collected the clinical and image data. SZ, SC, and JL read and kept the record of all images. TL and JS wrote the manuscript. SP and SS reviewed and re-edited the manuscript. All authors contributed to the article and approved the submitted version.

FUNDING

This work was supported by the Guangzhou Municipal Science and Technology Planning Project (CN) (202002030235) and Guangdong Medical Science and Technology Research Fund (C2018001, A2019080).

ACKNOWLEDGMENTS

We thank all the study participants and the medical teams. This study was approved by the institutional research board of Guangdong Provincial People's Hospital, Guangdong Academy of Medical Sciences.

SUPPLEMENTARY MATERIAL

The Supplementary Material for this article can be found online at: https://www.frontiersin.org/articles/10.3389/fonc.2021.724656/full#supplementary-material

REFERENCES

1. Bitencourt AG, Graziano L, Osorio CA, Guatelli CS, Souza JA, Mendonca MH, et al. MRI Features of Mucinous Cancer of the Breast: Correlation With Pathologic Findings and Other Imaging Methods. *AJR Am J Roentgenol* (2016) 206:238–46. doi: 10.2214/AJR.15.14851
2. Skotnicki P, Sas-Korczynska B, Strzepek L, Jakubowicz J, Blecharz P, Reinfuss M, et al. Pure and Mixed Mucinous Carcinoma of the Breast: A Comparison of Clinical Outcomes and Treatment Results. *Breast J* (2016) 22:529–34. doi: 10.1111/tbj.12621
3. Marrazzo E, Frusone F, Milana F, Sagona A, Gatzemeier W, Barbieri E, et al. Mucinous Breast Cancer: A Narrative Review of the Literature and a Retrospective Tertiary Single-Centre Analysis. *Breast* (2020) 49:87–92. doi: 10.1016/j.breast.2019.11.002
4. Di Saverio S, Gutierrez J, Avisar E. A Retrospective Review With Long Term Follow Up of 11,400 Cases of Pure Mucinous Breast Carcinoma. *Breast Cancer Res Treat* (2008) 111:541–7. doi: 10.1007/s10549-007-9809-z
5. Chaudhry AR, El Khoury M, Gotra A, Eslami Z, Omeroglu A, Omeroglu-Altinel G, et al. Imaging Features of Pure and Mixed Forms of Mucinous Breast Carcinoma With Histopathological Correlation. *Br J Radiol* (2019) 92:20180810. doi: 10.1259/bjr.20180810
6. Yap Y-S, Lu Y-S, Tamura K, Lee JE, Ko EY, Park YH, et al. Insights Into Breast Cancer in the East vs the West: A Review. *JAMA Oncol* (2019) 5:1489–96. doi: 10.1001/jamaoncol.2019.0620
7. Sardanelli F, Boetes C, Borisch B, Decker T, Federico M, Gilbert FJ, et al. Magnetic Resonance Imaging of the Breast: Recommendations From the EUSOMA Working Group. *Eur J Cancer* (2010) 46:1296–316. doi: 10.1016/j.ejca.2010.02.015
8. Shen S, Zhou Y, Xu Y, Zhang B, Duan X, Huang R, et al. A Multi-Centre Randomised Trial Comparing Ultrasound vs Mammography for Screening Breast Cancer in High-Risk Chinese Women. *Br J Cancer* (2015) 112:998–1004. doi: 10.1038/bjc.2015.33
9. Ferre R, Aldis A, AlSharif S, Omeroglu A, Mesurolle B. Differentiation of Fibroadenomas and Pure Mucinous Carcinomas on Dynamic Contrast-Enhanced MRI of the Breast Using Volume Segmentation for Kinetic Analysis: A Feasibility Study. *AJR Am J Roentgenol* (2016) 206:253–8. doi: 10.2214/AJR.15.14709
10. Igarashi T, Ashida H, Morikawa K, Motohashi K, Fukuda K. Use of BI-RADS-MRI Descriptors for Differentiation Between Mucinous Carcinoma and Fibroadenoma. *Eur J Radiol* (2016) 85:1092–8. doi: 10.1016/j.ejrad.2016.03.012
11. Shin YG, Kim EK, Kim MJ, Yoon JH, Moon HJ. Magnetic Resonance Imaging and Pathological Characteristics of Pure Mucinous Carcinoma in the Breast According to Echogenicity on Ultrasonography. *Ultrasonography* (2017) 36:131–8. doi: 10.14366/usg.16028
12. Wang PL, Zheng FY, Lu Q, Xia HS, Huang BJ, Liu LM, et al. Imaging Features of Pure Mucinous Breast Carcinoma: Correlation With Extracellular Mucus Content. *Clin Radiol* (2019) 74:569.e569–569.e517. doi: 10.1016/j.crad.2019.01.031
13. Zhang H, Qiu L, Peng Y. The Sonographic Findings of Micropapillary Pattern in Pure Mucinous Carcinoma of the Breast. *World J Surg Oncol* (2018) 16:151. doi: 10.1186/s12957-018-1449-8
14. Kim JY, Park G, Lee SA, Nam Y. Analysis of Machine Learning-Based Assessment for Elbow Spasticity Using Inertial Sensors. *Sensors (Basel)* (2020) 20:1622. doi: 10.3390/s20061622
15. Yun J, Park JE, Lee H, Ham S, Kim N, Kim HS. Radiomic Features and Multilayer Perceptron Network Classifier: A Robust MRI Classification Strategy for Distinguishing Glioblastoma From Primary Central Nervous System Lymphoma. *Sci Rep* (2019) 9:5746. doi: 10.1038/s41598-019-42276-w
16. Yao Y, Cifuentes J, Zheng B, Yan M. Computer Algorithm can Match Physicians' Decisions About Blood Transfusions. *J Transl Med* (2019) 17:340. doi: 10.1186/s12967-019-2085-y
17. Mao B, Ma J, Duan S, Xia Y, Tao Y, Zhang L. Preoperative Classification of Primary and Metastatic Liver Cancer *via* Machine Learning-Based Ultrasound Radiomics. *Eur Radiol* (2021) 30:4576–86. doi: 10.1007/s00330-020-07562-6
18. Nguyen DT, Kang JK, Pham TD, Batchuluun G, Park KR. Ultrasound Image-Based Diagnosis of Malignant Thyroid Nodule Using Artificial Intelligence. *Sensors (Basel)* (2020) 20:1822. doi: 10.3390/s20071822
19. Adler DD, Carson PL, Rubin JM, Quinn-Reid D. Doppler Ultrasound Color Flow Imaging in the Study of Breast Cancer: Preliminary Findings. *Ultrasound Med Biol* (1990) 16:553–9. doi: 10.1016/0301-5629(90)90020-d
20. Wang X-L, Tao L, Zhou X-L, Wei H, Sun J-W. Initial Experience of Automated Breast Volume Scanning (ABVS) and Ultrasound Elastography in Predicting Breast Cancer Subtypes and Staging. *Breast* (2016) 30:130–5. doi: 10.1016/j.breast.2016.09.012
21. Choi Y, Boo Y. Comparing Logistic Regression Models With Alternative Machine Learning Methods to Predict the Risk of Drug Intoxication Mortality. *Int J Environ Res Public Health* (2020) 17:897. doi: 10.3390/ijerph17030897
22. Fan L, Strasser-Weippl K, Li J-J, St Louis J, Finkelstein DM, Yu K-D, et al. Breast Cancer in China. *Lancet Oncol* (2014) 15:e279–89. doi: 10.1016/S1470-2045(13)70567-9

23. Hu Y, Yang Y, Gu R, Jin L, Shen S, Liu F, et al. Does Patient Age Affect the PPV3 of ACR BI-RADS Ultrasound Categories 4 and 5 in the Diagnostic Setting? *Eur Radiol* (2018) 28:2492–8. doi: 10.1007/s00330-017-5203-3
24. Durmus T, Stöckel J, Slowinski T, Thomas A, Fischer T. The Hyperechoic Zone Around Breast Lesions – An Indirect Parameter of Malignancy. *Ultraschall Med* (2014) 35:547–53. doi: 10.1055/s-0034-1385342
25. Tamaki K, Sasano H, Ishida T, Ishida K, Miyashita M, Takeda M, et al. The Correlation Between Ultrasonographic Findings and Pathologic Features in Breast Disorders. *Jpn J Clin Oncol* (2010) 40:905–12. doi: 10.1093/jjco/hyq070

Conflict of Interest: The authors declare that the research was conducted in the absence of any commercial or financial relationships that could be construed as a potential conflict of interest.

Publisher's Note: All claims expressed in this article are solely those of the authors and do not necessarily represent those of their affiliated organizations, or those of the publisher, the editors and the reviewers. Any product that may be evaluated in this article, or claim that may be made by its manufacturer, is not guaranteed or endorsed by the publisher.

frontiers in Oncology

ORIGINAL RESEARCH
published: 17 January 2022
doi: 10.3389/fonc.2021.793709

Peritumoral Enhancement for the Evaluation of Myometrial Invasion in Low-Risk Endometrial Carcinoma on Dynamic Contrast-Enhanced MRI

Tingting Cui[1†], Feng Shi[2†], Bei Gu[3], Yanfang Jin[1], Jinsong Guo[1], Chao Zhang[1], Jie Ren[1] and Yunlong Yue[1]*

[1] Department of MR, Beijing Shijitan Hospital, Capital Medical University, Beijing, China, [2] Department of Pathology, Beijing Shijitan Hospital, Capital Medical University, Beijing, China, [3] Department of Obstetrics and Gynecology, Beijing Shijitan Hospital, Capital Medical University, Beijing, China

OPEN ACCESS

Edited by:
Marie-France Penet, Johns Hopkins University, United States

Reviewed by:
Gunnar Kristensen, Oslo University Hospital, Norway
Anna Myriam Perrone, Sant'Orsola-Malpighi Polyclinic, Italy

***Correspondence:**
Yunlong Yue
yueyunlong@bjsjth.cn

[†]These authors have contributed equally to this work and share first authorship

Specialty section:
This article was submitted to Cancer Imaging and Image-directed Interventions, a section of the journal Frontiers in Oncology

Received: *12 October 2021*
Accepted: *20 December 2021*
Published: *17 January 2022*

Citation:
Cui T, Shi F, Gu B, Jin Y, Guo J, Zhang C, Ren J and Yue Y (2022) Peritumoral Enhancement for the Evaluation of Myometrial Invasion in Low-Risk Endometrial Carcinoma on Dynamic Contrast-Enhanced MRI. Front. Oncol. 11:793709. doi: 10.3389/fonc.2021.793709

Objectives: To explore the clinical value of subendometrial enhancement (SEE), irregular thin-layered peritumoral early enhancement (ITLPE) and focal irregular peritumoral early enhancement (FIPE) on dynamic contrast-enhanced magnetic resonance imaging (DCE-MRI) for myometrial invasion in patients with low-risk endometrial carcinoma.

Methods: Seventy-seven patients with low-risk endometrial carcinoma who preoperatively underwent DCE-MRI were included. Two radiologists independently evaluated and recorded the occurrences of SEE, ITLPE and FIPE on DCE-MRI in all patients. Interobserver agreement was calculated between the two radiologists, and the relationships between SEE, ITLPE, FIPE, and myometrial invasion were analyzed based on histologic findings. For statistically significant findings, the sensitivity and specificity were calculated, and the differences in myometrial invasion evaluations were analyzed. For those with no statistical significance, images were compared with the histopathologic sections.

Results: Inter-observer agreement was good (k = 0.80; 95%CI, 0.577–0.955) for SEE, and very good (k = 0.88; 95%CI, 0.761–0.972) (k = 0.86; 95%CI, 0.739–0.973) for ITLPE and FIPE. After consensus, SEE was identified in 12/77 (15.6%) patients; ITLPE and FIPE were found in 53/77 (68.8%) and 30/77 (39.0%) patients, respectively. SEE and ITLPE were significantly correlated with myometrial infiltration (P = 0.000), but FIPE were not (P = 0.725).The sensitivity and specificity of SEE and ITLPE for myometrial invasion in patients with low-risk endometrial carcinoma were 95.0 and 52.9%, and 85.0 and 88.0%, respectively. The area under the curve (AUC) of SEE and ITLPE for myometrial invasion were 0.740 (95%CI, 0.584–0.896), and 0.866 (95%CI, 0.763–0.970), respectively. The sensitivity and specificity were statistically different between SEE and ITLPE for the detection of myometrial invasion (P = 0.031, 0.016). According to the comparison between FIPE and histopathologic findings, the irregular

endomyometrial junction was found in 30/77 (38.9%) cases, 24/30 (80.0%) with myometrial infiltration and 6/30 (20.0%) cases without myometrial infiltration.

Conclusions: FIPE was the irregular endomyometrial junction. It can be found in patients with or without myometrial infiltration and may lead to the overestimation of myometrial invasion by SEE on DCE-MRI. ITLPE presented high diagnostic performance and specificity for myometrial invasion in patients with low-risk endometrial carcinoma.

Keywords: magnetic resonance imaging, endometrial carcinoma, uterus, dynamic contrast-enhanced imaging, risk classification

INTRODUCTION

Endometrial carcinoma is the most common gynecologic malignancy in women worldwide. The tumor has a global incidence of 417, 000 new cases and 97, 000 deaths in 2020 (1). The incidence of this disease in younger women has been increasing in parallel with increases in obesity, nulliparity, and polycystic ovarian syndrome (2–5). Approximately 5–30% of all reported endometrial carcinoma cases were diagnosed in younger women (6–8). For those patients, fertility preservation should be taken into consideration when deciding optimal management. Progestogen therapy might be an option in patients with low-grade endometrioid carcinoma in the absence of any myometrial invasion based on medical imaging (9, 10). Generally, the younger women diagnosed with endometrial carcinoma usually have a better outcome, because the tumor tends to present with favorable disease features, such as a favorable histologic subtype, with a lower grade lesion and minimal or absent myometrial invasion (11–16). Endometrioid adenocarcinoma (favorable histologic subtype), G1 and G2 (lower tumor grade), Stage IA (no or less than half myometrial invasion) are at low risk according to the European Society for Medical Oncology (ESMO) clinical practice guideline for risk classification of endometrial cancer (17). Information about histologic subtype and tumor grade can be acquired by curettage; however, curettage does not give information on myometrial invasion. Therefore, myometrium infiltration assessments are needed preoperatively in patients with low-risk endometrial carcinoma so that fertility-sparing progestogen therapy can be prescribed in these patients.

Magnetic resonance imaging (MRI) is considered to be a reliable modality for the evaluation of myometrial invasion of endometrial carcinoma for its excellent soft tissue contrast (18). Myometrial invasion is often assessed by previously published standards as follows: an interrupted junctional zone (JZ) on T2-weighted MR images and subendometrial enhancement (SEE) on dynamic contrast-enhanced (DCE) images. According to previous studies, low signal intensity JZ is the boundary between the endometrium and myometrium based on T2-weighted MR images, and SEE is the thin-layered enhancement between the endometrium and myometrium on DCE images (19, 20). However, JZ may be poorly visible due to age, menstrual cycle, acyeterion or hormone mimetics. Therefore, the diagnostic accuracy of myometrial invasion is lower if done only with T2-weighted images (21, 22). Nowadays, the diagnostic efficiency of myometrial invasion has been improved by DCE-MRI and diffusion-weighted imaging (DWI). In young women with endometrial cancer who want fertility-sparing progestogen therapy, DCE-MRI has been found superior to DWI in excluding myometrial invasion (23). With temporal and spatial resolution improvements, the sensitivity of SEE on DCE-MRI for myometrial invasion has ranged from 70 to 90%, but the specificity can be as low as 30% (24–26). The SEE is not easily detected in premenopausal patients, except during the proliferative phase of the menstrual cycle (27).This may result in a lower specificity for myometrial invasion assessments. Therefore, improving the specificity of DCE-MRI in detecting myometrial invasion in patients with low-risk endometrial cancer may be a new challenge.

Irregular thin-layered peritumoral early enhancement (ITLPE) and focal irregular peritumoral early enhancement (FIPE) were described firstly by Fujii et al. as the detailed information about the interface between endometrial carcinoma and myometrium by DCE-MRI. ITLPE was found to be related to myometrial invasion, although FIPE as a controversial finding for myometrial infiltration (26, 28). To the best of our knowledge, there are only a few publications about the diagnostic performance of ITLPE in assessing myometrial invasion in patients with low-risk endometrial carcinoma and further study of FIPE.

In this study, we aimed to assess the relationship between SEE, ITLPE, FIPE, and myometrial invasion and evaluated the diagnostic performance of SEE and ITLPE for myometrial invasion in patients with low-risk endometrial carcinoma. In addition, we compared FIPE with histopathologic findings.

MATERIAL AND METHODS

Study Population

After being approved by the Institutional Review Board and obtaining informed consents, a total of 96 consecutive patients pathologically diagnosed as endometrioid carcinoma were included

Abbreviations: SEE, subendometrial enhancement; DCE-MRI, dynamic contrast-enhanced magnetic resonance imaging; ITLPE, irregular thin-layered peritumoral early enhancement; FIPE, focal irregular peritumoral early enhancement; ESMO, European Society for Medical Oncology; JZ, junctional zone; DWI, diffusion-weighted imaging.

at our hospital from June 2017 to March 2021. All patients underwent preoperative pelvic DCE-MRI. According to the ESMO clinical practice guidelines for endometrial carcinoma, patients with low-risk endometrioid carcinoma (2009 FIGO stage IA, G1/G2) were enrolled. The exclusion criteria were the following: 1) patients who were diagnosed by biopsy (n = 8); 2) patients who received tumor-related treatments (radiotherapy or chemotherapy) before the pelvic DCE-MRI scan (n = 4); 3) the time between DCE-MRI and surgery was >30 days (n = 3); 4) poor image quality (n = 4). Seventy-seven patients (40–77 years; mean 60 years) were eventually included in the study.

MRI Protocol

MR examination was performed with a 1.5 T MR scanner (Ingenia, Philips Healthcare, The Netherlands) using a 32-channel phased-array body coil. All patients were asked to fast at least 4 h before the MRI examination. A series of MR sequences were performed: 1) sagittal T2-weighted imaging-turbo spin-echo (T2WI-TSE); 2) axial T2WI-TSE; 3) axial T1-weighted imaging (T1WI)-mDIXON; and 4) axial diffusion-weighted imaging (DWI). Subsequently, DCE-MRI with a flip angle of 15° was acquired. At the second dynamic, 0.2 mmol/kg of contrast agent (Gadopentetate Dimeglumine Injection, CONSUN) was administered intravenously at a rate of 2.0 ml/s and followed by the same amount of 0.9% saline flush; Twenty-five dynamics were obtained consecutively, with a temporal resolution of 7.8s, and the acquisition time was 196 s. MRI sequences and parameters are shown in **Table 1**.

Image Analysis

Image analysis was performed by two radiologists (with 20 and 25 years of experience in pelvic MRI, respectively) who were unaware of the depth of myometrial invasion (no myometrial invasion, tumor confined to the endometrium; superficial myometrial invasion, invading <50% of the myometrium; and deep myometrial invasion, invading >50% of the myometrium), tumor grade and surgical findings, except for the general diagnosis of endometrioid carcinoma. They independently evaluated and recorded occurrences of SEE, ITLPE and FIPE on DCE-MRI. Any discrepancy was resolved by consensus. Based on DCE-MRI, SEE was treated as a thin enhancement layer between the endometrium and myometrium (**Figure 1**), and was regular and smooth. According to the previous report (26), ITLPE was defined as an irregular thin-layered enhancement of the peritumoral area on early DCE images (**Figure 2**), and FIPE was the focal irregular enhancement of the peritumoral area, protruding toward the uterine cavity on early DCE images (**Figures 3A, B**).

Histologic Analysis

All of the 77 patients underwent hysterectomy and bilateral adnexectomy with or without pelvic or para-aortic lymph node dissection. Histopathologic information, namely, histologic subtype, tumor grade, and depth of myometrial invasion, was available for all patients. The cases where FIPE were detected on images were compared with the histopathologic findings, and the histopathologic sections were reviewed by the same pathologist. The criteria for myometrial invasion and irregular endomyometrial junction followed previously published standards (29, 30). A diagnosis of myometrial invasion could be made when neoplastic epithelial cells were surrounded by myometrium without intervening endometrial stroma. Also, myometrial invasion could also be diagnosed when jagged infiltrative contour and traditional desmoplastic stromal reaction were present. The irregular endomyometrial junction was defined as an endomyometrial interface with one or more undulations that measured not less than 2 to 3 mm in magnitude.

Statistical Analysis

Statistical analysis was performed with SPSS software (Version 22.0). Interobserver agreement between the two radiologists was calculated by the weighted Cohen's kappa; the k value of 0.81–1.00 indicated very good agreement, 0.61–0.80 indicated good, 0.41–0.60 indicated moderate, 0.21–0.40 indicated fair, and 0.01–0.20 indicated poor. Analysis of the relationship between SEE, ITLPE, FIPE, and myometrial invasion based on histopathologic findings was performed with the χ^2 or Fisher's exact test. According to the histopathologic findings, the sensitivity and specificity of SEE and ITLPE for myometrial invasion were calculated. The diagnostic performance of SEE and ITLPE for myometrial invasion was assessed by area under the curve (AUC) of the receiver operator characteristic (ROC) curve. The differences in sensitivity and specificity between SEE and ITLPE in evaluating myometrial invasion were analyzed with McNemar's test. A two-tailed P-value of <0.05 was considered statistically significant.

RESULTS

MRI Findings

Radiologist 1 identified 10/77 (12.9%) patients with SEE, 55/77 (71.4%) patients with ITLPE and 27/77 (35.1%) patients with FIPE, whereas Radiologist 2 identified 14/77 (18.2%) patients with SEE, 51/77 (66.2%) patients with ITLPE and 32/77 (41.6%) patients with FIPE. Inter-observer agreement was good (k = 0.80;

TABLE 1 | MRI protocol: sequences and parameters.

Sequence	Scanning plane	Repetition time (TR)/Echo time (TE) (ms)	Matrix size	Slice thickness/Gap (mm)	Field of view (mm)
T2WI-TSE	Sagittal	2,500/120	280 × 308	6/0.6	250 × 278
T2WI-TSE	Axial	3,000/110	268 × 253	4/0.5	240 × 240
T1WI-mDIXON	Axial	5.8/1.8	224 × 175	3/0	400 × 317
EPI (b = 0, 1,000 s/mm^2)	Axial	3,659/84	144 × 110	6/0.6	400 × 300
DCE-T1WI-mDIXON	Sagittal	5.8/1.73	188 × 188	2.5/0	300 × 300

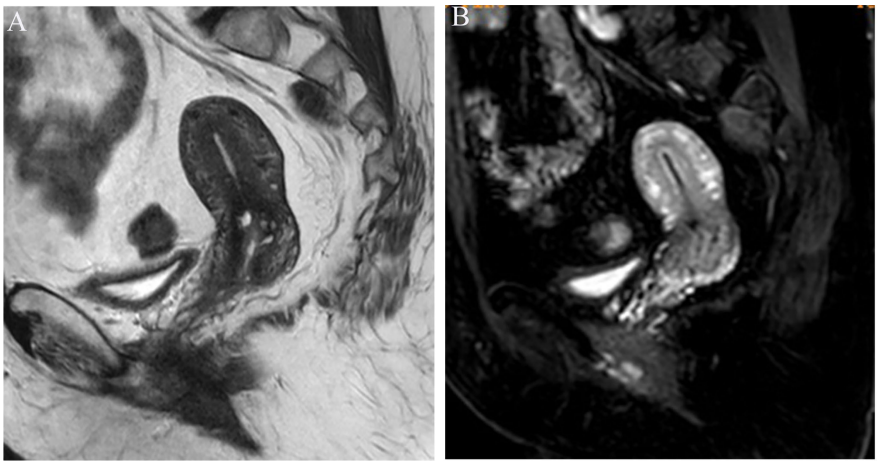

FIGURE 1 | **(A)** Sagittal-T2WI image, no definitive lesion is found in the uterine cavity. **(B)** Early (25.1 s) sagittal-DCE image shows the SEE, a thin enhancement layer between the endometrium and myometrium that is regular and smooth. This case was histologically proven to have endometrioid carcinoma, G1 with no myometrial invasion.

95% CI, 0.577–0.955) for SEE, and very good (k = 0.88; 95% CI, 0.761–0.972) (k = 0.86; 95% CI, 0.739–0.973) for ITLPE and FIPE. After consensus, SEE was identified in 12/77 (15.6%) patients. ITLPE and FIPE were found in 53/77 (68.8%) and 30/77 (39.0%) patients, respectively. A statistically significant relationship was found between SEE, ITLPE, and myometrial infiltration (P = 0.000), but not FIPE (P = 0.725). The detailed information is shown in **Table 2**.

The sensitivity and specificity of SEE and ITLPE for diagnosing myometrial invasion in patients with low-risk endometrial carcinoma are shown in **Table 3**. The AUC values of SEE and ITLPE for diagnosing myometrial invasion were 0.740 (95% CI, 0.584–0.896) and 0.866 (95% CI, 0.763–0.970), respectively (**Figure 4**). Eleven cases were misdiagnosed by SEE, 8 cases were overestimated, and 3 cases were underestimated. For the overestimated cases, SEE was recognized as incomplete by the presence of FIPE in 6 cases (**Figure 3**) and ITLPE in 2 cases (**Figure 5**). For the underestimated cases, complete SEE seemed to be visible despite the presence of myometrial infiltration. Similarly, 11 cases were misdiagnosed based on ITLPE, 9 cases were underestimated and 2 cases were overestimated. ITLPE could not be identified with or without the presence of FIPE for the

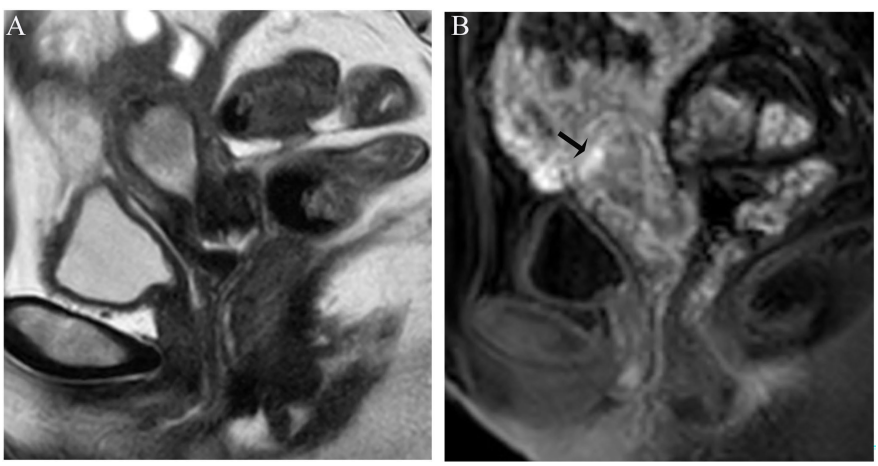

FIGURE 2 | **(A)** Sagittal-T2WI image, the tumor has moderate signal intensity and is found in the uterine cavity. **(B)** Early (32.9 s) sagittal-DCE image shows an irregular thin-layered enhancement (ITLPE); an irregular thin-layered enhancement in front of the tumor (black arrow). This case was histologically proven to have endometrioid carcinoma, G2 with superficial myometrial invasion.

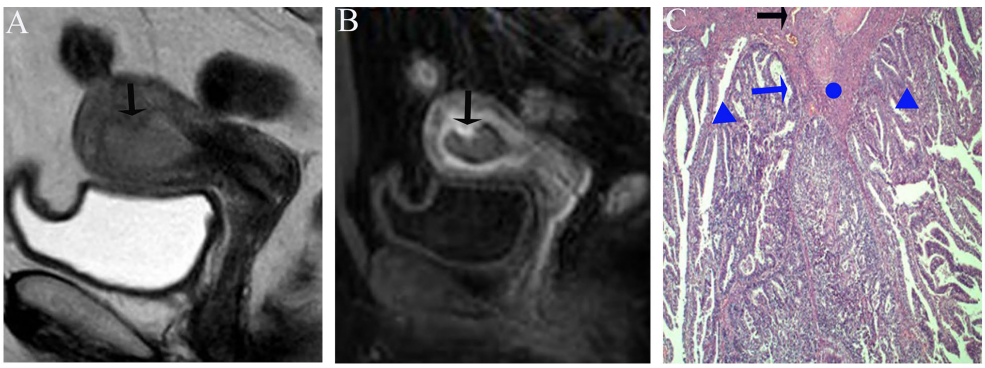

FIGURE 3 | **(A)** Sagittal-T2WI image, the tumor has moderate signal intensity and is found in the uterine cavity. The focal myometrium protrudes toward the lesion (black arrow). **(B)** Early (25.1 s) sagittal-DCE image shows the FIPE, a focal irregular enhancement (black arrow). **(C)** The photomicrograph (HE, 200×) shows the irregular endomyometrial junction (blue arrow) with the dilated vessels (black arrow) of the myometrium (circle). Note the undulating contour and extension of the myometrium between the tumors (triangle). This case was histologically proven to have endometrioid carcinoma, G1 with no myometrial invasion, and was overestimated by SEE.

underestimated cases (**Figure 6**). For the overestimated cases, ITLPE seemed to be visible despite the tumor being confined to the endometrium.

Pathologic Findings and Comparison

The histopathologic subtype of these 77 endometrial carcinoma cases was endometrioid adenocarcinoma; 17/77 (22.1%) had no myometrial infiltration, and 60/77 (77.9%) had superficial myometrial infiltration. In all, 41/77 (53.2%) tumors were classified as grade 1 and 36/77 (46.8%) tumors as grade 2. Based on these histopathologic characteristics, all patients were classified as low-risk.

According to the comparison between FIPE and the histopathologic results, irregular endomyometrial junction can be found in 30/77 (38.9%) patients, 24/30 (80.0%) with myometrial infiltration, and 6/30 (20.0%) without myometrial infiltration (**Figures 3**, **7**).

DISCUSSION

Over recent years, DCE-MRI has been widely used in gynecological tumors, especially in the assessment of myometrial invasion in endometrial carcinoma (31, 32). The superior spatial and temporal resolution of DCE-MRI allowed us to observe more detailed information about the interface between the tumor and myometrium, such as ITLPE and FIPE. Our study demonstrated that the sensitivity and specificity for detecting myometrial invasion using SEE and ITLPE on DCE-MRI were 95.0, 52.9% and 85.0, 88.0%, respectively. Fujii et al. reported values of 96.6%, 32.1–46.4%, respectively, by using SEE (26). In our study, the specificity of ITLPE was higher than SEE, and higher than that of Fujii et al. In addition, in our results, the diagnostic performance of ITLPE for myometrial invasion in low-risk endometrial carcinoma was higher compared with SEE. Therefore, ITLPE that presented with high diagnostic performance and specificity maybe an efficient method to help younger patients avoid unnecessary hysterectomy. However, for the misdiagnosed cases, the main reason was that ITLPE seemed to be difficult to identify. Further temporal and spatial resolution improvements on DCE-MRI might enable more confident detection of ITLPE in future studies. Radiologists and gynecologists need the accurate identification of ITLPE to improve the diagnostic efficiency and specificity of myometrial infiltration.

The specificity of SEE for myometrial invasion was low in both our study and that of Fujii et al. The primary reason for the lower specificity was that we did not fully realize the nature of FIPE; thus, the presence of FIPE caused SEE to be misrecognized as incomplete. The comparison between the images and histopathologic findings indicated that FIPE was actually irregular endomyometrial junction caused by carcinomatous

TABLE 2 | Correlation between SEE, FIPE, ITLPE, and myometrial invasion.

	SEE		FIPE		ITLPE	
	(+)	(–)	(+)	(–)	(+)	(–)
Myometrial invasion						
(+)	3	57	24	36	51	9
(–)	9	8	6	11	2	15
P	0.000		0.725		0.000	

TABLE 3 | Diagnostic performance of SEE and ITLPE.

n = 77	Sensitivity (%)	Specificity (%)
SEE	95.0 (57/60)	52.9 (9/17)
ITLPE	85.0 (51/60)	88.0 (15/17)
P	0.031	0.016

overgrowth without myometrial invasion. The irregular endomyometrial junction lent the appearance that the myometrium protruded toward the tumor with peripherally dilated vessels, which were found on the histopathologic tissue section (29). Ali et al. (30)reported that irregular endomyometrial junction was found in 57% of the surgical specimens of endometrial carcinoma. In our study, irregular endomyometrial junction was found in patients with or without myometrial infiltration, which was consistent with the study by Ali et al. In addition, our statistical analysis showed no association between FIPE and myometrial invasion. Therefore, FIPE should be taken into consideration in assessment of myometrial infiltration in low-risk endometrial carcinoma by only using SEE.

Previous reports have not recommended MRI for the surgical staging of endometrial carcinoma because of the poor-to-moderate accuracy in detecting high-risk factors, namely, deep myometrial infiltration and cervical stromal invasion (33, 34). However, ESMO, the European Society for Radiotherapy (ESTRO) & Oncology and the European Society of Gynaecological Oncology (ESGO) consensus conference on

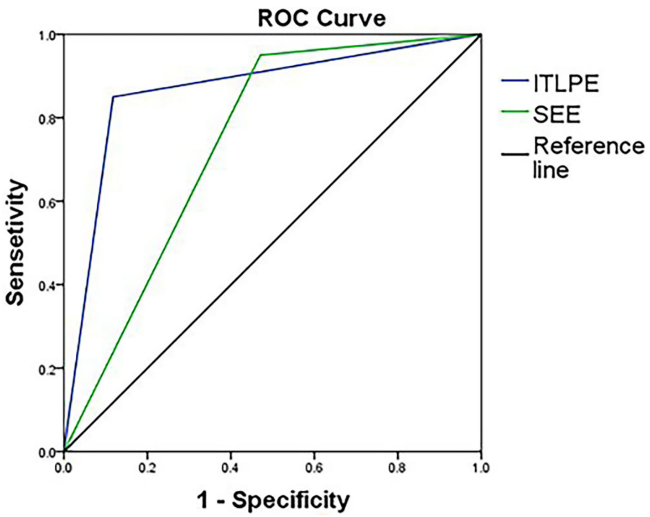

FIGURE 4 | Receiver operating characteristic curve of SEE and ITLPE for myometrial invasion in patients with low-risk endometrial carcinoma.

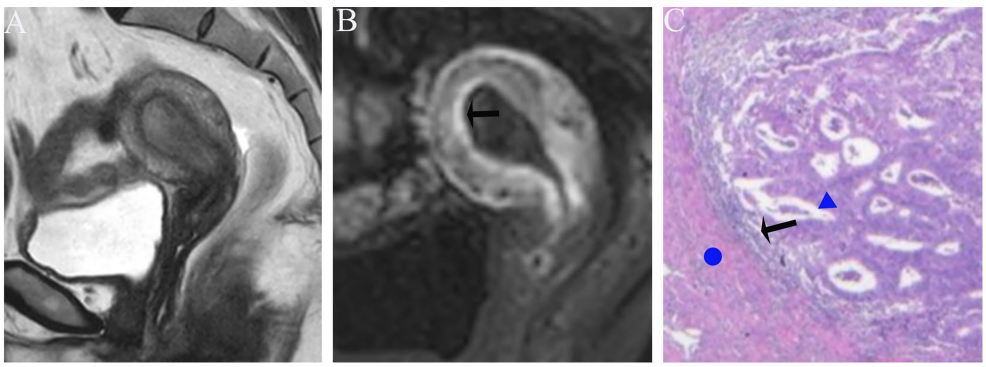

FIGURE 5 | **(A)** Sagittal-T2WI image, the tumor has moderate signal intensity and is found in the uterine cavity. **(B)** Early (32.9 s) sagittal-DCE image shows that the ITLPE seem to be visible at the anterior myometrium (black arrow). **(C)** A low-power photomicrograph (HE, 40×) shows the presence of endometrial stroma components (black arrow) between the tumor (triangle) and myometrium (circle). This case was histologically proven to have endometrioid carcinoma, G2 with no myometrial invasion, and was overestimated by SEE.

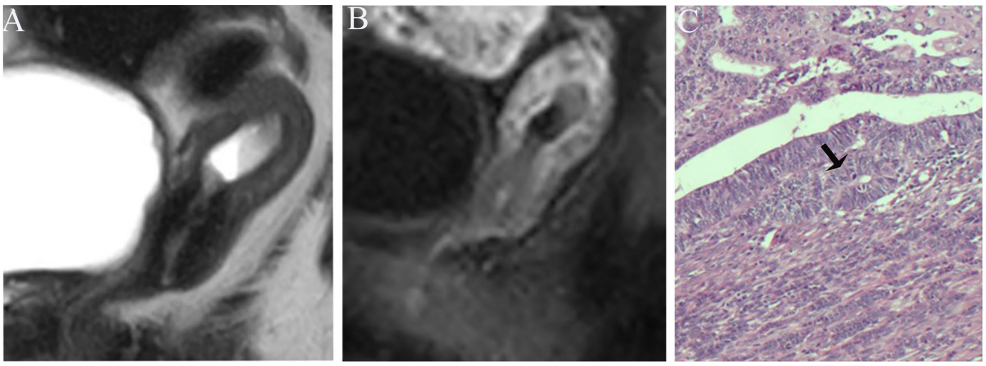

FIGURE 6 | **(A)** Sagittal-T2WI image, the tumor has moderate signal intensity and is found at the bottom of the uterus. **(B)** Early (32.9 s) sagittal-DCE image shows that the ITLPE seem not to be visible. **(C)** The photomicrograph (HE, 200×) shows that the tumor is surrounded by myometrium without intervening endometrial stroma components (black arrow). This case was histologically proven to have endometrioid carcinoma, G1 with superficial myometrial invasion, and is underestimated by ITLPE.

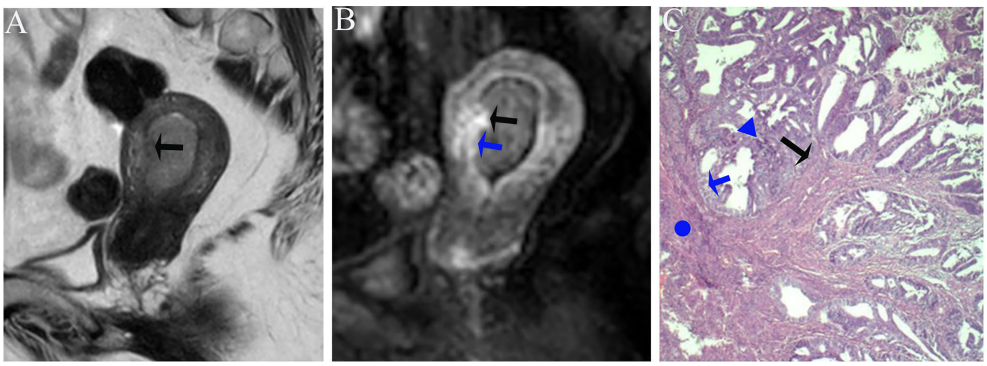

FIGURE 7 | **(A)** Sagittal-T2WI image, the tumor has moderate signal intensity and is found in the uterine cavity with focal myometrium protruding toward the lesion (black arrow). **(B)** Early (25.1 s) sagittal-DCE image shows the FIPE (black arrow) and ITLPE (blue arrow). **(C)** The photomicrograph (HE, 200×) shows that the tumor (triangle) is surrounded by the myometrium (circle) without intervening endometrial stroma components (blue arrow), but the irregular endomyometrial junction (undulating contour) can be found (black arrow). This case was histologically proven to have endometrioid carcinoma, G2 with superficial myometrial invasion.

endometrial cancer (9) indicated that MRI was preferred method for detecting tumors confined to the endometrium in patients with low-risk endometrial carcinoma who might have a chance to undergo fertility-sparing progestogen therapy. In clinical practice, radiologists and gynecologists should take FIPE into account when assessing myometrial infiltration by using SEE on DCE-MRI. Then, they should look for ITLPE, which may show evidence of myometrial infiltration when an intact SEE is not detected.

There are some limitations in our study. First, the sample size is relatively small, especially regarding the patients without myometrial invasion due to its low incidence (22.1%). Secondly, the age range of patients was large (40–77 years), and some patients were postmenopausal. These factors may lead to bias in the diagnostic performance of low-risk endometrial carcinoma. Further studies should be performed in a large sample of young premenopausal patients with further improvement of the temporal and spatial resolution on DCE-MRI.

DATA AVAILABILITY STATEMENT

The original contributions presented in the study are included in the article/supplementary material. Further inquiries can be directed to the corresponding author.

ETHICS STATEMENT

The studies involving human participants were reviewed and approved by Beijing Shijitan Hospital, Capital Medical

University. Written informed consent for participation was not required for this study in accordance with the national legislation and the institutional requirements. Written informed consent was not obtained from the individual(s) for the publication of any potentially identifiable images or data included in this article.

AUTHOR CONTRIBUTIONS

TC, FS, and YY designed the study. CZ and JR collected the data. TC and JG analyzed the data. BG, YJ, and FS reviewed the data and interpreted the statistical analysis. TC drafted the manuscript. All authors contributed to the article and approved the submitted version.

REFERENCES

1. Sung H, Ferlay J, Siegel RL, Laversanne M, Soerjomataram I, Jemal A, et al. Global Cancer Statistics 2020: GLOBOCAN Estimates of Incidence and Mortality Worldwide for 36 Cancers in 185 Countries. *CA Cancer J Clin* (2021) 71(3):209–49. doi: 10.3322/caac.21660
2. Raglan O, Kalliala I, Markozannes G, Cividini S, Gunter MJ, Nautiyal J, et al. Risk Factors for Endometrial Cancer: An Umbrella Review of the Literature. *Int J Cancer* (2019) 145(7):1719–30. doi: 10.1002/ijc.31961
3. Moore K, Brewer MA. Endometrial Cancer: Is This a New Disease? *Am Soc Clin Oncol Educ Book* (2017) 37:435–42. doi: 10.1200/edbk_175666
4. Soliman PT, Oh JC, Schmeler KM, Sun CC, Slomovitz BM, Gershenson DM, et al. Risk Factors for Young Premenopausal Women With Endometrial Cancer. *Obstet Gynecol* (2005) 105(3):575–80. doi: 10.1097/01.AOG.0000154151.14516.f7
5. Burleigh A, Talhouk A, Gilks CB, McAlpine JN. Clinical and Pathological Characterization of Endometrial Cancer in Young Women: Identification of a Cohort Without Classical Risk Factors. *Gynecol Oncol* (2015) 138(1):141–6. doi: 10.1016/j.ygyno.2015.02.028
6. Uharcek P, Mlyncek M, Ravinger J, Matejka M. Prognostic Factors in Women 45 Years of Age or Younger With Endometrial Cancer. *Int J Gynecol Cancer* (2008) 18(2):324–8. doi: 10.1111/j.1525-1438.2007.00997.x
7. Navarria I, Usel M, Rapiti E, Neyroud-Caspar I, Pelte MF, Bouchardy C, et al. Young Patients With Endometrial Cancer: How Many Could be Eligible for Fertility-Sparing Treatment? *Gynecol Oncol* (2009) 114(3):448–51. doi: 10.1016/j.ygyno.2009.05.038
8. Garg K, Soslow RA. Endometrial Carcinoma in Women Aged 40 Years and Younger. *Arch Pathol Lab Med* (2014) 138(3):335–42. doi: 10.5858/arpa.2012-0654-RA
9. Colombo N, Creutzberg C, Amant F, Bosse T, González-Martín A, Ledermann J, et al. ESMO-ESGO-ESTRO Consensus Conference on Endometrial Cancer: Diagnosis, Treatment and Follow-Up. *Int J Gynecol Cancer* (2016) 26(1):2–30. doi: 10.1097/igc.0000000000000609
10. Trojano G, Olivieri C, Tinelli R, Damiani GR, Pellegrino A, Cicinelli E. Conservative Treatment in Early Stage Endometrial Cancer: A Review. *Acta BioMed* (2019) 90(4):405–10. doi: 10.23750/abm.v90i4.7800
11. Harris KL, Maurer KA, Jarboe E, Werner TL, Gaffney D. LVSI Positive and NX in Early Endometrial Cancer: Surgical Restaging (and No Further Treatment If N0), or Adjuvant ERT? *Gynecol Oncol* (2020) 156(1):243–50. doi: 10.1016/j.ygyno.2019.09.016
12. Ebina Y, Katabuchi H, Mikami M, Nagase S, Yaegashi N, Udagawa Y, et al. Japan Society of Gynecologic Oncology Guidelines 2013 for the Treatment of Uterine Body Neoplasms. *Int J Clin Oncol* (2016) 21(3):419–34. doi: 10.1007/s10147-016-0981-1
13. Amant F, Mirza MR, Koskas M, Creutzberg CL. Cancer of the Corpus Uteri. *Int J Gynaecol Obstet* (2018) 143 Suppl 2:37–50. doi: 10.1002/ijgo.12612
14. Yamazawa K, Seki K, Matsui H, Kihara M, Sekiya S. Prognostic Factors in Young Women With Endometrial Carcinoma: A Report of 20 Cases and Review of Literature. *Int J Gynecol Cancer* (2000) 10(3):212–22. doi: 10.1046/j.1525-1438.2000.010003212.x
15. Arora V, Quinn MA. Endometrial Cancer. *Best Pract Res Clin Obstet Gynaecol* (2012) 26(3):311–24. doi: 10.1016/j.bpobgyn.2011.12.007
16. Lee NK, Cheung MK, Shin JY, Husain A, Teng NN, Berek JS, et al. Prognostic Factors for Uterine Cancer in Reproductive-Aged Women. *Obstet Gynecol* (2007) 109(3):655–62. doi: 10.1097/01.Aog.0000255980.88205.15
17. Colombo N, Preti E, Landoni F, Carinelli S, Colombo A, Marini C, et al. Endometrial Cancer: ESMO Clinical Practice Guidelines for Diagnosis, Treatment and Follow-Up. *Ann Oncol* (2013) 24 Suppl 6:vi33–8. doi: 10.1093/annonc/mdt353
18. Haldorsen IS, Salvesen HB. Staging of Endometrial Carcinomas With MRI Using Traditional and Novel MRI Techniques. *Clin Radiol* (2012) 67(1):2–12. doi: 10.1016/j.crad.2011.02.018
19. Scoutt LM, McCarthy SM, Flynn SD, Lange RC, Long F, Smith RC, et al. Clinical Stage I Endometrial Carcinoma: Pitfalls in Preoperative Assessment With MR Imaging. Work in Progress. *Radiology* (1995) 194(2):567–72. doi: 10.1148/radiology.194.2.7824739
20. Seki H, Kimura M, Sakai K. Myometrial Invasion of Endometrial Carcinoma: Assessment With Dynamic MR and Contrast-Enhanced T1-Weighted Images. *Clin Radiol* (1997) 52(1):18–23. doi: 10.1016/s0009-9260(97)80300-5
21. Ito K, Matsumoto T, Nakada T, Nakanishi T, Fujita N, Yamashita H. Assessing Myometrial Invasion by Endometrial Carcinoma With Dynamic MRI. *J Comput Assist Tomogr* (1994) 18(1):77–86. doi: 10.1097/00004728-199401000-00017
22. Sironi S, Taccagni G, Garancini P, Belloni C, DelMaschio A. Myometrial Invasion by Endometrial Carcinoma: Assessment by MR Imaging. *AJR Am J Roentgenol* (1992) 158(3):565–9. doi: 10.2214/ajr.158.3.1738995
23. Lin G, Huang YT, Chao A, Ng KK, Yang LY, Ng SH, et al. Influence of Menopausal Status on Diagnostic Accuracy of Myometrial Invasion in Endometrial Cancer: Diffusion-Weighted and Dynamic Contrast-Enhanced MRI at 3 T. *Clin Radiol* (2015) 70(11):1260–8. doi: 10.1016/j.crad.2015.06.097
24. Nakao Y, Yokoyama M, Hara K, Koyamatsu Y, Yasunaga M, Araki Y, et al. MR Imaging in Endometrial Carcinoma as a Diagnostic Tool for the Absence of Myometrial Invasion. *Gynecol Oncol* (2006) 102(2):343–7. doi: 10.1016/j.ygyno.2005.12.028
25. Horváth K, Pete I, Vereczkey I, Dudnyikova A, Gődény M. Evaluation of the Accuracy of Preoperative MRI in Measuring Myometrial Infiltration in Endometrial Carcinoma. *Pathol Oncol Res* (2014) 20(2):327–33. doi: 10.1007/s12253-013-9699-9
26. Fujii S, Kido A, Baba T, Fujimoto K, Daido S, Matsumura N, et al. Subendometrial Enhancement and Peritumoral Enhancement for Assessing Endometrial Cancer on Dynamic Contrast Enhanced MR Imaging. *Eur J Radiol* (2015) 84(4):581–9. doi: 10.1016/j.ejrad.2015.01.004
27. Yamashita Y, Harada M, Sawada T, Takahashi M, Miyazaki K, Okamura H. Normal Uterus and FIGO Stage I Endometrial Carcinoma: Dynamic Gadolinium-Enhanced MR Imaging. *Radiology* (1993) 186(2):495–501. doi: 10.1148/radiology.186.2.8421757
28. Fujii S, Kido A, Mikami Y, Matsumura N, Konishi I, Togashi K. Peritumoral Enhancement in Endometrial Cancer on Dynamic Contrast-Enhanced Imaging: Radiologic-Pathologic Correlation. *J Obstet Gynaecol Res* (2014) 40(5):1445–9. doi: 10.1111/jog.12318
29. Cole AJ, Quick CM. Patterns of Myoinvasion in Endometrial Adenocarcinoma: Recognition and Implications. *Adv Anat Pathol* (2013) 20(3):141–7. doi: 10.1097/PAP.0b013e31828d17cc
30. Ali A, Black D, Soslow RA. Difficulties in Assessing the Depth of Myometrial Invasion in Endometrial Carcinoma. *Int J Gynecol Pathol* (2007) 26(2):115–23. doi: 10.1097/01.pgp.0000233165.56385.0b
31. Nougaret S, Horta M, Sala E, Lakhman Y, Thomassin-Naggara I, Kido A, et al. Endometrial Cancer MRI Staging: Updated Guidelines of the European Society of Urogenital Radiology. *Eur Radiol* (2019) 29(2):792–805. doi: 10.1007/s00330-018-5515-y
32. Himoto Y, Lakhman Y, Fujii S, Morita S, Mueller JJ, Leitao MMJr., et al. Multiparametric Magnetic Resonance Imaging Facilitates the Selection of Patients Prior to Fertility-Sparing Management of Endometrial Cancer. *Abdom Radiol (NY)* (2021) 46(9):4410–9. doi: 10.1007/s00261-021-03050-7

33. Vandecaveye V, Dresen R, De Keyzer F. Novel Imaging Techniques in Gynaecological Cancer. *Curr Opin Oncol* (2017) 29(5):335–42. doi: 10.1097/cco.0000000000000385
34. Luomaranta A, Leminen A, Loukovaara M. Magnetic Resonance Imaging in the Assessment of High-Risk Features of Endometrial Carcinoma: A Meta-Analysis. *Int J Gynecol Cancer* (2015) 25(5):837–42. doi: 10.1097/igc.0000000000000194

Conflict of Interest: The authors declare that the research was conducted in the absence of any commercial or financial relationships that could be construed as a potential conflict of interest.

Publisher's Note: All claims expressed in this article are solely those of the authors and do not necessarily represent those of their affiliated organizations, or those of the publisher, the editors and the reviewers. Any product that may be evaluated in this article, or claim that may be made by its manufacturer, is not guaranteed or endorsed by the publisher.

frontiers in Oncology

ORIGINAL RESEARCH
published: 27 January 2022
doi: 10.3389/fonc.2022.807402

Downgrade BI-RADS 4A Patients Using Nomogram Based on Breast Magnetic Resonance Imaging, Ultrasound, and Mammography

Yamie Xie[1,2], *Ying Zhu*[1], *Weimin Chai*[3], *Shaoyun Zong*[2], *Shangyan Xu*[1], *Weiwei Zhan*[1] *and Xiaoxiao Zhang*[1*]

[1] Department of Ultrasound, Ruijin Hospital, Shanghai Jiao Tong University School of Medicine, Shanghai, China, [2] College of Medicine, Kunming University of Science and Technology, Department of Ultrasound, The First People's Hospital of Yunnan Province, Kunming, China, [3] Department of Radiology, Ruijin Hospital, Shanghai Jiao Tong University School of Medicine, Shanghai, China

OPEN ACCESS

Edited by:
Pilar López-Larrubia, Spanish National Research Council (CSIC), Spain

Reviewed by:
Bilgin Kadri Aribas, Bülent Ecevit University, Turkey
Begüm Demirler Şimir, Ankara Yildirim Beyazit University, Turkey

***Correspondence:**
Xiaoxiao Zhang
xiaoxiao_8499@126.com

Specialty section:
This article was submitted to Breast Cancer, a section of the journal Frontiers in Oncology

Received: *02 November 2021*
Accepted: *03 January 2022*
Published: *27 January 2022*

Citation:
Xie Y, Zhu Y, Chai W, Zong S, Xu S, Zhan W and Zhang X (2022) Downgrade BI-RADS 4A Patients Using Nomogram Based on Breast Magnetic Resonance Imaging, Ultrasound, and Mammography. Front. Oncol. 12:807402. doi: 10.3389/fonc.2022.807402

Objectives: To downgrade BI-RADS 4A patients by constructing a nomogram using R software.

Materials and Methods: A total of 1,717 patients were retrospectively analyzed who underwent preoperative ultrasound, mammography, and magnetic resonance examinations in our hospital from August 2019 to September 2020, and a total of 458 patients of category BI-RADS 4A (mean age, 47 years; range 18–84 years; all women) were included. Multivariable logistic regression was used to screen out the independent influencing parameters that affect the benign and malignant tumors, and the nomogram was constructed by R language to downgrade BI-RADS 4A patients to eligible category.

Results: Of 458 BI-RADS 4A patients, 273 (59.6%) were degraded to category 3. The malignancy rate of these 273 lesions is 1.5% (4/273) (<2%), and the sensitivity reduced to 99.6%, the specificity increased from 4.41% to 45.3%, and the accuracy increased from 63.4% to 78.8%.

Conclusion: By constructing a nomogram, some patients can be downgraded to avoid unnecessary biopsy.

Keywords: Breast Imaging Reporting and Data System, magnetic resonance imaging, ultrasound, breast tumor, mammography

INTRODUCTION

According to statistics, the number of new cases of breast cancer among Chinese women reached 0.42 million in 2020, accounting for 18% of the global breast cancer rate. It ranks first in the incidence of female cancer, and the mortality rate ranks fourth in China (1). The incidence of breast cancer in women has been increasing year by year; female breast cancer has surpassed lung cancer as the most commonly diagnosed cancer, with an estimated 2.3 million new cases (2). Considering the

high sensitivity of MRI in the detection of breast diseases, more and more patients will add MRI examination when suspicious lesions are found in mammography or ultrasonography. According to the breast imaging report and data system (BI-RADS), category 4 (2% ≤ malignant rate < 95%); category 5 (malignant rate ≥ 95%) (3, 4). The guidelines recommend that the lesions above or equal to category 4 undergo core needle biopsy to clarify the histopathological type, and the positive predictive value (PPV) spans a large range. An analysis of data from 1.6 million women's breast cancer surveillance associations showed that 66.8% of biopsy results were benign (5), the positive predictive value (PPV) of 4A patients is less than 10%, a large part of the pathology of biopsy specimens is confirmed to be benign, and the high sensitivity and low specificity lead to unnecessary invasive examinations. Therefore, a better way to stratify and manage patients belonging to category 4 is needed.

The main purpose of this study is to downgrade category 4A lesions to avoid unnecessary biopsy. Since BI-RADS 4B, 4C, and 5 patients are still within the puncture range even if they are degraded, the degrading factors of these patients are not considered in our study.

MATERIALS AND METHODS

Study Participants

This retrospective study was approved by the Ethics Committee of the Ruijin Hospital, Shanghai Jiao Tong University School of Medicine. The consent to participate in the study for patients was waived due to the retrospective study and all identity data of patients are undistinguishable. The study was carried out in conformity to the Declaration of Helsinki (as revised in 2013). From August 2019 to September 2020, 6,312 patients underwent breast surgery or core needle biopsy and obtained clear pathological results, including 2,252 females who went through ultrasound, mammography, and magnetic resonance imaging examinations simultaneously. Among the 2,252 patients, 535 were excluded due to the following reasons: (a) the location of the lesions shown by the three imaging ways was inconsistent (n = 35), (b) incomplete clinical data (n = 26), (c) part of the images was unclear (n = 35), (d) the interval between the three imaging examinations was more than 1 month (n = 40), (e) patients who have been diagnosed with BI-RADS category 6 (n = 49), and (f) non-mass enhancement (n = 350). In the end, 1,717 patients constituted the study group. Among them, there are 458 patients in category 4A, (mean age, 47 years; range 18–88 years; all women) patient characteristics is shown in **Table 1**. Basic BI-RADS classification information of patients is shown in **Table 2**.

Imaging Technique

The mammography examination uses the GE Senographe 2000D machine: the projection positions are mainly in the internal and external oblique position (MLO position) and the head and tail position (CC position). If necessary, local compression magnified irradiation and special body position irradiation were given.

All the breast MRI examinations were performed with a 1.5-T unit (MAGNETOM Aera, Siemens Healthcare) with a dedicated 18-channel phased-array breast coil. The patient was in the prone position, and the breasts were naturally suspended in the breast coil. The scanning range included bilateral axillary and bilateral upper and lower boundaries of the breast. The protocol included axial T1-weighted, T2-weighted fat-suppressed, diffusion-weighted imaging (DWI, b value is 1000 s/mm^2), T1-weighted fat-suppressed dynamic enhancement scan: 1 stage no enhancement 90 s + 5 stage enhancement (90 s × 5) after injection of 20 ml of gadolinium meglumine, and then the images were uploaded to the PACS system. Postprocessing included T1-weighted subtraction, T1-weighted maximum intensity projection, and subtracted sagittal reconstruction; the apparent diffusion coefficient (ADC) was measured; and the time–signal intensity curve (TIC) was obtained.

The ultrasound system used Mindray Resona 7, a linear array probe, and the frequency is 10.0 to 14.0 MHz. Choose the breast model, the patient takes the supine position, the arm is raised or abducted, and the breast and axilla are fully exposed. Ultrasound examination of the entire breast should be from the posterior

TABLE 1 | Patient characteristics (all patients are women).

Characteristics	Datum
Age (years)	
Mean ± standard deviation	47.0 ± 12.1
Median*	47 (18–88)
Mass mobility	
Well	360 (78.6)
Poor	98 (21.4)
Hormones	
Use	50 (10.9)
Unused	408 (89.1)
Family history	
Yes	33 (7.2)
No	425 (92.8)
History of breast surgery	
Yes	51 (11.1)
No	407 (88.9)
Tenderness	
Yes	52 (11.4)
No	406 (88.6)
Mass texture	
Soft	148 (32.3)
Hard	310 (67.7)

*Unless otherwise indicated, data are numbers of patients, with percentages in parentheses. *Data are the median, with the range in parentheses.*

TABLE 2 | Basic BI-RADS classification information of patients.

		Benign (%)	Malignant (%)	Total
BI-RADS	3	29 (100.0)	0 (0.0)	29
	4A	414 (90.4)	44 (9.6)	458
	4B	110 (57.6)	81 (42.4)	191
	4C	91 (16.8)	450 (88.2)	541
	5	14 (2.8)	484 (97.2)	498
	Total	658 (100.0)	1,059 (100.0)	1,717

Unless otherwise indicated, the value is the number of patients and the percentage in parentheses. A total of 1,717 patients with BI-RADS classification were included, and 458 patients with 4A classification were studied. BI-RADS, Breast Imaging Reporting and Data System.

axillary line to the parasternal line, with the nipple as the center to scan the entire breast, the nipple-areola complex area, and its affiliated lymph nodes. When checking the blood flow in the lesion, the probe should be placed lightly and not pressurized, to avoid the loss of small blood vessel compression. Shear wave elastography (SWE) is converted to the SWE model when the longest axis view of the lesion is displayed on the 2D image, and the probe should be handled gently.

Imaging Evaluation

The analyzed images were downloaded from the hospital's PACS system in DICOM format. Two people engaged in breast research (YZ and YX, with 4 and 12 years of experience in breast diagnosis) are also proficient in ultrasound, mammography, and magnetic resonance diagnostic images. Radiologists, without knowing the pathological results, according to the fifth edition of the ACR BI-RADS lexicon, used the ultrasound images (add elasticity, blood flow, and the maximum diameter of the mass), magnetic resonance images (add ADC, DWI, and subtraction), and mammography images for evaluation. When one of the three images shows an obvious mass, it is defined as masses; otherwise, it is classified as no mass enhancement.

Statistical Analysis

Continuous variables are expressed as the mean ± standard deviation, and categorical variables are presented as frequencies and percentages. Univariable analyses are performed by Student's *t*-test or one-way ANOVA when normally distributed, or the Mann–Whitney *U* test when not normally distributed.

For this study, based on the BI-RADS lexicon, the clinical indicators included the patient's age, history of hormone therapy, the activity of the mass, the mass texture, family history of breast cancer, history of breast surgery, and whether there is tenderness. Variables showing $p < 0.05$ in univariable analysis were considered possible predictors and were entered in multivariable logistic regression. The independent influencing factors of benign and malignant tumors were screened out using multivariable logistic regression.

Convert continuous variables into categorical variables to facilitate the drawing of the nomogram: the best cutoff value is obtained by Youden index (ADC value is 1.035×10^{-3} mm^2/s, SWEmax is 72.61 KPa). Patients were divided into three groups based on their age according to the United States Cancer Screening Guidelines (6) and the epidemiological characteristics of breast cancer in China. The total score of each patient is obtained by assigning each index of the patient and adding up all the scores. The pathological results were used as the "gold standard", and the area under the receiver operating characteristic curve (AUC) was calculated after determining a cutoff value of total points by analyzing the nomogram. Sensitivity, specificity, and accuracy are calculated: BI-RADS score of 2–3, benign; BI-RADS score 4 or above, malignant. Using the area under the receiver operating characteristic curve (ROC) and the calibration curve, evaluate the diagnostic accuracy. The software SPSS Statistics (version 26.0, USA) and R software (version 4.0.5) were used for data analysis. A *p*-value of <0.05 was considered significantly different.

RESULTS

Pathological Features

Of 458 patients, 44 are malignant, namely, 19 cases (43.2%) of invasive ductal carcinoma, 13 cases (29.5%) of ductal carcinoma in situ, 4 cases (9.1%) of papillary carcinoma, 1 case (2.3%) of malignant phyllodes tumor, 1 case (2.3%) of small B-cell lymphoma, 3 cases (6.8%) of invasive lobular carcinoma, 2 cases (4.5%) of lobular carcinoma *in situ*, and 1 case (2.3%) of mucinous carcinoma. In addition, adenopathy, papilloma, fibroadenoma, benign phyllodes tumor, sclerosing adenopathy, and accompanied by ductal dilatation were the most common benign lesions.

Imaging and Clinical Factors

The variables were assessed in a univariable logistic regression analysis, and the variables with outcomes of $p < 0.05$ were entered into multivariable logistic regression. The results in **Table 3** showed that TIC curve ($p = 0.000$), ADC value ($p = 0.043$), mass margin ($p = 0.018$), calcification morphology ($p = 0.000$), SWE max ($p = 0.024$), and age groups ($p = 0.000$) were independent variables for differentiating between benign and malignant tumors, and DWI signal is excluded in the multivariable logistic regression analysis, which may have a strong correlation with the ADC value. Display these independent predictors as a nomogram (**Figure 1A**) and the calibration curve (**Figure 1B**) showed floating around the baseline, indicating that the model is suitable well. Then, a straight line is drawn upwards, to the point of the axis on the top, to acquire the points received based on covariates, respectively. Total points are calculated by adding all the points obtained from every covariate. The final sum is located on the total points axis, and a straight line was drawn downwards from there to obtain the probability of risk degree. The ROC curve (**Figure 2**) showed that the AUC of the model was 85.9. Through the nomogram, the cutoff score to distinguish between benign and malignant was 106 points, and the risk degree was 0.063. A patient (**Figure 3**) whose risk is less than 0.063 will be downgraded. Thus, 59.6% (273/458) of patients were downgraded by nomogram, and 4 malignant patients were downgraded to BI-RADS 3 (**Table 4**). The sensitivity of the overall classification of the mass was reduced from 100% to 99.6%, and the specificity was increased from 4.41% to 45.3%. The accuracy increased from 63.4% to 78.8%.

DISCUSSION

Breast cancer has become a global disease. The main age of breast cancer in Chinese women is between 45 and 60 years old (7). The increasing detection rate of early breast cancer and suitable treatment has successfully reduced the mortality rate of breast

TABLE 3 | Differential regression analysis of imaging and clinical indexes of benign and malignant lesions of class 4A (only showing the difference of imaging indexes with statistical significance).

Variables	Univariable logistic analysis		Multivariable logistic analysis	
	ORs (95% CI)	*p*-Value	ORs (95% CI)	*p*-Value
TIC curve		0.000*		0.000*
Persistent	1.0 (Reference)		1.0 (Reference)	
Plateau	5.26 (2.42,11.42)	0.000*	4.43 (1.73,11.37	0.002*
Washout	9.88 (4.35,22.45)	0.000*	11.23 (4.13,30.52)	0.000*
DWI	2.07 (1.038,4.14)	0.039*	1.77 (0.77,4.07)	0.178
ADC	4.56 (2.39,8.71)	0.000*	2.23 (1.02,4.84)	0.043*
Edge		0.000*		0.018*
Circumscribed	1.0 (Reference)		1.0 (Reference)	
Irregular	2.70 (0.94,7.80)	0.066	4.46 (1.22,16.32)	0.024*
Spiculated	40.42 (7.05,231.61)	0.000*	18.98 (2.11,170.99)	0.009*
Calcifications	3.53 (1.72,7.24)	0.001*	5.76 (2.30,14.43)	0.000*
SWEmax	2.29 (1.14,4.62)	0.02*	2.79 (1.15,6.79)	0.024*
Age (years)		0.005*		0.000*
<40	1.0 (Reference)		1.0 (Reference)	
40–60	1.06 (0.48,2.34)	0.889	1.55 (0.62,3.89)	0.349
>60	3.23 (1.37.7.61)	0.007*	9.55 (2.99,30.51)	0.000*
Tenderness	1.31 (0.45,3.830	0.620		
Mass mobility	1.8 (0.74,4.41)	0.19		
Family history	5.26 (0.65,4.84)	0.27		
Hormone therapy	0.57 (0.17,1.92)	0.35		
Breast surgery	0.78 (0.27,2.28)	0.65		
Skin changes/Nipple discharge	0.43 (0.06,3.01)	0.42		

** The significance of the difference between Benign and Malignant. Data in parentheses are 95% confidence intervals. ORs, odds ratios; CI, confidence interval; TIC, time–signal intensity curve; ADC, apparent diffusion coefficient; DWI, diffusion-weighted imaging.*

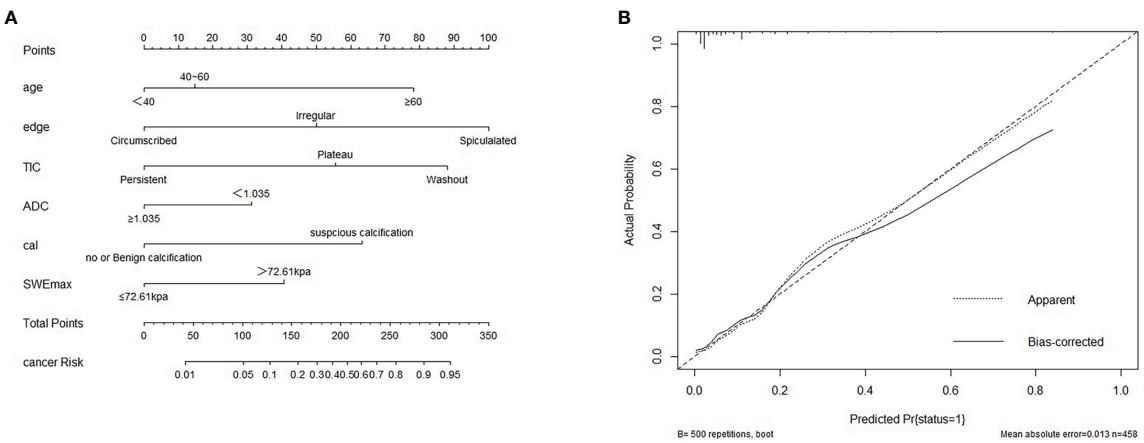

FIGURE 1 | **(A)** Nomogram for predicting benign and malignant mass in category 4A patients. **(B)** Calibration curve based on model. cal, calcification morphology; TIC, time–signal intensity curve; ADC, apparent diffusion coefficient.

cancer. For patients with no-dense gland breasts, mammography was the preferred examination, but for Asian females with dense gland breasts, ultrasound and magnetic resonance examination proved more advantageous. For this batch of patients who underwent three imaging modalities, the sensitivity of the results was very high, and the specificity was very low.

All patients with a final BI-RADS score of 4 or 5 received a diagnostic core needle biopsy or open surgery was performed to determine the histopathologic diagnosis, as recommended by the American College of Radiology. Previous studies showed how to downgrade BI-RADS 4A relatively safely, to have these patients followed up instead of undergoing an immediate biopsy. For example, Flowers et al. (8) proposed that BI-RADS 4A is defined as a low-risk disease, which can be clinically evaluated and followed up instead of performing a biopsy immediately. The classification interval of benign and malignant masses is between categories 3 and 4A, and because the positive predictive value (PPV) of BI-RADS 4A patients is less than 10%, a large part of the pathology after biopsy is confirmed to be benign, leading to an unnecessary invasive examination. Therefore, the author

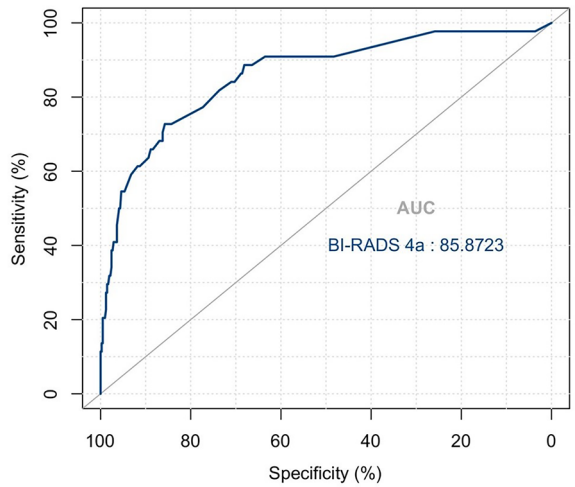

FIGURE 2 | ROC curve for predicting benign and malignant masses in category 4a patients. AUC = 85.9.

believes that it is necessary to further analyze which indicators are different between benign and malignant masses, which patients are suitable for short-term follow-up, and which are suitable for biopsy, to establish a predictive model of risk factors in category 4A patients. This study is based on Chinese samples; the results showed that 273/458 (59.6%) of BI-RADS 4A patients could be degraded and the malignant rate of the degraded patients was 4/273 (1.5%); the histopathological types of 4 false-negative patients were small B-cell lymphoma, ductal epithelial dysplasia, low-grade ductal carcinoma *in situ*, and solid papillary carcinoma *in situ*. Small B-cell lymphomas in hematological diseases can be differentiated based on medical history, and the remaining 3 missed diagnoses can be treated according to the progress of the disease during regular follow-up. Especially for young patients less than 40 years old, 73.7% (101/137) were downgraded to BI-RADS 3. Only one case was wrongly degraded, and the pathological type was *in situ* solid papillary carcinoma. The overall accuracy, especially the specificity, can be significantly improved without significantly reducing the sensitivity.

Selecting the malignant signs with the highest risk to construct a nomogram can help distinguish benign and malignant lesions and improve the diagnostic value. Among them, the TIC curve, ADC value, mass edge, calcification morphology, age, and SWEmax were identified as independent predictors of benign and malignant tumors, which are the same as the previous study (9–11). No matter from the multivariable logistic regression analysis or the visualization of the nomogram, it can be seen that the edge spiculated of the tumor is the most powerful indicator to predict the malignant tumor. The malignant risk of masses with spiculated edge is 18.98 times that of clear margin. Because the malignant mass grows to infiltrate, the formation of traction on the surrounding tissue can be manifested as a spiculated sign. In addition to morphological characteristics, hemodynamic characteristics also play an important role in predicting benign and malignant masses. Jiang (10) believes that the TIC curve can objectively and accurately assess the dynamic enhancement characteristics of the diseased tissue, and has high specificity and sensitivity for the differential diagnosis of breast diseases. The risk of malignancy of the washout TIC curve is 11.23 times that of the non-enhanced or continuously rising TIC curve. Similarly, ADC values are used to visualize and quantify the random movement of water molecules in human tissues. Studies have shown that the ADC value can distinguish malignant and benign breast lesions and improve diagnostic specificity (11). Breast cancer is usually expressed as a low ADC image signal, which is attributed to the increase of cell density, and the restriction of the diffusion of water molecules due to changes in the microstructure of the cells. SWEmax is related to benign and malignant tumors (12). In the new version of the BI-RADS guidelines, elastography has become a useful tool for breast examination and tumor assessment. Meta-analysis shows that elastography can help differentiate benign from malignant breast lesions, improve the diagnostic accuracy of malignant breast lesions, and reduce unnecessary breast biopsy (13).

In our study, among the clinical factors, the patient's age is the most significant predictor, while other factors (such as tenderness, mass activity, hormone therapy, history of breast surgery, skin changes/nipple discharge, and family history of breast cancer) have no significant difference between benign and malignant tumors. This may be due to the large proportion of benign lesions in patients with category 4A, the unobvious clinical manifestations, or the limited sample size. Research by Jagpreet (14) also confirmed that family history of breast cancer or hormone use was not an important predictor of breast cancer, and the risk of breast cancer increased with age. Among the selected 4A patients, malignant risk in patients from the 40 to 60 years old group and older than 60 years old group is 1.55 times and 9.55 times that of the less than 40 years old group. According to the BI-RADS 4 category, it can be divided into 4A, 4B, and 4C subtypes (15, 16). It is found that there is a positive correlation between the malignancy rate of each subtype and the age group, and the difference is statistically significant. Similarly, Raza (17) also found that age is an important clinical factor in predicting malignant tumors. They suggested that for older patients, the threshold of biopsy should be lowered, and even biopsy should be performed on tumors with benign imaging features. It was also reported that the malignant rate of category 3 of nodules was more than 2% in patients over 60 years old (6), which further proved that age was the most important clinical factor influencing the benign and malignant masses in any category of mass. Our research divides the age of BI-RADS 4A patients into 3 groups (malignant rate): <40 years old (7.3%); 40–60 years old (7.7%); >60 years old (20.7%) ($p < 0.001$), which proves that older is an important risk factor for breast cancer. Our results were consistent with the above previous studies. There were currently a variety of breast cancer risk assessment models, and the existing risk prediction models were generally similar (18–20).

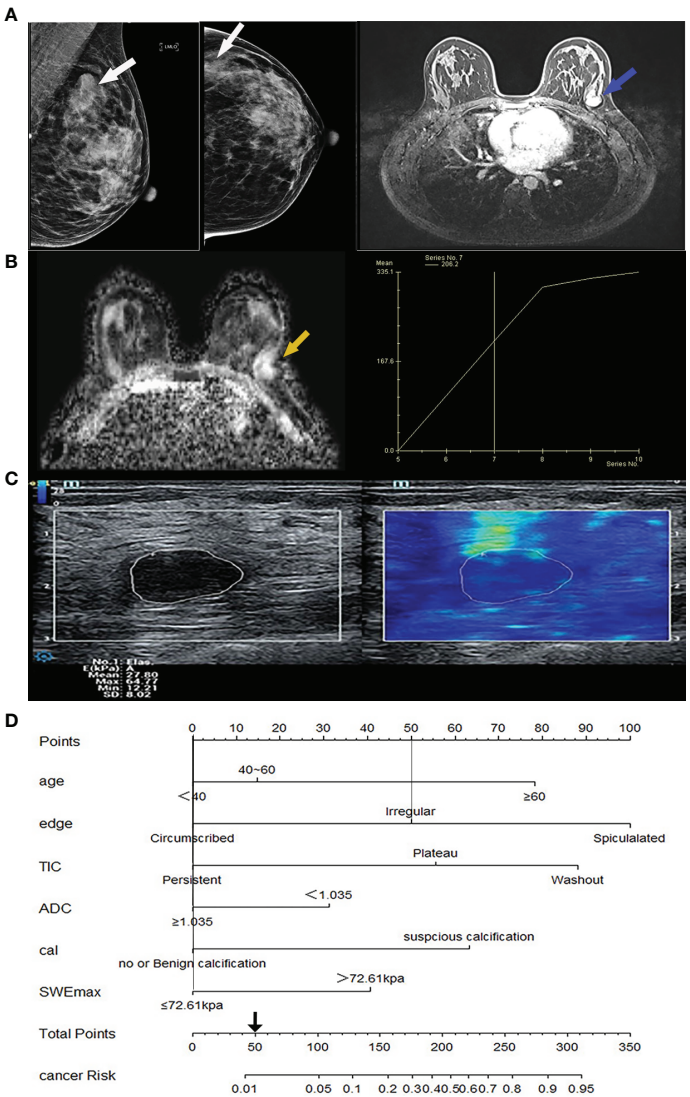

FIGURE 3 | Image from a 32-year-old woman suffering from fibroadenoma BI-RADS category 4A lesions. **(A)** Mammography imaging on the left (lesion indicated by white arrows) and the first phase of magnetic resonance dynamic enhanced transverse axial images on the right (lesion indicated by blue arrows) showed a lobulated mass near the chest wall, without calcification. **(B)** Magnetic resonance transverse axial ADC image showed a high signal value of 1.4×10^{-3} mm^2/s of the lesion on the left (indicated by yellow arrows) with ascending TIC curve on the right. **(C)** The ultrasound shear wave elastography shows SWEmax = 64.77 KPa. **(D)** In the comprehensive score of Nomogram, only the marginal irregularity (lobed) accounted for 50 points, which was less than 106 points, and it was downgraded into BI-RADS 3 category. cal, calcification morphology; TIC, time-signal intensity curve; ADC, apparent diffusion coefficient.

TABLE 4 | BI-RADS classification information for eligible patients after downgrade.

		Benign (%)	Malignant (%)	Total
BI-RADS	3	298 (98.7)	4 (1.3)	302
	4A	145 (76.7)	40 (21.6)	185
	4B	110 (57.6)	81 (42.4)	191
	4C	91 (16.8)	450 (88.2)	541
	5	14 (2.8)	484 (97.2)	498
	Total	658 (100.0)	1,059 (100.0)	1,717

Unless otherwise indicated, the value is the number of patients and the percentage in parentheses. BI-RADS, Breast Imaging Reporting and Data System.

This study has some limitations. First of all, this article only degrades the patients who are classified as BI-RADS category 4A. Because even if patients above category 4A are degraded, they are still within the scope of biopsy. Therefore, patients of categories 4B, 4C, and 5 are not considered in our study. Secondly, we did not evaluate the consistency between observers, but previous studies have shown that the feasibility of guidelines makes the results of the report not significantly different between junior and experienced radiologists (15). Finally, this study did not include the immunohistochemical results to predict the model because

these factors are obtained after biopsy, which may limit the clinical application of the model.

CONCLUSION

In short, by combining the BI-RADS lexicon and clinical indicators to perform downgrading for BI-RADS 4A patients, a large number of patients can be prevented from undergoing invasive biopsy, and clinical resources can be saved.

DATA AVAILABILITY STATEMENT

The raw data supporting the conclusions of this article will be made available by the authors, without undue reservation.

ETHICS STATEMENT

The studies involving human participants were reviewed and approved by the Ethics Committee of the Ruijin Hospital, Shanghai Jiao Tong University School of Medicine. Written informed consent for participation was not required for this study in accordance with the national legislation and the institutional requirements.

AUTHOR CONTRIBUTIONS

XZ, WZ, and WC contributed to conception and design of the study. YX performed the statistical analysis. YX wrote the first draft of the manuscript. SZ, SX, YZ, and XZ wrote sections of the manuscript. All authors contributed to manuscript revision, read, and approved the submitted version.

REFERENCES

1. Cao W, Chen HD, Yu YW, Chen WQ. Changing Profiles of Cancer Burden Worldwide and in China: A Secondary Analysis of the Global Cancer Statistics 2020. *Chin Med J* (2021) 134(7):783–91. doi: 10.1097/CM9.0000000000001474
2. Hyuna S, Ferlay J, Siegel RL, Laversanne M, Soerjomataram I, Jemal A, et al. Global Cancer Statistics 2020: GLOBOCAN Estimates of Incidence and Mortality Worldwide for 36 Cancers in 185 Countries. *CA: Cancer J Clin* (2021) 71(3):209–49. doi: 10.3322/caac.21660
3. Sickles EA, D'Orsi CJ, Bassett LW, Appleton CM, Berg WA, Burnside ES, et al. ACR BI-RADS® Mammography. In: *ACR BI-RADS® Atlas, Breast Imaging Reporting and Data System*. Reston, VA: American College of Radiology (2013). Available at: https://www.acr.org/Clinical-Resources/Reporting-and-Data-Systems/Bi-Rads/Permissions.
4. Mendelson EB, Böhm-Vélez M, Berg WA, Whitman GJ, Feldman MI, Madjar H, et al. ACR BI-RADS® Ultrasound. In: *ACR BI-RADS® Atlas, Breast Imaging Reporting and Data System*. Reston, VA: American College of Radiology (2013). Available at: https://www.acr.org/Clinical-Resources/Reporting-and-Data-Systems/Bi-Rads/Permissions.
5. Weaver DL, Rosenberg RD, Barlow WE, Ichikawa L, Carney PA, Kerlikowske K, et al. Pathologic Findings From the Breast Cancer Surveillance Consortium: Population-Based Outcomes in Women Undergoing Biopsy After Screening Mammography. *Cancer* (2006) 106(4):732–42. doi: 10.1002/cncr.21652
6. Lee CS, Berg JM, Berg WA. Cancer Yield Exceeds 2% for BI-RADS 3 Probably Benign Findings in Women Older Than 60 Years in the National Mammography Database. *Radiology* (2021) 299(3):550–58. doi: 10.1148/radiol.2021204031
7. He J, Chen WQ, Li N, Shen HB, Li J, Wang Y, et al. [China Guideline for the Screening and Early Detection of Female Breast Cancer(2021, Beijing)]. *Zhonghua Zhong Liu Za Zhi* (2021) 43(4):357–82. doi: 10.11735/j.issn.1004-0242.2021.03.A001
8. Flowers CI, O'Donoghue C, Moore D, Goss A, Kim D, Kim JH, et al. Reducing False-Positive Biopsies: A Pilot Study to Reduce Benign Biopsy Rates for BI-RADS 4a/B Assessments Through Testing Risk Stratification and New Thresholds for Intervention. *Breast Cancer Res Treat* (2013) 139(3):769–77. doi: 10.1007/s10549-013-2576-0
9. Pinker-Domenig K, Bogner W, Gruber S, Bickel H, Duffy S, Schernthaner M, et al. High Resolution MRI of the Breast at 3 T: Which BI-RADS? Descriptors Are Most Strongly Associated With the Diagnosis of Breast Cancer? *Eur Radiol* (2012) 22(2):322–30. doi: 10.1007/s00330-011-2256-6
10. Jiang Z, Yin J. Performance Evaluation of Texture Analysis Based on Kinetic Parametric Maps From Breast DCE-MRI in Classifying Benign From Malignant Lesions. *J Surg Oncol* (2020) 121(8):1181–90. doi: 10.1002/jso.25901
11. Zhang M, Horvat JV, Bernard-Davila B, Marino MA, Leithner D, Ochoa-Albiztegui R, et al. Multiparametric MRI Model With Dynamic Contrast-Enhanced and Diffusion-Weighted Imaging Enables Breast Cancer Diagnosis With High Accuracy. *J Magnetic Resonance Imaging* (2019) 49(3):864–74. doi: 10.1002/jmri.26285
12. Altıntas Y, Bayrak M, Alabaz dÖ, Celiktas M. A Qualitative and Quantitative Assessment of Simultaneous Strain, Shear Wave, and Point Shear Wave Elastography to Distinguish Malignant and Benign Breast Lesions. *Acta Radiol* (2021) 62(9):1155–62. doi: 10.1177/0284185120961422
13. Xia G, Xu Q, Xu Z, Ping X, Yan W, Chen Y. Real-Time Elastography for the Differentiation of Benign and Malignant Breast Lesions: A Meta-Analysis. *Breast Cancer Res Treat* (2011) 130(1):11–8. doi: 10.1007/s10549-011-1745-2
14. Chhatwal J, Alagoz O, Lindstrom MJ, Kahn CE, Shaffer KA, Burnside ES. A Logistic Regression Model Based on the National Mammography Database Format to Aid Breast Cancer Diagnosis. *Ajr Am J Roentgenol* (2009) 192(4):1117–27. doi: 10.2214/AJR.07.3345
15. Yoon JH, Min JK, Moon HJ, Jin YK, Kim EK. Subcategorization of Ultrasonographic BI-RADS Category 4: Positive Predictive Value and Clinical Factors Affecting it. *Ultrasound Med Biol* (2011) 37(5):693–9. doi: 10.1016/j.ultrasmedbio.2011.02.009
16. Noonpradej S, Wangkulangkul P, Woodtichartpreecha P, Laohawiriyakamol S. Prediction for Breast Cancer in BI-RADS Category 4 Lesion Categorized by Age and Breast Composition of Women in Songklanagarind Hospital. *Asian Pacif J Cancer Prev* (2021) 22(2):531–6. doi: 10.31557/APJCP.2021.22.2.531
17. Raza S, Goldkamp AL, Chikarmane SA, Birdwell RL. US of Breast Masses Categorized as BI-RADS 3, 4, and 5: Pictorial Review of Factors Influencing Clinical Management. *Radiographics A Rev Publ Radiol Soc North America Inc* (2010) 30(5):1199–213. doi: 10.1148/rg.305095144
18. Hsu W, Zhou X, Petruse A, Chau N, Lee-Felker S, Hoyt A. Role of Clinical and Imaging Risk Factors in Predicting Breast Cancer Diagnosis Among BI-RADS 4 Cases. *Clin Breast Cancer* (2019) 19(1):e142–51. doi: 10.1016/j.clbc.2018.08.008
19. Timmers JM, Verbeek AL, Inthout J, Pijnappel RM, Broeders MJ, den Heeten GJ. Breast Cancer Risk Prediction Model: A Nomogram Based on Common Mammographic Screening Findings. *Eur Radiol* (2013) 23(9):2413–19. doi: 10.1007/s00330-013-2836-8
20. Zhao Y, Xiong P, Mccullough LE, Miller EE, Li H, Huang Y, et al. Comparison of Breast Cancer Risk Predictive Models and Screening Strategies for Chinese Women. *J Womens Health* (2017) 26(3):294–302. doi: 10.1089/jwh.2015.5692

Conflict of Interest: The authors declare that the research was conducted in the absence of any commercial or financial relationships that could be construed as a potential conflict of interest.

this article, or claim that may be made by its manufacturer, is not guaranteed or endorsed by the publisher.

frontiers in Oncology

ORIGINAL RESEARCH
published: 23 February 2022
doi: 10.3389/fonc.2022.795265

Differentiation Between Benign and Metastatic Breast Lymph Nodes Using Apparent Diffusion Coefficients

*Reza Fardanesh[1], Sunitha B. Thakur[1,2], Varadan Sevilimedu[3], Joao V. Horvat[1], Roberto Lo Gullo[1], Jeffrey S. Reiner[1], Sarah Eskreis-Winkler[1], Nikita Thakur[1,4] and Katja Pinker[1]**

[1] Department of Radiology, Memorial Sloan Kettering Cancer Center, New York, NY, United States, [2] Department of Medical Physics, Memorial Sloan Kettering Cancer Center, New York, NY, United States, [3] Department of Epidemiology and Biostatistics, Memorial Sloan Kettering Cancer Center, New York, NY, United States, [4] Touro College of Osteopathic Medicine, Middletown, NY, United States

OPEN ACCESS

Edited by:
Samata Kakkad,
Merck, United States

Reviewed by:
Cyril Jaudet,
Centre François Baclesse, France
Jerome Gabriel Pousin
Université de Lyon, INSA de Lyon, France

***Correspondence:**
Katja Pinker
pinkerdk@mskcc.org

Specialty section:
This article was submitted to Breast Cancer, a section of the journal Frontiers in Oncology

Received: 14 October 2021
Accepted: 28 January 2022
Published: 23 February 2022

Citation:
Fardanesh R, Thakur SB, Sevilimedu V, Horvat JV, Gullo RL, Reiner JS, Eskreis-Winkler S, Thakur N and Pinker K (2022) Differentiation Between Benign and Metastatic Breast Lymph Nodes Using Apparent Diffusion Coefficients. Front. Oncol. 12:795265. doi: 10.3389/fonc.2022.795265

The aim of this study was to determine the range of apparent diffusion coefficient (ADC) values for benign axillary lymph nodes in contrast to malignant axillary lymph nodes, and to define the optimal ADC thresholds for three different ADC parameters (minimum, maximum, and mean ADC) in differentiating between benign and malignant lymph nodes. This retrospective study included consecutive patients who underwent breast MRI from January 2017–December 2020. Two-year follow-up breast imaging or histopathology served as the reference standard for axillary lymph node status. Area under the receiver operating characteristic curve (AUC) values for minimum, maximum, and mean ADC (min ADC, max ADC, and mean ADC) for benign *vs* malignant axillary lymph nodes were determined using the Wilcoxon rank sum test, and optimal ADC thresholds were determined using Youden's Index. The final study sample consisted of 217 patients (100% female, median age of 52 years (range, 22–81), 110 with benign axillary lymph nodes and 107 with malignant axillary lymph nodes. For benign axillary lymph nodes, ADC values ($\times 10^{-3}$ mm^2/s) ranged from 0.522–2.712 for mean ADC, 0.774–3.382 for max ADC, and 0.071–2.409 for min ADC; for malignant axillary lymph nodes, ADC values ($\times 10^{-3}$ mm^2/s) ranged from 0.796–1.080 for mean ADC, 1.168–1.592 for max ADC, and 0.351–0.688 for min ADC for malignant axillary lymph nodes. While there was a statistically difference in all ADC parameters ($p<0.001$) between benign and malignant axillary lymph nodes, boxplots illustrate overlaps in ADC values, with the least overlap occurring with mean ADC, suggesting that this is the most useful ADC parameter for differentiating between benign and malignant axillary lymph nodes. The mean ADC threshold that resulted in the highest diagnostic accuracy for differentiating between benign and malignant lymph nodes was 1.004×10^{-3} mm^2/s, yielding an accuracy of 75%, sensitivity of 71%, specificity of 79%, positive predictive value of 77%, and negative predictive value of 74%. This mean ADC threshold is lower than the European Society of

Breast Imaging (EUSOBI) mean ADC threshold of 1.300×10^{-3} mm^2/s, therefore suggesting that the EUSOBI threshold which was recently recommended for breast tumors should not be extrapolated to evaluate the axillary lymph nodes.

Keywords: breast cancer, prognostic factors, lymph nodes, diffusion-weighted imaging, apparent diffusion coefficient, MRI

INTRODUCTION

Unspecific axillary lymphadenopathy is often encountered in breast imaging. It may be caused by various benign conditions (1, 2) or more recently after COVID-19 vaccinations (3, 4); therefore, patients with a personal history or concurrent diagnosis of breast cancer in particular can pose a diagnostic dilemma. In patients with breast cancer, axillary lymph node status is an important prognostic factor (5) and one of the strongest predictors of late distant recurrence (6). Sentinel lymph node biopsy is a standard procedure in early-stage breast cancer patients with clinically negative axillary lymph nodes (7), with a reported sensitivity of 58%–72% (8–10) and accuracy of 75% (11). However, while it is a minimally invasive procedure, it is associated with several morbidities, e.g., lymphedema (8.2%) (12), seroma (19.5%), localized swelling, pain and paresthesia, infectious neuropathy, decreased arm strength, and shoulder stiffness (13).

In both scenarios of lymphadenopathy with and without a personal history of breast cancer, the use of a non-invasive imaging technique for the accurate assessment of axillary nodal status is thus desirable. On magnetic resonance imaging (MRI), differentiating between malignant and benign axillary lymph nodes is challenging when the evaluation is made solely on the basis of morphological criteria (14–16). Indeed, prior studies evaluating the axilla with MRI have reported a mean accuracy of only 75% (range, 71%–85%) in predicting axillary metastasis (17–19).

The addition of functional imaging parameters such as diffusion-weighted imaging (DWI) to dynamic contrast-enhanced MRI, i.e., in a multiparametric MRI framework, has been shown to improve diagnostic accuracy for evaluating breast tumors (20–23). DWI using apparent diffusion coefficient (ADC) mapping has a reported sensitivity of up to 96% and specificity of up to 100% for breast cancer detection (24, 25). While the primary use of DWI is to improve the differentiation between benign and malignant lesions to prevent unnecessary breast biopsies (26–29), in recent years, DWI has also shown promise in axillary lymph node mapping (15, 30, 31).

Recently, the European Society of Breast Imaging (EUSOBI) provided evidenced-based levels of diffusion restriction for breast tumors, aiming towards the assessment of breast lesions using DWI in an objective way (32). In daily clinical practice, benign axillary lymph nodes can nevertheless present with a wide range of ADC mean values, some even falling well below the lower limit of the range prescribed by EUSOBI for benign tumors. While several studies have shown that ADC values are promising to differentiate between benign and malignant lymph nodes in breast cancer patients, the possible range of ADC values for benign axillary lymph nodes and its associated possible clinical indications has yet to be delineated. In addition, it remains unknown how the recently proposed levels of diffusion restriction for breast tumors would perform in axillary lymph nodes, i.e., if they can be extrapolated to the axilla.

Therefore, the aim of this study was to determine the range of ADC values for benign axillary lymph nodes in contrast to malignant lymph nodes, and to define the optimal ADC threshold for three different ADC parameters (minimum, maximum, and mean ADC) in differentiating between benign and malignant lymph nodes. Secondarily, to determine if the mean ADC threshold recently prescribed by EUSOBI for the differentiation of benign and malignant breast tumors can be extrapolated to evaluate axillary lymph nodes, the study aimed to compare the performance of mean ADC using the optimal mean ADC threshold as determined in this study as opposed to the threshold prescribed by EUSOBI.

MATERIALS AND METHODS

Patients

This retrospective study was approved by the institutional review board at Memorial Sloan Kettering Cancer Center and the requirement for informed consent was waived. All study procedures were conducted according to the Declaration of Helsinki. Two separate groups of consecutive patients who underwent breast MRI at a tertiary care center from January 2017–December 2020 were identified. Group one (patients with benign axillary lymph nodes) were patients with a Breast Imaging and Reporting and Data System (BI-RADS) score of 1 or 2 on MRI and subsequent negative two-year follow-up breast MRI. Of 268 patients who fulfilled these criteria, 158 patients were excluded due to either DWI sequences not performed or no measurable axillary lymph nodes in the field of view of DWI. Group two (patients with metastatic axillary lymph nodes, i.e., malignant lymph nodes) were patients with a BI-RADS score of 6 on MRI with a subsequent biopsy that showed morphologically abnormal adenopathy. Of 317 patients who fulfilled these criteria, 210 patients were excluded due to either DWI sequences not performed, axillary lymph nodes not in the field of view of DWI, or only post-neoadjuvant MRI exam available. The final study sample consisted of 217 patients, 110 who had benign lymph nodes and 107 who had malignant lymph nodes.

Magnetic Resonance Imaging Protocol

All MRI examinations were performed using a 3 Tesla system (Discovery MR750; GE Healthcare, Chicago, IL) with a dedicated

16-channel phased-array breast coil (Vanguard, Sentinelle Medical, Toronto, Canada), with patients in the prone position. A standard multiparametric breast protocol was performed including axial T2-weighted imaging with and without fat saturation, DWI with ADC mapping, and dynamic contrast-enhanced imaging after an injection of a standard dose of contrast agent (0.1 mmol/kg bodyweight).

Axial DWI was performed using single-shot spin echo sequence with echo-planar imaging readouts, with b-values of 0 and 800 s/mm^2. Parameters were as follows: TR, 6000 ms; TE, minimum, flip angle, 90º; acquisition matrix, 192 × 192; reconstructed matrix, 256 × 256; FOV, 28–38 cm; slice thickness, 3.9 mm; NEX, 3; slice gap, 0–1 mm; fat suppression, special; parallel imaging, ASSET; acquisition time, 3-4 minutes. Dual shim volumes were placed over both breasts to optimize the B_0 homogeneity.

Image Analysis

All MR images were reviewed by one radiologist with subspecialty training in breast MRI interpretation. Lymph nodes were identified on the ADC map by using conventional MR imaging information as a reference. Measurements were performed by placing a region of interest (ROI) of 0.5 mm diameter on lesions. 2D regions of interest (ROIs) measuring at least 5 mm were drawn manually on ADC maps within the solid portion on the largest section of lymph node. ADC values were measured three times in three different evaluation sessions and averaged as means ± standard deviations.

Statistical Analysis

Descriptive characteristics were summarized using medians and interquartile ranges (IQR).

Minimum, maximum, and mean ADC (min ADC, max ADC, and mean ADC) were compared between benign and malignant lymph nodes using the Wilcoxon rank sum test. To compare the accuracy of these three ADC parameters in discriminating between benign and malignant axillary lymph nodes, area under the receiver operating characteristic curve (AUC) with 95% confidence intervals were compared using DeLong's test for correlated receiving operating characteristic curves (33), with Bonferroni correction for multiple comparisons ($\alpha^\star = 0.016$).

Thresholds (optimal cut-off points) for discriminating between benign and malignant axillary lymph nodes using the three parameters were estimated using Youden's Index, and sensitivity, specificity, positive predictive value (PPV), negative predictive value (NPV), and accuracy for each parameter were determined at the corresponding optimal thresholds. Sensitivity and specificity of the mean ADC parameter using the determined optimal threshold for axillary lymph nodes *vs*. the EUSOBI ADC threshold for breast tumors were compared using McNemar's test with continuity correction. All statistical analysis was done using R 3.6.3.

RESULTS

Patient Characteristics

The study sample consisted of 217 patients (100% female) with a median age of 52 years (range, 22–81). All patients with benign axillary lymph nodes had no known prior history of breast cancer.

Range of ADC Values of Benign and Malignant Axillary Lymph Nodes

In patients with benign axillary lymph nodes, ADC values (× 10^{-3} mm^2/s) ranged from 0.522–2.712 for mean ADC, 0.774–3.382 for max ADC, and 0.071–2.409 for min ADC. The median values (× 10^{-3} mm^2/s) of mean ADC, max ADC, and min ADC in these patients were 1.214 (median IQR from 1.022–1.469), 1.674 (median IQR 1.370-2.122), and 0.764 (median IQR 0.535-0.981), respectively (**Table 1**) (**Figures 1**, **2**).

In patients with malignant axillary lymph nodes, ADC values (× 10^{-3} mm^2/s) ranged from 0.432–1.570 for mean ADC, 0.478–2.203 for max ADC, and 0.008–1.251 for min ADC. The median values (× 10^{-3} mm^2/s) of mean ADC, max ADC, and min ADC in these patients were 0.942 (median IQR 0.796–1.080), 1.392 (median IQR 1.168–1.592), and 0.540 (median IQR 0.351–0.688), respectively (**Table 1**) (**Figure 3**).

While there was a statistically difference in all ADC parameters ($p < 0.001$) between benign and malignant axillary lymph nodes (**Table 1**), boxplots for mean (**Figure 4A**), max (**Figure 4B**), and min ADC (**Figure 4C**) illustrate that there is an overlap of benign and malignant nodes which is the least for ADC mean, indicating that this is the most useful metric.

ADC Thresholds for Differentiating Between Benign and Malignant Axillary Lymph Nodes

The optimal mean ADC threshold for differentiating between benign and malignant axillary lymph nodes was 1.004 × 10^{-3}mm^2/s, yielding an accuracy of 75% (95% CI 0.688, 0.807), sensitivity of 71% (95% CI 0.615, 0.794), specificity of 79% (95% CI 0.703, 0.863), PPV of 77% (95% CI 0.672, 0.847), and NPV of 74% (95% CI 0.648, 0.814) (**Figure 5A**).

The optimal max ADC threshold for differentiating between malignant and benign axillary lymph nodes was 1.740 × 10^{-3} mm^2/s, yielding an accuracy of 69% (95% CI 0.62, 0.748), sensitivity of 91% (95% CI 0.835, 0.954), specificity of 47%

TABLE 1 | Comparison of ADC parameters between benign and malignant lymph nodes.

Characteristic (median value)	Overall (n = 217)	Benign (n = 110)	Malignant (n = 107)	p-value
ADC mean (× 10^{-3} mm^2/s)	1.033 (0.911, 1.254)	1.214 (1.022, 1.469)	0.942 (0.796, 1.080)	1.506×10^{-14}
ADC max (× 10^{-3} mm^2/s)	1.486 (1253, 1.772)	1.674 (1.370, 2.122)	1.392 (1.168, 1.592)	1.284×10^{-7}
ADC min (× 10^{-3} mm^2/s)	0.642 (0.462, 0.841)	0.764 (0.535, 0.981)	0.540 (0.351, 0.688)	2.197×10^{-8}

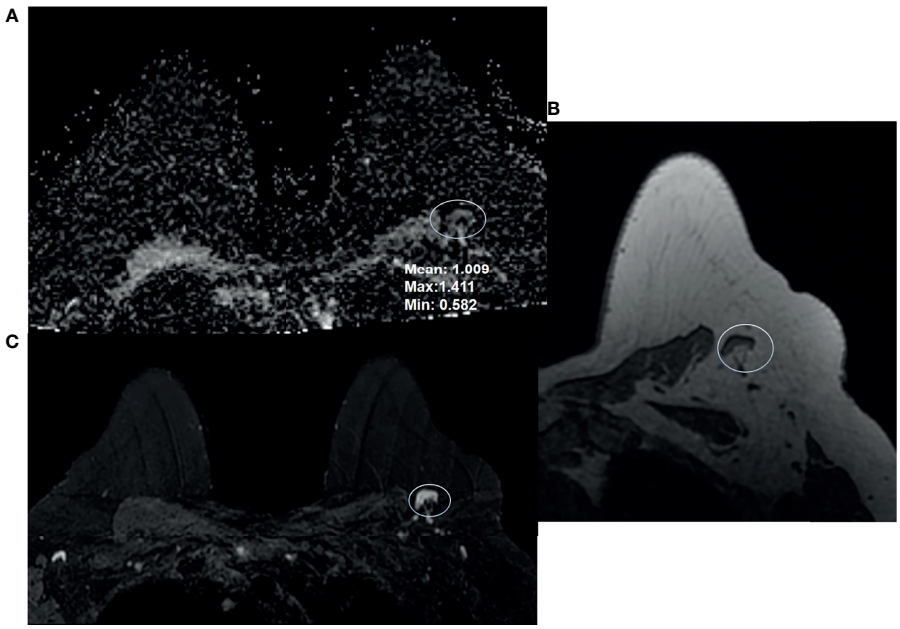

FIGURE 1 | 68-year-old woman presented for high-risk screening breast MRI exam. She had a family history of cancer, and was BRCA1 and ATM positive. Breast MRI shows a benign appearing left axillary level 1 lymph node: **(A)** ADC, **(B)** T1-weighted non-fat saturated, and **(C)** T2-weighted fat saturated axial sequences.

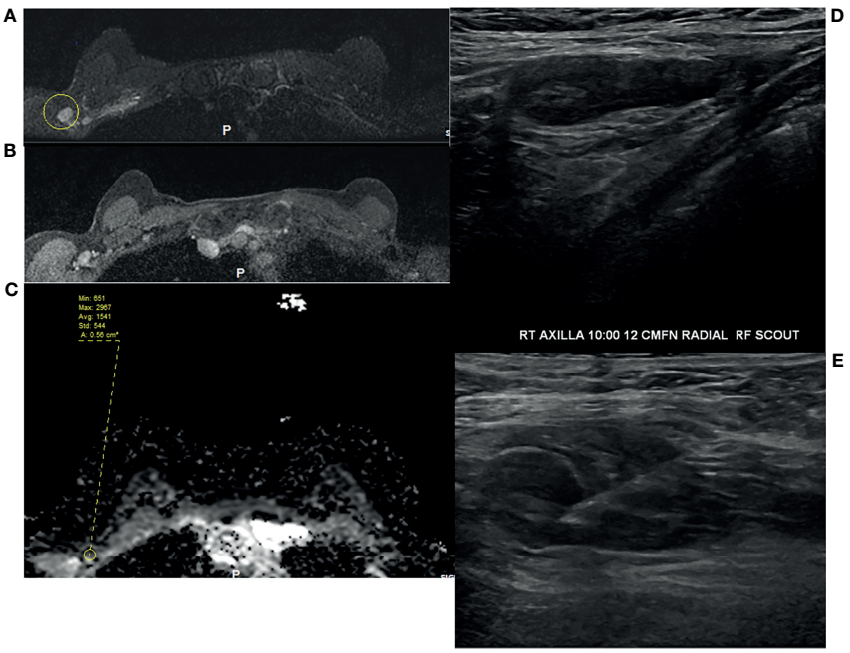

FIGURE 2 | 49-year-old woman underwent routine screening breast MRI exam. She received a dose of the COVID vaccine in the right arm a few months prior to her breast MRI. Enlarged right axillary lymph nodes were identified on breast MRI. **(A)** T2-weighted fat saturated image, **(B)** T1-weighted fat saturated post-contrast image, and **(C)** ADC. She subsequently underwent diagnostic ultrasound and ultrasound-guided fine needle aspiration **(D, E)**, which yielded benign results.

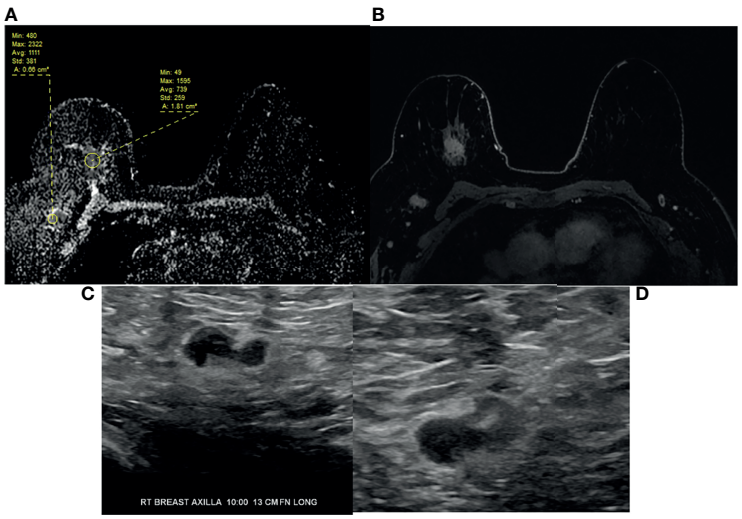

FIGURE 3 | 64-year-old woman with right breast 12:00 axis triple negative invasive ductal carcinoma and right axillary lymphadenopathy as seen on **(A)** ADC, **(B)** T1-weighted fat saturated post-contrast image. **(C)** Targeted ultrasound shows borderline cortical thickening of the right axillary lymph node. **(D)** Ultrasound-guided fine needle aspiration confirmed metastatic adenopathy. Note the difference in ADC values between primary breast and right axillary adenopathy, e.g., mean ADC 0.739 versus 1.111.

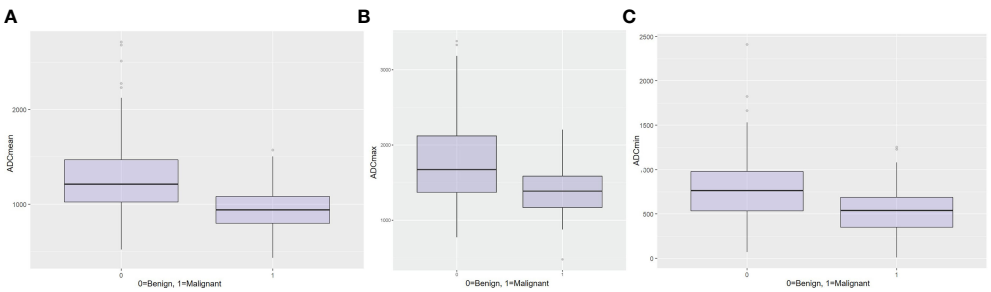

FIGURE 4 | Boxplots for **(A)** mean ADC, **(B)** maximum ADC, and **(C)** minimum ADC for the differentiation between benign and malignant axillary lymph nodes.

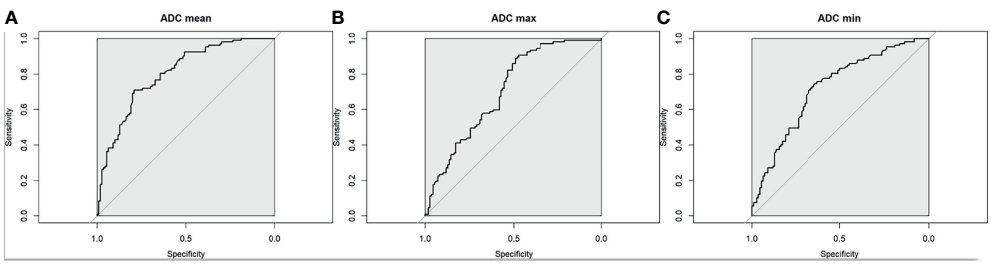

FIGURE 5 | Receiver operating characteristic curve for **(A)** mean ADC, **(B)** maximum ADC, and **(C)** minimum ADC for the differentiation between benign and malignant axillary lymph nodes.

(95% CI 0.377, 0.57), PPV of 63% (95% CI 0.545, 0.702), and NPV of 84% (95% CI 0.723, 0.92) (**Figure 5B**).

The optimal min ADC threshold for differentiating between malignant and benign axillary lymph nodes was 0.692×10^{-3} mm^2/s, yielding an accuracy of 69% (95% CI 0.625, 0.752), sensitivity of 76% (95% CI 0.665, 0.835), specificity of 63% (95% CI 0.53, 0.718), PPV of 66% (95% CI 0.573, 0.747), and NPV of 73% (95% CI 0.625, 0.813) (**Figure 5C**).

Comparison of the Determined Optimal Mean ADC Threshold *vs*. EUSOBI Mean ADC Threshold

Compared with the determined optimal mean ADC threshold of 1.004×10^{-3}mm^2/s, when the EUSOBI mean ADC threshold of 1.300×10^{-3} mm^2/s was applied to axillary lymph nodes, it had lower discriminative power to differentiate between benign and malignant axillary lymph nodes, yielding an accuracy of 66% (95% CI 0.60, 0.73), with a sensitivity of 94% (95% CI 0.88, 0.98), specificity of 39% (95% CI 0.30, 0.49), PPV of 60% (95% CI 0.52, 0.68), and NPV of 88% (95% CI 0.75, 0.95). While the EUSOBI mean ADC threshold had a significantly higher sensitivity than the optimal mean ADC threshold ($p \leq 0.001$), it had a significantly lower specificity ($p < 0.001$). Specifically, there were 6 false-negative findings using the EUSOBI mean ADC threshold versus 31 false-negative findings using the optimal mean ADC threshold, while there were 67 false-positive findings using the EUSOBI mean ADC threshold versus 23 false-positive findings using the optimal mean ADC threshold. An ADC mean threshold of 1.004×10^{-3} would have obviated 66% of recommendations for biopsies in benign lymph nodes.

We further validated our findings by performance of an analysis based on an internal validation cohort obtained by random sampling of 50% of the original cohort, which yielded similar results: (a) the minimum, maximum, and mean ADC values were significantly different between benign and malignant nodes, (b) the ROC obtained by using mean ADC values was significantly better than those obtained by using minimum and maximum values ($p = 0.04664$ and 0.00336, respectively), (c) sensitivity was better with the EUSOBI threshold (*vs* the proposed ADC mean threshold) (McNemar test $p = 0.004427$) while specificity was better with the proposed ADC mean threshold of 1.004×10^{-3} (McNemar's test $p = 0.0001$) and (d) mean ADC values provided the least overlap between benign and malignant nodes.

DISCUSSION

In this study, while significant differences were observed when comparing the median values all ADC parameters (mean ADC, max ADC, and min ADC) between benign and malignant axillary lymph nodes, results show that there is a significant overlap of ADC values of benign and malignant nodes. The least overlap in ADC values occurred with mean ADC, suggesting that this is the most useful ADC parameter for differentiating between benign and malignant axillary lymph nodes. The mean ADC threshold that resulted in the highest diagnostic accuracy for differentiating between benign and malignant lymph nodes was 1.004×10^{-3} mm^2/s, which is lower than the EUSOBI mean ADC threshold of 1.300×10^{-3} mm^2/s which was recently recommended for breast tumors but not for axillary lymph nodes per se.

The median values of mean ADC, max ADC, and min ADC were significantly lower for malignant *vs*. benign axillary lymph nodes, in agreement with the findings from a meta-analysis of ten studies, where the mean ADC value of metastatic lymph nodes was also significantly lower than that of benign axillary lymph nodes (34). Our data indicate, however, that while these differences were significant ($p < 0.001$), the range of possible ADC values for benign axillary lymph nodes was wide, overlapping with the range of possible ADC values for malignant axillary lymph nodes both in our study as well as in previous studies in the literature.

Previously published data have shown that malignant nodes can also present with a range of ADC values from 0.666×10^{-3} mm^2/s to 1.369×10^{-3} mm^2/s (21, 23–25), with the discrepancies between studies most likely due to differences in nodal tumor burden. Yamaguchi et al. (21) reported a mean ADC value of metastatic axillary lymph nodes ranging from 0.553×10^{-3} mm^2/s to 1.135×10^{-3} mm^2/s. Fornasa et al. (30, 35) reported a mean ADC value of 0.878×10^{-3} mm^2/s (range, $0.30–1.20 \times 10^{-3}$ mm^2/s) in 43 metastatic axillary lymph nodes. Our study found the median value of mean ADC to be 1.214×10^{-3} mm^2/s (range, $0.522–2.712 \times 10^{-3}$ mm^2/s).

In our study, a similar range was also identified for benign axillary lymph nodes, which had a mean ADC ranging from $0.522–2.712 \times 10^{-3}$ mm^2/s, max ADC from $1.788–3.382 \times 10^{-3}$ mm^2/s, and min ADC from $0.71–2.409 \times 10^{-3}$ mm^2/s. These values overlap with that of malignant axillary lymph nodes not only with those in our study but also with those reported in the literature (36–38). This overlap can present diagnostic challenges, e.g., in patients with a current or past personal history of breast cancer or in the setting of morphologically abnormal yet benign lymph nodes due to conditions such as vaccination. As the degree of overlap was least for mean ADC, this suggests that it would be the most useful ADC parameter for characterizing axillary lymph nodes.

In our study, the optimal mean ADC threshold for differentiating between benign and malignant nodes was 1.004×10^{-3} mm^2/s, which is in line with prior studies investigating axillary lymph nodes in patients with breast cancer (36, 37). For example, Hasanzadeh et al. reported that the optimal mean ADC cut-off value for differentiating between metastatic and non-metastatic axillary lymph nodes was 0.904×10^{-3} mm^2/s, which yielded a higher specificity (88.9%) and accuracy (91.8%) than min ADC or max ADC (39). Yamaguchi et al. (36) reported a sensitivity and specificity of 85% and 81%, respectively, for differentiating metastatic from non-metastatic axillary lymph nodes using a cut-off ADC value of 0.852. Kamitani et al. (37) reported a sensitivity of 53.8%, specificity of 86.9%, PPV of 56.0%, NPV of 85.9%, and accuracy of 79.1% with a mean ADC $\leq 1.05 \times 10^{-3}$ mm^2/s.

The EUSOBI International Breast DWI working group recently issued a consensus and mission statement that included acquisition parameters for standard breast DWI sequences including specifications of b values, fat saturation, spatial resolution, and repetition and echo times, as well as levels of diffusion restriction/hindrance in the breast based on the published literature on breast DWI to allow the assessment of breast lesions in an objective way (32). The use of ADC values measured at the high b value of 800 s/mm^2 was recommended,

with diffusion levels in lesions classified as follows: very low (ADC = ≤ 0.9 × 10^{-3} mm^2/sec); low (ADC = 0.9–1.3 × 10^{-3} mm^2/s); intermediate (ADC = 1.3–1.7 × 10^{-3} mm^2/s); high (ADC = 1.7–2.1 × 10^{-3} mm^2/s) and very high (ADC > 2.1 x 10^{-3} mm^2/s) (32). Lesions with very low and ADC values are considered suspicious for malignancy and biopsy is recommended for these lesions. However, it was unclear how the recently proposed levels of diffusion restriction for breast tumor perform in axillary lymph nodes.

In our study, based on ROC curve analysis, the optimal mean ADC threshold for differentiating between malignant and benign lymph nodes was 1.004 × 10^{-3} mm^2/s, resulting in a diagnostic accuracy of 75%. This threshold is lower the EUSOBI mean ADC that is recommended for breast tumors. When the EUSOBI mean ADC threshold was applied to axillary lymph nodes in our study, the diagnostic accuracy dropped to 66%. Moreover, the specificity also dropped from 79% to 39%. This suggests that the EUSOBI mean ADC threshold for characterizing breast tumors does not equally apply to the characterization of axillary lymph nodes and different thresholds are needed for these entities. However, it has to be noted that the optimal mean ADC threshold of 1.004 × 10^{-3} mm^2/s yielded a lower sensitivity than the EUSOBI mean ADC; thus, if the threshold of 1.004 × 10^{-3} mm^2/s is used, recommendations for biopsy versus follow-up will have to be made carefully in consideration of the clinical context.

Another option would be to consciously select a more conservative threshold that decreases specificity and increases sensitivity. It has been shown in breast tumors that the selection of ADC cut-off values to characterize breast tumors can be dependent on the expectations from DWI (40). Higher cut-off values are desirable for increasing sensitivity, whereas lower cut-off values are desirable for increasing specificity. The recent American College of Radiology Imaging Network 6702 trial evaluated the ADC values of undiagnosed breast lesions (BI-RADS 3, 4, or 5) identified at DCE-MRI and proposed an ADC cut-off of 1.68 × 10^{-3} mm^2/s to improve specificity without affecting sensitivity (41). For the assessment of axillary lymph nodes, currently it seems that the suspicion of malignancy should therefore be interpreted in conjunction with the patient's history (past or current diagnosis of breast cancer, vaccination status), lymph node morphology (cortical thickness), and if applicable the ADC values of the index cancer.

This study has limitations. It was a single-center study and therefore it was difficult to predict how the thresholds might perform with data acquired using different imaging protocols. Nevertheless, the thresholds were in line with prior studies from different institutions performed in patients with breast cancer. In our study, a single-shot EPI DWI sequence was used, and therefore, our results may not be extrapolated to other DWI sequences. In addition, there are constant improvements in DWI techniques (42, 43) and the use of more advanced techniques may further improve axillary lymph node assessment. In this study, long-term stability of axillary lymph nodes indicated by least two years of negative follow-up MRI was required to establish benign status. Therefore, we did not include datag acquired with the recently implemented advanced high-spatial-resolution multishot multiplexed sensitivity-encoding DWI at our institution, but this will be the focus of a future study.

In conclusion, benign axillary lymph nodes can present with a wide range of ADC values. While there are significant differences in ADC values between benign and malignant axillary lymph nodes, radiologists should be aware of a significant overlap, with mean ADC possibly being the most useful ADC parameter in this context. The mean ADC threshold that provided the highest diagnostic accuracy for differentiation between benign and malignant axillary lymph nodes is lower than the threshold recommended by EUSOBI for breast tumors; hence, the latter threshold should not be extrapolated to the axilla to avoid unnecessary biopsies.

DATA AVAILABILITY STATEMENT

The datasets generated during and/or analyzed during the current study are available from the corresponding author on reasonable request. Requests to access these datasets should be directed to KP, pinkerdk@mskcc.org.

ETHICS STATEMENT

The studies involving human participants were reviewed and approved by Institutional Review Board, Memorial Sloan Kettering Cancer Center. Written informed consent for participation was not required for this study in accordance with the national legislation and the institutional requirements.

AUTHOR CONTRIBUTIONS

KP, RF, ST, and VS contributed to conception and design of the study. RF, JH, RL, JR, ESW, and NT organized the database. VS performed the statistical analysis. RF wrote the first draft of the manuscript. JH, RL, JR, and ESW wrote sections of the manuscript. All authors contributed to revising the manuscript and approved the submitted version of the manuscript.

FUNDING

This research was funded in part through the NIH/NCI Cancer Center Support Grant P30 CA008748 and the NIH/NCI UG3 CA239861 grant.

ACKNOWLEDGMENTS

The authors thank Joanne Chin, MFA, ELS, for her help in editing this manuscript.

REFERENCES

1. Chetlen A, Nicholson B, Patrie JT, Harvey JA. Is Screening Detected Bilateral Axillary Adenopathy on Mammography Clinically Significant? *Breast J* (2012) 18:582–7. doi: 10.1111/tbj.12040
2. Patel T, Given-Wilson RM, Thomas V. The Clinical Importance of Axillary Lymphadenopathy Detected on Screening Mammography: Revisited. *Clin Radiol* (2005) 60:64–71. doi: 10.1016/j.crad.2004.05.007
3. Polack FP, Thomas SJ, Kitchin N, Absalon J, Gurtman A, Lockhart S, et al. Safety and Efficacy of the BNT162b2 Mrna Covid-19 Vaccine. *N Engl J Med* (2020) 383:2603–15. doi: 10.1056/NEJMoa2034577
4. Oliver S, Gargano J, Marin M, Wallace M, Curran K, Chamberland M, et al. The Advisory Committee on Immunization Practices' Interim Recommendation for Use of Moderna COVID-19 Vaccine — United States, December 2020. *MMWR Morb Mortal Wkly Rep* (2021) 69:1653–1656. doi: 10.15585/mmwr.mm695152e1
5. Fisher B, Bauer M, Wickerham DL, Redmond CK, Fisher ER, Cruz AB, et al. Relation of Number of Positive Axillary Nodes to the Prognosis of Patients With Primary Breast Cancer. An NSABP Update. *Cancer* (1983) 52:1551–7. doi: 10.1002/1097-0142(19831101)52:9<1551::aid-cncr2820520902>3.0.co;2-3
6. Yamashita H, Ogiya A, Shien T, Horimoto Y, Masuda N, Inao T, et al. Clinicopathological Factors Predicting Early and Late Distant Recurrence in Estrogen Receptor-Positive, HER2-Negative Breast Cancer. *Breast Cancer* (2016) 23:830–43. doi: 10.1007/s12282-015-0649-0
7. Lyman GH, Somerfield MR, Giuliano AE. Sentinel Lymph Node Biopsy for Patients With Early-Stage Breast Cancer: 2016 American Society of Clinical Oncology Clinical Practice Guideline Update Summary. *J Oncol Pract* (2017) 13:196–8. doi: 10.1200/jop.2016.019992
8. Weiser MR, Montgomery LL, Susnik B, Tan LK, Borgen PI, Cody HS. Is Routine Intraoperative Frozen-Section Examination of Sentinel Lymph Nodes in Breast Cancer Worthwhile? *Ann Surg Oncol* (2000) 7:651–5. doi: 10.1007/s10434-000-0651-3
9. Krishnamurthy S, Meric-Bernstam F, Lucci A, Hwang RF, Kuerer HM, Babiera G, et al. A Prospective Study Comparing Touch Imprint Cytology, Frozen Section Analysis, and Rapid Cytokeratin Immunostain for Intraoperative Evaluation of Axillary Sentinel Lymph Nodes in Breast Cancer. *Cancer* (2009) 115:1555–62. doi: 10.1002/cncr.24182
10. Vanderveen KA, Ramsamooj R, Bold RJ. A Prospective, Blinded Trial of Touch Prep Analysis Versus Frozen Section for Intraoperative Evaluation of Sentinel Lymph Nodes in Breast Cancer. *Ann Surg Oncol* (2008) 15:2006–11. doi: 10.1245/s10434-008-9944-8
11. Pogacnik A, Klopcic U, Grazio-Frković S, Zgajnar J, Hocevar M, Vidergar-Kralj B. The Reliability and Accuracy of Intraoperative Imprint Cytology of Sentinel Lymph Nodes in Breast Cancer. *Cytopathology* (2005) 16:71–6. doi: 10.1111/j.1365-2303.2004.00212.x
12. Ballal H, Hunt C, Bharat C, Murray K, Kamyab R, Saunders C. Arm Morbidity of Axillary Dissection With Sentinel Node Biopsy Versus Delayed Axillary Dissection. *ANZ J Surg* (2018) 88:917–21. doi: 10.1111/ans.14382
13. Renaudeau C, Lefebvre-Lacoeuille C, Campion L, Dravet F, Descamps P, Ferron G, et al. Evaluation of Sentinel Lymph Node Biopsy After Previous Breast Surgery for Breast Cancer: GATA Study. *Breast* (2016) 28:54–9. doi: 10.1016/j.breast.2016.04.006
14. Chung J, Youk JH, Kim JA, Gweon HM, Kim EK, Ryu YH, et al. Role of Diffusion-Weighted MRI: Predicting Axillary Lymph Node Metastases in Breast Cancer. *Acta Radiol* (2014) 55:909–16. doi: 10.1177/0284185113509094
15. Razek AA, Lattif MA, Denewer A, Farouk O, Nada N. Assessment of Axillary Lymph Nodes in Patients With Breast Cancer With Diffusion-Weighted MR Imaging in Combination With Routine and Dynamic Contrast MR Imaging. *Breast Cancer* (2016) 23:525–32. doi: 10.1007/s12282-015-0598-7
16. Clauser P, Mann R, Athanasiou A, Prosch H, Pinker K, Dietzel M, et al. A Survey by the European Society of Breast Imaging on the Utilisation of Breast MRI in Clinical Practice. *Eur Radiol* (2018) 28:1909–18. doi: 10.1007/s00330-017-5121-4
17. Scaranelo AM, Eiada R, Jacks LM, Kulkarni SR, Crystal P. Accuracy of Unenhanced MR Imaging in the Detection of Axillary Lymph Node Metastasis: Study of Reproducibility and Reliability. *Radiology* (2012) 262:425–34. doi: 10.1148/radiol.11110639
18. Hieken TJ, Trull BC, Boughey JC, Jones KN, Reynolds CA, Shah SS, et al. Preoperative Axillary Imaging With Percutaneous Lymph Node Biopsy Is Valuable in the Contemporary Management of Patients With Breast Cancer. *Surgery* (2013) 154:831–8; discussion 838-40. doi: 10.1016/j.surg.2013.07.017
19. Abe H, Schacht D, Kulkarni K, Shimauchi A, Yamaguchi K, Sennett CA, et al. Accuracy of Axillary Lymph Node Staging in Breast Cancer Patients: An Observer-Performance Study Comparison of MRI and Ultrasound. *Acad Radiol* (2013) 20:1399–404. doi: 10.1016/j.acra.2013.08.003
20. Pinker K, Bickel H, Helbich TH, Gruber S, Dubsky P, Pluschnig U, et al. Combined Contrast-Enhanced Magnetic Resonance and Diffusion-Weighted Imaging Reading Adapted to the "Breast Imaging Reporting and Data System" for Multiparametric 3-T Imaging of Breast Lesions. *Eur Radiol* (2013) 23:1791–802. doi: 10.1007/s00330-013-2771-8
21. Pinker K, Bogner W, Baltzer P, Gruber S, Bickel H, Brueck B, et al. Improved Diagnostic Accuracy With Multiparametric Magnetic Resonance Imaging of the Breast Using Dynamic Contrast-Enhanced Magnetic Resonance Imaging, Diffusion-Weighted Imaging, and 3-Dimensional Proton Magnetic Resonance Spectroscopic Imaging. *Invest Radiol* (2014) 49:421–30. doi: 10.1097/rli.0000000000000029
22. Pinker K, Bogner W, Baltzer P, Karanikas G, Magometschnigg H, Brader P, et al. Improved Differentiation of Benign and Malignant Breast Tumors With Multiparametric 18fluorodeoxyglucose Positron Emission Tomography Magnetic Resonance Imaging: A Feasibility Study. *Clin Cancer Res* (2014) 20:3540–9. doi: 10.1158/1078-0432.Ccr-13-2810
23. Jacobs MA, Stearns V, Wolff AC, Macura K, Argani P, Khouri N, et al. Multiparametric Magnetic Resonance Imaging, Spectroscopy and Multinuclear (^{23}Na) Imaging Monitoring of Preoperative Chemotherapy for Locally Advanced Breast Cancer. *Acad Radiol* (2010) 17:1477–85. doi: 10.1016/j.acra.2010.07.009
24. Amornsiripanitch N, Bickelhaupt S, Shin HJ, Dang M, Rahbar H, Pinker K, et al. Diffusion-Weighted MRI for Unenhanced Breast Cancer Screening. *Radiology* (2019) 293:504–20. doi: 10.1148/radiol.2019182789
25. Chen X, Li WL, Zhang YL, Wu Q, Guo YM, Bai ZL. Meta-Analysis of Quantitative Diffusion-Weighted MR Imaging in the Differential Diagnosis of Breast Lesions. *BMC Cancer* (2010) 10:693. doi: 10.1186/1471-2407-10-693
26. Ei Khouli RH, Jacobs MA, Mezban SD, Huang P, Kamel IR, Macura KJ, et al. Diffusion-Weighted Imaging Improves the Diagnostic Accuracy of Conventional 3.0-T Breast MR Imaging. *Radiology* (2010) 256:64–73. doi: 10.1148/radiol.10091367
27. Yabuuchi H, Matsuo Y, Kamitani T, Setoguchi T, Okafuji T, Soeda H, et al. Non-Mass-Like Enhancement on Contrast-Enhanced Breast MR Imaging: Lesion Characterization Using Combination of Dynamic Contrast-Enhanced and Diffusion-Weighted MR Images. *Eur J Radiol* (2010) 75:e126–32. doi: 10.1016/j.ejrad.2009.09.013
28. Kul S, Cansu A, Alhan E, Dinc H, Gunes G, Reis A. Contribution of Diffusion-Weighted Imaging to Dynamic Contrast-Enhanced MRI in the Characterization of Breast Tumors. *AJR Am J Roentgenol* (2011) 196:210–7. doi: 10.2214/ajr.10.4258
29. Partridge SC, DeMartini WB, Kurland BF, Eby PR, White SW, Lehman CD. Quantitative Diffusion-Weighted Imaging as an Adjunct to Conventional Breast MRI for Improved Positive Predictive Value. *AJR Am J Roentgenol* (2009) 193:1716–22. doi: 10.2214/ajr.08.2139
30. Fornasa F, Nesoti MV, Bovo C, Bonavina MG. Diffusion-Weighted Magnetic Resonance Imaging in the Characterization of Axillary Lymph Nodes in Patients With Breast Cancer. *J Magn Reson Imaging* (2012) 36:858–64. doi: 10.1002/jmri.23706
31. Ahmed AAI, Doaa Ibrahim H, Hasan A-A. Diagnostic Accuracy of Apparent Diffusion Coefficient Value in Differentiating Metastatic Form Benign Axillary Lymph Nodes in Cancer Breast. *Egypt J Radiol Nucl Med* (2014) 45:1011–6. doi: 10.1016/j.ejrnm.2014.06.003
32. Baltzer P, Mann RM, Iima M, Sigmund EE, Clauser P, Gilbert FJ, et al. Diffusion-Weighted Imaging of the Breast-a Consensus and Mission Statement From the EUSOBI International Breast Diffusion-Weighted Imaging Working Group. *Eur Radiol* (2020) 30:1436–50. doi: 10.1007/s00330-019-06510-3
33. DeLong ER, DeLong DM, Clarke-Pearson DL. Comparing the Areas Under Two or More Correlated Receiver Operating Characteristic Curves: A Nonparametric Approach. *Biometrics* (1988) 44:837–45. doi: 10.2307/2531595
34. Zhou M, Lu B, Lv G, Tang Q, Zhu J, Li J, et al. Differential Diagnosis Between Metastatic and Non-Metastatic Lymph Nodes Using DW-MRI: A Meta-

Analysis of Diagnostic Accuracy Studies. *J Cancer Res Clin Oncol* (2015) 141:1119–30. doi: 10.1007/s00432-014-1895-9
35. Fornasa F, Pinali L, Gasparini A, Toniolli E, Montemezzi S. Diffusion-Weighted Magnetic Resonance Imaging in Focal Breast Lesions: Analysis of 78 Cases With Pathological Correlation. *Radiol Med* (2011) 116:264–75. doi: 10.1007/s11547-010-0602-4
36. Yamaguchi K, Schacht D, Nakazono T, Irie H, Abe H. Diffusion Weighted Images of Metastatic as Compared With Nonmetastatic Axillary Lymph Nodes in Patients With Newly Diagnosed Breast Cancer. *J Magn Reson Imaging* (2015) 42:771–8. doi: 10.1002/jmri.24829
37. Kamitani T, Hatakenaka M, Yabuuchi H, Matsuo Y, Fujita N, Jinnouchi M, et al. Detection of Axillary Node Metastasis Using Diffusion-Weighted MRI in Breast Cancer. *Clin Imaging* (2013) 37:56–61. doi: 10.1016/j.clinimag.2012.02.014
38. Nakai G, Matsuki M, Harada T, Tanigawa N, Yamada T, Barentsz J, et al. Evaluation of Axillary Lymph Nodes by Diffusion-Weighted MRI Using Ultrasmall Superparamagnetic Iron Oxide in Patients With Breast Cancer: Initial Clinical Experience. *J Magn Reson Imaging* (2011) 34:557–62. doi: 10.1002/jmri.22651
39. Hasanzadeh F, Faeghi F, Valizadeh A, Bayani L. Diagnostic Value of Diffusion Weighted Magnetic Resonance Imaging in Evaluation of Metastatic Axillary Lymph Nodes in a Sample of Iranian Women With Breast Cancer. *Asian Pac J Cancer Prev* (2017) 18:1265–70. doi: 10.22034/apjcp.2017.18.5.1265
40. Partridge SC, McDonald ES. Diffusion Weighted Magnetic Resonance Imaging of the Breast: Protocol Optimization, Interpretation, and Clinical Applications. *Magn Reson Imaging Clin N Am* (2013) 21:601–24. doi: 10.1016/j.mric.2013.04.007
41. Rahbar H, Zhang Z, Chenevert TL, Romanoff J, Kitsch AE, Hanna LG, et al. Utility of Diffusion-Weighted Imaging to Decrease Unnecessary Biopsies Prompted by Breast MRI: A Trial of the ECOG-ACRIN Cancer Research Group (A6702). *Clin Cancer Res* (2019) 25:1756–65. doi: 10.1158/1078-0432.Ccr-18-2967
42. Daimiel Naranjo I, Lo Gullo R, Morris EA, Larowin T, Fung MM, Guidon A, et al. High-Spatial-Resolution Multishot Multiplexed Sensitivity-Encoding Diffusion-Weighted Imaging for Improved Quality of Breast Images and Differentiation of Breast Lesions: A Feasibility Study. *Radiol Imaging Cancer* (2020) 2:e190076. doi: 10.1148/rycan.2020190076
43. Bogner W, Pinker-Domenig K, Bickel H, Chmelik M, Weber M, Helbich TH, et al. Readout-Segmented Echo-Planar Imaging Improves the Diagnostic Performance of Diffusion-Weighted MR Breast Examinations at 3.0 T. *Radiology* (2012) 263:64–76. doi: 10.1148/radiol.12111494

Conflict of Interest: KP received payment for activities not related to the present article including lectures and service on speakers bureaus and for travel/accommodations/meeting expenses unrelated to activities listed from the European Society of Breast Imaging (MRI educational course, annual scientific meeting), AURA Health Technologies GmbH and Siemens Healthineers.

The remaining authors declare that the research was conducted in the absence of any commercial or financial relationships that could be construed as a potential conflict of interest.

Publisher's Note: All claims expressed in this article are solely those of the authors and do not necessarily represent those of their affiliated organizations, or those of the publisher, the editors and the reviewers. Any product that may be evaluated in this article, or claim that may be made by its manufacturer, is not guaranteed or endorsed by the publisher.

frontiers in Oncology

ORIGINAL RESEARCH
published: 23 March 2022
doi: 10.3389/fonc.2022.798704

Paclitaxel Chemotherapy Elicits Widespread Brain Anisotropy Changes in a Comprehensive Mouse Model of Breast Cancer Survivorship: Evidence From *In Vivo* Diffusion Weighted Imaging

Lauren D. Otto[1], *Kathryn L. G. Russart*[1,2], *Praveen Kulkarni*[3], *Dana M. McTigue*[4], *Craig F. Ferris*[3] *and Leah M. Pyter*[1,2,4,5*]

[1] Institute for Behavioral Medicine Research, Ohio State University Wexner Medical Center, Columbus, OH, United States, [2] Arthur G. James Comprehensive Cancer Center and Solove Research Institute, Ohio State University, Columbus, OH, United States, [3] Center for Translational Neuroimaging, Department of Psychology and Pharmaceutical Sciences, Northeastern University, Boston, MA, United States, [4] Department of Neuroscience, Ohio State University, Columbus, OH, United States, [5] Department of Psychiatry and Behavioral Health, Ohio State University, Columbus, OH, United States

OPEN ACCESS

Edited by:
Ellen Ackerstaff,
Memorial Sloan Kettering Cancer Center, United States

Reviewed by:
Aisling Chaney,
Stanford University, United States
Ravindra Deshpande,
Wake Forest School of Medicine, United States

***Correspondence:**
Leah M. Pyter
leah.pyter@osumc.edu

Specialty section:
This article was submitted to Cancer Imaging and Image-directed Interventions, a section of the journal Frontiers in Oncology

Received: 01 December 2021
Accepted: 22 February 2022
Published: 23 March 2022

Citation:
Otto LD, Russart KLG, Kulkarni P, McTigue DM, Ferris CF and Pyter LM (2022) Paclitaxel Chemotherapy Elicits Widespread Brain Anisotropy Changes in a Comprehensive Mouse Model of Breast Cancer Survivorship: Evidence From In Vivo Diffusion Weighted Imaging. Front. Oncol. 12:798704. doi: 10.3389/fonc.2022.798704

Breast cancer is one of the most common diseases in the United States with 1 in 8 women developing the disease in her lifetime. Women who develop breast cancer are often post-menopausal and undergo a complex sequence of treatments including surgery, chemotherapy, and aromatase inhibitor therapy. Both independently and through potential interactions, these factors and treatments are associated with behavioral comorbidities reported in patients (e.g., fatigue), although the underlying neurobiological mechanisms are poorly understood. Currently, brain imaging is the most feasible way to assess neurobiology in patients. Indeed, breast cancer patients display alterations in white matter connections and chemotherapy is associated with decreased white and gray matter in the corpus callosum and cortex as well as decreased hippocampal volume. However, imaging in breast cancer rodent models is lacking, impeding translation of the mechanistic neurobiological findings made possible through modeling. Furthermore, current rodent models of breast cancer often lack the complexity of typical multimodal breast cancer treatments, thereby limiting translational value. The present study aimed to develop a comprehensive model of post-menopausal breast cancer survival using immunocompetent ovariectomized mice, including an orthotopic syngeneic tumor, surgical tumor removal, chemotherapy, and aromatase inhibitor therapy. Using this model, we systematically investigated the cumulative effects of chemotherapy and hormone replacement therapy on neurostructure and behavior using diffusion weighted imaging, open field test, and spontaneous alternation test. Our previous findings, in a simplified chemotherapy-only model, indicate that this regimen of chemotherapy causes circulating and central inflammation concurrent with reduced locomotor activity. The

current study, in the more comprehensive model, has recapitulated the peripheral inflammation coincident with reduced locomotor activity as well as demonstrated that chemotherapy also drives widespread changes in brain anisotropy. Validating the clinical relevance of this comprehensive rodent breast cancer model will allow for additional neurobiological investigations of the interactions among various cancer components associated with behavioral comorbidities, as well as the relationship between these mechanisms and neurostructural imaging changes that can be measured in cancer patients.

Keywords: survivor, DTI/DWI, fatigue, translational, mammary tumor, cytokines, comorbidities

INTRODUCTION

Over 3.8 million women in the United States are breast cancer survivors, with more than 280,000 new diagnoses predicted for 2021 (1). With advances in treatment and screening, 90% of these patients survive at least 5 years (1). However, 17-98% of patients and survivors report negative behavioral side effects before, during, and after treatment, including fatigue, mood disorders, and cognitive impairments (2–4). Fatigue is one of the most common behavioral comorbidities in breast cancer patients (5) and is often reported after chemotherapy treatment but can also occur even before chemotherapy, suggesting additive causal roles of stress, tumor biology, and surgery (6). Fatigue can persist years after treatment ends (7–9). Even mild behavioral consequences undeniably reduce quality-of-life, which in turn reduces work performance and employability (10, 11), increases medical costs (12), and decreases treatment adherence (13–15).

The central mechanisms of cancer-associated fatigue are not yet elucidated, but fatigue after chemotherapy treatment is associated with altered brain microstructure (16, 17). For example, fatigued breast cancer survivors display dynamic differences in white matter connections between specific regions of the brain (18). Furthermore, chemotherapy treatment corresponds with reduced white and gray matter in the corpus callosum and cortex (19) and reduced hippocampal volume (20). In some cases, these structural changes persist over 20 years post-chemotherapy (21) and may be progressive (22). However, these effects vary with chemotherapeutic agent and regimen and radiotherapy treatment (23, 24). Microstructural damage analyzed by diffusion tensor imaging (DTI) has also been reported with fatigue in non-oncological human diseases (25, 26).

In addition to structural brain changes, chemotherapy, as well as surgery and tumor biology, causes systemic inflammation (27, 28). Indeed, circulating proinflammatory markers in chemotherapy patients (e.g., c-reactive protein and interleukin [IL]-6) positively correlate with behavioral comorbidities including fatigue (29–33). Using rodent models, both tumors and chemotherapy independently cause behavioral abnormalities and increases in circulating and neuroinflammatory markers (34). Indeed, peripheral inflammatory signals from a tumor or from cell death caused by chemotherapy treatment can propagate into the brain and result in local neuroinflammation that alters neuronal functions and behavior (33). Systemic and neuroinflammation have also been implicated in structural changes in white and gray matter (35).

Current research on the neurobiological mechanisms underlying these breast cancer behavioral comorbidities has limitations as many rodent models are lacking critical components of the typical breast cancer paradigm: syngeneic, orthotopic, estrogen receptor positive (ER+) tumors (often no tumors), post-menopausal reproductive status (many studies in males), tumor resection surgery, repeated chemotherapy cycles, and various other consecutive treatments (e.g., aromatase inhibitors). As most breast cancer patients are post-menopausal, have ER+ tumor status, and receive anti-estrogen therapy, the inclusion of these aspects in a model of breast cancer enhances validity, particularly given the known role of estrogen in mood, cognition, and brain structure (36–39). Combining imaging techniques, such as diffusion weighted imaging (DWI), with neurobiological analyses in comprehensive rodent breast cancer models will improve the current translatability of mechanistic research findings. Our goal for this project was to create a comprehensive breast cancer mouse model that incorporates multiple clinically relevant factors that could influence the brain to more accurately represent the breast cancer patient and treatment experience and to understand their combined effects using a translational neuroimaging technique. Our extensive model of a typical post-menopausal breast cancer patient includes inducing a syngeneic, orthotopic, ER+ mammary tumor with subsequent surgical removal by radical mastectomy, then a repeated chemotherapy regimen, followed by long-term aromatase inhibitor treatment in an ovariectomized (modeling post-menopause) female mouse.

MATERIALS AND METHODS

Animals

Nulliparous, female, 8- to 9-week old Balb/c mice (Charles River, Wilmington, MA, USA) were housed 5/cage and acclimated to the temperature-controlled (22 ± 1°C) vivarium under a 14:10 light:dark cycle (lights off at 14:00 h). Rodent chow (Harlan 7912) and water were available *ad libitum* throughout the study. Cotton nestlets and plastic huts were provided for nesting and

enrichment, and mice were acclimated to handling twice/week. All experiments were approved by the Ohio State University Institutional Animal Care and Use Committee and carried out in accordance with the National Institutes of Health Guide for the Care and Use of Laboratory Animals (NRC, 2011). All efforts were made to minimize animal suffering and to reduce the number of mice used.

Experimental Design

All mice were ovariectomized (OVX) under isoflurane vapors, and following 1 week of recovery, mammary tumors were induced. Tumors were allowed to grow (approximately 3 weeks) and then were surgically resected. Mice were then separated into one of four groups: (1) vehicle + control, (2) vehicle + aromatase inhibitor, (3) chemotherapy + control, (4) chemotherapy + aromatase inhibitor. After 1 dose of chemotherapy, 1 cohort of treatment-balanced mice underwent diffusion weighted imaging (DWI). After 6 rounds of chemotherapy, behavioral tests, DWI, and gene expression analyses were conducted in a second cohort. A third cohort had 40 days of aromatase inhibitor treatment, then cognitive behavioral tests and DWI were conducted (**Figure 1**).

Cells

The murine, mammary, non-metastatic 67NR cancer cell line was used in this study. Importantly, this cell line is ER+ consistent with the majority (~80%) of breast tumors in women (40). The cells were grown in DMEM with 10% FBS, 2 mM $_{L}$-glutamine, 1 mM non-essential amino acids, and 5mL Penn-Strep antibiotic at 37°C with 5% CO_2 as previously described (41–43). Cells were harvested and suspended 1:1 in matrigel (47743-706, VWR, Radnor, PA, USA) immediately prior to use.

Tumor Survival Mouse Model

Our tumor "survivor" model of breast cancer was induced 1 week after surgical ovariectomy in all mice using methods previously reported (43, 44). Briefly, tumors were surgically induced in all mice under isoflurane vapor anesthetization by injecting 1 x 10^6 67NR mammary tumor cells in matrigel, described above, into the 4th mammary fat pad. This procedure results in an *in situ* primary mammary carcinoma (45) that does not metastasize (46), which eliminates the need for immunocompromised mice. Body mass and tumor dimensions were measured twice/week. Mice that failed to develop a tumor were removed from the study. When the tumors reached 15 x 10 mm in size (approximately 3 weeks), a modified radical mastectomy procedure was used to completely remove the tumor. Mice were anesthetized and tumors were surgically removed along with mammary tissue, fat, and inguinal lymph nodes where necessary. Tumors weighed 0.96 ± 0.32 at resection, on average, and there were no statistically significant differences between groups ($p > 0.05$). Buprenorphine (0.05 mg/kg; s.c.) was administered immediately after surgery, and every 6-12 h over 3 days as needed. Complete tumor resection was verified at necropsy and mice with recurrent tumors were excluded from analyses. A pilot study (n=5-6/group) was conducted to confirm the menopausal-like state caused by OVX. OVX significantly reduced circulating estrogen levels ($p > 0.05$) and halted estrous cycling ($p > 0.01$) approximately 3 weeks after ovariectomy (**Supplementary Figure 1**).

Drug Treatments

The common breast cancer chemotherapeutic drug, paclitaxel (T7191, Sigma-Aldrich, St. Louis, MO, USA), was administered in a series of six intraperitoneal injections (30 mg/kg body mass) or vehicle every other day as previously described (47–50) unless

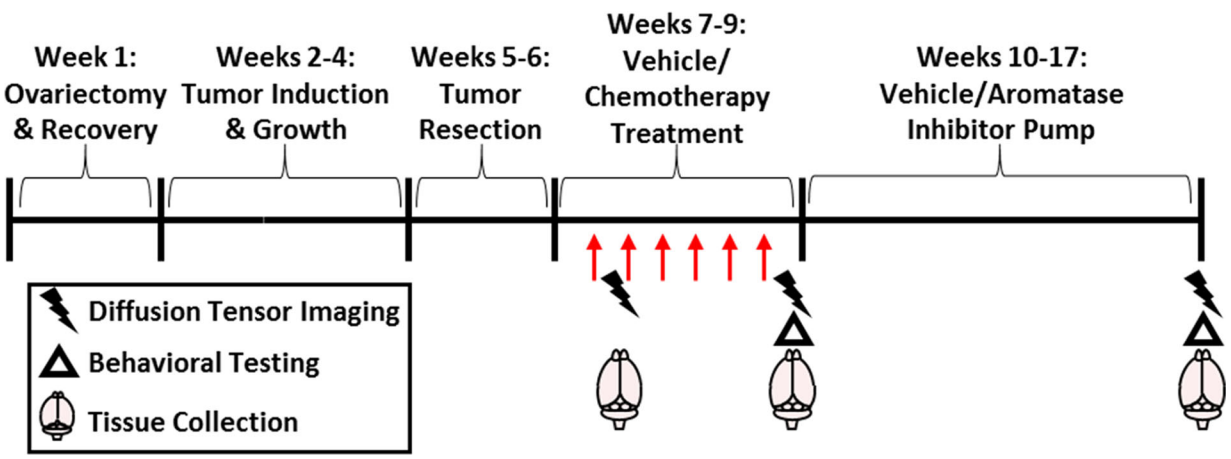

FIGURE 1 | Experimental Overview. Mice were ovariectomized followed by 1 week of recovery and then surgical mammary tumor induction. After 1.5 cm diameter tumor growth, the tumor was resected. Paclitaxel chemotherapy or vehicle (30 mg/kg; i.p.; 5-7 doses) with/without subsequent letrazole (10 µg/day over 57 days) or control treatment was administered. Brain imaging and tissue collection occurred after the first dose of chemotherapy, after the final dose, or after letrozole treatment. Behavioral testing was recorded after chemotherapy or letrozole treatments.

otherwise noted. The regimen was modeled after the 4-8 doses of paclitaxel separated by 1-3 weeks for breast cancer patients. Every other day dosing for this regimen was determined using mouse lifespan calculations (10 human years ~ 2 mouse months) (48). One week after the last chemotherapy injection, mini-osmotic pumps (7223, model 2006; Alzet, Cupertino, CA, USA) containing either the aromatase inhibiting (reduces estrogen) drug, letrozole (Sigma-Aldrich), or control were surgically implanted subcutaneously. After 40 days of treatment, Alzet pumps were replaced with fresh letrozole containing pumps. Letrozole (L6545, Sigma-Aldrich, St. Louis, MO, USA) was dissolved in 10% dimethyl sulfoxide (DMSO) in PBS. Each mouse received 10 μg letrozole/day (51) over 57 days. Aromatase inhibitors are used frequently in the treatment of breast cancer and letrozole is the most studied aromatase inhibitor in mice (52). The dosage was chosen based on its effectiveness in reducing mammary tumor growth in mice, the goal of aromatase inhibitor therapy in humans, and previous studies (51, 53, 54). The duration of treatment is a scaled down version of clinical treatment based on mouse lifespan calculations (10 human years ~ 2 mouse months).

Diffusion Weighted Imaging

One day after 1 round of chemotherapy, 1-2 days after 6 rounds of chemotherapy, or after 57 days of letrozole treatment (see **Figure 1**), mouse brains were imaged *in vivo*. Diffusion weighted imaging (DWI) was conducted at The Ohio State University small animal imaging core (Columbus, OH, USA) using a 9.7 T BioSpec 94/30 horizontal bore magnet (Bruker, Billerica, MA, USA) with a mouse brain phased array coil and ParaVision™ 5.1 software. Mice were anesthetized with isoflurane. Images were acquired with a spin-echo echo-planar-imaging (EPI) pulse sequence with the following acquisition protocol: TR/TE = 400/17.8 ms, 8 EPI segments, and 20 non-collinear gradient directions with a single *b*-value shell at 900 s/mm^2, and one image with a *b*-value of 0 s/mm^2 (b0). Geometrical parameters were six slices, each 0.313 mm thick (brain volume) with an in-lane resolution of 0.15x0.15 mm^2 (matrix size 112 x 100; FOV 30 mm^2). Each acquisition took approximately 44 min, and the entire MRI protocol lasted about 1 h 13 min. The body temperature and respiration rates of mice were monitored using the Monitoring and Gating SAII system (Small Animal Instruments, Inc. Stony Brook, NY, USA) throughout imaging.

DWI images were analyzed to produce maps of fractional anisotropy (FA), apparent diffusion coefficient (ADC), linear diffusivity (L1), and radial anisotropy (RA) with procedures previously described (55, 56) using MATLAB and MedINRIA (1.9.0[1]) software. Each image was screened for movement artifacts, and acquisition points with motion artifacts were eliminated from further analysis. All images were aligned and registered to a 3D Mouse Brain Atlas© with 134 segmented and annotated brain regions (Ekam Solutions; Boston, MA) for voxel- and region based statistical comparisons (55) using MIVA software (http://ccni.wpi.edu). For each mouse, the b0 image was registered with the b0 template using a six-parameter rigid-body transformation. The co-registration parameters were then applied to the DWI-indexed maps for the different indices of anisotropy. Normalization was performed on the maps because they provided the most detailed visualization of brain structures, and these normalizations were applied to all DWI indexed maps and smoothed with a 0.3-mm Gaussian kernel. The "nearest neighbor" option was used following registration and normalization to ensure FA and RD values were not significantly affected by the pre-processing steps.

All image transformations and statistical analyses were carried out using EVA (Ekam Visualization and analysis, Ekam Solutions LLC, Boston, MA) and in-house MATLAB® based software. For each mouse, the B0 image was co-registered with the MRI brain atlas using a 9 degree affine transformation [T]. A completely segmented map-file for each subject was generated using [T^{-1}] matrix. While generating map file nearest-neighbor interpolation was used to avoid mixing of segmented ROI's. The statistical parameters (mean, median, std dev etc.) for each ROIs and for each indices were computed based on this map file and information was exported to comma separated value (CSV) file. For each subject, each ROI and each diffusion indices mean, std deviation, mode, minimum and maximum values were reported. Statistical differences in measures of DWI between experimental groups were determined using a nonparametric Mann-Whitney U Test (alpha set at 5%). The formula below was used to account for false discovery from multiple comparisons.

$$P_{(i)} \leq \frac{i}{V} \frac{q}{c(V)}$$

P(i) is the p value based on the t test analysis. Each of 134 ROIs (i) within the brain containing (V) ROIs was ranked in order of its probability value. The false-positive filter value q was set to 0.2 and the predetermined c(V) set at unity.

Behavioral Testing

Total locomotion in a novel environment was assessed using the open field test. Mice were placed into the corner of a 40.6 x 40.6 cm photobeam arena (San Diego Instruments, San Diego, CA, USA) that was lightly covered with corncob bedding. Mice were allowed to freely explore for 15 min. The apparatus was cleaned with 70% ethanol between each mouse. Locomotor measures were analyzed using PAS Data Reporter (San Diego Instruments) and reported as beam breaks.

Working memory and speed in a novel environment were tested during the spontaneous alternation test. Each mouse was placed into the center of a Y-maze consisting of 3 equal-length gray acrylic arms (40 L x 8 W x 15 H cm) at angles of 120° and allowed to explore the entire maze for 3 min. Each test was recorded using an overhead camera and tracked using ANY-Maze video tracking software (Stoelting Co., Sand Diego, CA USA). A successful alternation was defined as successive entries into each of the 3 arms in any order. The percent spontaneous alternation was calculated as the number of successful alternations divided by the total number of possible alternations and multiplied by 100. Locomotor speed (m/s) was tracked using the ANY-Maze software.

Tissue Collection

Tissues were collected two days after one dose of chemotherapy, one day after the final dose of chemotherapy, or after 7 weeks of letrozole treatment. Mice were rapidly decapitated, blood was collected using heparinized tubes, and specific brain regions (hippocampus and frontal cortex) were immediately dissected out and frozen on dry ice. Spleens and tumors were also collected and weighed.

Plasma Cytokine Concentrations

As DWI changes were only significant directly after the final dose of chemotherapy, we focused inflammation analyses on this timepoint rather than after 1 dose of chemotherapy or after aromatase inhibitor treatment. At this timepoint, plasma cytokines were measured using a custom 7-plex Meso-Scale Discovery (MSD) immunoassay plate (U-PLEX Biomarker Group 1 (ms) assay, SECTOR, MSD Cat. No. K15069L-2) according to the manufacturer's instructions. This assay measured protein levels of interferon gamma (*IFNγ*), interleukin 1 beta (*IL-1β*), interleukin 2 (*IL-2*), interleukin 6 (*IL-6*), interleukin 10 (*IL-10*), chemokine (C-X-C motif) ligand 1 (*CXCL1*), and tumor necrosis factor alpha (*TNFα*). Intraplate variability for all analytes was <5%.

Gene Array

Total RNA was extracted from the brain hippocampus and frontal cortex of vehicle- or paclitaxel-treated mice using Qiagen RNeasy Mini Kits (CA, USA). RNA concentrations and quality were determined (NanoDrop, DE, USA), then RNA from both regions were combined equally. Five hundred ng of isolated RNA was reverse transcribed using the RT^2 First Strand Kit (Qiagen, Cat. No. 330231, Frederick, MD, USA). Expression of eighty-four genes associated with mouse innate and adaptive immune responses was analyzed simultaneously using the RT^2 Profiler PCR array (Qiagen, Cat. No. PAMM-032ZE). RT^2 SYBR Green qPCR master mix (Qiagen, Cat. No. 330522) was used following the manufacturer's instructions. Gene expression was normalized using the geometric mean of a panel of housekeeping genes including Beta actin (*Actb*), Beta-2 microglobulin (*B2m*), glyceraldehyde 3-phosphate dehydrogenase (*Gapdh*), Beta-glucoronidase (*Gusb*), and Heat shock protein HSP 90-beta (*Hsp90ab1*). Relative gene expression of individual samples was calculated by the comparative C_T method ($2^{-\Delta\Delta CT}$) and results are shown as fold change from the average vehicle expression value. As the sample size in this gene array was low, we conducted validation RT-qPCR of *Icam* in the hippocampus and frontal cortex, separately. We found a significant increase in *Icam* expression in the frontal cortex ($p < 0.05$) but not the hippocampus ($p > 0.1$) (**Supplementary Figure 2**), suggesting that the frontal cortex was driving the increase with chemotherapy in the gene array.

Immunohistochemistry

One to 2 days following the final dose of paclitaxel chemotherapy, mice were anesthetized and perfused using 4% paraformaldehyde. Briefly, brains were placed in 4% paraformaldehyde overnight and then into a 30% sucrose solution for 3-4 days. Brains were frozen, cut at 10μm on a cryostat, and mounted. Sections were immunolabeled for Iba1 or GFAP as previously described (Invitrogen) (57). Next, three images from hypothalamus (paraventricular nucleus and lateral hypothalamic nucleus) and hippocampus (CA3 region) were collected for each brain, and the immunoreactive area of GFAP and Iba1 of each section was quantified using image analysis (Image J). Area data was divided by scan area and the data from the 3 sections for each brain were averaged and group means compared (**Supplementary Figure 3**). Further immunohistochemistry was conducted to investigate white matter specifically. We stained for myelin (eriochrome cyanine) and oligodendrocytes (glutathione s-transferase pi – GSTpi). We could not interpret the results due to the neurostructural abnormalities (e.g., lack of corpus callosum) endemic to the Balb/c mouse strain (58–60). These developmental abnormalities were observed in mice regardless of treatment group. Thus, we could not proceed with statistical analyses or subsequent conclusions based on these immunohistochemical data.

Statistical Analyses

Statistical analyses of behavioral, gene expression, imaging, and cytokine data were performed using unpaired, parametric, two-tailed t-tests (post-chemotherapy) or one-way ANOVA (post-AI) followed by Tukey's correction HSD or multiple Student's *t*-tests controlling for multiple comparisons based on a *priori* hypotheses (Statview version 5.0.1 software, Scientific Computing, Cary, NC, USA). Nonparametric Mann-Whitney U tests were used when the assumptions of normality and equal variances were not met. Data were considered statistically significant when $p \leq 0.05$ and are presented as mean ± standard error of the mean (SEM).

RESULTS

Chemotherapy Reduced Locomotor Activity

One day after the final dose of paclitaxel, mice treated with paclitaxel had reduced locomotor activity compared with vehicle-treated mice in the open field test (**Figure 2A**, $t_{16} = 2.62$, $p = 0.02$). Similarly, speed in the spontaneous alternations test approached significantly different between mice treated with 6 doses of paclitaxel or vehicle (**Figure 2B**, $t_{11} = 1.98$, $p = 0.07$). Following subsequent chronic letrozole treatment, speed recovered (**Figure 2C**, $F_{1,18} = 0.04$, $p = 0.85$), but letrozole moderately increased speed in the spontaneous alternations test (**Figure 2C**, $F_{1,18} = 4.00$, $p = 0.06$). No differences in percent spontaneous alternations (working spatial memory) were observed at either time point ($p > 0.05$; **Supplementary Figure 4**).

Chemotherapy Induced Widespread Changes in DWI Anisotropy

Few changes in fractional anisotropy (FA), apparent diffusion coefficient (ADC), radial anisotropy (RA), or linear diffusivity (L1) occurred 1 day after 1 dose of chemotherapy (**Supplementary Tables 1–4**) or following repeated chemotherapy plus chronic aromatase inhibitor treatment (**Supplementary Tables 9–12**). In contrast, 1 day after the final dose of the paclitaxel regimen, chemotherapy increased FA and decreased ADC throughout many

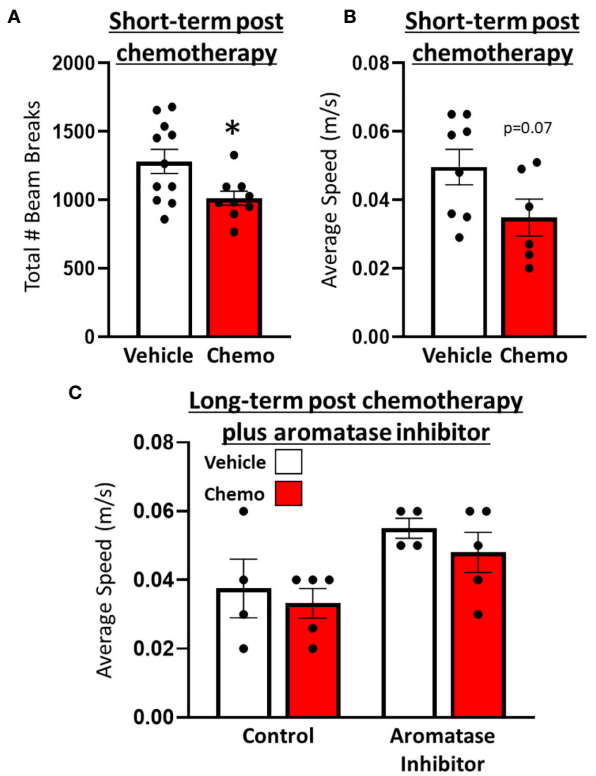

FIGURE 2 | Paclitaxel chemotherapy induced a transient decrease in locomotor activity following the final dose in survivor mice. **(A)** Locomotion in an open field test 1 day following the final dose of paclitaxel (n=9) or vehicle (n=11). **(B)** Average speed (m/s) in a spontaneous alternations test following the final dose of paclitaxel (n=6) or vehicle (n=8). **(C)** Average speed (m/s) in a spontaneous alternations test following aromatase inhibitor treatment (n=4/group). Unpaired parametric two-tailed t tests were used for the short-term time point, and a one-way ANOVA was used for the long-term time point. Nonparametric Mann-Whitney U tests were used when the assumptions of normality and equal variances were not met. *p<0.05.

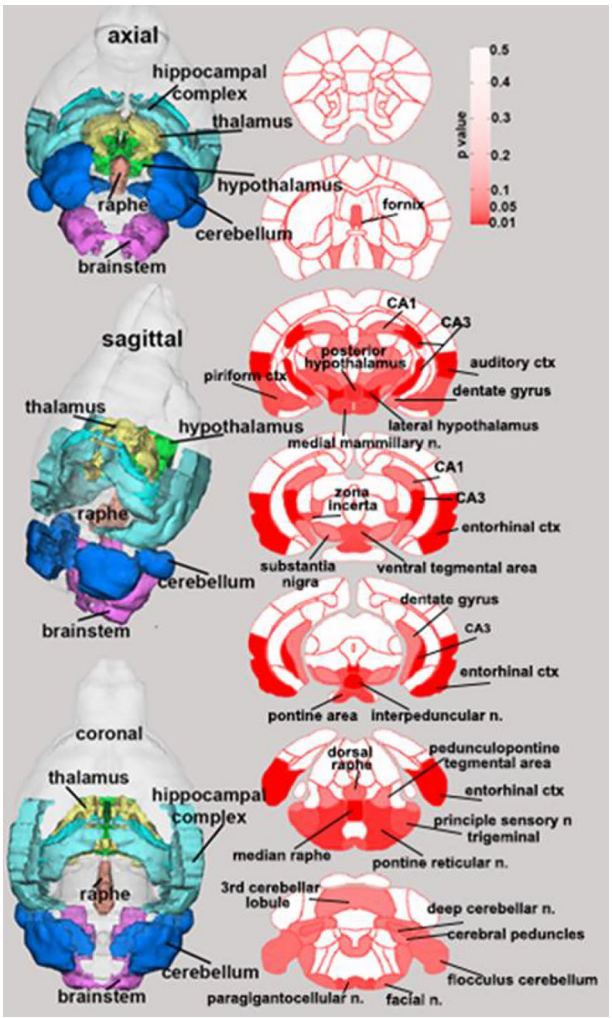

FIGURE 3 | Paclitaxel chemotherapy consistently increased fractional anisotropy following the final dose in survivor mice. Axial, sagittal, and coronal views of fractional anisotropy probability maps calculated from diffusion weighted imaging are shown. Paclitaxel n=8, vehicle n=8. Unpaired parametric two-tailed t tests were used for statistical analyses. Nonparametric Mann-Whitney U tests were used when the assumptions of normality and equal variances were not met.

areas of the brain, including the hippocampus, midbrain, medulla, pons, hypothalamus, thalamus, amygdala, and cerebellum (**Figure 3** and **Supplementary Tables 5–8**). FA data are represented by probability heat maps that illustrate the statistical differences between mice treated with 6 doses of paclitaxel compared to mice treated with vehicle (**Figure 3**). Mice exposed to 6 doses of chemotherapy had increased FA in numerous brain regions that regulate various behaviors, including the CA3 region of the hippocampus and throughout the hypothalamus (summarized in **Table 1**, full analyses in **Supplementary Table 5**). Conversely, ADC was largely decreased throughout the brain in mice treated with chemotherapy (summarized in **Table 2**, full analyses in **Supplementary Table 6**).

Chemotherapy Induced Peripheral Inflammation

Spleens and plasma were collected from mice 1 day after the 6th injection of chemotherapy. Chemotherapy treatment induced splenomegaly (**Figure 4A**, $t_7 = 5.81$, $p = 0.0007$), increased circulating inflammatory proteins including TNFα (**Figure 4B**, $\chi^2 = 8.22$, $p = 0.004$), IFNγ (**Figure 4C**, $t_6 = 2.34$, $p = 0.06$), IL-6 (**Figure 4D**, $\chi^2 = 6.91$, $p = 0.009$), IL-2 (**Figure 4E**, $\chi^2 = 9.41$, $p = 0.002$), IL-1β (**Figure 4F**, $\chi^2 = 3.77$, $p = 0.05$), CXCL1 (**Figure 4G**, $t_9 = 2.89$, $p = 0.02$), and increased the anti-inflammatory protein IL-10 (**Figure 4H**, $\chi^2 = 5.44$, p = 0.02).

Chemotherapy Altered Hippocampal and Frontal Cortex Inflammatory Gene Expression

Based on the widespread changes in anisotropy suggesting neuroinflammation (55) in regions that regulate locomotion following 6 doses of chemotherapy, a quantitative PCR array

TABLE 1 | Brain regions where paclitaxel significantly increased fractional anisotropy.

Brain Area	p-value	Brain Area	p-value	Brain Area	p-value	Brain Area	p-value
interpeduncular area	0.001	medial mammillary area	0.01	basal amygdaloid area	0.02	cerebellar nuclear area	0.04
median raphe area	0.001	pyramidal tracts	0.02	zona incerta	0.02	flocculus cerebellum	0.04
CA3	0.002	principal sensory nucleus trigeminal	0.02	reticular thalamic area	0.02	anterior hypothalamic area	0.04
lateral caudal hypothalamic area	0.004	lateral rostral hypothalamic area	0.02	ventral medial hypothalamic area	0.03	medial amygdaloid area	0.05
entorhinal cortex	0.004	ventral tegmental area	0.02	fornix	0.03	dentate gyrus	0.05
posterior hypothalamic area	0.005	olivary complex	0.02	dorsal raphe	0.03	anterior pretectal thalamic area	0.05
pontine reticular nucleus oral	0.007	medial lemniscus	0.02	crus of ansiform lobule	0.03	cuneate area	0.05
lateral lemniscus	0.01	ambiguus area	0.02	paramedian lobule	0.03	cerebral peduncle	0.05
anterior thalamic area	0.01	lateral paragigantocellular area	0.02	decussation superior cerebellar peduncle	0.04	spinal trigeminal nuclear area	0.05
pontine area	0.01	caudal piriform cortex	0.02	facial nucleus	0.04		

(For all regions Vehicle < Paclitaxel). Unpaired parametric two-tailed t tests were used for statistical analyses. Nonparametric Mann-Whitney U tests were used when the assumptions of normality and equal variances were not met.

for innate and adaptive immune response genes was conducted in combined hippocampus/frontal cortex tissues (**Figure 5**). Four genes were significantly changed after 6 doses of chemotherapy ($p < 0.05$) such that *Cd80* and *Icam1* expression was significantly increased with chemotherapy whereas *Stat1* and *Cd38* expression was significantly decreased with chemotherapy. An additional seven genes approached significant changes with chemotherapy treatment ($p < 0.1$) such that *Cd68*, *Il5*, and *Casp1* expression was increased with chemotherapy and *Nod2, Cxcl10, TLR2*, and *Cd86* expression was decreased. Further, chemotherapy did not alter percent Iba-1 and GFAP area, measured *via* immunohistochemistry, in the hippocampus and hypothalamus ($p > 0.1$; **Supplementary Figure 3**).

DISCUSSION

As breast cancer patients have a combination of clinical factors affecting their health, treatment, and recovery, comprehensive rodent models with greater translational value are needed to accurately identify biological targets for intervention. The present mouse model, to our knowledge, is the first to depict a typical breast cancer patient using an ovariectomy (post-menopausal woman), an orthotopic, syngeneic, ER+ mammary tumor, tumor resection, chemotherapy, and then aromatase inhibitor treatment. This inclusive model is particularly useful for studying synergistic or additive effects of these independent factors. Indeed, breast cancer patients do not face singular biological insults, they face multiple complex factors, often simultaneously. Additional factors typical of the cancer experience, including stressors, advanced age, and infections, could also be added to this model depending on the specific scientific questions being investigated. This model was created to be dynamic and expandable with the capability to investigate a multitude of hypotheses in various fields of study (e.g., aging, radiation, stressors, surgical complications).

In this study, we assessed the extent to which a cumulative breast cancer model recapitulates the fatigue observed in many breast cancer patients. Fatigue in humans has multiple components, including reduced locomotor activity, motivation,

TABLE 2 | Brain regions where paclitaxel significantly decreased apparent diffusion coefficient.

Brain Area	p-value	Brain Area	p-value	Brain Area	p-value	Brain Area	p-value
posterior hypothalamic area	0.002	pontine reticular nucleus oral	0.02	pedunculopontine tegmental area	0.02	entorhinal cortex	0.04
central amygdaloid area	0.002	pontine reticular nucleus caudal	0.02	mesencephalic reticular formation	0.03	infralimbic cortex	0.04
medial lemniscus	0.003	ventral tegmental area	0.02	parabrachial area	0.03	globus pallidus	0.04
median raphe area	0.009	extended amygdala	0.02	lateral septal area	0.03	medial septal area	0.04
medial mammillary area	0.01	reticulotegmental nucleus	0.02	crus of ansiform lobule	0.03	lateral amygdaloid area	0.05
anterior pretectal thalamic area	0.01	lateral posterior thalamic area	0.02	insular caudal ctx	0.03	parafascicular thalamic area	0.05
dorsal raphe	0.02	periaqueductal gray	0.02	dentate gyrus	0.03	caudate putamen	0.05
fornix	0.02	dorsal medial hypothalamic area	0.02	lemniscal area	0.03		

(For all regions Vehicle > Paclitaxel). Unpaired parametric two-tailed t tests were used for statistical analyses. Nonparametric Mann-Whitney U tests were used when the assumptions of normality and equal variances were not met.

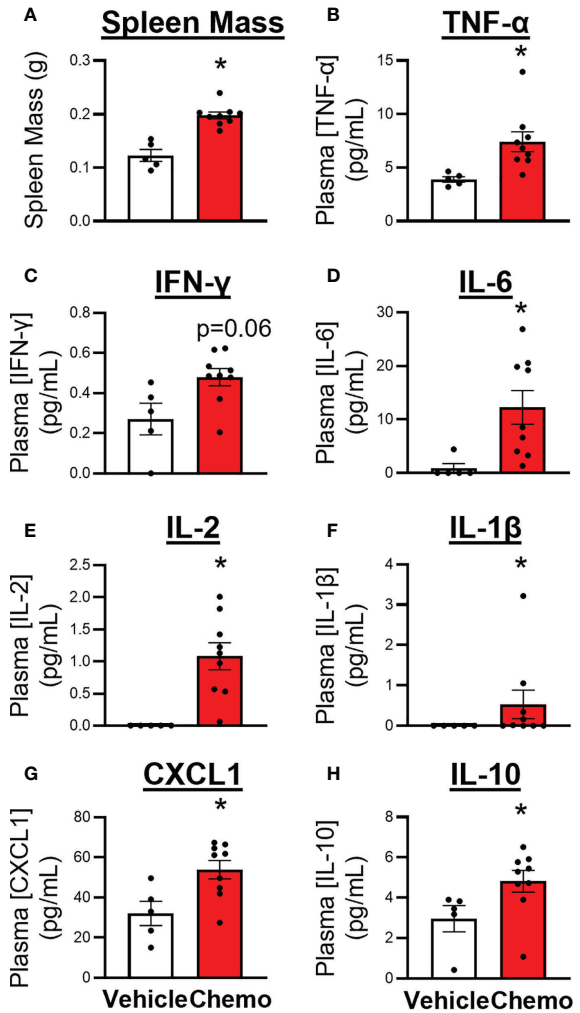

FIGURE 4 | Paclitaxel chemotherapy increased circulating inflammatory markers following the final dose in survivor mice. **(A)** Spleen mass, plasma levels of pro- and anti- inflammatory cytokines, **(B)** TNFα, **(C)** IFNγ, **(D)** IL-6, **(E)** IL-2, **(F)** IL–1β, **(G)** CXCL1, and **(H)** IL-10. Paclitaxel n=9, vehicle n=5. Unpaired parametric two-tailed t tests were used for statistical analyses. Nonparametric Mann-Whitney U tests were used when the assumptions of normality and equal variances were not met. *p<0.05.

and cognition. Chemotherapy did not significantly affect cognition-based behavior in a spontaneous alternations test (percent spontaneous alternations – **Supplementary Figure 1**) but did significantly reduce locomotor activity after the final dose of chemotherapy (**Figure 1**). Locomotor activity assessment in cancer patients often uses wrist actigraphy and smartwatches to track movement, which is similar to our measurement of movement in the open field test (61–63). The timing of the observed locomotor activity reduction, which occurred shortly after chemotherapy, was consistent with other human and rodent studies (7, 49, 64, 65). Specifically, paclitaxel (used in this model), induces fatigue in humans and reduces locomotor activity in rodents (49, 65, 66). Of note, our previous work using ovary-intact, tumor-free mice indicates that paclitaxel induces central but not muscle-related reduced locomotor activity (49). We have also previously demonstrated that tumor resection reduces locomotor activity on its own (43), indicating that in the present study chemotherapy may exacerbate tumor resection-induced reduced locomotor activity. Additional behavioral testing is warranted to dissect the potential cognitive, memory, and motivational components of fatigue in the present comprehensive model.

As behavioral comorbidities, including fatigue, have been previously associated with white matter structural abnormalities in women (18), we used diffusion weighted imaging to evaluate brain structure changes after various aspects of the treatment regimen. To our knowledge, this is the first study of MRI in mice treated with chemotherapy. Minimal changes after 1 dose of paclitaxel were observed. Whereas, after the final dose of paclitaxel, imaging analysis indicated a transient global chemotherapy-induced increase in fractional anisotropy (FA) and decrease in apparent diffusion coefficient (ADC) in the brain. When mice were allowed to recover from chemotherapy and receive an aromatase inhibitor, these FA and ADC alterations resolved. Specifically, FA and ADC alterations were absent after 1 dose, although previous work indicates that reduced locomotor activity is already detectable at this time (49), suggesting that FA and ADC may not directly relate to reduced locomotor activity. While DWI was used to specifically assess white matter changes within the brain, broad and diffuse FA and ADC changes were observed after the 6th dose of paclitaxel, likely indicating widespread inflammation throughout white and gray matter of the brain. Indeed, these measures of anisotropy are reported to reflect alterations in gray matter microarchitecture associated with neuroinflammation following brain injury (55). In support of this interpretation, we have previously observed transient neuroinflammation in otherwise naïve mice treated with chemotherapy (47, 48). Immunohistochemistry was conducted to further investigate specific white matter changes. As Balb/c mice have neurostructural abnormalities (e.g., lack of corpus callosum) (58–60) the results of myelin and oligodendrocyte staining were not interpretable. These developmental abnormalities were observed in mice regardless of treatment group. Thus, we could not proceed with statistical analyses or subsequent conclusions based on these immunohistochemical data. Many brain regions affected by chemotherapy are part of the ascending reticular activating system which is involved in consciousness. Future studies will focus on resting-state functional connectivity analysis of functional MRI (fMRI) to better understand how chemotherapy globally affects communication between brain areas.

Inflammatory pathways are involved in a host of behavioral and cognitive disorders, including fatigue and depression in humans and rodents (67). Consistent with these studies, the current study has recapitulated the peripheral inflammation coincident with reduced locomotor activity as well as demonstrated that chemotherapy also drives widespread changes in brain anisotropy in this more comprehensive breast cancer model. In

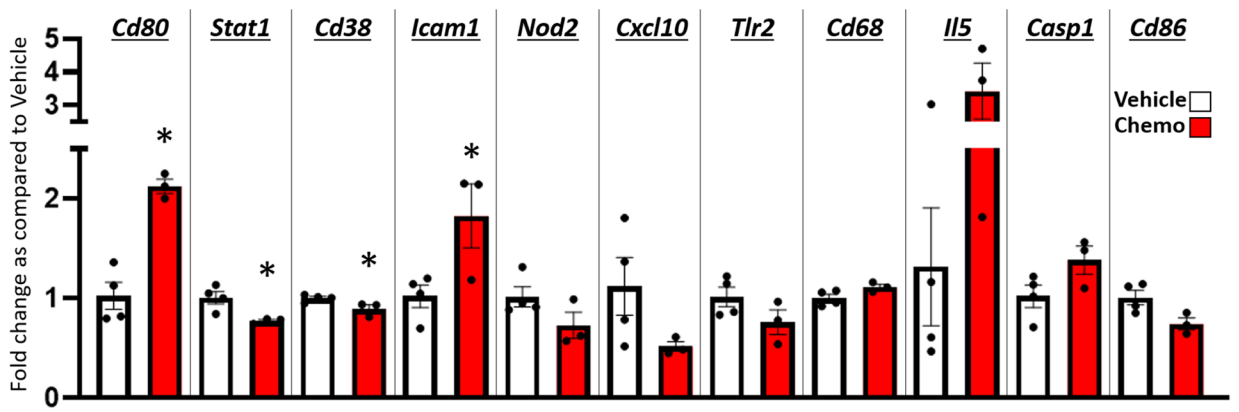

FIGURE 5 | Paclitaxel chemotherapy dynamically alters gene expression in the hippocampus and hypothalamus combined. Relative gene expression shown as fold change as compared to vehicle average of multiple inflammation related genes. Paclitaxel n=3, vehicle n=4. Unpaired parametric two-tailed t tests were used for statistical analyses. Nonparametric Mann-Whitney U tests were used when the assumptions of normality and equal variances were not met. *p<0.05.

addition, our pooled hippocampal and frontal cortex samples showed a modest number of genes that contribute to the migration, function, and/or recognition of antigen by immune cells were altered directly after chemotherapy treatment. Inflammatory differences between vehicle- and chemotherapy-treated mice using this comprehensive model may be less dramatic than in simpler models that only administer chemotherapy as the vehicle controls in this study received multiple inflammatory insults (OVX surgery, tumor induction, tumor resection) (68, 69). The immunohistochemical analysis of Iba-1 and GFAP labeling, markers of microglia and astrocytes, respectively, remained comparable between groups 1-2 days after the final dose of chemotherapy. We have previously shown transient neuroinflammation with this chemotherapy regimen in ovary-intact, tumor free mice (47–49, 64). This neuroinflammation is present at 6 hours after the final dose but not 72 hours. Given the cross-sectional nature of this study and the dynamic activation of glial cells, it is possible that we missed the glial morphological activation state as measured by Iba-1 and GFAP staining. This investigation of neuroinflammation is not comprehensive and future studies will investigate neuroinflammation overtime by measurement of a more comprehensive spread of inflammatory markers, including CD68 and IL-1 protein.

Coincident with inflammation and reduced locomotor activity, the present DWI data indicate some areas of high structural alterations, including the hippocampal CA3 region, the auditory and entorhinal cortices of the temporal lobe, the interpeduncular nucleus of the midbrain tegmentum, the median raphe and pontine reticular nucleus of the pons, and the posterior hypothalamus. In addition to locomotor activity, these brain regions regulate other behaviors that can be impaired in cancer patients during and after treatment (e.g., cognition, mood).

This study has some limitations. First, the transcriptional and immunohistochemistry analyses sample sizes were relatively low. Larger sample sizes were used for behavior, DWI, and circulating inflammatory marker analyses. Further studies are needed to delineate the underlying mechanisms of global anisotropy changes seen with chemotherapy in the DWI data. Also, neuroinflammation was examined cross-sectionally and at a transcriptional, not protein, level. Further tests are needed to expand upon the potential cognitive, motivational, and locomotive behavioral consequences in this model. Notably, breast cancer patients often receive a combination of chemotherapeutics as well as radiation, which is not accounted for in this study and warrants future investigations. Future studies could expand this model to incorporate multiple chemotherapeutics and radiation. Finally, this study uses young (~4.5 – 6.5 months at the time of behavioral and biological analyses) ovariectomized mice, whereas a natural menopause would add even greater clinical translatability (70, 71).

Taken together, this study establishes a useful and comprehensive rodent model of breast cancer that combines menopausal status, tumor growth, surgery, chemotherapy, and aromatase inhibitors in sequence and results in inflammation, neuroimaging alterations, and reduced locomotor activity consistent with many breast cancer patients. This model will continue to be advantageous for investigating how multiple complex biological aspects of the breast cancer experience interact to cause the cognitive and behavioral comorbidities that reduce quality of life for breast cancer patients and their loved ones. Furthermore, the neurobiological mechanisms and associated brain imaging that are established using this rodent model could be used to infer the appropriate intervention targets based on comparable imaging in patients.

DATA AVAILABILITY STATEMENT

The original contributions presented in the study are included in the article/**Supplementary Material**. Further inquiries can be directed to the corresponding author.

ETHICS STATEMENT

All experiments were approved by the Ohio State University Institutional Animal Care and Use Committee and carried out in accordance with the National Institutes of Health Guide for the Care and Use of Laboratory Animals (NRC, 2011). All efforts were made to minimize animal suffering and to reduce the number of mice used.

AUTHOR CONTRIBUTIONS

LP designed experiments. KR, LP, and LO analyzed and interpreted data. LO, KR, and LP wrote manuscript. PK and CF analyzed and interpreted diffusion weighted imaging data. DM provided data for immunohistochemistry. All authors reviewed the final manuscript. All authors contributed to the article and approved the submitted version.

FUNDING

This work was supported by The Ohio State University Medical Center, a CCTS core grant UL1TR001070, and NIH R01CA21690 (LP).

ACKNOWLEDGMENTS

The authors thank Lindsay Strehle, Browning Haynes, Shireen Desai, Austin Hillvert, Savannah Bever, Dr. Anna Bratasz, Jasskiran Kaur, and Ping Wei for technical assistance. We also thank Dr. Dondrae Coble and Jen Staten for animal husbandry.

SUPPLEMENTARY MATERIAL

The Supplementary Material for this article can be found online at: https://www.frontiersin.org/articles/10.3389/fonc.2022.798704/full#supplementary-material

Supplementary Figure 1 | Ovariectomy induces menopausal-like state in Balb/c mice. **(A)** Ovariectomy halts estrous cycling. **(B)** Ovariectomy significantly decreases circulating estrogen concentrations.

Supplementary Figure 2 | Paclitaxel chemotherapy increased *Icam* expression in the frontal cortex but not the hippocampus following the final dose in survivor mice. **(A)** Hippocampus, **(B)** Frontal cortex. Unpaired parametric two-tailed t tests were used for statistical analyses. Nonparametric Mann-Whitney U tests were used when the assumptions of normality and equal variances were not met. *p<0.05

Supplementary Figure 3 | Paclitaxel chemotherapy does not alter Iba-1 or GFAP percent area in the hippocampus or hypothalamus following the final dose in survivor mice. **(A)** Hippocampal Iba-1% area, **(B)** Hypothalamic Iba-1% area, **(C)** Hippocampal GFAP % area, **(D)** Hypothalamic GFAP % area. Paclitaxel n=4, vehicle n=3. Unpaired parametric two-tailed t tests were used for statistical analyses. Nonparametric Mann-Whitney U tests were used when the assumptions of normality and equal variances were not met. *p<0.05.

Supplementary Figure 4 | Neither paclitaxel chemotherapy nor aromatase inhibitor treatment affected percent spontaneous alternations. **(A)** Percent spontaneous alternations in the spontaneous alternations test following the final dose of paclitaxel (n=8/group). **(B)** Percent spontaneous alternations in the spontaneous alternations test following aromatase inhibitor treatment. Aromatase inhibitor n=5, control n=4. Unpaired parametric two-tailed t tests were used for statistical analyses. Nonparametric Mann-Whitney U tests were used when the assumptions of normality and equal variances were not met. *p<0.05.

REFERENCES

1. The American Cancer Society. *How Common Is Breast Cancer*? Atlanta: American Cancer Society (2021).
2. Karthikeyan G, Jumnani D, Prabhu R, Manoor U, Supe S. Prevalence of Fatigue Among Cancer Patients Receiving Various Anticancer Therapies and Its Impact on Quality of Life: A Cross-Sectional Study. *Indian J Palliative Care* (2012) 18(3):165. doi: 10.4103/0973-1075.105686
3. Norden DM, Bicer S, Clark Y, Jing R, Henry CJ, Wold LE, et al. Tumor Growth Increases Neuroinflammation, Fatigue and Depressive-Like Behavior Prior to Alterations in Muscle Function. *Brain Behav Immun* (2015) 43:76–85. doi: 10.1016/j.bbi.2014.07.013
4. Patel SK, Wong AL, Wong FL, Breen EC, Hurria A, Smith M, et al. Inflammatory Biomarkers, Comorbidity, and Neurocognition in Women With Newly Diagnosed Breast Cancer. *JNCI: J Natl Cancer Inst* (2015) 107 (8):1–7. doi: 10.1093/jnci/djv131
5. Bower JE, Ganz PA. *Symptoms: Fatigue and Cognitive Dysfunction*. Heidelberg: Springer, Cham (2015). doi: 10.1007/978-3-319-16366-6_5
6. Simó M, Rifà-Ros X, Rodriguez-Fornells A, Bruna J. Chemobrain: A Systematic Review of Structural and Functional Neuroimaging Studies. *Neurosci Biobehav Rev* (2013) 37(8):1311–21. doi: 10.1016/j.neubiorev.2013.04.015
7. Berger A, Kumar G, LeVan T, Meza J. Symptom Clusters And Quality Of Life Over 1 Year In Breast Cancer Patients Receiving Adjuvant Chemotherapy. *Asia-Pac J Oncol Nurs* (2020) 7(2):134–40. doi: 10.4103/apjon.apjon_57_19
8. Cella D, Davis K, Breitbart W, Curt G. Cancer-Related Fatigue: Prevalence of Proposed Diagnostic Criteria in a United States Sample of Cancer Survivors. *J Clin Oncol* (2001) 19(14):3385–91. doi: 10.1200/JCO.2001.19.14.3385
9. Prue G, Rankin J, Allen J, Gracey J, Cramp F. Cancer-Related Fatigue: A Critical Appraisal. *Eur J Cancer* (2006) 42(7):846–63. doi: 10.1016/j.ejca.2005.11.026
10. Boykoff N, Moieni M, Subramanian SK. Confronting Chemobrain: An in-Depth Look at Survivors' Reports of Impact on Work, Social Networks, and Health Care Response. *J Cancer Survivorship* (2009) 3(4):223–32. doi: 10.1007/s11764-009-0098-x
11. Jagsi R, Hawley ST, Abrahamse P, Li Y, Janz NK, Griggs JJ, et al. Impact of Adjuvant Chemotherapy on Long-Term Employment of Survivors of Early-Stage Breast Cancer. *Cancer* (2014) 120(12):1854–62. doi: 10.1002/cncr.28607
12. Pisu M, Azuero A, McNees P, Burkhardt J, Benz R, Meneses K. The Out of Pocket Cost of Breast Cancer Survivors: A Review. *J Cancer Survivorship* (2010) 4(3):202–9. doi: 10.1007/s11764-010-0125-y
13. Innominato PF, Giacchetti S, Moreau T, Bjarnason GA, Smaaland R, Focan C, et al. Fatigue and Weight Loss Predict Survival on Circadian Chemotherapy for Metastatic Colorectal Cancer. *Cancer* (2013) 119(14):2564–73. doi: 10.1002/cncr.28072
14. Satin JR, Linden W, Phillips MJ. Depression as a Predictor of Disease Progression and Mortality in Cancer Patients. *Cancer* (2009) 115(22):5349–61. doi: 10.1002/cncr.24561
15. Stilley C, DiMartini A, de Vera M, Flynn W, King J, Sereika S, et al. Individual and Environmental Correlates and Predictors of Early Adherence and Outcomes After Liver Transplantation. *Prog Transplant* (2010) 20(1):58–66. doi: 10.7182/prtr.20.1.c903845857104k83
16. Kesler SR, Wefel JS, Hosseini SMH, Cheung M, Watson CL, Hoeft F. Default Mode Network Connectivity Distinguishes Chemotherapy-Treated Breast Cancer Survivors From Controls. *Proc Natl Acad Sci* (2013) 110(28):11600–5. doi: 10.1073/pnas.1214551110

17. McDonald BC, Saykin AJ. Alterations in Brain Structure Related to Breast Cancer and Its Treatment: Chemotherapy and Other Considerations. *Brain Imaging Behav* (2013) 7(4):374–87. doi: 10.1007/s11682-013-9256-x
18. Hampson JP, Zick SM, Khabir T, Wright BD, Harris RE. Altered Resting Brain Connectivity in Persistent Cancer Related Fatigue. *NeuroImage: Clin* (2015) 8:305–13. doi: 10.1016/j.nicl.2015.04.022
19. Deprez S, Amant F, Smeets A, Peeters R, Leemans A, van Hecke W, et al. Longitudinal Assessment of Chemotherapy-Induced Structural Changes in Cerebral White Matter and Its Correlation With Impaired Cognitive Functioning. *J Clin Oncol* (2012) 30(3):274–81. doi: 10.1200/JCO.2011.36.8571
20. Bergouignan L, Lefranc JP, Chupin M, Morel N, Spano JP, Fossati P. Breast Cancer Affects Both the Hippocampus Volume and the Episodic Autobiographical Memory Retrieval. *PLoS One* (2011) 6(10):e25349. doi: 10.1371/journal.pone.0025349
21. Koppelmans V, de Ruiter MB, van der Lijn F, Boogerd W, Seynaeve C, van der Lugt A, et al. Global and Focal Brain Volume in Long-Term Breast Cancer Survivors Exposed to Adjuvant Chemotherapy. *Breast Cancer Res Treat* (2012) 132(3):1099–106. doi: 10.1007/s10549-011-1888-1
22. Brown M, Stemmer S, Simon J, Stears J, Jones R, Cagnoni P, et al. White Matter Disease Induced by High-Dose Chemotherapy: Longitudinal Study With MR Imaging and Proton Spectroscopy. *AJNR Am J Neuroradiol* (1998) 19(2):217–21.
23. Dolev T, Ben-David M, Shahadi I, Freed Y, Zubedat S, Aga-Mizrachi S, et al. Attention Dysregulation in Breast Cancer Patients Following a Complementary Alternative Treatment Routine: A Double-Blind Randomized Trial. *Integr Cancer Ther* (2021) 20:153473542110194. doi: 10.1177/15347354211019470
24. Menning S, de Ruiter MB, Veltman DJ, Boogerd W, Oldenburg HSA, Reneman L, et al. Changes in Brain White Matter Integrity After Systemic Treatment for Breast Cancer: A Prospective Longitudinal Study. *Brain Imaging Behav* (2018) 12(2):324–34. doi: 10.1007/s11682-017-9695-x
25. Genova HM, Rajagopalan V, DeLuca J, Das A, Binder A, Arjunan A, et al. Examination of Cognitive Fatigue in Multiple Sclerosis Using Functional Magnetic Resonance Imaging and Diffusion Tensor Imaging. *PLoS One* (2013) 8(11):e78811. doi: 10.1371/journal.pone.0078811
26. Nystedt J, Nilsson M, Jönsen A, Nilsson P, Bengtsson A, Lilja Å., et al. Altered White Matter Microstructure in Lupus Patients: A Diffusion Tensor Imaging Study. *Arthritis Res Ther* (2018) 20(1):1–11. doi: 10.1186/s13075-018-1516-0
27. Diakos CI, Charles KA, McMillan DC, Clarke SJ. Cancer-Related Inflammation and Treatment Effectiveness. *Lancet Oncol* (2014) 15(11): e493–e503. doi: 10.1016/S1470-2045(14)70263-3
28. Saxena S, Maze M. Impact on the Brain of the Inflammatory Response to Surgery. *La Presse Médicale* (2018) 47(4):e73–81. doi: 10.1016/j.lpm.2018.03.011
29. Bower JE. Behavioral Symptoms in Patients With Breast Cancer and Survivors. *J Clin Oncol* (2008) 26(5):768–77. doi: 10.1200/JCO.2007.14.3248
30. Kurz K, Fiegl M, Holzner B, Giesinger J, Pircher M, Weiss G, et al. Fatigue in Patients With Lung Cancer Is Related With Accelerated Tryptophan Breakdown. *PLoS One* (2012) 7(5):e36056. doi: 10.1371/journal.pone.0036956
31. Lanser L, Kink P, Egger EM, Willenbacher W, Fuchs D, Weiss G, et al. Inflammation-Induced Tryptophan Breakdown Is Related With Anemia, Fatigue, and Depression in Cancer. *Front Immunol* (2020) 11:249. doi: 10.3389/fimmu.2020.00249
32. Pertl MM, Hevey D, Boyle NT, Hughes MM, Collier S, O'Dwyer A-M, et al. C-Reactive Protein Predicts Fatigue Independently of Depression in Breast Cancer Patients Prior to Chemotherapy. *Brain Behav Immun* (2013) 34:108–19. doi: 10.1016/j.bbi.2013.07.177
33. Santos JC, Pyter LM. Neuroimmunology of Behavioral Comorbidities Associated With Cancer and Cancer Treatments. *Front Immunol* (2018) 9:1195. doi: 10.3389/fimmu.2018.01195
34. Schrepf A, Lutgendorf SK, Pyter LM. Pre-Treatment Effects of Peripheral Tumors on Brain and Behavior: Neuroinflammatory Mechanisms in Humans and Rodents. *Brain Behav Immun* (2015) 49:1–17. doi: 10.1016/j.bbi.2015.04.010
35. Marsland AL, Gianaros PJ, Kuan DC-H, Sheu LK, Krajina K, Manuck SB. Brain Morphology Links Systemic Inflammation to Cognitive Function in Midlife Adults. *Brain Behav Immun* (2015) 48:195–204. doi: 10.1016/j.bbi.2015.03.015
36. Albert KM, Newhouse PA. Estrogen, Stress, and Depression: Cognitive and Biological Interactions. *Annu Rev Clin Psychol* (2019) 15(1):399–423. doi: 10.1146/annurev-clinpsy-050718-095557
37. Baker JM, Al-Nakkash L, Herbst-Kralovetz MM. Estrogen–Gut Microbiome Axis: Physiological and Clinical Implications. *Maturitas* (2017) 103:45–53. doi: 10.1016/j.maturitas.2017.06.025
38. Korol DL. Role of Estrogen in Balancing Contributions From Multiple Memory Systems. *Neurobiol Learn Memory* (2004) 82(3):309–23. doi: 10.1016/j.nlm.2004.07.006
39. McEwen BS, Alves SE. Estrogen Actions in the Central Nervous System[1]. *Endocr Rev* (1999) 20(3):279–307. doi: 10.1210/edrv.20.3.0365
40. Lumachi F. Current Medical Treatment of Estrogen Receptor-Positive Breast Cancer. *World J Biol Chem* (2015) 6(3):231. doi: 10.4331/wjbc.v6.i3.231
41. Aslakson CJ, Miller FR. Selective Events in the Metastatic Process Defined by Analysis of the Sequential Dissemination of Subpopulations of a Mouse Mammary Tumor. *Cancer Res* (1992) 52(6):1399–405.
42. Dexter DL, Kowalski HM, Blazar BA, Fligiel Z, Vogel R, Gloria H, et al. Heterogeneity of Tumor Cells From a Single Mouse Mammary Tumor. *Cancer Res* (1978) 38(10):3174–81.
43. Santos JC, Bever SR, Sullivan KA, Pyter LM. Cancer and Cancer Survival Modulates Brain and Behavior in a Time-of-Day-Dependent Manner in Mice. *Sci Rep* (2019) 9(1):1–14. doi: 10.1038/s41598-019-42880-w
44. Pyter LM, Suarez-Kelly LP, Carson WE, Kaur J, Bellisario J, Bever SR. Novel Rodent Model of Breast Cancer Survival With Persistent Anxiety-Like Behavior and Inflammation. *Behav Brain Res* (2017) 330:108–17. doi: 10.1016/j.bbr.2017.05.011
45. Miller FR, Medina D, Heppner GH. Preferential Growth of Mammary Tumors in Intact Mammary Fatpads. *Cancer Res* (1981) 41(10):3863–7.
46. Miller FR, Miller BE, Heppner GH. Characterization of Metastatic Heterogeneity Among Subpopulations of a Single Mouse Mammary Tumor: Heterogeneity in Phenotypic Stability. *Invasion Metastasis* (1983) 3 (1):22–31.
47. Grant C, Loman BR, Bailey MT, Pyter LM. Manipulations of the Gut Microbiome Alter Chemotherapy-Induced Inflammation and Behavioral Side Effects in Female Mice. *Brain Behav Immun* (2021) 95:401–12. doi: 10.1016/J.BBI.2021.04.014
48. Loman BR, Jordan KR, Haynes B, Bailey MT, Pyter LM. Chemotherapy-Induced Neuroinflammation Is Associated With Disrupted Colonic and Bacterial Homeostasis in Female Mice. *Sci Rep* (2019) 9(1):1–16. doi: 10.1038/s41598-019-52893-0
49. Sullivan KA, Grant C, Jordan KR, Vickery SS, Pyter LM. Voluntary Wheel Running Ameliorates Select Paclitaxel Chemotherapy-Induced Sickness Behaviors and Associated Melanocortin Signaling. *Behav Brain Res* (2021) 399:1–12. doi: 10.1016/j.bbr.2020.113041
50. Sullivan KA, Grant C, Jordan KR, Obrietan K, Pyter LM. Paclitaxel Chemotherapy Disrupts Behavioral and Molecular Circadian Clocks in Mice. *Brain Behav Immun* (2022) 99:106–18. doi: 10.1016/J.BBI.2021.09.011
51. Jelovac D, Macedo L, Goloubeva OG, Handratta V, Brodie AMH. Additive Antitumor Effect of Aromatase Inhibitor Letrozole and Antiestrogen Fulvestrant in a Postmenopausal Breast Cancer Model. *Cancer Res* (2005) 65(12):5439–44. doi: 10.1158/0008-5472.CAN-04-2782
52. Waks AG, Winer EP. Breast Cancer Treatment. *JAMA* (2019) 321(3):288. doi: 10.1001/jama.2018.19323
53. Jayaraman S, Hou X, Kuffel MJ, Suman VJ, Hoskin TL, Reinicke KE, et al. Antitumor Activity of Z-Endoxifen in Aromatase Inhibitor-Sensitive and Aromatase Inhibitor-Resistant Estrogen Receptor-Positive Breast Cancer. *Breast Cancer Res* (2020) 22(1):51. doi: 10.1186/s13058-020-01286-7
54. Yue W, Savinov A, Brodie A. Effect of Aromatase Inhibitors on Growth of Mammary Tumors in a Nude Mouse Model. *Cancer Res* (1995) 55(14):3073–7.
55. Kulkarni P, Kenkel W, Finklestein SP, Barchet TM, Ren J, Davenport M, et al. Use of Anisotropy, 3d Segmented Atlas, and Computational Analysis to Identify Gray Matter Subcortical Lesions Common to Concussive Injury From Different Sites on the Cortex. *PLoS One* (2015) 10(5):1–19. doi: 10.1371/journal.pone.0125748
56. Sinkevicius KW, Morrison TR, Kulkarni P, Cagliostro MKC, Iriah S, Malmberg S, et al. *RNaseT2* Knockout Rats Exhibit Hippocampal Neuropathology and Deficits in Memory. *Dis Models Mech* (2018) 11(6). doi: 10.1242/dmm.032631

57. Pukos N, McTigue DM. Delayed Short-Term Tamoxifen Treatment Does Not Promote Remyelination or Neuron Sparing After Spinal Cord Injury. *PLoS One* (2020) 15(7):1–24. doi: 10.1371/journal.pone.0235232
58. Morin CL, Dolina S, Robertson RT, Ribak CE. An Inbred Epilepsy-Prone Substrain of BALB/c Mice Shows Absence of the Corpus Callosum, an Abnormal Projection to the Basal Forebrain, and Bilateral Projections to the Thalamus. *Cereb Cortex* (1994) 4(2):119–28. doi: 10.1093/cercor/4.2.119
59. Wahlsten D. Deficiency of the Corpus Callosum: Incomplete Penetrance and Substrain Differentiation in BALB/c Mice. *J Neurogenetics* (1989) 5(1):61–76. doi: 10.3109/01677068909167265
60. Wahlsten D. Genetic and Developmental Defects of the Mouse Corpus Callosum. *Experientia* (1989) 45(9):828–38. doi: 10.1007/BF01954057
61. Beauchamp UL, Pappot H, Holländer-Mieritz C. The Use of Wearables in Clinical Trials During Cancer Treatment: Systematic Review. *JMIR MHealth UHealth* (2020) 8(11):e22006. doi: 10.2196/22006
62. Innominato PF, Lim AS, Palesh O, Clemons M, Trudeau M, Eisen A, et al. The Effect of Melatonin on Sleep and Quality of Life in Patients With Advanced Breast Cancer. *Supportive Care Cancer* (2016) 24(3):1097–105. doi: 10.1007/s00520-015-2883-6
63. Komarzynski S, Huang Q, Levi FA, Palesh OG, Ulusakarya A, Bouchahda M, et al. The Day After: Correlates of Patient-Reported Outcomes With Actigraphy-Assessed Sleep in Cancer Patients at Home (inCASA Project). *Sleep* (2019) 42(10):1–12. doi: 10.1093/sleep/zsz146
64. Jordan KR, Loman BR, Bailey MT, Pyter LM. Gut Microbiota-Immune-Brain Interactions in Chemotherapy-Associated Behavioral Comorbidities. *Cancer* (2018) 124(20):3990–9. doi: 10.1002/cncr.31584
65. Pusztai L, Mendoza TR, Reuben JM, Martinez MM, Willey JS, Lara J, et al. Changes in Plasma Levels of Inflammatory Cytokines in Response to Paclitaxel Chemotherapy. *Cytokine* (2004) 25(3):94–102. doi: 10.1016/j.cyto.2003.10.004
66. Lu H, Zha S, Zhang W, Wang Q, Jiang D, Xu X, et al. A Systematic Review and Meta-Analysis of Nab-Paclitaxel Mono-Chemotherapy for Metastatic Breast Cancer. *BMC Cancer* (2021) 21(1):1–15. doi: 10.1186/s12885-021-08441-z
67. Lee C-H, Giuliani F. The Role of Inflammation in Depression and Fatigue. *Front Immunol* (2019) 10:1696. doi: 10.3389/fimmu.2019.01696
68. Au A, Feher A, McPhee L, Jessa A, Oh S, Einstein G. Estrogens, Inflammation and Cognition. *Front Neuroendocrinol* (2016) 40. doi: 10.1016/j.yfrne.2016.01.002
69. Yang T, Velagapudi R, Terrando N. Neuroinflammation After Surgery: From Mechanisms to Therapeutic Targets. *Nat Immunol* (2020) 21(11):1319–26. doi: 10.1038/s41590-020-00812-1
70. Baeza I, de Castro NM, Giménez-Llort L, de la Fuente M. Ovariectomy, a Model of Menopause in Rodents, Causes a Premature Aging of the Nervous and Immune Systems. *J Neuroimmunol* (2010) 219(1–2):90–9. doi: 10.1016/j.jneuroim.2009.12.008
71. Souza VR, Mendes E, Casaro M, Antiorio ATFB, Oliveira FA, Ferreira CM. *Description of Ovariectomy Protocol in Mice*. New York: Humana Press (2019). pp. 303–9. doi: 10.1007/978-1-4939-8994-2_29

Conflict of Interest: The authors declare that the research was conducted in the absence of any commercial or financial relationships that could be construed as a potential conflict of interest.

frontiers | Frontiers in Oncology

ORIGINAL RESEARCH
published: 01 April 2022
doi: 10.3389/fonc.2022.843436

Radiomics Based on Digital Mammography Helps to Identify Mammographic Masses Suspicious for Cancer

*Guangsong Wang[1], Dafa Shi[1], Qiu Guo[1], Haoran Zhang[1], Siyuan Wang[1] and Ke Ren[1,2]**

[1] Xiang'an Hospital, Xiamen University, Xiamen, China, [2] Xiamen Key Laboratory of Endocrine-Related Cancer Precision Medicine, Xiamen, China

Objectives: This study aims to build radiomics model of Breast Imaging Reporting and Data System (BI-RADS) category 4 and 5 mammographic masses extracted from digital mammography (DM) for mammographic masses characterization by using a sensitivity threshold similar to that of biopsy.

Materials and Methods: This retrospective study included 288 female patients (age, 52.41 ± 10.31) who had BI-RADS category 4 or 5 mammographic masses with an indication for biopsy. The patients were divided into two temporal set (training set, 82 malignancies and 110 benign lesions; independent test set, 48 malignancies and 48 benign lesions). A total of 188 radiomics features were extracted from mammographic masses on the combination of craniocaudal (CC) position images and mediolateral oblique (MLO) position images. For the training set, Pearson's correlation and the least absolute shrinkage and selection operator (LASSO) were used to select non-redundant radiomics features and useful radiomics features, respectively, and support vector machine (SVM) was applied to construct a radiomics model. The receiver operating characteristic curve (ROC) analysis was used to evaluate the classification performance of the radiomics model and to determine a threshold value with a sensitivity higher than 98% to predict the mammographic masses malignancy. For independent test set, identical threshold value was used to validate the classification performance of the radiomics model. The stability of the radiomics model was evaluated by using a fivefold cross-validation method, and two breast radiologists assessed the diagnostic agreement of the radiomics model.

Results: In the training set, the radiomics model obtained an area under the receiver operating characteristic curve (AUC) of 0.934 [95% confidence intervals (95% CI), 0.898–0.971], a sensitivity of 98.8% (81/82), a threshold of 0.22, and a specificity of 60% (66/110). In the test set, the radiomics model obtained an AUC of 0.901 (95% CI, 0.835–0.961), a sensitivity of 95.8% (46/48), and a specificity of 66.7% (32/48). The radiomics model had relatively stable sensitivities in fivefold cross-validation (training set, 97.39% ± 3.9%; test set, 98.7% ± 4%).

OPEN ACCESS

Edited by:
Samata Kakkad, Merck, United States

Reviewed by:
Ning Mao, Peking University People's Hospital, China
Stacey Winham, Mayo Clinic, United States

***Correspondence:**
Ke Ren
renke816@163.com

Specialty section:
This article was submitted to Cancer Imaging and Image-directed Interventions, a section of the journal Frontiers in Oncology

Received: *25 December 2021*
Accepted: *04 March 2022*
Published: *01 April 2022*

Citation:
Wang G, Shi D, Guo Q, Zhang H, Wang S and Ren K (2022) Radiomics Based on Digital Mammography Helps to Identify Mammographic Masses Suspicious for Cancer. Front. Oncol. 12:843436. doi: 10.3389/fonc.2022.843436

Conclusion: The radiomics method based on DM may help reduce the temporarily unnecessary invasive biopsies for benign mammographic masses over-classified in BI-RADS category 4 and 5 while providing similar diagnostic performance for malignant mammographic masses as biopsies.

Keywords: breast (diagnostic), breast cancer, Mammografy, Radiomic analysis, BI-RADS (Breast imaging reporting and data system)

INTRODUCTION

In 2020, female breast cancer (BC) became the most common type of cancer with an estimated 2.3 million new cases (11.7%), followed by lung cancer (11.4%) (1). Treatment of BC relies on conducting an accurate diagnosis, including histological, molecular, and clinical phenotypes. Non-invasive imaging techniques such as mammography, ultrasound, and magnetic resonance (MR) are available for qualitative and quantitative analysis of BC in clinical practice. The American College of Radiology Breast Imaging Reporting and Data System (BI-RADS) is a standardized assessment structure that enables radiologists to clearly and concisely communicate results of breast imaging to referring physicians (2). In the fifth edition of the BI-RADS atlas (3), category 4 and 5 breast lesions are defined as suspicious cancerous lesions, and a biopsy is recommended for further diagnosis. Recent studies have shown that a large number of benign lesions are present in category 4 and 5 breast lesions, particularly in the mammography reporting system, exposing these patients to invasive biopsies (4–6). Depending on the technique, the sensitivity values of biopsy results ranged from 87% to >97% (7–9).

Radiomics is a high-throughput image mining technique that aims to enhance the predictive power of medical images by quantifying the morphology, intensity distribution, and texture patterns of lesions. Recent investigators have examined the role of mammography, ultrasound, and MR radiomics in the prediction of molecular subtypes (10–12), lymph node metastasis (13–15), response to neoadjuvant chemotherapy (16–18), recurrence risk (19, 20), and disease-free survival (21, 22) of BC. However, with the initiative of precision medicine (23–25), the reduction in overdiagnosis and overtreatment of breast lesions through non-invasive radiomics method is also a topic worth investigating.

There are four main findings of breast lesions on diagnostic mammography images: masses, calcifications, architectural distortion, and asymmetries. One large sample study (26) showed that BC most often presented as mass at 56%, followed by calcifications at 29%, asymmetry at 12%, and architectural deformities at 4%, and another small sample study (27) suggest that approximately 50% of breast lesions presenting as a mass were ultimately confirmed benign lesions. In addition, mass may be the only finding or one of the combined findings of breast lesions in mammography (we defined these masses as mammographic masses). Although experienced radiologists have a high diagnostic accuracy in identifying benign and malignant mammographic masses, less experienced radiologists sometimes make excess errors (28) such as benign mammographic masses are over-classified as BIRADS category 4 or even 5.

A previous study has shown that combining both craniocaudal (CC) and mediolateral oblique (MLO) positions radiomics data had good classification performance between HER2-enriched BC and non-HER2-enriched BC (11). Here, we combined both CC and MLO positions radiomics data aimed to explore a model with a sensitivity more than 98% for the characterization of BI-RADS category 4 and 5 mammographic masses, thereby achieving a reduction in biopsies of benign lesions at a very low rate of missed malignant lesions.

MATERIALS AND METHODS

Patients

This retrospective study was granted approval by the local institutional board, and written informed consent was waived. A total of 288 patients' clinical and mammographic images data were included in this study from December 2018 to February 2021. The inclusion criteria were as follows: (a) patients who had suspected breast tumor accepted mammography and (b) patients with mass as defined by BI-RADS mammography lexicon (occupancy structures with protrude outward in contour on both CC and MLO position images) and classified in category 4 or 5. The exclusion criteria were as follows: (a) patients without a clear benign or malignant pathological result; (b) patients who had multifocal or bilateral mammographic masses; (c) patients accepted biopsy before mammography examination; (d) patients underwent any treatment before mammography screening, including surgery, chemotherapy or radiotherapy, and anti-HER2 therapy.

Imaging and Saving Acquisition

All patients were examined with a GE Senographe Essential (GE Medical Systems, Waukesha, WI), and all mammographic images were saved at 12-bit quantization level and 100-μm pixel size. The mammographic images were not further processed or normalized (29, 30).

Radiomics Analysis of Mammographic Masses

Both CC and MLO position images of all patients were used to conduct mammographic mass masking, and the CC radiomics features and MLO radiomics features were extracted as separate features. Two breast radiologists (radiologist 1, 4 years'

experience; radiologist 2, 10 years' experience) who were blinded to the pathological results manually masked the masses in 3Dslicer 4.10.2 (www.slicer.org) (**Figure 1**). A total of 188 radiomics features were extracted from mammographic masses by using the Pyradiomics python package, including 4 shape features, 34 density features, and 150 texture features. Shape features were used to quantify the size and regularity of the mammographic masses, including maximum two-dimensional (2D) diameter and perimeter to surface ratio, with a lower value of perimeter-to-surface ratio indicating a more regular mammographic mass. First-order features refer to radiologically relevant information about the density of mammographic masses such as mean value and kurtosis. Texture features were calculated based on gray-level co-occurrence matrix, gray-level dependence matrix, gray-level run-length matrix, gray-level size zone matrix, and neighborhood gray-tone difference matrix, which were used to quantify the randomness, correlations, variation, homogeneity, and heterogeneity of mammographic masses. The detailed formulae for the calculation of the radiomics features can be found here (31), and the data from radiologist 1 were used to build a radiomics model.

Patients Grouping and Feature Selection

The patients were divided into two temporal sets based on the order in which they accepted their mammography examinations. The training set consisted of the first two-thirds of patients, and the independent test set comprised the last one-third of patients. In order to avoid some potential bias such as model over-fitting, we applied Pearson's correlation and the least absolute shrinkage and selection operator (LASSO) regression to screen out non-redundant and useful radiomics features in the training set, respectively. For the Pearson's correlation method, each radiomics feature generated 187 correlation coefficients and 1 corresponding mean absolute correlation coefficient. If two radiomics features had a coefficient exceeding 0.8, the radiomics feature with the larger mean absolute correlation coefficient was deleted. This was implemented in R software version 4.0.1 with package "caret." For the LASSO regression (alpha=1, no elastic net), a 10-fold cross-validation method with 1 standard error of the minimum mean-square error criteria was used to select radiomics features (32), and corresponding λ values were also be calculated. In this study, the radiomics features with non-zero coefficient at the suitable value of parameter λ were determined as useful radiomics features. This was implemented in R software version 4.0.1 with "glmnet" package.

Radiomics Model Construction and Testing

The malignant mammographic masses were coded as 1, and the benign mammographic masses were coded as 0. The support vector machines (SVMs) with linear kernel (output predicted probability and other parameters are default parameters) were used to construct a radiomics model in this study because of popularity and efficiency in BC (33). This was done in R software version 4.0.1 with "e1071" package. The useful radiomics features were used to construct a radiomics model in the training set for distinguishing between benign and malignant mammographic masses. The receiver operating characteristic curve (ROC) analysis was used to evaluate the classification performance of the radiomics model, including the area under the receiver operating characteristic curve (AUC), the probability threshold value (cut-point) of higher than 98% sensitivity, and corresponding specificity (5). The independent test set was

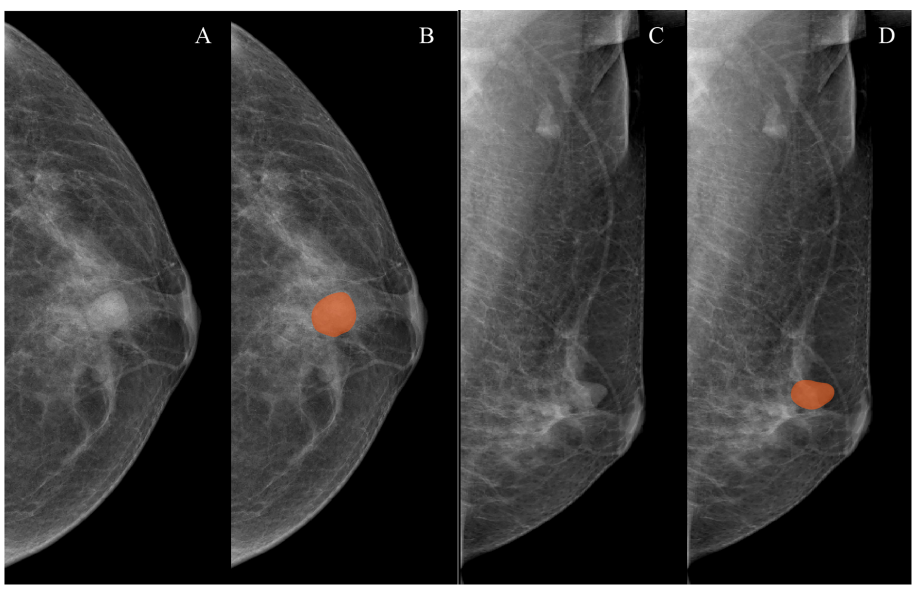

FIGURE 1 | Examples of mammographic masses masking on digital mammography images. **(A, C)** Craniocaudal (CC) position images and mediolateral oblique position (MLO) images, respectively. **(B, D)** Manually drawn areas of mammographic masses masking on CC and MLO images, respectively.

used to test the results of the training set by using the "predict" function, and the probability threshold value was also tested. The ROC analysis was implemented in R software version 4.0.1 with package "pROC." The workflow of this study is reported in **Figure 2**.

Relative Importance of Useful Radiomics Features

The magnitude of the coefficients in the LASSO algorithm were used to measure the relative weight of useful features as previously described (34, 35). Furthermore, the useful features were grouped by category, such as shape feature group, first-order feature group, and texture feature group, which were added sequentially to the final SVM model, and the AUC of each addition was calculated to assess whether all three groups of useful features contributed to the model.

Radiomics Model Stability

In this study, a fivefold cross-validation method was used to evaluate the stability of radiomics model. In order not to break the concealment of the test set data, a fivefold cross-validation method was performed separately in the training and test sets. Specifically, the training and test sets were divided into 10 subsets each by fivefold cross-validation method. The "predict" function of R was used to test the diagnostic performance of the radiomics model in these subsets, and the mean and standard deviation of AUCs, sensitivities, and specificities were calculated to measure the stability of the radiomics model. The fivefold cross-validation method was performed in R software version 4.0.1 with package "caret."

Reproducibility Assessment

The intra-class correlation coefficients (ICCs) of interobserver (radiologist 1 vs. radiologist 2) were calculated to evaluate the reproducibility of the radiomics features extraction. All data from radiologists 1 and 2 were used as separate test sets so that a kappa value for both radiologists could be calculated to assess the diagnostic reproducibility of the radiomics model.

Statistical Analysis

All statistical analyses were performed in R software version 4.0.1. All ROC analysis were based on package "pROC," and the differences of AUC were calculated on Delong's test. All confidence intervals (CI) were derived from 1,000 bootstrap replicates. All statistical tests were two-sided, and the Bonferroni's method was used to adjust for multiple comparisons.

RESULTS

Clinical Data of Patients

This study included 288 female patients (age, 52.41± 10.31) with solitary BI-RADS category 4 or 5 mammographic masses, including 130 cases of malignant mammographic masses and 158 cases of benign mammographic masses. The malignant mammographic masses include invasive ductal carcinoma (n=51), invasive lobular carcinoma (n=37), mucinous carcinoma (n=22), and ductal carcinoma *in situ* (n=20), while benign mammographic masses include fibroadenomas (n=87), adenosis (n=38), and hyperplasia (n=33).

Patients Grouping and Feature Selection

The training set included 82 malignant and 110 benign mammographic masses; the independent test set consisted of 48 malignant and 48 benign mammographic masses. Baseline characteristics of study population in training and test sets are reported in **Table 1**, including age, mass size, mass shape, mass margin, breast density, and BI-RADS category. The Pearson's correlation method screened out 32 non-redundant radiomics features (**Supplementary Figure S1**), and the LASSO method further selected 14 useful radiomics features (**Figures 3A, B**).

Radiomics Model Construction and Testing

In the training set, the radiomics model obtained an AUC of 0.934 (95% CI, 0.898–0.971), a threshold of 0.22, a sensitivity of 98.8% [81/82], and a specificity of 60% [66/110]. In the test set, the

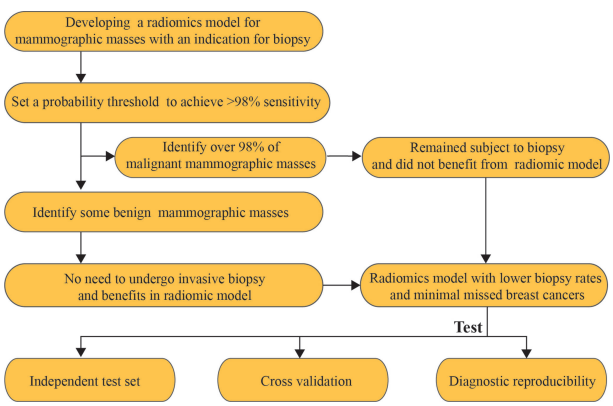

FIGURE 2 | Workflows of this study.

TABLE 1 | Baseline characteristics of study population in training and test sets.

Characters	Training set			Test set		
	Malignant(n= 82)	Benign(n= 110)	*p*-value	Malignant(n= 48)	Benign(n= 48)	*p*-value
Age (mean ± SD, years)	54.2 ± 10.94	50.38 ± 9.71	0.013	56.66 ± 10.33	49.75 ± 8.76	<0.001
Size (mean ± SD, cm)	1.5 ± 0.51	1.34 ± 0.42	0.021	1.69 ± 0.58	1.3 ± 0.42	<0.001
Shape			0.002			<0.001
Round or oval	10 (12.2%)	34 (30.9%)		5 (10.4%)	20 (41.7%)	
Irregular	72 (87.8%)	76 (69.1%)		43 (89.6%)	28 (58.3%)	
Margin			<0.001			<0.001
Circumscribed	5 (6.1%)	16 (14.5%)		3 (6.3%)	12 (25%)	
Ill-defined	26 (31.7%)	82 (74.5%)		22 (45.8%)	33 (68.8%)	
Spiculated	51 (62.2%)	12 (10.9%)		23 (47.9%)	3 (6.3%)	
Breast density			0.169			0.094
Entirely fatty	7 (8.5%)	15 (13.6%)		4 (8.3%)	7 (14.6%)	
Scattered fibroglandular	37 (45.1%)	58 (52.7%)		22 (45.8%)	29 (60.4%)	
Heterogeneously dense	38 (46.3%)	37 (33.6%)		22 (45.8%)	12 (25%)	
Extremely dense	…	…				
BI-RADS category			<0.001			0.031
4	64 (78%)	105 (95.5%)		38 (79.2%)	46 (95.8%)	
5	18 (22%)	5 (4.5%)		10 (20.8%)	2 (4.2%)	

Student's t-test for normally distributed continuous variable (age and size); Pearson's chi-square test for categorical variables (shape, margin, breast density, BI-RADS categories, and pathological results).

SD, standard deviation; BI-RADS, breast imaging reporting and data system.

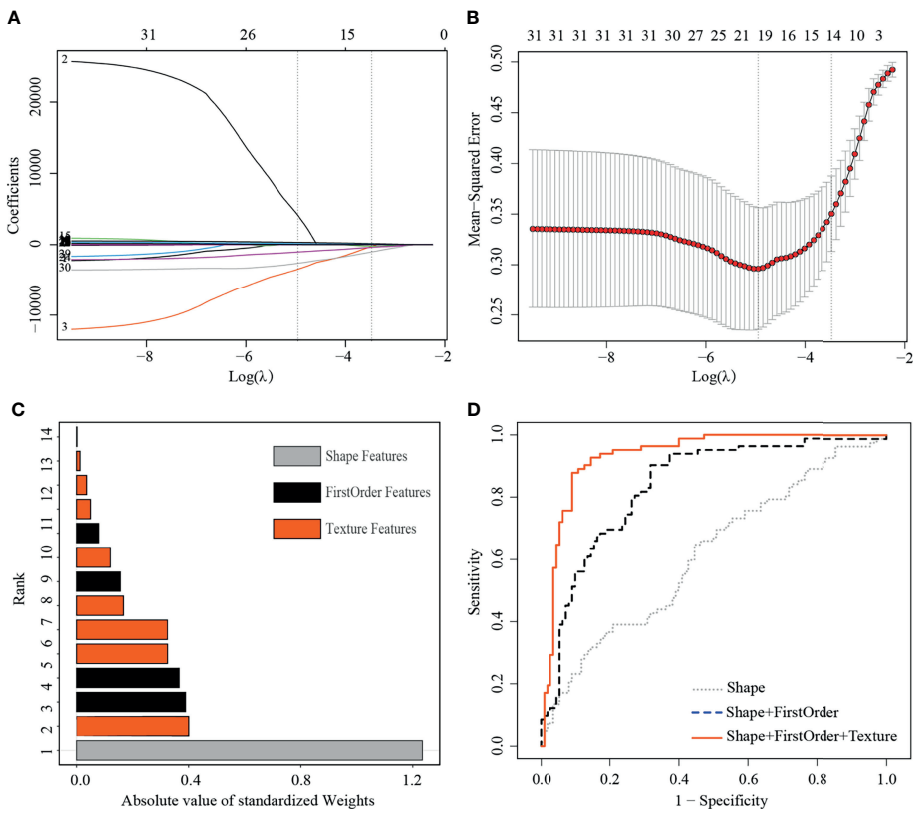

FIGURE 3 | Least absolute shrinkage and selection operator (LASSO) selection process, absolute values of weights, and receiver operating characteristic curves (ROC) of 14 useful radiomics features in training set. **(A)** LASSO coefficient profiles of the 32 non-redundant features. The y-axis represents coefficient of each feature. The optimal value of λ was 0.0345, and the optimal log(λ) was –3.37, resulting in 14 non-zero coefficients. **(B)** Mean square error path using tenfold cross-validation. **(C)** Absolute value of weights generated by the LASSO algorithms for the optimal log(λ) value. **(D)** The ROC curves for a combination of shape feature, first order features, and texture features.

radiomics model obtained an AUC of 0.901 (95% CI, 0.835–0.961), a sensitivity of 95.8% [46/48], and a specificity of 66.7% [32/48] (**Figure 4A**).

Relative Importance of Useful Radiomics Features

For the useful single radiomics feature, perimeter-to-surface ratio from shape features had the largest absolute weight value of 1.234, followed by coarseness from texture features of 0.4 and mean from first-order features of 0.389 (**Figure 3C**, details in **Table 2**). For useful single-category radiomics features, texture feature group obtained the largest absolute weight value of 1.435, followed by shape feature group of 1.234, and lastly by first-order feature group of 0.96 (**Figure 3C**, details in **Table 2**). When shape feature group, first-order feature group, and texture feature group were added sequentially to the final SVM model, ROC analysis showed a significant increase in AUC for each addition (shape feature group, AUC=0.613; shape feature group plus first-order feature group, AUC=0.835; first-order feature group plus and first-order feature group plus texture feature group, AUC=0.934; p<0.001 for each addition) (**Figure 3D**, details in **Table 3**).

Radiomics Model Stability

In the training set, the average AUC was 0.9 ± 0.038, average sensitivity was 97.39% ± 3.9%, and average specificity was 50% ± 12.5%. In the test set, the average AUC was 0.915 ± 0.062, average sensitivity was 98.7% ± 4%, and average specificity was 36.7% ± 8.6% (**Figure 4B**, details in **Table 4** and **Supplementary Figure S2**).

Reproducibility Assessment

Of the 188 extracted radiomics feature, more than 95% [180/188] radiomics features obtained good reproducibility (ICC>0.75) between radiologist 1 and radiologist 2. The radiomics model obtained good agreement between radiologist 1 and radiologist 2 (Cohen's kappa=0.748; 95% CI, 0.67–0.825; p<0.001).

TABLE 2 | Absolute value of weights of selected useful radiomics features in training set.

Feature category	Feature name	Absolute weights
Shape	MLO/Sphericity	1.234
FirstOrder	CC/Mean	0.389
	MLO/Uniformity	0.366
	CC/Skewness	0.156
	MLO/Mean	0.079
Texture	MLO/NGTDM Coarseness	0.4
	MLO/GLSZM GrayLevelNonUniformity	0.325
	CC/GLDM SmallDependenceHighGrayLevelEmphasis	0.324
	MLO/GLDM LargeDependenceLowGrayLevelEmphasis	0.167
	CC/NGTDM Coarseness	0.12
	CC/NGTDM Busyness	0.05
	MLO/GLCM InverseDifferenceNormalized	0.036
	CC/GLSZM ZoneVariance	0.012
	CC/GLCM ClusterProminence	0.001

CC, craniocaudal; MLO, mediolateral oblique; NGTDM, neighborhood gray-tone difference matrix; GLSZM, gray-level size zone matrix; GLDM, gray-level dependence matrix; GLCM, gray-level co-occurrence matrix.

DISCUSSION

In this study, we built a radiomics model with similar sensitivity to biopsy for predicting malignancy of BI-RADS category 4 and 5 mammographic masses by using the combination of CC and MLO position images from DM. In both training and test sets, the radiomics model obtained specificity by over 60% while preserving sensitivity more than 95.8%. Both AUC and sensitivity were relatively stable, while the specificity was not so stable. These experimental results suggest that the non-invasive

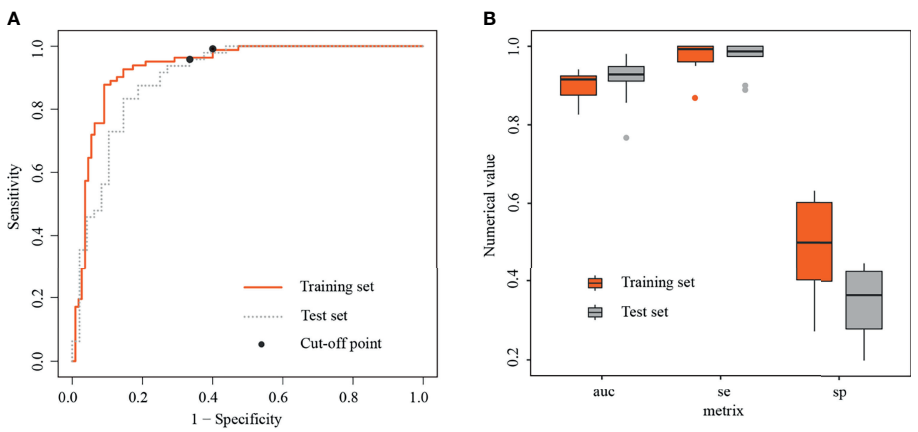

FIGURE 4 | Receiver operating characteristic curves and boxplots in training and test sets. **(A)** Receiver operating characteristic curves (ROC) in training and test sets, with black dots representing threshold=0.22. **(B)** Boxplots of area under the curves (AUCs), sensitivities, and specificities generated by fivefold cross-validation in training and test sets, respectively.

TABLE 3 | Classification performance of selected shape feature, first order features, and texture features in classifying malignancies and benign lesions in the training set.

Features	AUC*	*p*-value†
Shape	0.613 (0.528, 0.695)	…
Shape+FirstOrder	0.835 (0.774, 0.888)	…
Shape+FirstOrder+Texture	0.934 (0.898, 0.968)	…
Shape vs (Shape+FirstOrder)	…	<0.001 (0.017)
Shape vs (Shape+FirstOrder+Texture)	…	<0.001 (0.017)
(Shape+FirstOrder) vs (Shape+FirstOrder+Texture)	…	<0.001 (0.017)

**Numbers in parentheses are 95% confidence intervals.*
†Numbers in parentheses are the significance level.
AUC, area under the receiver operating characteristic curve.

TABLE 4 | Classification performance of radiomics model in fivefold cross-validation.

Data set	Fivefold CV	Pathology results			AUC	Sensitivity (%)	Specificity (%)
		Malignant	Benign	p			
Training set	–Fold 1	67	87	0.653	0.941 (0.898, 0.977)	98.5 [66/67]	50.6 [44/87]
	Fold 1	15	23		0.910 (0.806, 0.997)	100 [15/15]	39.1 [9/23]
	–Fold 2	65	88	0.901	0.927 (0.881, 0.965)	100 [65/65]	30.7 [27/88]
	Fold 2	17	22		0.912 (0.786, 1)	100 [17/17]	27.2 [6/22]
	–Fold 3	62	91	0.302	0.926 (0.878, 0.967)	95.2 [59/62]	58.2 [53/91]
	Fold 3	20	19		0.856 (0.713, 0.966)	95 [19/20]	63.2 [12/19]
	–Fold 4	67	87	0.653	0.920 (0.871, 0.962)	98.5 [66/67]	63.2 [55/87]
	Fold 4	15	23		0.826 (0.672, 0.954)	100 [15/15]	43.5 [10/23]
	–Fold 5	67	87	0.653	0.919 (0.872, 0.960)	100 [67/67]	49.4 [43/87]
	Fold 5	15	23		0.864 (0.742, 0.965)	86.7 [13/15]	60.9 [14/23]
	Mean± SD	…	…		*0.9 ± 0.038*	*97.39 ± 3.9*	*50 ± 12.5*
Test set	–Fold 1	38	39	0.798	0.919 (0.846, 0.976)	97.4 [37/38]	33.3 [13/39]
	Fold 1	10	9		0.967 (0.867, 1)	100 [10/10]	44.4 [4/9]
	–Fold 2	38	38	1	0.912 (0.837, 0.968)	100 [38/38]	23.7 [9/38]
	Fold 2	10	10		0.980 (0.920, 1)	100 [10/10]	20 [2/10]
	–Fold 3	39	38	0.798	0.947 (0.883, 0.994)	97.4 [38/39]	44.7 [17/38]
	Fold 3	9	10		0.856 (0.667, 1)	100 [9/9]	40 [4/10]
	–Fold 4	39	38	0.798	0.937 (0.879, 0.981)	100 [39/39]	26.3 [10/38]
	Fold 4	9	10		0.911 (0.688, 1)	88.9 [8/9]	40 [4/10]
	–Fold 5	38	39	0.798	0.949 (0.887, 0.993)	97.4 [37/38]	43.6 [17/39]
	Fold 5	10	9		0.767 (0.500, 1)	90 [9/10]	33.3 [3/9]
	Mean± SD	…	…		*0.915 ± 0.062*	*98.7 ± 4*	*36.7 ± 8.6*

CV, cross validation; AUC, area under the receiver operating characteristic curve; SD, standard deviation.

imaging radiomics method could achieve similar sensitivity to biopsy while avoiding some benign mammographic masses to undergo unnecessary invasive biopsy.

We are aware of several papers that use mammographic radiomics data to differentiate between benign and malignant breast lesions (30, 36–38), and we are aware that several of these papers incorporated morphological features (36, 37), and several that did not (30, 38). However, most breast lesions that present alone as calcification, architectural distortion, or asymmetries tend to lack distinct grayscale contrast boundaries, which compromises the masking of tumors. Besides, non-invasive imaging techniques with similar biopsy sensitivity are important for differentiating between benign and malignant BI-RADS category 4 and 5 breast lesions for which invasive biopsy was already indicated. To the best of our knowledge, this is the first study to use mammographic radiomics data to predict the malignancy of BI-RADS category 4 and 5 mammographic masses with a sensitivity similar to that of a biopsy, and we believe that the radiomics model is more limited but more relevant.

When using radiomics data to predict the malignancy of breast lesions, commonly used mammography images include CC position alone (37, 39), mixed CC and MLO position (30, 36), and combination of CC position and MLO position (40, 41). Gupta et al. demonstrated that the corresponding first-order and texture features of mammographic masses between CC position and MLO position were not strongly correlated (42), suggesting that the inclusion of first-order and texture features from multiple mammographic positions may impact the accuracy of diagnosis of mammographic masses. Ma et al. has shown that by combining both CC and MLO position, radiomics data had higher classification performance between HER2-enriched BC and non-HER2-enriched BC than using CC position alone and MLO position alone (11). Hence, we applied both CC and MLO position radiomics data to predict the malignancy of mammographic masses suspicious for cancer, and the results showed that this method had good classification performance.

Recent studies have shown that the use of a single random training–test set split may lead to unreliable results in small

sample radiomics machine learning studies (43). In our study, we divided the training and test sets based on the chronological order in which patients underwent mammography examinations, and we performed random fivefold cross-validation in training and test sets, respectively, to assess the stability of the radiomics model. Although the specificity gives a large error (12.5%, 8.6%), the AUC (0.038, 0.062) and sensitivity (3.9%, 4%) were relatively stable. This is consistent with previous findings that cross-validation may lead to large error bars for small sample sizes (44).

Of the 188 mammographic radiomics features, the feature selection method screened out 14 useful features in the training set (n=192, ratio 14:1). As suggested by Gillies et al., each radiomics feature requires at least 10 samples to support in a classifier (45). Previous publication has shown that maximum 2D diameter is a useful feature for predicting BC (37). In this study, we found a significant positive correlation between maximum 2D diameter and gray-level size zone matrix-based gray level non-uniformity in the CC position images (r=0.82, p<0.001) and MLO position images (r=0.924, p<0.001) of the training set (**Figure 5**). Thus, the maximum 2D diameter feature was removed when filtering features in the Pearson's correlation analysis. It is worth noting that although the size feature was not included in our radiomics model, we do not consider it unimportant in predicting malignancy of mammographic masses suspicious for cancer.

Of the 14 useful mammographic radiomics features, perimeter-to-surface ratio had the greatest weight value of 1.234, suggesting that morphological features remain important in identifying benign lesions or malignancies for mammographic masses suspicious for cancer. The mean density obtained moderate weight values of 0.389 and 0.079, which was higher in the malignant group than in the benign group, indicating that the malignant mammographic masses tend to be higher density than benign mammographic masses. In addition, the malignant group had higher value for inverse difference normalized, zone variance, gray level non-uniformity, and busyness, and lower value for uniformity, skewness, coarseness, small-dependence high gray-level emphasis, and large-dependence low-gray level emphasis, indicating more heterogeneity of malignant mammographic masses in the density and texture patterns (31) (**Figure 6**). This experimental result is consistent with the pathological fact that malignant tumors tend to be heterogeneous, while benign lesions tend to be homogeneous (46).

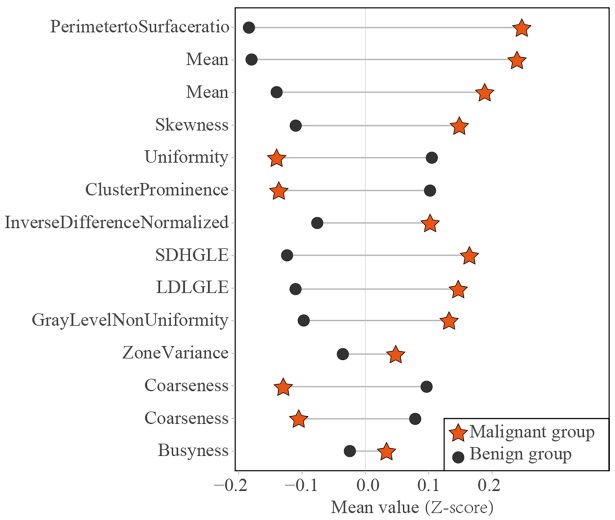

FIGURE 6 | Dumbbell diagram of the mean value of 14 useful radiomics features between the malignant and benign groups in the training set. SDHGLE, small-dependence high gray-level emphasis; LDLGLE, large-dependence low gray-level emphasis.

Admittedly, our study has several limitations. First, mammographic radiomics data for this study were collected from a single center with a limited number of participants, and further multicenter testing is needed. Second, the mammographic masses were masked by manual method; however, good inter-observer reproducibility was obtained in feature extraction and model diagnosis. Some publications indicate that semi-automatic

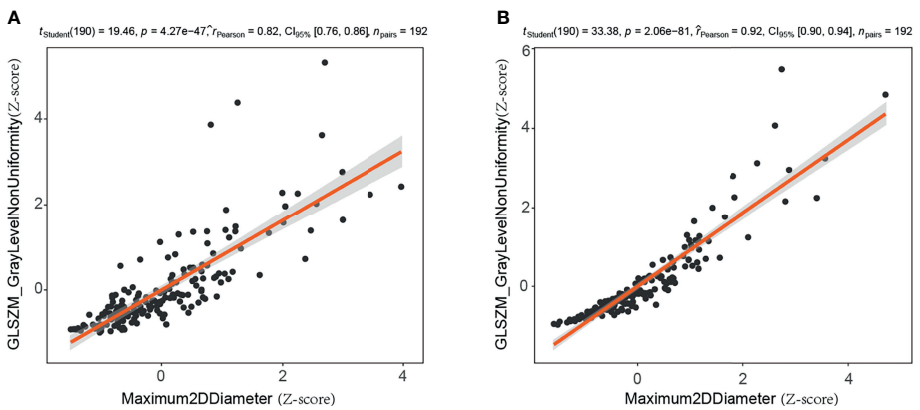

FIGURE 5 | Correlation analysis of maximum two-dimensional diameter and gray level non-uniformity (gray-level size zone matrix based) in training set. **(A)** Craniocaudal (CC) position images; **(B)** mediolateral oblique (MLO) position images. 2D, two-dimensional; GLSZM, gray-level size zone matrix.

segmentation method had higher inter-observer reproducibility (47, 48). Further work is needed to construct a semi-automatic segmentation method for mammographic masses. Finally, the radiomics model was constructed by 2D images, which may lose some important information of mammographic masses. However, some publications showed that 2D radiomics features had higher classification performance than 3D radiomics features in lung cancer (47, 48).

In conclusion, a mammographic radiomics model combining both CC and MLO position images had excellent sensitivity and moderate specificity in differentiating malignancies and benign lesions for BI-RADS category 4 and 5 mammographic masses. It may help reduce the temporarily unnecessary invasive biopsies for benign mammographic masses while providing similar diagnostic performance for malignant mammographic masses as biopsies.

DATA AVAILABILITY STATEMENT

The raw data supporting the conclusions of this article will be made available by the authors, without undue reservation.

ETHICS STATEMENT

The studies involving human participants were reviewed and approved by the Ethics Committee of Xiang'an Hospital of Xiamen University. Written informed consent for participation was not required for this study in accordance with the national legislation and the institutional requirements.

AUTHOR CONTRIBUTIONS

Study concept and design: GW and DS. Acquisition of data: HZ, QG, and SW. Analysis of data: GW, DS. Drafting of the manuscript: GW, DS, HZ, and SW. Critical revision: QG and KR. Statistical analysis: GW and DS. Study supervision: QG and KR. All authors contributed to the article and approved the submitted version.

FUNDING

This work was supported by the Scientific Research Foundation for Advanced Talents, Xiang'an Hospital of Xiamen University (no. PM201809170011).

SUPPLEMENTARY MATERIAL

The Supplementary Material for this article can be found online at: https://www.frontiersin.org/articles/10.3389/fonc.2022.843436/full#supplementary-material

REFERENCES

1. Sung H, Ferlay J, Siegel RL, Laversanne M, Soerjomataram I, Jemal A, et al. Global Cancer Statistics 2020: GLOBOCAN Estimates of Incidence and Mortality Worldwide for 36 Cancers in 185 Countries. *CA Cancer J Clin* (2021) 71:209–49. doi: 10.3322/caac.21660
2. Rao AA, Feneis J, Lalonde C. Ojeda-Fournier H. A Pictorial Review of Changes in the BI-RADS Fifth Edition. *Radiographics* (2016) 36:623–39. doi: 10.1148/rg.2016150178
3. Balleyguier C, Arfi-Rouche J, Boyer B, Gauthier E, Helin V, Loshkajian A, et al. A New Automated Method to Evaluate 2D Mammographic Breast Density According to BI-RADS® Atlas Fifth Edition Recommendations. *Eur Radiol* (2019) 29:3830–8. doi: 10.1007/s00330-019-06016-y
4. Strobel K, Schrading S, Hansen NL, Barabasch A, Kuhl CK. Assessment of BI-RADS Category 4 Lesions Detected With Screening Mammography and Screening US: Utility of MR Imaging. *Radiology* (2015) 274:343–51. doi: 10.1148/radiol.14140645
5. Bickelhaupt S, Jaeger PF, Laun FB, Lederer W, Daniel H, Kuder TA, et al. Radiomics Based on Adapted Diffusion Kurtosis Imaging Helps to Clarify Most Mammographic Findings Suspicious for Cancer. *Radiology* (2018) 287:761–70. doi: 10.1148/radiol.2017170273
6. Alì M, D'Amico NC, Interlenghi M, Maniglio M, Fazzini D, Schiaffino S, et al. A Decision Support System Based on BI-RADS and Radiomic Classifiers to Reduce False Positive Breast Calcifications at Digital Breast Tomosynthesis: A Preliminary Study. *Appl Sci* (2021) 11:2503. doi: 10.3390/app11062503
7. Ciatto S, Houssami N, Ambrogetti D, Bianchi S, Bonardi R, Brancato B, et al. Accuracy and Underestimation of Malignancy of Breast Core Needle Biopsy: The Florence Experience of Over 4000 Consecutive Biopsies. *Breast Cancer Res Treat* (2007) 101:291–7. doi: 10.1007/s10549-006-9289-6
8. Wang M, He X, Chang Y, Sun G, Thabane L. A Sensitivity and Specificity Comparison of Fine Needle Aspiration Cytology and Core Needle Biopsy in Evaluation of Suspicious Breast Lesions: A Systematic Review and Meta-Analysis. *Breast* (2017) 31:157–66. doi: 10.1016/j.breast.2016.11.009
9. Youk JH, Kim EK, Kim MJ, Lee JY, Oh KK. Missed Breast Cancers at US-Guided Core Needle Biopsy: How to Reduce Them. *Radiographics* (2007) 27:79–94. doi: 10.1148/rg.271065029
10. Leithner D, Horvat JV, Marino MA, Bernard-Davila B, Jochelson MS, Ochoa-Albiztegui RE, et al. Radiomic Signatures With Contrast-Enhanced Magnetic Resonance Imaging for the Assessment of Breast Cancer Receptor Status and Molecular Subtypes: Initial Results. *Breast Cancer Res* (2019) 21:106. doi: 10.1186/s13058-019-1187-z
11. Ma W, Zhao Y, Ji Y, Guo X, Jian X, Liu P, et al. Breast Cancer Molecular Subtype Prediction by Mammographic Radiomic Features. *Acad Radiol* (2019) 26:196–201. doi: 10.1016/j.acra.2018.01.023
12. Guo Y, Hu Y, Qiao M, Wang Y, Yu J, Li J, et al. Radiomics Analysis on Ultrasound for Prediction of Biologic Behavior in Breast Invasive Ductal Carcinoma. *Clin Breast Cancer* (2018) 18:e335–e44. doi: 10.1016/j.clbc.2017.08.002
13. Han L, Zhu Y, Liu Z, Yu T, He C, Jiang W, et al. Radiomic Nomogram for Prediction of Axillary Lymph Node Metastasis in Breast Cancer. *Eur Radiol* (2019) 29:3820–9. doi: 10.1007/s00330-018-5981-2
14. Sun Q, Lin X, Zhao Y, Li L, Yan K, Liang D, et al. Deep Learning vs. Radiomics for Predicting Axillary Lymph Node Metastasis of Breast Cancer Using Ultrasound Images: Don't Forget the Peritumoral Region. *Front Oncol* (2020) 10:53. doi: 10.3389/fonc.2020.00053
15. Yang J, Wang T, Yang L, Wang Y, Li H, Zhou X, et al. Preoperative Prediction of Axillary Lymph Node Metastasis in Breast Cancer Using Mammography-Based Radiomics Method. *Sci Rep* (2019) 9:4429. doi: 10.1038/s41598-019-40831-z
16. Wang Z, Lin F, Ma H, Shi Y, Dong J, Yang P, et al. Contrast-Enhanced Spectral Mammography-Based Radiomics Nomogram for the Prediction of Neoadjuvant Chemotherapy-Insensitive Breast Cancers. *Front Oncol* (2021) 11:605230. doi: 10.3389/fonc.2021.605230

17. Liu Z, Li Z, Qu J, Zhang R, Zhou X, Li L, et al. Radiomics of Multiparametric MRI for Pretreatment Prediction of Pathologic Complete Response to Neoadjuvant Chemotherapy in Breast Cancer: A Multicenter Study. *Clin Cancer Res* (2019) 25:3538–47. doi: 10.1158/1078-0432.Ccr-18-3190
18. DiCenzo D, Quiaoit K, Fatima K, Bhardwaj D, Sannachi L, Gangeh M, et al. Quantitative Ultrasound Radiomics in Predicting Response to Neoadjuvant Chemotherapy in Patients With Locally Advanced Breast Cancer: Results From Multi-Institutional Study. *Cancer Med* (2020) 9:5798–806. doi: 10.1002/cam4.3255
19. Yu F, Hang J, Deng J, Yang B, Wang J, Ye X, et al. Radiomics Features on Ultrasound Imaging for the Prediction of Disease-Free Survival in Triple Negative Breast Cancer: A Multi-Institutional Study. *Br J Radiol* (2021) 94:20210188. doi: 10.1259/bjr.20210188
20. Li H, Zhu Y, Burnside ES, Drukker K, Hoadley KA, Fan C, et al. MR Imaging Radiomics Signatures for Predicting the Risk of Breast Cancer Recurrence as Given by Research Versions of MammaPrint, Oncotype DX, and PAM50 Gene Assays. *Radiology* (2016) 281:382–91. doi: 10.1148/radiol.2016152110
21. Park H, Lim Y, Ko ES, Cho HH, Lee JE, Han BK, et al. Radiomics Signature on Magnetic Resonance Imaging: Association With Disease-Free Survival in Patients With Invasive Breast Cancer. *Clin Cancer Res* (2018) 24:4705–14. doi: 10.1158/1078-0432.Ccr-17-3783
22. Xiong L, Chen H, Tang X, Chen B, Jiang X, Liu L, et al. Ultrasound-Based Radiomics Analysis for Predicting Disease-Free Survival of Invasive Breast Cancer. *Front Oncol* (2021) 11:621993. doi: 10.3389/fonc.2021.621993
23. Collins FS, Varmus H. A New Initiative on Precision Medicine. *N Engl J Med* (2015) 372:793–5. doi: 10.1056/NEJMp1500523
24. Hodson R. Precision Medicine. *Nature* (2016) 537:S49. doi: 10.1038/537S49a
25. Jameson JL, Longo DL. Precision Medicine–Personalized, Problematic, and Promising. *N Engl J Med* (2015) 372:2229–34. doi: 10.1056/NEJMsb1503104
26. Venkatesan A, Chu P, Kerlikowske K, Sickles EA, Smith-Bindman R. Positive Predictive Value of Specific Mammographic Findings According to Reader and Patient Variables. *Radiology* (2009) 250:648–57. doi: 10.1148/radiol.2503080541
27. Varela C, Karssemeijer N, Hendriks JH, Holland R. Use of Prior Mammograms in the Classification of Benign and Malignant Masses. *Eur J Radiol* (2005) 56:248–55. doi: 10.1016/j.ejrad.2005.04.007
28. Boyer B, Canale S, Arfi-Rouche J, Monzani Q, Khaled W, Balleyguier C. Variability and Errors When Applying the BIRADS Mammography Classification. *Eur J Radiol* (2013) 82:388–97. doi: 10.1016/j.ejrad.2012.02.005
29. Wang L, Yang W, Xie X, Liu W, Wang H, Shen J, et al. Application of Digital Mammography-Based Radiomics in the Differentiation of Benign and Malignant Round-Like Breast Tumors and the Prediction of Molecular Subtypes. *Gland Surg* (2020) 9:2005–16. doi: 10.21037/gs-20-473
30. Li Z, Yu L, Wang X, Yu H, Gao Y, Ren Y, et al. Diagnostic Performance of Mammographic Texture Analysis in the Differential Diagnosis of Benign and Malignant Breast Tumors. *Clin Breast Cancer* (2018) 18:e621-e7. doi: 10.1016/j.clbc.2017.11.004
31. van Griethuysen JJM, Fedorov A, Parmar C, Hosny A, Aucoin N, Narayan V, et al. Computational Radiomics System to Decode the Radiographic Phenotype. *Cancer Res* (2017) 77:e104–e7. doi: 10.1158/0008-5472.Can-17-0339
32. Tibshirani R. Regression Shrinkage and Selection *via* the Lasso. *J R Stat Soc Ser B-Methodol* (1996) 58:267–88. doi: 10.1111/j.2517-6161.1996.tb02080.x
33. Ozer ME, Sarica PO, Arga KY. New Machine Learning Applications to Accelerate Personalized Medicine in Breast Cancer: Rise of the Support Vector Machines. *Omics* (2020) 24:241–6. doi: 10.1089/omi.2020.0001
34. Li JW, Cao YC, Zhao ZJ, Shi ZT, Duan XQ, Chang C, et al. Prediction for Pathological and Immunohistochemical Characteristics of Triple-Negative Invasive Breast Carcinomas: The Performance Comparison Between Quantitative and Qualitative Sonographic Feature Analysis. *Eur Radiol* (2022) 32(3):1590–600. doi: 10.1007/s00330-021-08224-x
35. Li Z, Chen F, Zhang S, Ma X, Xia Y, Shen F, et al. The Feasibility of MRI-Based Radiomics Model in Presurgical Evaluation of Tumor Budding in Locally Advanced Rectal Cancer. *Abdom Radiol (NY)* (2022) 47:56–65. doi: 10.1007/s00261-021-03311-5
36. Mao N, Yin P, Wang Q, Liu M, Dong J, Zhang X, et al. Added Value of Radiomics on Mammography for Breast Cancer Diagnosis: A Feasibility Study. *J Am Coll Radiol* (2019) 16:485–91. doi: 10.1016/j.jacr.2018.09.041
37. Li H, Mendel KR, Lan L, Sheth D, Giger ML. Digital Mammography in Breast Cancer: Additive Value of Radiomics of Breast Parenchyma. *Radiology* (2019) 291:15–20. doi: 10.1148/radiol.2019181113
38. Karahaliou A, Skiadopoulos S, Boniatis I, Sakellaropoulos P, Likaki E, Panayiotakis G, et al. Texture Analysis of Tissue Surrounding Microcalcifications on Mammograms for Breast Cancer Diagnosis. *Br J Radiol* (2007) 80:648–56. doi: 10.1259/bjr/30415751
39. Acciavatti RJ, Cohen EA, Maghsoudi OH, Gastounioti A, Pantalone L, Hsieh MK, et al. Incorporating Robustness to Imaging Physics Into Radiomic Feature Selection for Breast Cancer Risk Estimation. *Cancers (Basel)* (2021) 13(21):5497. doi: 10.3390/cancers13215497
40. Lei C, Wei W, Liu Z, Xiong Q, Yang C, Yang M, et al. Mammography-Based Radiomic Analysis for Predicting Benign BI-RADS Category 4 Calcifications. *Eur J Radiol* (2019) 121:108711. doi: 10.1016/j.ejrad.2019.108711
41. Wang S, Sun Y, Li R, Mao N, Li Q, Jiang T, et al. Diagnostic Performance of Perilesional Radiomics Analysis of Contrast-Enhanced Mammography for the Differentiation of Benign and Malignant Breast Lesions. *Eur Radiol* (2022) 32:639–49. doi: 10.1007/s00330-021-08134-y
42. Gupta S, Markey MK. Correspondence in Texture Features Between Two Mammographic Views. *Med Phys* (2005) 32:1598–606. doi: 10.1118/1.1915013
43. An C, Park YW, Ahn SS, Han K, Kim H, Lee SK. Radiomics Machine Learning Study With a Small Sample Size: Single Random Training-Test Set Split may Lead to Unreliable Results. *PloS One* (2021) 16:e0256152. doi: 10.1371/journal.pone.0256152
44. Varoquaux G. Cross-Validation Failure: Small Sample Sizes Lead to Large Error Bars. *Neuroimage* (2018) 180:68–77. doi: 10.1016/j.neuroimage.2017.06.061
45. Gillies RJ, Kinahan PE, Hricak H. Radiomics: Images Are More Than Pictures, They Are Data. *Radiology* (2016) 278:563–77. doi: 10.1148/radiol.2015151169
46. Wang X, Wan Q, Chen H, Li Y, Li X. Classification of Pulmonary Lesion Based on Multiparametric MRI: Utility of Radiomics and Comparison of Machine Learning Methods. *Eur Radiol* (2020) 30:4595–605. doi: 10.1007/s00330-020-06768-y
47. Shen C, Liu Z, Guan M, Song J, Lian Y, Wang S, et al. 2D and 3D CT Radiomics Features Prognostic Performance Comparison in Non-Small Cell Lung Cancer. *Transl Oncol* (2017) 10:886–94. doi: 10.1016/j.tranon.2017.08.007
48. Lacroix M, Frouin F, Dirand AS, Nioche C, Orlhac F, Bernaudin JF, et al. Correction for Magnetic Field Inhomogeneities and Normalization of Voxel Values Are Needed to Better Reveal the Potential of MR Radiomic Features in Lung Cancer. *Front Oncol* (2020) 10:43. doi: 10.3389/fonc.2020.00043

Conflict of Interest: The authors declare that the research was conducted in the absence of any commercial or financial relationships that could be construed as a potential conflict of interest.

frontiers | Frontiers in Oncology

ORIGINAL RESEARCH
published: 18 May 2022
doi: 10.3389/fonc.2022.854349

Deep Learning for Per-Fraction Automatic Segmentation of Gross Tumor Volume (GTV) and Organs at Risk (OARs) in Adaptive Radiotherapy of Cervical Cancer

Adrian L. Breto[‡], Benjamin Spieler[‡], Olmo Zavala-Romero[†], Mohammad Alhusseini, Nirav V. Patel, David A. Asher, Isaac R. Xu, Jacqueline B. Baikovitz, Eric A. Mellon, John C. Ford, Radka Stoyanova[*] and Lorraine Portelance

Department of Radiation Oncology, Sylvester Comprehensive Cancer Center, Miller School of Medicine, University of Miami, Miami, FL, United States

Background/Hypothesis: MRI-guided online adaptive radiotherapy (MRI-g-OART) improves target coverage and organs-at-risk (OARs) sparing in radiation therapy (RT). For patients with locally advanced cervical cancer (LACC) undergoing RT, changes in bladder and rectal filling contribute to large inter-fraction target volume motion. We hypothesized that deep learning (DL) convolutional neural networks (CNN) can be trained to accurately segment gross tumor volume (GTV) and OARs both in planning and daily fractions' MRI scans.

Materials/Methods: We utilized planning and daily treatment fraction setup (RT-Fr) MRIs from LACC patients, treated with stereotactic body RT to a dose of 45-54 Gy in 25 fractions. Nine structures were manually contoured. MASK R-CNN network was trained and tested under three scenarios: *(i)* Leave-one-out (LOO), using the planning images of N - 1 patients for training; *(ii)* the same network, tested on the RT-Fr MRIs of the "left-out" patient, *(iii)* including the planning MRI of the "left-out" patient as an additional training sample, and tested on RT-Fr MRIs. The network performance was evaluated using the Dice Similarity Coefficient (DSC) and Hausdorff distances. The association between the structures' volume and corresponding DSCs was investigated using Pearson's Correlation Coefficient, r.

Results: MRIs from fifteen LACC patients were analyzed. In the LOO scenario the DSC for Rectum, Femur, and Bladder was >0.8, followed by the GTV, Uterus, Mesorectum and Parametrium (0.6-0.7). The results for Vagina and Sigmoid were suboptimal. The performance of the network was similar for most organs when tested on RT-Fr MRI. Including the planning MRI in the training did not improve the segmentation of the RT-Fr MRI. There was a significant correlation between the average organ volume and the corresponding DSC (r = 0.759, p = 0.018).

OPEN ACCESS

Edited by:
Ellen Ackerstaff, Memorial Sloan Kettering Cancer Center, United States

Reviewed by:
Sharon Qi, UCLA, United States
Motoharu Sasaki, Tokushima University, Japan

***Correspondence:**
Radka Stoyanova
RStoyanova@med.miami.edu

[†]Present Address:
Olmo Zavala-Romero, Center for Ocean-Atmospheric Prediction Studies, Florida State University, Tallahassee, FL, United States

[‡]These authors have contributed equally to this work

Specialty section:
This article was submitted to Cancer Imaging and Image-directed Interventions, a section of the journal Frontiers in Oncology

Received: *13 January 2022*
Accepted: *29 March 2022*
Published: *18 May 2022*

Citation:
Breto AL, Spieler B, Zavala-Romero O, Alhusseini M, Patel NV, Asher DA, Xu IR, Baikovitz JB, Mellon EA, Ford JC, Stoyanova R and Portelance L (2022) Deep Learning for per-Fraction Automatic Segmentation of Gross Tumor Volume (GTV) and Organs at Risk (OARs) in Adaptive Radiotherapy of Cervical Cancer. Front. Oncol. 12:854349. doi: 10.3389/fonc.2022.854349

Conclusion: We have established a robust workflow for training MASK R-CNN to automatically segment GTV and OARs in MRI-g-OART of LACC. Albeit the small number of patients in this pilot project, the network was trained to successfully identify several structures while challenges remain, especially in relatively small organs. With the increase of the LACC cases, the performance of the network will improve. A robust auto-contouring tool would improve workflow efficiency and patient tolerance of the OART process.

Keywords: MRI-guided radiotherapy, cervical cancer, radiotherapy, adaptive radiotherapy, deep learning, convolutional neural networks

INTRODUCTION

Radiotherapy (RT) targets can be mobile, deformable structures (1). In non-adaptive RT, the target for fractionated treatment is defined based on a single pretreatment CT or MRI planning scan with a security margin added to account for anatomic variability (2, 3). The security margin must be large enough to prevent a geographic miss, which often translates into the inclusion of adjacent normal tissue that is vulnerable to radiation-related toxicity in the treated volume (4). An attractive alternative is Magnetic Resonance Image-guided online adaptive RT (MRI-g-OART). When an MRI-g-OART approach is used, daily MR setup scans provide accurate soft-tissue visualization of the target and organs-at-risk (OARs), allowing physicians to modify the original treatment plan based on the anatomy of the day. This approach has been shown to improve target coverage and OARs sparing compared to non-adaptive techniques, improving the therapeutic index of RT for various malignancies (5–10).

For patients with locally advanced cervical cancer (LACC) undergoing external beam radiotherapy (EBRT), changes in bladder and rectal filling contribute to large inter-fraction target volume motion (11). Conventional strategies to address this include expanding the planning target volume (PTV) by up to 2 cm, potentially exposing the bladder, rectum and bowel to elevated doses (12). Definitive RT for LACC using CT-based non-adaptive techniques has been associated with high incidences of early (27%) and late (10%) toxicity (13). In the acute setting, up to 25% of patients experience at least grade 3 gastrointestinal (GI) toxicity and 10% at least grade 3 genitourinary (GU) toxicity. Eighteen percent of patients require treatment interruptions of more than seven days due to the severity of acute symptoms (13). MRI-g-OART promises more conformal dose delivery than the expanded PTV approach, with the potential to improve clinical outcomes by limiting treatment interruptions associated with radiation-related toxicity (14–16).

Technical challenges to OART are not negligible. MRI-g-OART is time-intensive, requiring delineation of OARs near the target volume by the supervising radiation oncologist or a dedicated trained technologist while the patient remains immobile on the treatment table (17). Delays in the adaptive process can challenge patients' tolerance of OART and increase the likelihood of anatomic changes during the interval between image acquisition and completion of radiation delivery (17). Various strategies are under investigation to improve workflow efficiency, including the use of artificial intelligence (AI) deep learning (DL) techniques such as convolutional neural networks (CNN), already applied successfully in diagnostic imaging classification (18, 19).

In this study, we propose using the MASK R-CNN architecture for segmenting the GTV and OARs in a LACC MRI-g-OART treatment scenario. Generally, CNNs are used in image classification systems, where the system is trained on a collection of images and their labels, and then used to classify unseen images into their corresponding categories. The MASK R-CNN extends this into instance segmentation – where the network detects individual objects in the image, generates a mask to segment the object from the rest of the image, and assigns a class to the segmented object (20).

In the case of MRI data, the MASK R-CNN is used to segment and classify the GTV and OARs within the images. The MASK R-CNN architecture includes multiple sub-CNNs. First, the image is fed into a CNN backbone which generates feature maps. These feature maps are then provided to a region proposal network (RPN) which proposes regions that may contain objects of interest. At the second stage, the MASK R-CNN network predicts classes for each region of interest and a refined object mask. The MASK R-CNN outputs the refined masks of the classified objects, working as an automatic segmentation and classification algorithm.

We hypothesized that (*i*) MASK R-CNN can quickly and accurately segment GTVs and OARs in MRI-g-OART of LACC; (*ii*) MASK R-CNN, trained on the initial planning MRIs can segment images of OART fractions of an "unseen" patient, i.e. one whose initial RT planning MRI were not used to train the system; and *(iii)* augmentation of trained MASK R-CNN with the unseen patient's initial planning MRI ("transfer learning") can improve the segmentation of subsequent OART fractions.

MATERIALS AND METHODS

Study Cohort, MRI Acquisition and Contouring

MRI studies were selected from patients treated for LACC on the MRIdian® system (ViewRay, Inc., Mountain View, CA) and enrolled in our Institutional Review Board (IRB) approved registry.

Patients were treated using stereotactic body radiation therapy (SBRT) to a dose of 45-54 Gy in 25 fractions.

All MRIs were acquired on a 0.35T MRIdian combination MRI-g RT system. The MRI sequence used was a balanced steady-state free precession technique (True FISP), providing T2/T1-weighted contrast. Studies from the planning MR and daily MR image guidance acquired before every fraction were used. The planning MRIs were acquired with voxel dimensions of $1.5 \times 1.5 \times 1.5$ mm^3, and the following pulse sequence acquisition parameters: TR/TE = 3/1.27ms, flip angle = 60, bandwidth = 604 Hz/pixel, FOV = 501 × 300 × 360 mm (in left-right, anterior-posterior, and head-foot directions), and matrix size 334 × 200 × 240. The MRI of the treatment fractions were acquired with voxel dimensions of $1.5 \times 1.5 \times 3.0$ mm^3 and matrix size 360 × 310 × 144.

Across all patients, nine structures (GTV + cervix, uterus, parametrium, sigmoid, bladder, vagina, femur, rectum and mesorectum) were contoured for each patient in MIM. The volumes were delineated within a ROI from the top of the first sacral vertebra (S1) to the bottom of the lesser femoral trochanters. The contours from the treatment plan were used as a basis of the organ segmentation. The contours were checked and refined by radiation oncologists specialized in the treatment of gynecological cancers. Examples of these contours are shown in **Figure 1**.

Preprocessing of Images and Contours

A preprocessing pipeline, implemented in Python, has been developed to prepare the raw MR images and contours as inputs for the network. The image intensities were normalized to the interval of [0,1] by scaling the 1^{st} and 99^{th} percentiles of the original image intensities. From the whole MRI volume of data, only slides with at least one manual contour were used for network training. The dataset was augmented by flipping the images on the sagittal axis in order to increase the number of training examples. These images were saved into the PNG format at the original 2D resolution of the source MR.

MASK R-CNN: Training, Validating and Testing

The MASK R-CNN architecture (20) implemented in Tensorflow (21) was used for automated image segmentation and classification. Input images were resized from their native resolutions to an overall size of 512 × 512 pixels per slice. In addition to our data augmentation process, MASK R-CNN implements a layer of data augmentation. By random selection, some of the images were altered with up to two different data augmentation techniques selected from vertical flips, horizontal flips, rotations, multiplication, or Gaussian blur. The images were then fed into the network for training.

Initially, the network weights were loaded from a trained ImageNet model (22). Our network's training parameters were configured as described by Johnson (23).

The network is optimized through stochastic gradient descent (SGD) with the following hyperparameters: learning rate α = 0.001, momentum of 0.9 and decay of 10^{-6}. The training was performed using a batch size of 16 images. MASK R-CNN uses several different loss functions to evaluate and compute weights for the overall network: The RPN and the classifier head use cross-entropy loss and SoftMax loss, respectively, with smoothed L1 loss to refine their anchors and bounding boxes. The mask generator uses binary cross-entropy loss to refine its mask outputs. The individual loss functions are computed as:

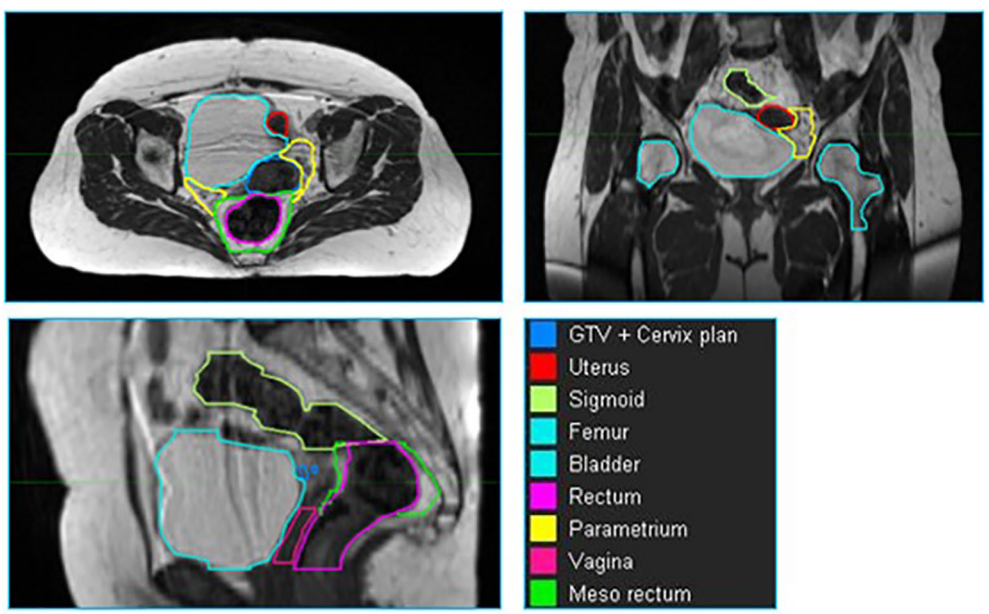

FIGURE 1 | An example of a cervix case provided to the neural network for training. The individual volumes are depicted in different colors.

$$Cross\text{-}entropy\ loss:\ -\sum_{c=1}^{M} y_{o,c}\ln\left(p_{o,\,c}\right)$$

where M is the number of classes, $y_{o,c}$ is a binary (1 or 0) indication if class label c is the correct classification for observation o, and p is the probability observation o is in class c.

$$Soft\ max\ cross\text{-}entropy\ loss: -\sum_{i=1}^{n}\sum_{c=1}^{M} y_{i_{o,c}}\ln(p_{i_{o,c}})$$

where n is the batch size, M is the number of classes, $yi_{o,c}$ is a binary (1 or 0) indication if class label c is the correct classification for observation o, and p is the probability observation o is in class c.

$$Binary\ cross\text{–}entropy: -\left(y_{o,c}\ln\left(p_{o,c}\right) + \left(1 - y_{o,c}\right)\ln\left(1 - p_{o,c}\right)\right)$$

where $y_{o,c}$ is a binary (1 or 0) indication if class label c is the correct classification for observation o, and p is the probability observation o is in class c. This is equivalent to the cross-entropy loss formula above in the instance where $M = 2$.

$$Smooth\ L1\ loss: \begin{cases} |\hat{y} - y|, & if\,|\hat{y} - y| > \alpha; \\ \frac{1}{\alpha}(\hat{y} - y)^2, & if\,|\hat{y} - y| \le \alpha \end{cases}$$

where α is 1, y is the predicted output, and $\hat{y}$ is the target output.

The training was run on a flexible number of epochs, with the stopping criteria defined as three epochs without an improvement in the combined average value of the loss functions in the validation set (10% of the training dataset).

The training was performed on a multi-GPU cluster computer (3 x NVIDIA Quadro RTX 8000, 48 GB memory each). Each model training took approximately 3.5 hours and the automatic segmentation process (inference) takes less than 50s. The system was implemented using Keras (24) and TensorFlow (21) Python libraries.

Mask R-CNN Output

Classification in Mask R-CNN was carried out *via* parallel prediction of contour masks and class labels, using the ResNet backbone network to determine the most appropriate object class, and then applying the masking branch for that class (20). The output was a binary mask representing an instance segmentation of the detected class. Separately, the network also produced a confidence parameter (between 0 and 1) for the class nominated by the RPN. The image and the accompanying mask were generated at the original resolution of the input, single axial images as described above. To recover the original RT-DICOM structure, we developed custom code to re-assemble the 2D masks into 3D contour volumes, integrated as part of the overall workflow. These RT-DICOMs are platform-agnostic and can be viewed in any RT treatment planning system. The output images may be viewed with any conventional image viewer.

Experimental Design and Statistical Analysis

The network's purpose is to generate automatic segmentation of OARs and GTVs for initial RT planning of a new patient and for daily re-contouring at the treatment images for patients receiving OART. Three different scenarios were considered:

i. Leave-one-out (LOO) - Training was conducted in LOO schema, whereby the planning images of N - 1 patients were used as training data for the network, and the excluded patient's planning image was used for testing. In the end, a total of N training sequences were performed, with each patient serving as a training example N - 1 times, and as a test example once.
ii. RT Fraction (RT-Fr) - We evaluated the network's effectiveness in contouring images from the treatment fractions of the unseen patient. The network trained in scenario (i) is tested on images from the treatment fractions of the excluded patient.
iii. Transfer learning - We investigated whether including the planning MRI of the unseen patient as an additional training sample to the trained network would allow the network to perform better on the treatment fraction MRIs for the same patient.

A schematic representation of the three scenarios can be found in **Figure 2**. For all scenarios detailed above, the overall network performance was assessed *via* summary statistics of the Dice Similarity Coefficient (DSCs) and 95% Hausdorff distances between manual and network-generated contours. We also investigated how the network performance is affected by the volume of the contoured structure by correlating the average volume of the manually contoured organ and the corresponding DSC between manual and network-generated contours using Pearson's Correlation Coefficient, r.

RESULTS

The MRIs of fifteen patients (median age 56, range 32 - 71) who received RT for LACC between 2017 through 2018 were analyzed. On average, 83 axial slices per patient were analyzed. **Table 1** shows the obtained DSCs and Hausdorff distances for the segmentation of the GTV and OARs in the three scenarios (**Figure 2**). In the first scenario, fifteen networks were trained from scratch using the MRIs from 14 patients and tested on the "left-out" patient. In this case, the best performance was achieved for Rectum, Femur, and Bladder (DSC > 0.8). The performance was moderate for the Mesorectum, Uterus, Parametrium, and GTV (DSC > 0.6). The results for the Vagina and Sigmoid were suboptimal (DSC ~ 0.4 - 0.5). The performance of the trained network on the left-out patient's treatment fraction (scenario ii) MRIs markedly improved for the Sigmoid and worsened for the Vagina. The performance of the network on the patient's treatment fraction after training on their planning MRI improves for the Uterus but deteriorates for the Femur and Vagina. In **Figure 3**, the manual and MASK R-CNN contours on the original MRI image from a patient with LACC are shown.

Figure 4 shows a plot of the average structure volume and the corresponding average DSC of the trained network. As can be seen in the figure, there was a significant association between the

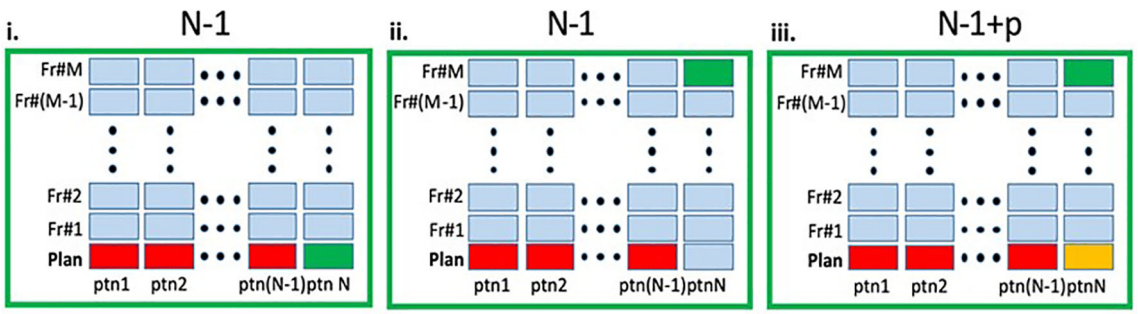

FIGURE 2 | Schematic representation of the experimental design. In each panel the columns represent the MRIs (planning and fraction 1 to M) for a given patient. The entire dataset contain total of N×(M+1) MRIs. i. *Leave-one-out (LOO)*: A deep learning (DL) network, marked as N - 1 was trained on the planning MRIs (red) from N - 1 patients and tested on the planning MRI of the left-out patient (green). ii. *RT-Fr*: The N - 1 network was tested on an MRI from an online adaptable radiotherapy fraction of the "left-out" patient (green). Note that the planning MRI from this patient was not used in the training. iii. *Transfer learning*: The planning MRI for patient N (yellow) is added to the N - 1 network, resulting in N - 1+p network, which is then tested on an MRI from RT-Fr of the "left-out" patient (green).

TABLE 1 | Dice Similarity Coefficients (DSC) and Hausdorff distances (HD) (mean ± SD) between the manual and network contours for each of the investigated scenarios.

	Scenario					
	LOO		RT-Fr		Transfer Learning	
	DSC	HD (mm)	DSC	HD (mm)	DSC	HD (mm)
Mesorectum	0.62 ± 0.11	2.65 ± 0.89	0.69 ± 0.12	3.13 ± 0.76	0.63 ± 0.11	3.84 ± 1.35
Rectum	0.85 ± 0.09	1.18 ± 0.49	0.88 ± 0.07	1.77 ± 0.55	0.85 ± 0.05	1.94 ± 0.76
Uterus	0.70 ± 0.23	3.54 ± 3.28	0.69 ± 0.36	3.29 ± 1.44	0.83 ± 0.08	3.50 ± 1.99
Vagina	0.41 ± 0.33	2.51 ± 2.00	0.18 ± 0.36	2.14 ± 0.10	0.04 ± 0.07	6.5 ± 0.10
Parametrium	0.62 ± 0.09	4.31 ± 2.34	0.58 ± 0.11	4.94 ± 1.02	0.59 ± 0.07	4.72 ± 1.63
Sigmoid	0.46 ± 0.26	7.41 ± 5.76	0.69 ± 0.22	8.26 ± 0.98	0.61 ± 0.03	8.26 ± 0.99
Femur	0.88 ± 0.06	2.97 ± 1.82	0.76 ± 0.12	1.68 ± 0.25	0.45 ± 0.37	1.68 ± 0.25
Bladder	0.81 ± 0.15	3.10 ± 3.57	0.75 ± 0.12	3.01 ± 1.32	0.82 ± 0.09	3.02 ± 1.32
GTV	0.67 ± 0.30	2.77 ± 1.73	0.61 ± 0.32	4.34 ± 2.83	0.60 ± 0.32	4.34 ± 2.83

LOO, leave-one-out; RT-Fr, Online Adaptive Radiotherapy Fraction; DSC, Dice Similarity Coefficient; GTV, Gross Tumor Volume; HD, Hausdorff distance.

average structure's volume and the corresponding DSC (r = 0.759, p=0.018).

For scenario iii: *Transfer Learning*, we experimented with the number of epochs to train the network on the unseen patient's planning MRI. We tested a varying number of epochs (20, 40, 80, 100, 200) of transfer learning and evaluated the change in performance on both the unseen and original training datasets. After these trials, we achieved the best overall performance using 20 epochs of transfer learning. In summary, the network's performance across the original training and validation exams was consistent with the results in **Table 1**.

DISCUSSION

This study evaluated the performance of the MASK R-CNN network for segmenting the OARs and GTVs in pelvic radiation for LACC. The imaging studies used included MR simulation scans performed in the initial planning phase and daily MR setup scans performed prior to each fraction in MRI-g-OART. Several developments were carried out related to the project: *(i)* the contours of the OARs and GTVs were converted from RT-DICOM to labeled segmentations, *(ii)* DSC and Hausdorff units were implemented to evaluate its performance, and *(iii)* the contours generated from the network were converted into RT-DICOM for transferring to the radiation treatment planning system. The network is universal and accepts images of any dimensions; there is no need for the extended processing often required in other DL approaches.

The network provided segmentations with variable accuracy for the individual organs. Visceral OARS are deformable and mobile, with volumes changing day-to-day based on factors such as stomach contents and stool passing through the intestinal tract. Mobile organs with low-contrast borders such as the Sigmoid presented a serious challenge. On the other hand, the higher contrast of the volume boundaries in organs like the Rectum and Bladder contributed to better segmentation. In these cases, for example, the boundaries are defined by a significant difference in the image intensity relative to the surrounding tissues and the DL contours appear to be smoother and more conformal than manual contours (**Figure 3**). On average, the DSC for the GTV was 0.64, requiring further improvement to be clinically applicable. It should be noted that in current MRI-g-OART workflow, the GTV is prioritized and highly scrutinized by the treating radiation

oncologist, a scenario likely to continue regardless of network developments. The association of the poor network performance with the smaller size of an organ (**Figure 4**) explains in part the results related to the Vagina. A difference in only a few pixels between the manual and network contours may have a large impact on the DCS (25). Conversely, the relatively large size may also be a contributing factor for the good performance for Rectum and Bladder.

To the best of our knowledge there are no published reports on segmentation of LACC OARs and GTVs on MRI. Chen et al (26) compared nine methods for segmenting cervical tumors (GTV) on 3D (18)FDG PET images from 50 patients; the highest DSC was 0.84 ± 0.007. The best results achieved by our networks for GTV were comparable DSC = 0.75 ± 0.01. The smaller sample size of the current study and the relatively lower signal-to-noise of MRI compared to PET should be noted. In Fu et al. (18), a CNN network was used to segment OARs: liver, kidney, stomach, bowel and duodenum in the treatment of pancreas, liver, stomach, adrenal gland, and prostate. Despite the significantly larger dataset of MRIs from 120 patients, the DSCs for these five structures were not markedly better. The duodenum was the most challenging structure in their study with DSC of ~0.60. The relatively robust performance of our networks despite training with small datasets is due in part of utilizing MASK R-CNN. Its backbone, the ResNet50 network, is pre-trained with images from the ImageNet database, containing over 14 million images. Instead of starting the training from scratch, the trained "weights" of ImageNet are used by default. This allows the network to be trained satisfactorily on new datasets with few examples.

The network trained for scenario i: LOO on patients' planning MRIs can be used for the automatic segmentation of OARs and GTVs on an MRI scan in initial RT planning of a new patient. To incorporate these developments into the clinical workflow, the quality of the generated contours must be deemed sufficient by radiation oncologists. While for some organs the results are suboptimal, a process has been created to incorporate the network into our workflow, and to continue its optimization as new datasets become available.

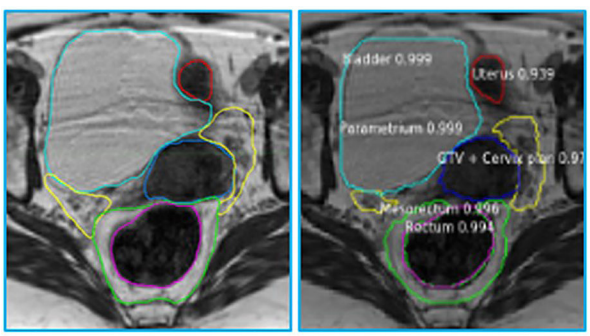

FIGURE 3 | Manual (left) and automatic (right) contours on the original MRI image from a patient with cervical cancer. The contours generated by MASK R-CNN contain a confidence estimate, a number between 0 and 1, with 0 representing mimmum and 1 maximum confidence that the class, assigned to the segmented volume is accurate. Please refer to **Figure 1** legend for color scheme.

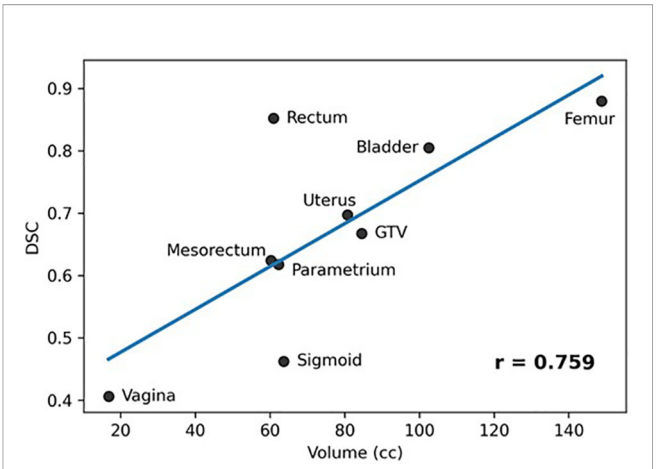

FIGURE 4 | Association between averages of manual stmctures' volumes and corresponding DCS (Pearson Coefficient = 0.759, p = 0.018).

The performance of the network in segmenting the planning MRI (scenario i: LOO) and the daily treatment fraction MRI (scenario ii: RT-Fr) was not markedly different. This second scenario is relevant to offline adaptive planning to account for changes in the tumor size or shape, and especially to online adaptive planning based on the anatomy of the day. In the latter case, fast and robust automated segmentation while the patient is on the table has the potential to decrease treatment time, improving patients' tolerance of OART and limiting anatomic changes in the interval between image acquisition and radiation delivery. Note that the treatment fraction MRIs were acquired with different sequence parameters. As shown by others (27) and in our work (28, 29), the variability in the data acquisition contribute to the generalization of the network. The fact that the network performance in scenario ii did not deteriorate indicates the generalizability of the approach.

We also investigated whether adding the simulation MRI to the training of the network (scenario iii: Transfer learning) improves the segmentation performance on subsequent fractions. The rationale was to learn the general anatomy of a patient, and then transfer this knowledge for the segmentation of planning fractions' MRIs. Overall, there was no clear improvement over scenario ii; segmentation performance improved for some structures and degraded for others.

Contouring multiple OARs is time-consuming and somewhat subjective. The process requires going back and forth between slices multiple times to determine the shape of the organ. On average, based on our and others experience (18), it takes close to two hours to manually contour the organs for the treatment plan. Our proposed automatic segmentation takes <3.5 min for a dataset. As discussed above, we assume that the automatic contours in some cases will need expert refinement. Based on preliminary data, the time to adjust the network generated contours in MIM is about 30 min, making the procedure substantially shorter than two hours.

The study has several limitations. The small number of subjects limits the network's performance. In fact, using the

LOO approach, fourteen patients were used in the training of the fifteen networks in scenario i. In the future, a larger set of patients' MRIs will be contoured to build the knowledge bank for the DL software.

In conclusion, our results demonstrate the promise of DL in volume segmentation of LACC. These developments provide a solid basis for the development of a robust auto-contouring tool to improve workflow efficiency and patient tolerance of the MRI-g-OART process.

DATA AVAILABILITY STATEMENT

The original contributions presented in the study are included in the article. Further inquiries can be directed to the corresponding author.

ETHICS STATEMENT

The studies involving human participants were reviewed and approved by IRB ID: 20160817 at University of Miami. The patients/participants provided their written informed consent to participate in this study.

AUTHOR CONTRIBUTIONS

RS and LP contributed to conception and design of the study. LP and EM provided patient imaging for use in study. JF established the MR acquisition sequences. AB modified CNN code and performed experiments. OZ-R provided network expertise. JB, BS, LP, DA, NP, and RS organized patient database and provided original volumes. RS, IX, and MA performed statistical analysis. RS, AB, and BS wrote the first draft of the manuscript. RS, IX, and MA performed statistical analysis. All authors contributed to manuscript revision, read, and approved the submitted version.

FUNDING

Research reported in this publication was supported by the National Cancer Institute of the National Institutes of Health under Award Numbers P30CA240139 and UO1CA239141.

REFERENCES

1. White IM, Scurr E, Wetscherek A, Brown G, Sohaib A, Nill S, et al. Realizing the Potential of Magnetic Resonance Image Guided Radiotherapy in Gynaecological and Rectal Cancer. *Br J Radiol* (2019) 92:20180670. doi: 10.1259/bjr.20180670
2. Hunt A, Hansen VN, Oelfke U, Nill S, Hafeez S. Adaptive Radiotherapy Enabled by MRI Guidance. *Clin Oncol (R Coll Radiol)* (2018) 30:711–9. doi: 10.1016/j.clon.2018.08.001
3. Rabe M, Thieke C, Düsberg M, Neppl S, Gerum S, Reiner M, et al. Real-Time 4DMRI-Based Internal Target Volume Definition for Moving Lung Tumors. *Med Phys* (2020) 47:1431–42. doi: 10.1002/mp.14023
4. Krishnan S, Chadha A, Suh Y, Chen H, Rao A, Das P, et al. Focal Radiation Therapy Dose Escalation Improves Overall Survival in Locally Advanced Pancreatic Cancer Patients Receiving Induction Chemotherapy and Consolidative Chemoradiation. *Int J Radiat Oncol Biol Phys* (2016) 94:755–65. doi: 10.1016/j.ijrobp.2015.12.003
5. Henke L, Kashani R, Robinson C, Curcuru A, DeWees T, Bradley J, et al. Phase I Trial of Stereotactic MR-Guided Online Adaptive Radiation Therapy (SMART) for the Treatment of Oligometastatic or Unresectable Primary Malignancies of the Abdomen. *Radiother Oncol* (2018) 126:519–26. doi: 10.1016/j.radonc.2017.11.032
6. Rudra S, Jiang N, Rosenberg S, Olsen J, Roach M, Wan L, et al. Using Adaptive Magnetic Resonance Image-Guided Radiation Therapy for Treatment of Inoperable Pancreatic Cancer. *Cancer Med* (2019) 8:2123–32. doi: 10.1002/cam4.2100
7. Foroudi F, Pham D, Bressel M, Hardcastle N, Gill S, Kron T. Comparison of Margins, Integral Dose and Interfraction Target Coverage With Image-Guided Radiotherapy Compared With Non-Image-Guided Radiotherapy for Bladder Cancer. *Clin Oncol (R Coll Radiol)* (2014) 26:497–505. doi: 10.1016/j.clon.2014.03.007
8. Rosenberg S, Henke L, Shaverdian N, Mittauer K, Wojcieszynski A, Hullett C, et al. A Multi-Institutional Experience of MR-Guided Liver Stereotactic Body Radiation Therapy. *Adv Radiat Oncol* (2019) 4:142–9. doi: 10.1016/j.adro.2018.08.005
9. Henke L, Olsen JR, Contreras JA, Curcuru A, DeWees T, Green OL, et al. Stereotactic MR-Guided Online Adaptive Radiation Therapy (SMART) for Ultracentral Thorax Malignancies: Results of a Phase 1 Trial. *Adv Radiat Oncol* (2019) 4:201–9. doi: 10.1016/j.adro.2018.10.003
10. Kishan AU, Tyran M, Steinberg ML, Holden SB, Cao M. MRI-Guided Dose-Escalated Salvage Radiotherapy for Bulky Bladder Neck Recurrence of Prostate Cancer. *Cureus* (2018) 10:e2360. doi: 10.7759/cureus.2360
11. Haripotepornkul NH, Nath SK, Scanderbeg D, Saenz C, Yashar CM. Evaluation of Intra- and Inter-Fraction Movement of the Cervix During Intensity Modulated Radiation Therapy. *Radiother Oncol* (2011) 98:347–51. doi: 10.1016/j.radonc.2010.11.015
12. Lee CM, Shrieve DC, Gaffney DK. Rapid Involution and Mobility of Carcinoma of the Cervix. *Int J Radiat Oncol Biol Phys* (2004) 58:625–30. doi: 10.1016/j.ijrobp.2003.09.060
13. Roszak A, Warenczak-Florczak Z, Bratos K, Milecki P. Incidence of Radiation Toxicity in Cervical Cancer and Endometrial Cancer Patients Treated With Radiotherapy Alone Versus Adjuvant Radiotherapy. *Rep Pract Oncol Radiother* (2012) 17:332–8. doi: 10.1016/j.rpor.2012.07.005
14. Tanderup K, Fokdal LU, Sturdza A, Haie-Meder C, Mazeron R, van Limbergen R, et al. Effect of Tumor Dose, Volume and Overall Treatment Time on Local Control After Radiochemotherapy Including MRI Guided Brachytherapy of Locally Advanced Cervical Cancer. *Radiother Oncol* (2016) 120:441–6. doi: 10.1016/j.radonc.2016.05.014
15. Asher D, Padgett KR, Llorente RE, Farnia BS, Ford JC, Gajjar SR, et al. Magnetic Resonance-Guided External Beam Radiation and Brachytherapy for a Patient With Intact Cervical Cancer. *Cureus* (2018) 10:e2577. doi: 10.7759/cureus.2577
16. Heijkoop ST, Langerak TR, Quint S, Bondar L, Mens JM, Heijmen BJ, et al. Clinical Implementation of an Online Adaptive Plan-of-the-Day Protocol for Nonrigid Motion Management in Locally Advanced Cervical Cancer IMRT. *Int J Radiat Oncol Biol Phys* (2014) 90:673–9. doi: 10.1016/j.ijrobp.2014.06.046
17. Acharya S, Fischer-Valuck BW, Kashani R, Parikh P, Yang D, Zhao T, et al. Online Magnetic Resonance Image Guided Adaptive Radiation Therapy: First Clinical Applications. *Int J Radiat Oncol Biol Phys* (2016) 94:394–403. doi: 10.1016/j.ijrobp.2015.10.015
18. Fu Y, Mazur TR, Wu X, Liu S, Chang X, Lu Y, et al. A Novel MRI Segmentation Method Using CNN-Based Correction Network for MRI-Guided Adaptive Radiotherapy. *Med Phys* (2018) 45:5129–37. doi: 10.1002/mp.13221
19. Elmahdy MS, Jagt T, Zinkstok RT, Qiao Y, Shahzad R, Sokooti H, et al. Robust Contour Propagation Using Deep Learning and Image Registration for Online

Adaptive Proton Therapy of Prostate Cancer. *Med Phys* (2019) 46:3329–43. doi: 10.1002/mp.13620
20. He K, Gkioxari G, Dollar P, Girshick R. Mask R-CNN. *IEEE Trans Pattern Anal Mach Intell* (2020) 42:386–97. doi: 10.1109/TPAMI.2018.2844175
21. Abadi M, Barham P, Chen J, Chen Z, Davis A, Dean J, et al. *12th {USENIX} Symposium on Operating Systems Design and Implementation ({OSDI} 16.* Savannah, GA: 12th USENIX Symposium on Operating Systems Design and Implementation. (2016). pp. 265–83.
22. Russakovsky O, Deng J, Su H, Krause J, Satheesh S, Ma S, et al. ImageNet Large Scale Visual Recognition Challenge. *Int J Comput Vision* (2015) 115:211–52. doi: 10.1007/s11263-015-0816-y
23. Johnson JW. Adapting Mask-RCNN for Automatic Nucleus Segmentation. arXiv. (2018). *Proceedings of the 2019 Computer Vision Conference* 2:1805.00500v1. doi: 10.1007/978-3-030-17798-0
24. Cholett F. (2013). Available at: https://github.com/fchollet/keras.
25. Reinke A, Tizabi MD, Eisenmann M, Maier-Hein L. Common Pitfalls and Recommendations for Grand Challenges in Medical Artificial Intelligence. *Eur Urol Focus* (2021) 7:710–2. doi: 10.1016/j.euf.2021.05.008
26. Chen L, Shen C, Zhou Z, Maquilan G, Albuquerque K, Folkert MR, et al. Automatic PET Cervical Tumor Segmentation by Combining Deep Learning and Anatomic Prior. *Phys Med Biol* (2019) 64:085019. doi: 10.1088/1361-6560/ab0b64
27. Gibson E, Hu Y, Ghavami N, Ahmed HU, Moore C, Emberton M, et al. Inter-Site Variability in Prostate Segmentation Accuracy Using Deep Learning. In: *Medical Image Computing and Computer Assisted Intervention - Miccai 2018*, vol. Pt Iv 11073. (2018). Granada, Spain: Medical Image Computing and Computer Assisted Intervention - MICCAI 2018. p. 506–14. doi: 10.1007/978-3-030-00937-3_58
28. Padgett KR, Swallen A, Pirozzi S, Piper J, Chinea FM, Abramowitz MC, et al. Towards a Universal MRI Atlas of the Prostate and Prostate Zones: Comparison of MRI Vendor and Image Acquisition Parameters. *Strahlenther Onkol* (2019) 195:121–30. doi: 10.1007/s00066-018-1348-5
29. Zavala-Romero O, Breto AL, Xu IR, Chang YC, Gautney N, Dal Pra A, et al. Segmentation of Prostate and Prostate Zones Using Deep Learning A Multi-MRI Vendor Analysis. *Strahlenther Onkol* (2020) 196:932–42. doi: 10.1007/s00066-020-01607-x

Author Disclaimer: The content is solely the responsibility of the authors and does not necessarily represent the official views of the National Institutes of Health.

Conflict of Interest: The authors declare that the research was conducted in the absence of any commercial or financial relationships that could be construed as a potential conflict of interest.

The handling editor EA declared a past co-authorship with the author RS.

Publisher's Note: All claims expressed in this article are solely those of the authors and do not necessarily represent those of their affiliated organizations, or those of the publisher, the editors and the reviewers. Any product that may be evaluated in this article, or claim that may be made by its manufacturer, is not guaranteed or endorsed by the publisher.

frontiers | Frontiers in Oncology

ORIGINAL RESEARCH
published: 23 June 2022
doi: 10.3389/fonc.2022.851192

Defining the Magnetic Resonance Features of Renal Lesions and Their Response to Everolimus in a Transgenic Mouse Model of Tuberous Sclerosis Complex

Shubhangi Agarwal[1], *Emilie Decavel-Bueff*[1], *Yung-Hua Wang*[1], *Hecong Qin*[1], *Romelyn Delos Santos*[1], *Michael J. Evans*[1,2,3] *and Renuka Sriram*[1]*

[1] Department of Radiology and Biomedical Imaging, University of California, San Francisco, San Francisco, CA, United States, [2] Department of Pharmaceutical Chemistry, University of California, San Francisco, San Francisco, CA, United States, [3] Helen Diller Family Comprehensive Cancer Center, University of California, San Francisco, San Francisco, CA, United States

OPEN ACCESS

Edited by:
Marie-France Penet, Johns Hopkins Medicine, United States

Reviewed by:
Martin Meier, Hannover Medical School, Germany
Xiaojun Zha, Anhui Medical University, China

***Correspondence:**
Renuka Sriram
renuka.sriram@ucsf.edu

Specialty section:
This article was submitted to Cancer Imaging and Image-directed Interventions, a section of the journal Frontiers in Oncology

Received: *09 January 2022*
Accepted: *24 May 2022*
Published: *23 June 2022*

Citation:
Agarwal S, Decavel-Bueff E, Wang YH, Qin H, Santos RD, Evans MJ and Sriram R (2022) Defining the Magnetic Resonance Features of Renal Lesions and Their Response to Everolimus in a Transgenic Mouse Model of Tuberous Sclerosis Complex. Front. Oncol. 12:851192. doi: 10.3389/fonc.2022.851192

Tuberous sclerosis complex (TSC) is an inherited genetic disorder characterized by mutations in *TSC1* or *TSC2* class of tumor suppressers which impact several organs including the kidney. The renal manifestations are usually in the form of angiomyolipoma (AML, in 80% of the cases) and cystadenomas. mTOR inhibitors such as rapamycin and everolimus have shown efficacy in reducing the renal tumor burden. Early treatment prevents the progression of AML; however, the tumors regrow upon cessation of therapy implying a lifelong need for monitoring and management of this morbid disease. There is a critical need for development of imaging strategies to monitor response to therapy and progression of disease which will also facilitate development of newer targeted therapy. In this study we evaluated the potential of multiparametric ^{1}H magnetic resonance imaging (mpMRI) to monitor tumor response to therapy in a preclinical model of TSC, the transgenic mouse A/J *Tsc2*$^{+/-}$. We found 2-dimensional T_2-weighted sequence with 0.5 mm slice thickness to be optimal for detecting renal lesions as small as 0.016 mm^3. Baseline characterization of lesions with MRI to assess physiological parameters such as cellularity and perfusion is critical for distinguishing between cystic and solid lesions. Everolimus treatment for three weeks maintained tumor growth at 36% from baseline, while control tumors displayed steady growth and were 70% larger than baseline at the end of therapy. Apparent diffusion coefficient, T_1 values and normalized T_2 intensity changes were also indictive of response to treatment. Our results indicate that standardization and implementation of improved MR imaging protocols will significantly enhance the utility of mpMRI in determining the severity and composition of renal lesions for better treatment planning.

Keywords: TSC, kidney, everolimus, mTOR, MRI, mp-MRI, AML

INTRODUCTION

Tuberous sclerosis complex (TSC) is an autosomal dominant syndrome caused by germline inactivating mutations in either allele of the genes *TSC1* or *TSC2*. The *TSC1/TSC2* tumor suppressor gene complex, also known as the Hamartin and Tuberin protein complex, negatively regulates mechanistic target of rapamycin (mTOR) complex 1 (mTORC1), a master regulator of cellular biosynthesis, resulting in proliferation, angiogenesis and uncontrolled cell growth. This disorder affects multiple organ systems and the clinical manifestations of TSC include tumors in brain, skin, heart, lungs, and kidneys and neurological conditions such as seizures, autism, and cognitive disability. The renal manifestations are usually in the form of angiomyolipoma (AML, in 70-80% of the cases) and cystadenomas and are one of the main causes of mortality and morbidity in patients with TSC (1). The severity of renal involvement is markedly increased in disease caused by *TSC2* compared to *TSC1* mutations (2). TSC renal cysts have a range of disease patterns and severity reflected by a clinical scoring system that has been developed independent of the Bosniak scale (3). These lesions are under-recognized for causing severe disease which manifests as hypertension and chronic kidney disease. Management of TSC cystic disease is not well-studied although controlling blood pressure (4) and treating with mTOR (5) inhibitors have shown benefit in reducing cystic burden.

Unlike sporadic AML tumors that are unilateral and smaller in size, those associated with TSC are multiple, bilateral, and asymptomatic. However, as they progress to larger lesions (>3 cm), they run the risk of bleeding and require prophylactic management to prevent renal impairment which can sometimes be fatal. Transarterial embolization of these lesions at high risk for bleeding has been shown to slow tumor growth and preserve renal function (6). However, repeat treatment is often required and necessitates regular radiographic follow-up. Thus, constant monitoring after diagnosis, for tumor growth and emergence of new tumors, is implicit in the management of TSC-associated AML.

mTOR pathway inhibitors such as everolimus and sirolimus are the first line of therapy against asymptomatic AML (7). Studies have shown that early treatment prevents the progression of AML and can in fact cause tumor shrinkage, but tumors regrow upon cessation of therapy, implying a lifelong need for monitoring and management. Therefore, imaging assessment of disease prevalence and treatment response is essential for management of this disease. Magnetic resonance imaging (MRI) is the recommended modality to follow these renal lesions that often have cystic components and are sometimes fat-poor (8).

The *Tsc2*$^{+/-}$ A/J mouse is heterozygous for deletion of exons 1-2 and is considered a good model to study TSC-related kidney disease because the mice develop age-related renal cysts and kidney tumors (cystadenomas and cystadenocarcinomas) with a defective mTOR pathway like that observed in human TSC-related tumors (9–11). This model has proven invaluable for evaluating numerous therapies (12–14) but the lack of longitudinal noninvasive measures of treatment effect is a significant barrier to full utilization of this model. In fact, this model has not been characterized with imaging modalities such as MRI which is an indispensable tool in the clinical workup of patients with TSC. Hence, the goal of this pilot study was to evaluate and optimize MR imaging protocols for monitoring renal lesions and to assess the potential of multiparametric ^{1}H MRI (mpMRI) to monitor tumor response to therapy in this preclinical transgenic mouse model of TSC.

MATERIALS AND METHODS

Animal Model

Six male A/J strain *Tsc2*$^{+/-}$ mice (courtesy Tuberous Sclerosis Complex Alliance), 6-7 months old, were studied (n = 3 control and n = 3 treatment). All procedures were approved by our Institutional Animal Care and Use Committee. The mice were treated with everolimus (RAD001, Sigma-Aldrich), 5 mg/kg administered intraperitoneally daily for a total of 3 weeks. Everolimus was dissolved in PEG 400 and 20% 2-hydroxypropylcylcodextrine in water + dimethylsulfoxide (DMSO, Sigma-Aldirch).

^{1}H MR Imaging

Tumor-bearing mice were imaged using a vertical wide bore 14.1T scanner (1,000 mT/cm gradients, Agilent) equipped with a millipede 40 mm ^{1}H coil for anatomic imaging. Mice were anesthetized with 1–2% inhalant isoflurane. Multiparametric imaging was performed which included T_2-weighted imaging for morphology, diffusion weighted images for cellularity, T_1-weighted images with variable flip angle for T_1 mapping followed by dynamic contrast enhanced (DCE) imaging for measuring perfusion. High resolution T_2-weighted images were acquired for anatomic references using a fast spin echo sequence with fat suppression and the following parameters: field of view, 30 x 30 mm; matrix size, 256 x 256; repetition time, 3 s; echo time, 10 ms; ETL 8; segments 32; NEX, 2; slice thickness 1 and 0.5 mm, interleaved acquisition in both axial and coronal orientations. High resolution 3D images were acquired using a fast spin echo sequence and the following parameters: repetition time, 200 ms; echo time, 9 ms; field of view, 30 x 30 mm; slab thickness, 64 mm; matrix size, 256 x 256 x 64 (128 for 0.5 mm thick slices); NEX, 2; slice thickness 0.5-mm. Diffusion weighted images with respiratory gating were acquired using the following parameters: matrix size, 128 × 128; field of view, 30 × 30 mm; slice thickness, 1 mm; *b*-values of 25, 180, 323, 508 s/mm^2. T_1 mapping was performed by acquiring gradient echo images with field of view, 30 x 30 mm; matrix size, 128 x 128; repetition time, 39 ms; echo time, 3 ms; slice thickness 1 mm with the following flip angles: 2, 5, 10, 15, 20, 30 and 40 degrees. Following T_1 mapping, a bolus of Gd-DTPA (0.27 mmol/kg, Magnevist, Bayer Healthcare, Whippany, NJ) was injected *via* the tail vein followed by 150 μL of saline flush. DCE MRI was performed with the following parameters: TE/TR =1.11/39 ms, 40° flip angle, 128′ 128 matrix, 30 x 30 mm FOV, 0.3125 x 0.3125 mm in-plane resolution, 1 mm slice thickness, 40 dummy scans (prior to contrast agent injection), and 5s temporal resolution with total 50 time points. After baseline imaging, the three mice were either

treated with everolimus and the remaining three were untreated controls. All the six mice were imaged weekly with the same imaging protocol for a total of three weeks.

Data Analysis

All image processing and analysis were performed using MATLAB (Mathworks, Natick, MA, USA), and IDL based in-house software BRIMAGE. All the data presented in this study is from 3 mice per cohort. T_2-weighted images were used to calculate the volume of tumor lesions in mice and were tracked over time by manually drawing regions of interest (ROIs) around them. T_2-weighted intensities for all lesions were calculated and normalized to blood vessel intensity to evaluate the serial changes and across groups. We normalized the T_2-weighted intensities to blood vessel intensity as we do not expect the latter to be affected by age and/or treatment. Apparent diffusion coefficient (ADC, mm^2/s) maps were generated as previously described (15) and mean tumor ADCs for the same ROIs. Briefly, ADC were estimated on the basis of mono-exponential fitting of diffusion-weighted signal of 4 b-values to the equation $S = S0 \bullet exp(-ADC \bullet b)$ using VNMRJ software (Agilent Technologies). Baseline T_1 maps and semi-quantitative analysis of DCE data was performed using the techniques previously described (16). We looked at the following semi-quantitative parameters based on dynamic Gd-DTPA concentration: 1) area under the curve (AUC): sum of Gd-DTPA concentrations at all time points; 2) initial area under the curve (iAUC): sum of Gd-DTPA concentration from contrast agent arrival to 90s after the arrival; 3) wash-in slope: approximate derivative of dynamic Gd-DTPA concentration curve from bolus arrival to the peak; 4) wash-out slope: the slope of linear regression of Gd-DTPA concentration from the time of peak enhancement to the last time point, with positive slopes allowed; 5) time to reach peak concentration and 6) peak concentration. We also evaluated the quantitative parameter K^{trans} (volume transfer constant) that represents the permeability using the Tofts model (16).

Statistical Analysis

Data are presented as mean ± standard error. Statistical analysis was performed using one- and two-way ANOVA and linear mixed model. One-way ANOVA was performed on total tumor burden, ADCs, normalized T_2 intensities and T_1 values of each group at baseline. A repeated measures one-way ANOVA with Tukey's *post hoc* tests was used to assess the impact of treatment on the two cohorts for the multiple imaging parameters. P-values < 0.05 were considered statistically significant. Statistical tests were performed using PRISM (GraphPad, La Jolla, CA, USA) and Stata 16 (StataCorp LLC, College Station, TX). Changes in imaging parameters of a lesion over time between treated and control mice were assessed *via* multilevel regression analyses. The linear mixed model analysis was conducted using 'mixed' function in Stata 16. Time was used as a continuous variable, and the overall linear trends in imaging parameters after therapy were obtained and reported.

Immunohistochemistry

Kidneys were harvested after the last imaging session at the end of the third week of treatment. Left and right kidneys were formalin-fixed and paraffin-embedded for histopathological analysis. Fixed kidney blocks were cut into 4 μm-thick sections on a Leica microtome (Buffalo Grove, IL, USA) in coronal orientation, then stained with hematoxylin and eosin (H&E), and Ki67/Rabbit antibody #9129 (Cell Signaling Technology Europe, B.V.). Brightfield images of lesions stained with H&E and Ki67 were acquired using a Nikon 6D microscope using a 40× power objection yielding a 0.22 μm in-plane resolution to focus on the lesions. Stitched images of the entire kidneys were acquired at 10x magnification to assess the distribution and properties of lesions. The lesions were sub-divided into three groups: cystic (filled with ≤ 25% cells), papillary (filled with > 25% cells) and solid lesions (filled with cells) (17). Images were visualized using the open-source software QuPath (18).

RESULTS

Optimal Detection of Renal Lesions Using T_2-Weighted Images

Male *Tsc2*$^{+/-}$ A/J mice, 6-7 months old, presented with bilateral adenomas and cystic lesions in the renal capsule and pelvis as shown in the representative images in **Figure 1**. T_2-weighted images were used to delineate the lesions and estimate their volumes. Tumor volumes were measured once a week for a total of four weeks. Interestingly, the majority of the lesions were observed around the renal peripheral capsule or pelvis (**Figure 1**). The average lesion size at this age was 0.4 ± 0.51 mm^3. The lesion size ranged from 0.016 to 5.12 mm^3 and 36 ± 5.7 lesions were detected on average in each mouse.

Owing to the early assessment of developing lesions and their locations, and the chosen slice thickness of 1 mm (in order to achieve high SNR in a short time), we investigated whether volumes derived from axial or coronal imaging sections were different. Representative T_2-weighted images of the abdomen acquired at axial and coronal orientations in shown in **Figures 2A, B**. **Figure 2C** shows the Pearson correlation analysis between the mean tumor volumes with a highly significant positive correlation (p= 0.004, r = 0.68). A Bland-Altman analysis of differences and agreement between the volumes showed that the majority of lesion volumes were well within the lines of agreement (**Figure 2D**).

However, considering that the majority (>90%) of the lesions were below 2 mm^3, we investigated if 0.5 mm thick imaging slices would yield a better estimate of the lesion volume and minimize the partial volume effect. For this analysis the mice were imaged in the axial orientation consecutively with 0.5 as well as 1 mm slice thickness interleaved to cover the entire kidney. A total of 122 lesions were identified in both data sets. Representative T_2-weighted images with 1 mm and 0.5 mm slice thickness are shown **Figures 2E, F**. A highly significant positive correlation (p<0.0001, r = 0.97) was obtained between the tumor volumes obtained by the two methods (data not shown). On average the lesion volumes estimated by 0.5 mm thick slice (1 ± 1.18 mm^3) were ~20% lower than when measured by 1 mm slice thickness T_2-weighted sequence (1.2 ± 1.3 mm^3). Analysis of the difference in volumes per lesion from the two different slice thickness images

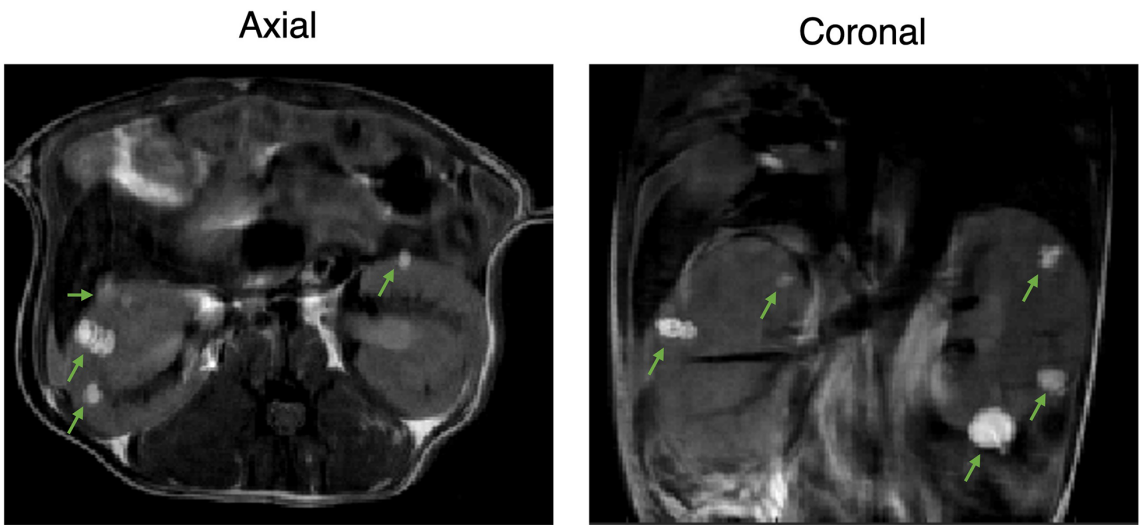

FIGURE 1 | Two-dimensional proton imaging of 6–7-month-old Tsc2 $^{+/-}$ A/J male mice. Representative 2D T_2-weighted images of the TSC mice with bilateral adenomas and cystic lesions in the renal capsule and pelvis at axial and coronal orientation. Lesions are indicated with green arrows.

showed that 1 mm thick images were overestimating the volumes significantly more for smaller lesions than larger lesions ($p<0.001$, **Figure 2G**). The lesions with volumes less than 0.25 mm^3 were overestimated by 2-fold when using 1 mm slice thickness, but gradually converged to similar volumes for the lesions of volume > 1 mm^3. A Bland-Altman analysis of differences and agreement between the volumes showed that majority of lesion volumes were well within the lines of agreement (**Figure 2H**).

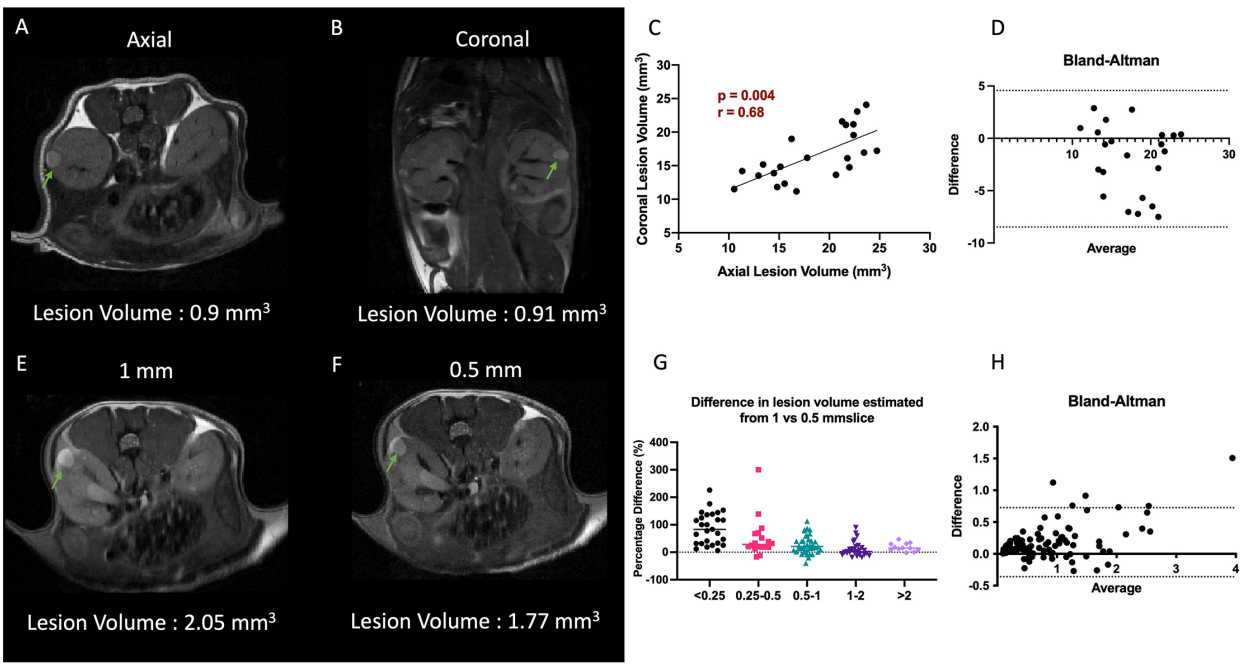

FIGURE 2 | Impact of slice orientation and thickness on volume estimation. **(A, B)** Representative T_2-weighted axial and coronal images. **(C)** Comparison of axial vs coronal slice orientation and its effect on the tumor volume estimation. **(D)** Bland-Altman plot of differences and averages from axial and coronal lesion volumes. **(E, F)** Representative T_2-weighted 1 mm and 0.5 mm slice thickness images. Lesions are highlighted with arrows. **(G)** Decrease in difference of volumes of lesion estimated from 0.5 and 1 mm thick slices as function of lesion volume. **(H)** Bland-Altman plot of differences and averages of lesion volumes from 1 mm and 0.5 mm thick images. Lesions are indicated with green arrows.

We further investigated whether 3-dimensional acquisition would have better sensitivity in detecting the smaller lesions. To do this we compared the SNR and acquisition time between 2D and 3D images acquired with 0.5 mm slice thickness equivalents. Representative 2D and 3D images with 0.5 mm slice thickness are shown in **Figure S1A**. **Figure S1B** lists the total acquisition time, signal to noise and contrast to noise ratio for 2D and 3D images. For the resolution that is required to detect small lesions, the 3D images took significantly more time and resulted in similar SNR and CNR compared to 2D. It is important to note that repetition time for 3D images was lower at 200 ms. The lesion volumes from 0.5 mm slice thickness images ranged between 1 – 3.1 mm^3. The Pearson correlation analysis of the tumor volumes estimated from 2D versus 3D sequences showed a significantly positive correlation (**Figure S1C**). No additional lesions were observed in 3D acquisition images that was not present in the 2D acquisition images.

Baseline Characterization of Diffusion and Perfusion Imaging

The mean ADC of lesions at baseline was 0.0019 ± 0.0006 mm^2/s with the values ranging from 0.0007 to 0.0033. The smallest lesion for which we were able to calculate the ADC was 0.61 mm^3. A histogram analysis of the values is given in **Figure S2**. The majority of the lesions (~73%) had ADC values higher than 0.0018 mm^2/s. We observed no correlation between baseline ADC and lesion volumes or normalized T_2 intensities (data not shown).

DCE analysis was performed on three mice at baseline and 21 lesions in total were identified. Two lesions representing the range of DCE parameters are shown in **Figure 3**. These selected lesions show the two distinct dynamic curves of the contrast agent and the corresponding physiological parameters and the mean and standard deviations of all the quantitative and semiquantitative parameters obtained of the representative lesions are tabulated in **Figure 3**. As shown in **Figure 3**, lesion 1 with higher volume had much slower wash-in of Gd-DTPA and peak concentration, compared to lesion 2 which showed a faster accumulation of the contrast agent and higher peak concentration. Lesion 2 also had faster wash-out and higher K^{trans}, i.e., permeability. The concentration maps overlaid on the lesions show the lack of contrast agent build-up within the center of lesion 1. Lesion 1 with higher ADC of 0.0022 mm^2/s had a significantly lower accumulation of the contrast agent as compared to lesion 2 with ADC of 0.0016 mm^2/s which showed a rapid uptake and washout of the contrast agent. The concentration curves of all the individual lesions are shown in **Figure S3**.

Clear patterns of perfusion parameters were visible in the different manifestations of cyst and cystadenomas in concordance

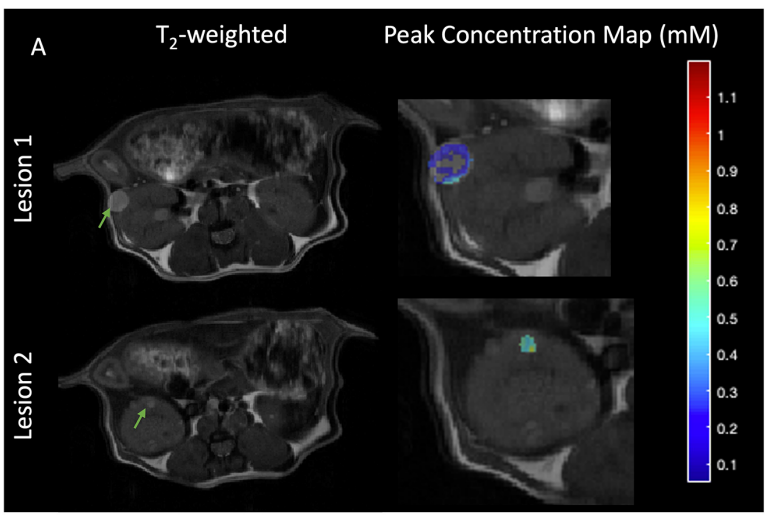

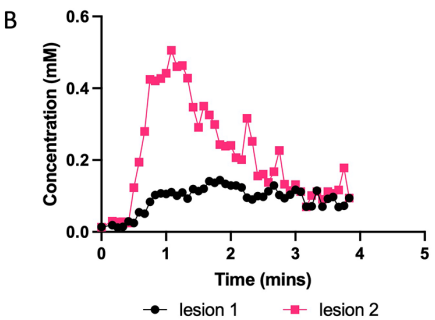

Parameter	Lesion 1	Lesion 2
Volume (mm^3)	5.12	0.625
ADC (mm^2/s)	0.0022	0.0016
T_2 intensity	11.13	8.68
Ktrans (min^{-1})	0.055	0.27
iAUC (mM)	1.95	6.38
Wash-out (10^{-2} mM/min)	-0.25	-0.13
Wash-in (mM/min)	0.52	1.74
Peak Concentration (mM)	0.5	0.14

FIGURE 3 | Representative cystic and cellular lesions and their baseline properties. **(A)** Representative T_2-weighted and magnevist peak concentration maps. **(B)** Dynamic curves of magnevist concentration from two lesions. Table with physiological and DCE parameters for the lesions. Lesions are indicated with green arrows.

with other imaging parameters. Correlation analysis showed that lesions with larger volumes had significantly lower K^{trans} (**Figure 4A**), slower washout (**Figure 4D**), lower iAUC (**Figure 4G**) and peak concentration (**Figure 4H**) indicating perfusion-impaired lesions. K^{trans} was also found to be significantly lower for lesions with higher ADCs (**Figure 4B**) and T_2 intensities (**Figure 4C**), representative of more cystic lesions (19). Washout was significantly faster for lesions with lower ADCs (**Figure 4E**) and T_2 intensities (**Figure 4F**) indicating solid adenomas (20). All the remaining correlations are shown in **Figure S4**. Lesions with larger volume and higher T_2 intensity had slower wash-in of Gd-DTPA although not significant. DCE-MRI enhancement pattern has been used to differentiate between truly cystic (no internal enhancement) and soft-tissue lesions (some internal enhancement). Lesion 1 in **Figure 3** is indicative of a cystic lesion.

Lesions with larger tumor volumes demonstrated much lower enhancement and permeability compared to smaller lesions. Lesions with higher ADCs and normalized T_2 intensities had lower permeability and slower clearance of contrast agent representative of cystic lesions. It was observed that lesions with slower clearance also had slower uptake of the contrast agent, although this trend was not significant.

Response of TSC Lesions to Treatment

We evaluated the changes in tumor volume to measure the effect of everolimus on *Tsc2*$^{+/-}$ mice. First, we compared the changes in total tumor burden from baseline in the two groups, everolimus-treated and untreated controls. On average it was observed that the tumors of mice treated with everolimus, after the initial increase in volume in the first week, did not demonstrate any further significant change in total tumor burden over the remaining three weeks (increased by 36 ± 20% by week 1, 39 ± 12% by week 2 and 39 ± 06% by week 4 compared to baseline) (**Figure 5A**). In contrast, tumors of mice in the control group increased in volume week over week (28 ± 23% by week 1, 62 ± 57% by week 2 and 71 ± 40% by week 4 compared to baseline). Mice treated with everolimus demonstrated a deceleration in total tumor burden compared to control, although a two-way ANOVA analysis showed that it was not statistically significant.

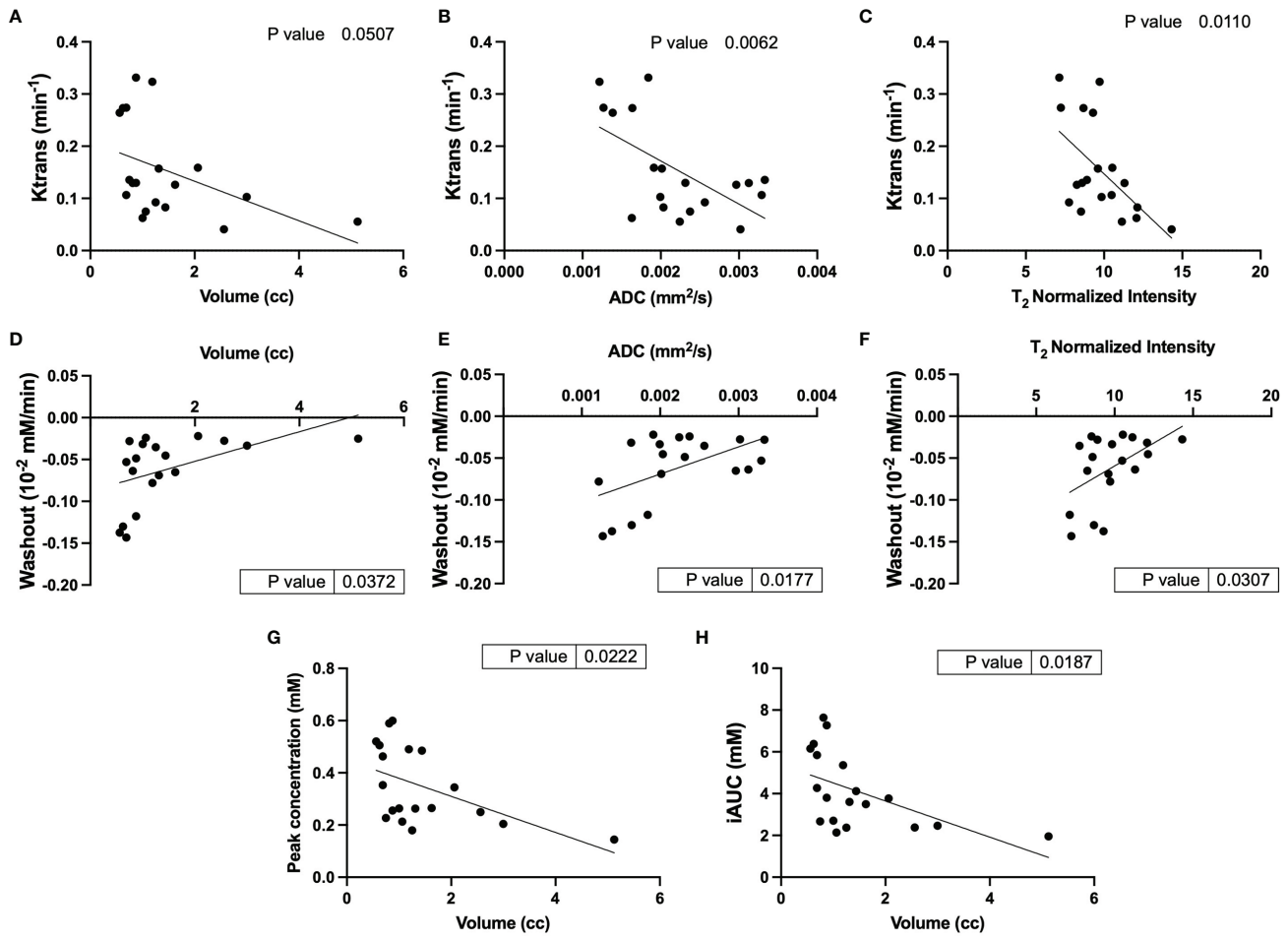

FIGURE 4 | Correlational analysis of quantitative and semi-quantitative DCE parameters and physiological parameters. Correlation of Ktrans with **(A)** volume, **(B)** ADC and **(C)** T2 normalized intensity; Washout correlated to **(D)** volume, **(E)** ADC and **(F)** T2 normalized intensity; and volume correlation with **(G)** peak concentration and **(H)** iAUC.

Supplementary Figure S5 demonstrates a representative example of change in volume for control and treated lesions and individual tumor burdens.

Mean tumor ADCs (**Figure 5B**) of treated mice increased over baseline at week 3 (2.3 ± 0.5 x 10^{-3} mm^2/s) while tumors in control mice either showed a decrease or maintained similar mean ADCs as baseline (1.95 ± 0.7 x 10^{-3} mm^2/s). One-way ANOVA analysis showed that ADCs were significantly different for treated cohort ($p<0.001$), and *post hoc* comparison showed that baseline ADC was lower than all the later time points ($p<0.01$). **Figure 5C** demonstrates a representative example of change in ADC for control and treated lesions. Increase in ADC for the treated lesion was observed whereas in control lesion a decrease in ADC was observed.

Closer analysis of the changes in lesions over time using linear mixed model analysis demonstrated a slight difference in the rates of change in ADC ($p = 0.0836$) and volumes ($p = 0.0898$), where ADC slightly increased and volumes slightly decreased for treated tumor while ADC slightly decreased, and volume slightly increased for control tumors (**Figure S6A, B**). **Figure S6C** shows the changes in T_1 in control and treated mice. We observed an increase in T_1 at week 3 (3.2 ± 0.85 secs) from baseline (2.97 ± 0.21 secs) in control mice and a decrease in T_1 of treated mice at week 3 (2.16 ± 0.9 secs) from baseline (2.63 ± 0.4 secs). Treated and control tumors showed statistically significant differential changes in T_1 ($p = 0.0495$), with treated tumors significantly decreasing (-0.0058/day) and control tumors significantly increasing (.0276/day) ($p = 0.0272$).

Normalized T_2 intensity changes showed opposite trends for control and treated mice. In control mice the intensities at week 1 (10.2 ± 2.5) was slightly higher than baseline (9.75 ± 1.4, **Figure S6D**). Following week 1 the intensities decreased to 8.6 ± 1 by week 2 and to 7.5 ± 0.8 by week 3. In treated mice the intensities increased slightly from 10.1 ± 1.6 at baseline to 11 ± 3.5 at week 1. Following week 1 the intensities increased to 12.6 ± 0.4 at week 3. Treated and control tumors showed statistically significant differential changes in T_2 intensities ($p = 0.0004$), with treated tumors significantly increasing (0.0841/day) and control tumors significantly decreasing

(-0.1058/day) ($p = 0.0084$).

This implies that with everolimus treatment the lesions had increased cystic characteristics and lesions in control group had higher cellular component. Studies have shown that papillary lesions tend to be hypointense (21) on T_2-weighted images as compared to cystic lesions (22).

Immunohistochemical Analysis of Lesions

We observed cystic, papillary, and solid lesions in kidneys stained with H&E for both treated and control cohort (**Figure 6**). We imaged left kidneys for all the 6 mice and

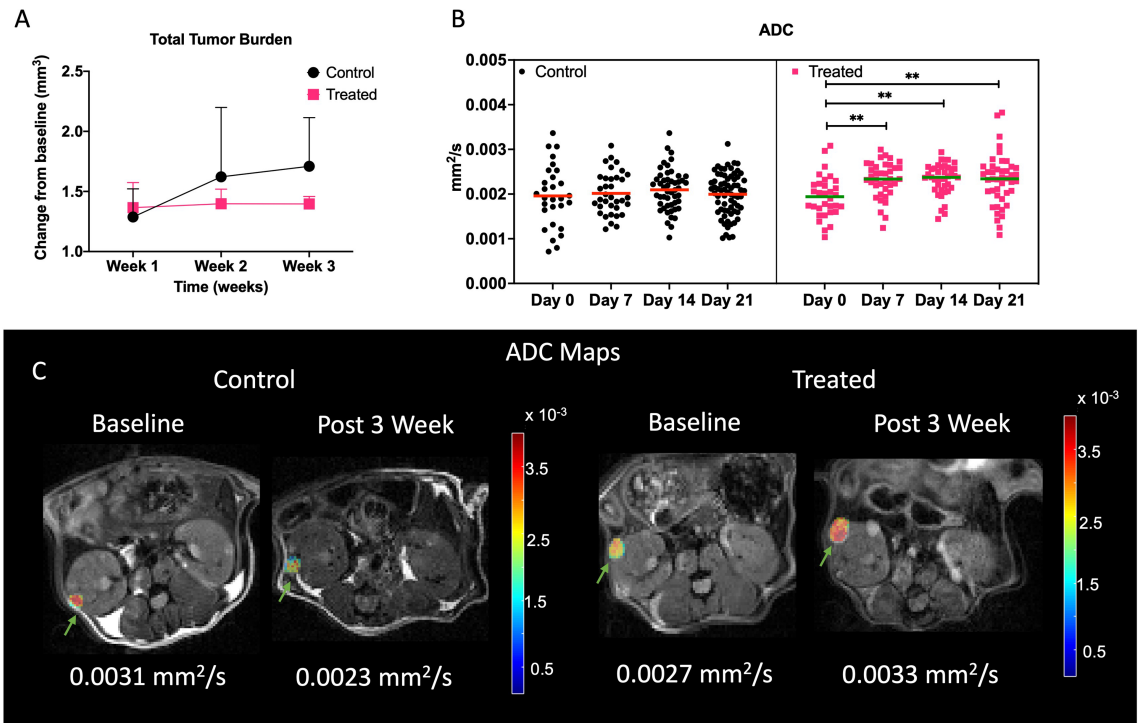

FIGURE 5 | Impact of treatment on physiological properties of lesions. **(A)** Lesion volume change with respect to baseline in control and treated mice. **(B)** Mean ADC of all the lesions in control and treated cohort over time. Representative ADC maps overlaid on diffusion weighted imaged at b = 25 s/mm^2 at baseline and week 3 for control and treated tumors **(C)**. Lesions are indicated with green arrows. ** indicates $p<0.01$

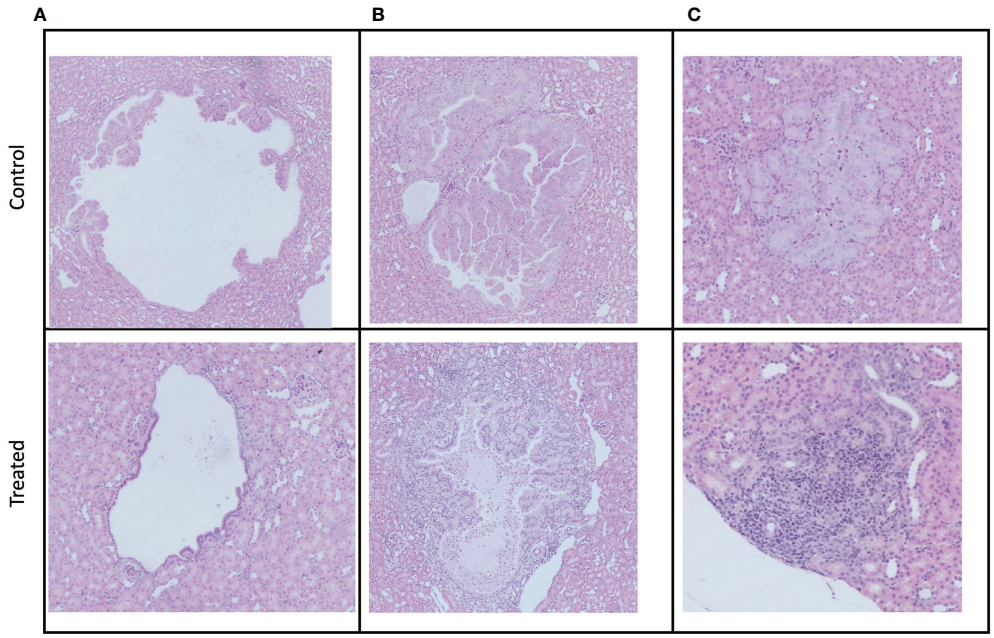

FIGURE 6 | Examples of the three different manifestations of kidney cystadenomas in control and treated mice. Tumors were harvested after week 3 imaging. All pictures were taken at a 10× magnification. **(A)** Cystic lesions. **(B)** Papillary lesions. **(C)** Solid lesions.

observed 26 cystic, 8 papillary and 9 solid lesions in control mice compared to 21 cystic, 2 papillary and 2 solid lesions in everolimus-treated mice. On average we observed more cystic lesions per kidney in treated mice (90% of total lesions) compared to control (61% of total lesions). Concomitantly, there were fewer solid lesions in the treated group. In control mice, we observed a similar distribution of solid (n = 9) and papillary lesions (n = 8) (figure not shown). We also examined the expression of Ki67 proliferation marker and histology by H&E staining to measure the cellularity of lesions. **Figure 7** shows the 40x magnification image of solid lesions stained with H&E and Ki67 antibody from treated and control groups. Qualitatively, we observed higher cellularity and proliferation in the control lesion in comparison to treated.

DISCUSSION

TSC is a lifelong disorder that affects approximately 2 million people worldwide (1). Although the majority of patients have a near-normal lifespan, the disease can cause high morbidity, decreased quality of life and mortality in 5-8% of patients (17). While the clinical manifestations of this disease vary among individuals, renal manifestations are one of the leading causes of deaths. Limited treatment options are available to patients with renal manifestations and primarily involve therapy with mTOR inhibitors and percutaneous embolization if bleeding is a risk (7). Patients must undergo lifelong therapy with surveillance as the preferred method for managing the disease in these patients (2).

The *Tsc2*$^{+/-}$ mouse model is known to have cystic disease starting from 6-12 months of age (9, 10, 18). In our study, we observed multiple lesions in both kidneys in 6–7-month-old mice. The lesions are termed cystadenomas and exhibit a spectrum of phenotypes, from pure cysts to cysts with papillary projections to solid adenomas. We observed similar phenotypes as demonstrated in the histopathological examination of lesions in the mice studied (**Figure 7**).

Our study identified optimal MR parameters for studying the size, distribution, and physiological properties of TSC lesions including cellularity, perfusion, and diffusion. In this work, MRI was shown to be an efficient modality for robustly identifying cysts as well as cystadenomas in 6-7-month-old *Tsc2*$^{+/-}$ mice. We observed good SNR and image quality for all scans. While we did not implement respiratory gating, we recognize that it might help eliminate motion artifacts and facilitate obtaining images with even higher SNR, especially considering the use of the vertical bore microimaging scanner used in this work. Similar to prior studies, T2-weighted images were used to localize the lesions which appeared as hyperintense regions indicative of a cystadenoma phenotype (23, 24). Woodrum et al. (10) observed an average of 13.00 ± 4.28 lesions/kidney in 5-month-old mice from IHC sections, while in our study we observed 18 ± 2.8 lesions/kidney. The slightly higher count could arise from the lesion count being performed only every 1mm in the tumor using IHC compared to the entire kidney region of the MRI images in our study.

Since change in lesion volumes is the main indicator of therapeutic response (RECIST criteria) it is critical to capture the distribution and size of lesions reliably. A 2D T_2-weighted

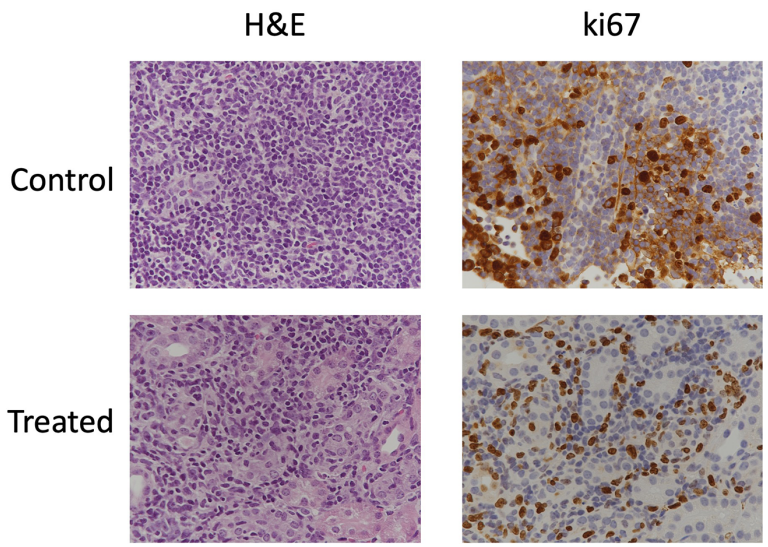

FIGURE 7 | Immunohistochemical stains of cellularity (H&E) and proliferation (Ki67) in solid lesions in control and treated mice.

imaging sequence with a smaller slice thickness of 0.5 mm at either axial or coronal orientation was found to be optimal. Although theoretically (based on 0.5 mm slice thickness) lesions of 0.0055 mm^3 volume should be detectable, 0.016 mm^3, the smallest lesion detectable in our study, could very well represent our detection limits based on observer performance.

Determining the composition of kidney lesions is critical in understanding the phenotype and morphology of lesions. AMLs are prone to bleeding as they increase in size. Techniques such as ADC and DCE measurements can provide us with information regarding cellularity and perfusion/permeability of the lesions. As seen in IHC images, the lesions differ in cellular composition. We observed that based on ADC values (**Figure S2**), the cysts being defined as those lesions with ADC > 0.0022 mm^2/s (25) comprised 19 out of 61 lesions, i.e., 31% were found to be cystic at baseline. Taouli et al. (26) measured the ADC of renal cell carcinoma (RCC) and benign lesions in kidney and found RCC to have a significantly lower ADC of 0.0014 mm^2/s than the benign lesions. They also showed that papillary RCC had lower ADC of 0.0012 mm^2/s than non-papillary RCC (0.0016 mm^2/s). Based on the same metrics 15% of the lesions in the mice are indicative of papillary phenotype. The proportion of the cystic to papillary lesions as characterized by ADC seems higher than that estimated by histopathology (10). This indicates that a more thorough correlation of MRI characteristics with histological assessment is necessary to better interpret the imaging findings, which is beyond the scope of this study.

Prior studies have shown the utility of quantitative and semi-quantitative DCE-MRI parameters as imaging biomarkers for assessing tumor aggressiveness and predicting response to therapy. We captured distinct kinetics of the contrast agent in different lesions (**Figure 4** and **S3**). We also observed that lesions with higher ADC similar to lesion 1 had significantly lower contrast agent accumulation in the center of the lesions, demonstrating limited perfusion towards the center of the lesion characteristic of cystic lesions (19, 25). Tumors with higher K^{trans} have been associated with better response to treatment (27, 28), as this indicates higher permeability and results in efficient delivery of therapeutic drug. Congruent to this we observed a lesion (not shown) with lower K^{trans} of 0.04 (baseline) that increased in volume from 2.5 mm^3 to 4 mm^3 after everolimus therapy. Conversely, a lesion with K^{trans} of 0.33 (baseline) decreased in volume from 1.5 mm^3 to 0.8 mm^3 after everolimus therapy. A study by Sun et al. (29) showed that differences in signal intensity as a response to contrast agent can also differentiate between clear cell and papillary RCCs, with clear cell RCC showing higher signal intensity change. Everolimus has been reported in previous studies to have anti-angiogenic effects (30, 31) and thus implementation of DCE-MRI in the standard imaging protocol for TSC will be critical in evaluating its activity.

Only three mice were imaged at baseline with DCE MRI in this study. Due to the loss of several mice early on during DCE imaging, this scan was omitted from our study at later time points. This could be due to impaired kidney function complicated by repeated contrast agent administration. Further studies are required to validate this theory. Treatment-induced changes in perfusion are critical to assess therapeutic efficacy and in future studies DCE MRI will be implemented for the entire course of imaging. Pharmacokinetic DCE-MRI has been increasingly applied in quantitative scientific research and clinical practice as studies have shown the utility of DCE-MRI parameters to predict the efficacy of chemotherapy (32) and to image activity of anti-angiogenic drugs (33, 34) noninvasively.

Analysis of baseline imaging characteristics demonstrates the importance of interpreting the lesion morphology for accurate scoring of disease. Therapeutic response is mostly measured by the change in lesion size, but other factors such as change in

cellularity, signal intensity and vascularization/perfusion could also aid in early prediction of therapeutic efficacy.

Studies of *Tsc2*$^{+/-}$ and other mouse models treated with rapamycin (an FDA-approved macrolide antibiotic that acts to inhibit the mTOR pathway, and analogs) have shown the ability to restore dysregulated mTOR signaling in cells with abnormal TSC1 and/or TSC2 (5, 10, 24, 35). However, these studies were disadvantaged by the lack of imaging follow-up to evaluate response over time to potentially adapt the therapeutic regimen and obtain an earlier assessment. We observed a 70% increase in total tumor burden in control mice from baseline over a 3-week period. On the other hand, the tumor burden in everolimus-treated mice increased by approximately 37% after one week of therapy and maintained that tumor burden for the remaining two weeks of therapy. This seems to indicate that after the initial effect, the drug might play more of a maintenance role in suppressing the mTORC1 pathway. Pollizzi et al. (36) observed a 7-fold reduction in tumor burden in *Tsc2*$^{+/-}$ mice treated with N-ethyl-N-nitrosourea to increase the incidence and severity of renal lesions after treating with 10 mg/kg everolimus PO QD (5/7 days per week). Of note, the age of mice in the study by Pollizzi et al. was 20 months, perhaps relevant to the lesser magnitude of change in the younger mice in our study.

In another study, treatment of A/J *Tsc2*$^{+/-}$ mice (9 months old) with 8 mg/kg of rapamycin weekly for 12 weeks, or daily for 4 weeks and weekly for another 8 weeks, had similar effects in reducing tumor burden (~80%) indicating that duration of treatment is more important than dose in eliciting a significant response (10). Interestingly, everolimus treatment in patients showed a significant decrease in AML after 3 months of treatment and a higher reduction upon 3-6 months of treatment (37). Thus, while we observed modest changes over 3 weeks of treatment in our study, continued treatment with everolimus could have resulted in a higher decrease in tumor burden, considering that our treatment was also initiated in younger mice than in prior studies. It is important to note that studies have shown that, in *Tsc2*$^{+/-}$ mice, therapeutic intervention demonstrates reduction in tumor volumes, but the cessation of therapy results in recovery of tumor growth (10, 14, 35), highlighting the importance of prolonged treatment and monitoring. As stated earlier, this was a pilot study evaluating the feasibility of incorporating mp-MRI for studying disease progression and treatment response in this transgenic mouse model. The sample size for this study was low and for future studies a larger cohort of mice per cohort should be evaluated. We recommend exploring different dosing range and schedule in TSC models with a larger sample size to determine the optimum dosage of everolimus to observe significant change in tumor volume.

In addition to tumor volume changes, the gold standard of response criteria, we investigated if mpMRI, such as ADC, T_2 weighted intensity and T_1, could inform on therapeutic efficacy earlier. Normalized T_2 intensity can be a useful measure for understanding the composition of a tumor. Studies have shown that different types of renal lesions show different signal properties. For example, lesions with fluid, edema, or impaired blood flow will appear hyperintense on a T_2 weighted image (21). In our study, we observed a decrease in T_2 intensity in control mice and an increase in everolimus-treated mice. This difference was even more significant when examined on a lesion-specific basis over time. We believe that this could be due to the anti-angiogenic effect of everolimus. In contrast, the lesions in control mice could become more cellular as they proliferate. The ADC changes in both the groups seem to validate this hypothesis, as we observed an increase in mean ADC post-everolimus treatment and a decrease in control mice. This demonstrates a decrease in cellularity, a hallmark of treatment efficacy (38). While ADC could provide an earlier indicator than volume changes, we were limited by the number of lesions we could track over time in our study. Diffusion weighted images were acquired at 1 mm slice thickness which could have resulted in our sequences not capturing lesions that were less than 0.5 mm in diameter after therapy. Interestingly, we observed three lesions that had resolved entirely after three weeks of therapy only in everolimus-treated mice. T_1 relaxation times have been shown to be an unreliable metric for differentiating between the types of lesions (39). The change in T_1 (ΔT_1) on the other hand has been shown to indicate response to therapy (40). That study showed that everolimus-treated (10 mg/kg for 7 days) RIF-1 fibrosarcoma- and B16/BL6 melanoma- bearing mice showed significant decreases in T_1 post-therapy. We observed a similar trend in our everolimus-treated mice, indicating that ΔT_1 can be a highly sensitive predictor of response to treatment.

Histopathological analysis of lesions after 3 weeks of treatment showed characteristic renal cystadenomas in both everolimus-treated and control mice (**Figure 7**). A higher percentage of papillary lesions (18%) and solid lesions (21%) was found in control kidney as compared to 8% of papillary and solid lesions in everolimus -treated kidney. A significantly lower tumor burden from papillary and solid cystadenomas in treated mice seems to indicate a specific everolimus effect on these adenomas. Auricchio et al. showed that the cystic lesions in rapamycin-treated mice had distinct reduction in cyst-lining cells as compared to control mice (12). In our study, too, we observed in the IHC images that cystic lesions of treated mice had a thinner lining of cells as compared to that in control mice (**Figure 7**). A more comprehensive analysis of IHC images and correlation with MR images at baseline would be invaluable in assessing specific effects of therapy on these different lesions non-invasively over time and useful for development of combinatorial targeted therapy.

A qualitative comparison of cellularity and proliferation from IHC images between solid cysts from both the cohorts showed higher cellularity and proliferation in control mice. In future, quantitative analysis of these IHC parameters along with ADC and tumor volume could provide better assessment of treatment response and mechanism of drug action. Evaluation of IHC markers associated with mTORC1 such as phospho-S6 (pS6), hypoxia-inducible factors (HIFs) and vascular endothelial growth factors (VEGFs) can inform upon the efficacy of its inhibition. Expression of pS6, HIF and VEGF are upregulated in Tsc2+/- models and studies have shown their reduction after treatment with mTOR inhibitors (30, 36, 41–43).

Previous studies have shown that combination treatments such as sorafenib and mTOR pathway inhibitors are also effective

in *Tsc2*$^{+/-}$ mouse models (10, 14, 24, 36). The utility of mp_MRI in evaluating cancer models such as renal cancer (44, 45), prostate cancer (46) and breast cancer (47) have been reported before. Future preclinical studies using *Tsc2*$^{+/-}$ and other TSC mouse models with mpMRI offer a rational approach to improving medical therapy for TSC-related tumors and other manifestations of TSC.

CONCLUSION

There is a critical need for development of non-invasive imaging strategies for TSC-derived tumor lesions to monitor the progression and relapse of the disease upon treatment. The current study shows the ability of multiparametric ^{1}H MRI in providing vital information regarding the tumor's characteristics non-invasively, thus allowing for a dynamic evaluation of the disease progression and treatment response. Our results show that high resolution 2D T_2-weighted images with thinner (0.5 mm) slice thickness can be used to capture tumor growth robustly. ADC maps showed that cellularity of tumor lesions with diameter less than 0.75 mm in size can be evaluated and can also be used to investigate the changes in cellularity as a response to therapy. Our study has laid the groundwork to use non-invasiveMRI to characterize the various renal manifestations of TSC and can be used to evaluate response to therapy since different lesions might respond differently to different treatments and can ultimately help tailor therapy.

DATA AVAILABILITY STATEMENT

The original contributions presented in the study are included in the article/**Supplementary Material**. Further inquiries can be directed to the corresponding author.

ETHICS STATEMENT

The animal study was reviewed and approved by UCSF IACUC.

AUTHOR CONTRIBUTIONS

SA performed the experiments, data analysis and drafted and edited the manuscript. ED-B assisted in performing imaging of mice and data analysis. Y-HW assisted in dosing and experiments. RDS performed the IHC staining of kidneys. HQ assisted in DCE modeling, statistical analysis as well as in critical evaluation. ME provided funding, critical guidance for the experiments and manuscript. RS provided funding, experimental/study design, critical guidance for the experiments, and was responsible for supervising the execution of the study, writing and editing of the manuscript. All authors have read and approved the final manuscript.

FUNDING

ME was supported by the American Cancer Society (30635-RSG-17-005-01-CCE) and a pilot grant from the LAM Foundation (LAM0143P01-20).

ACKNOWLEDGMENTS

We would like to thank the TSC Alliance® Preclinical Consortium for providing the Tsc2+/- transgenic mice.

SUPPLEMENTARY MATERIAL

The Supplementary Material for this article can be found online at: https://www.frontiersin.org/articles/10.3389/fonc.2022.851192/full#supplementary-material

Supplementary Figure 1 | Comparison between lesions captured *via* 2D and 3D image acquisition. **(A)** Representative 2D and 3D images of the kidney acquired at 0.5 mm slice thickness. Lesions are indicated with green arrows. **(B)** Comparison between image quality of 2D and 3D images. **(C)** Comparison of 2D vs 3D at 0.5 mm slice thickness lesion volumes.

Supplementary Figure 2 | Histogram analysis of ADC values of lesions at baseline.

Supplementary Figure 3 | Dynamic curves of contrast agent concentration in all the lesions at baseline.

Supplementary Figure 4 | Correlational analysis of DCE parameters and physiological parameters.

Supplementary Figure 5 | Representative T_2-weighted images of lesions at baseline and week 3 for control and treated tumors. Lesions are indicated with green arrows. Line graphs showing individual tumor burdens for untreated control and Everolimus treated mice.

Supplementary Figure 6 | Lesion-wise changes in **(A)** ADC **(B)** volumes, **(C)** T_1 and **(D)** normalized T_2 intensity of control and treated mice.

REFERENCES

1. Amin S, Lux A, Calder N, Laugharne M, Osborne J, O'callaghan F. Causes of Mortality in Individuals With Tuberous Sclerosis Complex. *Dev Med Child Neurol* (2017) 59:612–7. doi: 10.1111/dmcn.13352
2. Henske EP, Jóźwiak S, Kingswood JC, Sampson JR, Thiele EA. Tuberous Sclerosis Complex. *Nat Rev Dis Primers* (2016) 2:16035. doi: 10.1038/nrdp.2016.35
3. Bissler JJ, Kingswood JC. Renal Manifestation of Tuberous Sclerosis Complex. *Am J Med Genet Part C: Semin Med Genet* (2018) 178:338–47. doi: 10.1002/ajmg.c.31654
4. Schrier RW, Abebe KZ, Perrone RD, Torres VE, Braun WE, Steinman TI, et al. Blood Pressure in Early Autosomal Dominant Polycystic Kidney Disease. *N Engl J Med* (2014) 371:2255–66. doi: 10.1056/NEJMoa1402685
5. Siroky BJ, Towbin AJ, Trout AT, Schäfer H, Thamann AR, Agricola KD, et al. Improvement in Renal Cystic Disease of Tuberous Sclerosis Complex After

Treatment With Mammalian Target of Rapamycin Inhibitor. *J Pediatr* (2017) 187:318–322.e2. doi: 10.1016/j.jpeds.2017.05.015
6. Samuels JA. Treatment of Renal Angiomyolipoma and Other Hamartomas in Patients With Tuberous Sclerosis Complex. *CJASN* (2017) 12:1196–202. doi: 10.2215/CJN.08150816
7. Krueger DA, Northrup H, Northrup H, Krueger DA, Roberds S, Smith K, et al. Tuberous Sclerosis Complex Surveillance and Management: Recommendations of the 2012 International Tuberous Sclerosis Complex Consensus Conference. *Pediatr Neurol* (2013) 49:255–65. doi: 10.1016/j.pediatrneurol.2013.08.002
8. Kingswood JC, Bissler JJ, Budde K, Hulbert J, Guay-Woodford L, Sampson JR, et al. Review of the Tuberous Sclerosis Renal Guidelines From the 2012 Consensus Conference: Current Data and Future Study. *Nephron* (2016) 134:51–8. doi: 10.1159/000448293
9. Onda H, Lueck A, Marks PW, Warren HB, Kwiatkowski DJ. Tsc2+/– Mice Develop Tumors in Multiple Sites That Express Gelsolin and are Influenced by Genetic Background. *J Clin Invest* (1999) 104:687–95. doi: 10.1172/JCI7319
10. Woodrum C, Nobil A, Dabora SL. Comparison of Three Rapamycin Dosing Schedules in a/J Tsc2+/- Mice and Improved Survival With Angiogenesis Inhibitor or Asparaginase Treatment in Mice With Subcutaneous Tuberous Sclerosis Related Tumors. *J Transl Med* (2010) 8:14. doi: 10.1186/1479-5876-8-14
11. Kwiatkowski DJ. Animal Models of Lymphangioleiomyomatosis (LAM) and Tuberous Sclerosis Complex (TSC). *Lymphatic Res Biol* (2010) 8:51–7. doi: 10.1089/lrb.2009.0013
12. Auricchio N, Malinowska I, Shaw R, Manning BD, Kwiatkowski DJ. Therapeutic Trial of Metformin and Bortezomib in a Mouse Model of Tuberous Sclerosis Complex (TSC). *PloS One* (2012) 7:e31900. doi: 10.1371/journal.pone.0031900
13. Messina MP, Rauktys A, Lee L, Dabora SL. Tuberous Sclerosis Preclinical Studies: Timing of Treatment, Combination of a Rapamycin Analog (CCI-779) and Interferon-Gamma, and Comparison of Rapamycin to CCI-779. *BMC Pharmacol* (2007) 7:14. doi: 10.1186/1471-2210-7-14
14. Guo Y, Kwiatkowski DJ. Equivalent Benefit of Rapamycin and a Potent mTOR ATP-Competitive Inhibitor, MLN0128 (INK128), in a Mouse Model of Tuberous Sclerosis. *Mol Cancer Res* (2013) 11:467–73. doi: 10.1158/1541-7786.MCR-12-0605
15. Sriram R, Gordon J, Baligand C, Ahamed F, Delos Santos J, Qin H, et al. Non-Invasive Assessment of Lactate Production and Compartmentalization in Renal Cell Carcinomas Using Hyperpolarized 13c Pyruvate MRI. *Cancers* (2018) 10:313. doi: 10.3390/cancers10090313
16. Qin H, Zhang V, Bok RA, Santos RD, Cunha JA, Hsu I-C, et al. Simultaneous Metabolic and Perfusion Imaging Using Hyperpolarized 13c MRI Can Evaluate Early and Dose-Dependent Response to Radiation Therapy in a Prostate Cancer Mouse Model. *Int J Radiat Oncol Biol Phys* (2020) 107:887–96. doi: 10.1016/j.ijrobp.2020.04.022
17. Zöllner JP, Franz DN, Hertzberg C, Nabbout R, Rosenow F, Sauter M, et al. A Systematic Review on the Burden of Illness in Individuals With Tuberous Sclerosis Complex (TSC). *Orphanet J Rare Dis* (2020) 15:23. doi: 10.1186/s13023-019-1258-3
18. Finlay GA, Malhowski AJ, Polizzi K, Malinowska-Kolodziej I, Kwiatkowski DJ. Renal and Liver Tumors in *Tsc2* $^{+/-}$ Mice, a Model of Tuberous Sclerosis Complex, do Not Respond to Treatment With Atorvastatin, a 3-Hydroxy-3-Methylglutaryl Coenzyme A Reductase Inhibitor. *Mol Cancer Ther* (2009) 8:1799–807. doi: 10.1158/1535-7163.MCT-09-0055
19. Israel GM, Bosniak MA. MR Imaging of Cystic Renal Masses. *Magnet Resonance Imaging Clinics* (2004) 12:403–12. doi: 10.1016/j.mric.2004.03.006
20. van Oostenbrugge TJ, Fütterer JJ, Mulders PFA. Diagnostic Imaging for Solid Renal Tumors: A Pictorial Review. *Kidney Cancer* (2018) 2:79–93. doi: 10.3233/KCA-180028
21. Oliva MR, Glickman JN, Zou KH, Teo SY, Mortelé KJ, Rocha MS, et al. Renal Cell Carcinoma: T1 and T2 Signal Intensity Characteristics of Papillary and Clear Cell Types Correlated With Pathology. *Am J Roentgenol* (2009) 192:1524–30. doi: 10.2214/AJR.08.1727
22. Schieda N, Lim RS, McInnes MDF, Thomassin I, Renard-Penna R, Tavolaro S, et al. Characterization of Small (<4cm) Solid Renal Masses by Computed Tomography and Magnetic Resonance Imaging: Current Evidence and Further Development. *Diagn Intervent Imaging* (2018) 99:443–55. doi: 10.1016/j.diii.2018.03.004
23. Brown AB, Mahmood U, Cortes ML, Tang Y, Dai G, Stemmer-Rachamimov A, et al. Magnetic Resonance Imaging and Characterization of Spontaneous Lesions in a Transgenic Mouse Model of Tuberous Sclerosis as a Model for Endothelial Cell-Based Transgene Delivery. *Hum Gene Ther* (2005) 16:1367–76. doi: 10.1089/hum.2005.16.1367
24. Lee L, Sudentas P, Donohue B, Asrican K, Worku A, Walker V, et al. Efficacy of a Rapamycin Analog (CCI-779) and IFN-Gamma in Tuberous Sclerosis Mouse Models. *Genes Chromosomes Cancer* (2005) 42:213–27. doi: 10.1002/gcc.20118
25. Balyemez F, Aslan A, Inan I, Ayaz E, Karagöz V, Özkanlı SŞ, et al. Diffusion-Weighted Magnetic Resonance Imaging in Cystic Renal Masses. *CUAJ* (2017) 11:8. doi: 10.5489/cuaj.3888
26. Taouli B, Thakur RK, Mannelli L, Babb JS, Kim S, Hecht EM, et al. Renal Lesions: Characterization With Diffusion-Weighted Imaging Versus Contrast-Enhanced MR Imaging. *Radiology* (2009) 251:398–407. doi: 10.1148/radiol.2512080880
27. George ML, Dzik-Jurasz ASK, Padhani AR, Brown G, Tait DM, Eccles SA, et al. Non-Invasive Methods of Assessing Angiogenesis and Their Value in Predicting Response to Treatment in Colorectal Cancer. *Br J Surg* (2002) 88:1628–36. doi: 10.1046/j.0007-1323.2001.01947.x
28. Reynolds HM, Parameswaran BK, Finnegan ME, Roettger D, Lau E, Kron T, et al. Diffusion Weighted and Dynamic Contrast Enhanced MRI as an Imaging Biomarker for Stereotactic Ablative Body Radiotherapy (SABR) of Primary Renal Cell Carcinoma. *PloS One* (2018) 13:e0202387. doi: 10.1371/journal.pone.0202387
29. Sun MRM, Ngo L, Genega EM, Atkins MB, Finn ME, Rofsky NM, et al. Renal Cell Carcinoma: Dynamic Contrast-Enhanced MR Imaging for Differentiation of Tumor Subtypes—Correlation With Pathologic Findings. *Radiology* (2009) 250:793–802. doi: 10.1148/radiol.2503080995
30. Lane HA, Wood JM, McSheehy PMJ, Allegrini PR, Boulay A, Brueggen J, et al. mTOR Inhibitor RAD001 (Everolimus) Has Antiangiogenic/Vascular Properties Distinct From a VEGFR Tyrosine Kinase Inhibitor. *Clin Cancer Res* (2009) 15:1612–22. doi: 10.1158/1078-0432.CCR-08-2057
31. Agarwala SS, Case S. Everolimus (RAD001) in the Treatment of Advanced Renal Cell Carcinoma: A Review. *Oncol* (2010) 15:236–45. doi: 10.1634/theoncologist.2009-0141
32. Hillman GG, Singh-Gupta V, Zhang H, Al-Bashir AK, Katkuri Y, Li M, et al. Dynamic Contrast-Enhanced Magnetic Resonance Imaging of Vascular Changes Induced by Sunitinib in Papillary Renal Cell Carcinoma Xenograft Tumors. *Neoplasia* (2009) 11:910–20. doi: 10.1593/neo.09618
33. Bex A, Fournier L, Lassau N, Mulders P, Nathan P, Oyen WJG, et al. Assessing the Response to Targeted Therapies in Renal Cell Carcinoma: Technical Insights and Practical Considerations. *Eur Urol* (2014) 65:766–77. doi: 10.1016/j.eururo.2013.11.031
34. Rosen MA, Schnall MD. Dynamic Contrast-Enhanced Magnetic Resonance Imaging for Assessing Tumor Vascularity and Vascular Effects of Targeted Therapies in Renal Cell Carcinoma. *Clin Cancer Res* (2007) 13:770s–6s. doi: 10.1158/1078-0432.CCR-06-1921
35. Kenerson H, Dundon TA, Yeung RS. Effects of Rapamycin in the Eker Rat Model of Tuberous Sclerosis Complex. *Pediatr Res* (2005) 57:67–75. doi: 10.1203/01.PDR.0000147727.78571.07
36. Pollizzi K, Malinowska-Kolodziej I, Stumm M, Lane H, Kwiatkowski D. Equivalent Benefit of Mtorc1 Blockade and Combined PI3K-mTOR Blockade in a Mouse Model of Tuberous Sclerosis. *Mol Cancer* (2009) 8:38. doi: 10.1186/1476-4598-8-38
37. Brakemeier S, Vogt L, Adams L, Zukunft B, Diederichs G, Hamm B, et al. Treatment Effect of mTOR-Inhibition on Tissue Composition of Renal Angiomyolipomas in Tuberous Sclerosis Complex (TSC). *PloS One* (2017) 12:e0189132. doi: 10.1371/journal.pone.0189132
38. Fliedner FP, Engel TB, El-Ali HH, Hansen AE, Kjaer A. Diffusion Weighted Magnetic Resonance Imaging (DW-MRI) as a non-Invasive, Tissue Cellularity Marker to Monitor Cancer Treatment Response. *BMC Cancer* (2020) 20:134. doi: 10.1186/s12885-020-6617-x
39. Farraher SW, Jara H, Chang KJ, Ozonoff A, Soto JA. Differentiation of Hepatocellular Carcinoma and Hepatic Metastasis From Cysts and Hemangiomas With Calculated T2 Relaxation Times and the T1/T2

Relaxation Times Ratio. *J Magn Reson Imaging* (2006) 24:1333–41. doi: 10.1002/jmri.20758
40. Weidensteiner C, Allegrini PR, Sticker-Jantscheff M, Romanet V, Ferretti S, McSheehy PM. Tumour T1 Changes *In Vivo* are Highly Predictive of Response to Chemotherapy and Reflect the Number of Viable Tumour Cells – a Preclinical MR Study in Mice. *BMC Cancer* (2014) 14:88. doi: 10.1186/1471-2407-14-88
41. Zhang H, Cicchetti G, Onda H, Koon HB, Asrican K, Bajraszewski N, et al. Loss of Tsc1/Tsc2 Activates mTOR and Disrupts PI3K-Akt Signaling Through Downregulation of PDGFR. *J Clin Invest* (2003) 112:1223–33. doi: 10.1172/JCI200317222
42. Matsuki M, Adachi Y, Ozawa Y, Kimura T, Hoshi T, Okamoto K, et al. Targeting of Tumor Growth and Angiogenesis Underlies the Enhanced Antitumor Activity of Lenvatinib in Combination With Everolimus. *Cancer Sci* (2017) 108:763–71. doi: 10.1111/cas.13169
43. Dodd KM, Yang J, Shen MH, Sampson JR, Tee AR. Mtorc1 Drives HIF-1α and VEGF-A Signalling *via* Multiple Mechanisms Involving 4E-BP1, S6K1 and STAT3. *Oncogene* (2015) 34:2239–50. doi: 10.1038/onc.2014.164
44. Lopes Vendrami C, Parada Villavicencio C, DeJulio TJ, Chatterjee A, Casalino DD, Horowitz JM, et al. Differentiation of Solid Renal Tumors With Multiparametric MR Imaging. *Radiographics* (2017) 37:2026–42. doi: 10.1148/rg.2017170039
45. Canvasser NE, Kay FU, Xi Y, Pinho DF, Costa D, de Leon AD, et al. Diagnostic Accuracy of Multiparametric Magnetic Resonance Imaging to Identify Clear Cell Renal Cell Carcinoma in Ct1a Renal Masses. *J Urol* (2017) 198:780–6. doi: 10.1016/j.juro.2017.04.089
46. Stabile A, Giganti F, Rosenkrantz AB, Taneja SS, Villeirs G, Gill IS, et al. Multiparametric MRI for Prostate Cancer Diagnosis: Current Status and Future Directions. *Nat Rev Urol* (2020) 17:41–61. doi: 10.1038/s41585-019-0212-4
47. Marino MA, Helbich T, Baltzer P, Pinker-Domenig K. Multiparametric MRI of the Breast: A Review: Multiparametric MRI of the Breast. *J Magn Reson Imaging* (2018) 47:301–15. doi: 10.1002/jmri.25790

Conflict of Interest: The authors declare that the research was conducted in the absence of any commercial or financial relationships that could be construed as a potential conflict of interest.

frontiers | Frontiers in Oncology

REVIEW
published: 08 July 2022
doi: 10.3389/fonc.2022.844790

Diffusion Breast MRI: Current Standard and Emerging Techniques

Ashley M. Mendez[1], *Lauren K. Fang*[1], *Claire H. Meriwether*[1], *Summer J. Batasin*[1], *Stéphane Loubrie*[1], *Ana E. Rodríguez-Soto*[1] *and Rebecca A. Rakow-Penner*[1,2*]

[1] Department of Radiology, University of California San Diego, La Jolla, CA, United States, [2] Department of Bioengineering, University of California San Diego, La Jolla, CA, United States

The role of diffusion weighted imaging (DWI) as a biomarker has been the subject of active investigation in the field of breast radiology. By quantifying the random motion of water within a voxel of tissue, DWI provides indirect metrics that reveal cellularity and architectural features. Studies show that data obtained from DWI may provide information related to the characterization, prognosis, and treatment response of breast cancer. The incorporation of DWI in breast imaging demonstrates its potential to serve as a non-invasive tool to help guide diagnosis and treatment. In this review, current technical literature of diffusion-weighted breast imaging will be discussed, in addition to clinical applications, advanced techniques, and emerging use in the field of radiomics.

Keywords: imaging biomarker, breast cancer, diffusion tensor (DT) MRI, non-gaussian diffusion, restriction spectrum imaging, diffusion weighted (DW) breast MRI, diagnostic breast imaging, radiomics

OPEN ACCESS

Edited by:
Samata Kakkad,
Merck, United States

Reviewed by:
Hadassa Degani,
Weizmann Institute of Science, Israel
Rita G. Nunes,
Universidade de Lisboa, Portugal

***Correspondence:**
Rebecca A. Rakow-Penner
rrakowpenner@health.ucsd.edu

Specialty section:
This article was submitted to Breast Cancer, a section of the journal Frontiers in Oncology

Received: *28 December 2021*
Accepted: *11 May 2022*
Published: *08 July 2022*

Citation:
Mendez AM, Fang LK, Meriwether CH, Batasin SJ, Loubrie S, Rodríguez-Soto AE and Rakow-Penner RA (2022) Diffusion Breast MRI: Current Standard and Emerging Techniques. Front. Oncol. 12:844790. doi: 10.3389/fonc.2022.844790

INTRODUCTION

The history of the role of magnetic resonance imaging (MRI) in visualizing breast cancer dates back to the 1980s, when it was discovered that breast malignancies enhanced significantly compared to normal breast tissue with the use of gadolinium contrast-enhanced MRI (1–3). In the decades since then, an abundance of evidence has emerged supporting the use of dynamic contrast enhanced (DCE)-MRI in the breast, with applications ranging from high risk screening and lesion characterization, to preoperative staging and breast cancer surveillance (1). At present, DCE protocols have been accepted as the standard technique in the MRI evaluation of breast cancer by the American College of Radiology (ACR) (4). While DCE-MRI demonstrates high sensitivity in the detection of malignancy, it requires the administration of intravenous contrast, which is invasive, poses a potential risk for unknown long term gadolinium-related side effects, and is contraindicated in certain patient populations, such as pregnant women.

Diffusion-weighted imaging (DWI) has emerged as both a complementary and potentially alternative technique to evaluate the breast. By measuring the diffusion of water molecules, quantified as the apparent diffusion coefficient (ADC), DWI provides insight into the micro-structural features of tissues (**Figure 1**). *In vivo*, the diffusion of water molecules can be categorized into three principal physical modes: free, hindered, and restricted (including partially restricted) (5–8). Free diffusion in tissues represents the random (Brownian), unhindered motion of water molecules, following a Gaussian distribution (5). Hindered diffusion represents the impeded motion of water molecules secondary to extracellular obstacles, such as high tumor cellularity (5). Restricted diffusion in tissues represents the inhibited motion of water molecules secondary to intracellular obstacles, such

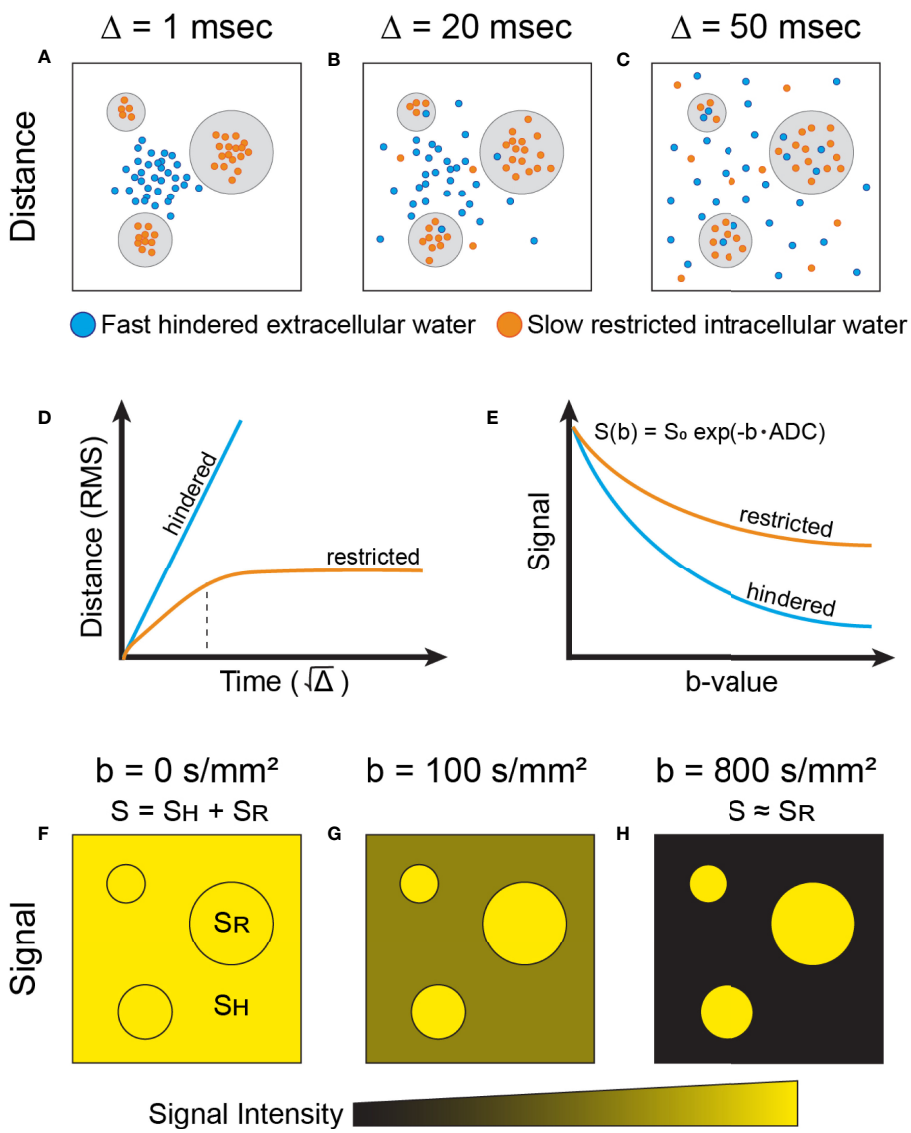

FIGURE 1 | Simplified physical basis of advanced diffusion imaging. Water molecules moving at two different speeds are shown: fast-moving (free and hindered) which exist in extracellular space (blue), and slow-moving (restricted) molecules that are trapped intracellularly by the plasma membrane (orange). Note that exchange between the extra- and intracellular compartments also exists, dictated by membrane permeability. The schematic shows the dispersion of these water molecular diffusing across cellular compartments, at different timescales (Δ) of **(A)** 1msec, **(B)** 20 msec, and **(C)** 50 msec. **(D)** The root mean square (RMS) distance of water molecules experiencing hindered diffusion is linear with respect to the $\sqrt{\Delta}$ (i.e. Gaussian diffusion, blue). In contrast, slow-moving water molecules in the intracellular compartment display Gaussian diffusion behavior (linear) at very short timescales (panel **D**, orange), dictated by the compartment's intrinsic diffusivity (5). At intermediary timescales, molecules reach the plasma membrane boundary that restricts movement, indicated by the dotted black vertical line. Past this, the net squared displacement becomes sublinear with time and is dependent on the dimensions of the compartment. To note, at very long diffusion timescales (Δ>1s), restricted water diffusion becomes principally governed by the exchange rate between the intra- and extracellular compartments (5). **(E)** In DW-MRI, the measured signal (S) decays exponentially (in the case of Gaussian diffusion) with respect to b-value due to loss of spin coherence caused by dispersion of water molecules. Thus, the signal decay from water molecules experiencing hindered diffusion (blue) is faster than from water molecules experiencing restricted diffusion (orange). The measured diffusion signal at different b-value weighting **(F–H)** reflects the relative dephasing of water molecules in different tissue compartments. At short timescales **(A, F),** the measured signal, S, contains combined information from both hindered (S_H) and restricted (S_R) water signal. At progressively longer timescales **(B, C, G, H)**, signal from hindered water dissipates more quickly than that from restricted water due to increased motion along the diffusion gradient axis, and the measured signal begins to arise predominantly from the restricted water signal (5). As shown in panel **(E)**, restricted water will retain more signal at higher b-values than hindered water and, correspondingly, have a lower ADC than hindered water.

as a cell-membranes, and follows a non-Gaussian distribution (5). To note, whereas hindered extracellular diffusion is independent of diffusion time (dictated by the time delay between diffusion sensitizing gradients), restricted diffusion is dependent on the diffusion time, membrane permeability, and the size of the restricting cellular compartments (5).

The degree of diffusion weighting in standard DWI is measured by the b-value (s/mm^2), a parameter determined by multiple experimental variables including the gradient strength, gradient duration, and time delay between diffusion sensitizing gradients (5, 9). The ADC value, defined as the average area occupied by a water molecule per unit time (mm^2/s), can be estimated from the signal measured from two different acquisitions, one with diffusion weighting (non-zero b-value) and one without (b=0 s/mm^2), according to the formula

$$S_D = S_0 e^{-b \cdot ADC} \quad [1]$$

where S_D is the diffusion weighted signal intensity, S_0 is the signal intensity without diffusion weighting and b is the diffusion sensitization factor in s/mm^2 (10). Equation 1 assumes a single tissue compartment and hence mono-exponential decay (Gaussian diffusion), which is an approximation for a given tissue at a specified b-value range. At typical clinically used diffusion times (e.g. 50-100 ms), tissues with more hindered and restricted diffusion will often yield lower ADC values (3). Therefore, ADC may serve as a surrogate for tissue cellularity and thus an imaging biomarker for breast cancer (**Figure 2**). This review article will focus on standard and emerging DWI techniques and their application to breast imaging.

CLINICAL APPLICATIONS

Screening

The current ACR guidelines recommend screening mammography starting at the age of 40 for women with average risk of breast cancer. For women with higher than average risk—defined as having a ≥20% lifetime risk, genetic predisposition for breast cancer, or history of radiotherapy to the chest—or a personal history of breast cancer and dense breast tissue, annual contrast-enhanced breast MRI is recommended (11). At present, DCE-MRI is the standard of care, but the role of DWI in screening is being explored.

Superior performance of DWI in the evaluation of mammographically occult and non-palpable breast cancers, particularly in women with dense breasts, compared to mammography alone has been reported (12, 13). Greater visibility of mammographically occult breast cancer on DWI compared to ultrasound was shown by Amornsiripanitch et al. (14). Compared to DCE-MRI, Pinker et al. showed that current DWI as a stand-alone tool demonstrates inferior sensitivity and diagnostic performance (15). However, the combination of DCE and DWI increased specificity and maximized diagnostic accuracy (15). Therefore, although currently not part of the BI-RADS lexicon, the inclusion of DWI in the MRI evaluation of breast cancer is encouraged by the European Society of Breast Imaging (16).

Despite evidence showing the high diagnostic accuracy of breast MRI, the financial cost and long acquisition times limit widespread implementation as a screening method in women of average risk (17). These limitations inspired the development of abbreviated breast MRI (abMRI) protocols (17). A meta-analysis of five studies found that abMRI protocols, which included first contrast-enhanced acquisition subtracted (FAST) sequences, demonstrated comparable sensitivity and specificity to standard MRI protocols in the setting of breast cancer screening (17).

Unenhanced abbreviated protocols with DWI sequences have been developed to address the drawbacks of DCE imaging, including cost, invasiveness, and safety concerns regarding the potential long-term effects of gadolinium. Studies showed comparable specificity of unenhanced abbreviated protocols that include DWI compared to either abbreviated contrast enhanced protocols or standard full DCE-MRI acquisitions (12, 13, 18–22). However, several of these studies evaluated cohorts with known malignancy (12, 13, 18), and many found that abbreviated DWI had lower sensitivity than DCE-MRI (12, 13, 18, 19, 21). Unenhanced abbreviated protocols are partly limited by decreased lesion conspicuity and lower interreader agreement (18, 19, 21, 22). Overall, results suggest that an unenhanced abbreviated protocol can maintain high diagnostic performance and represent a potential

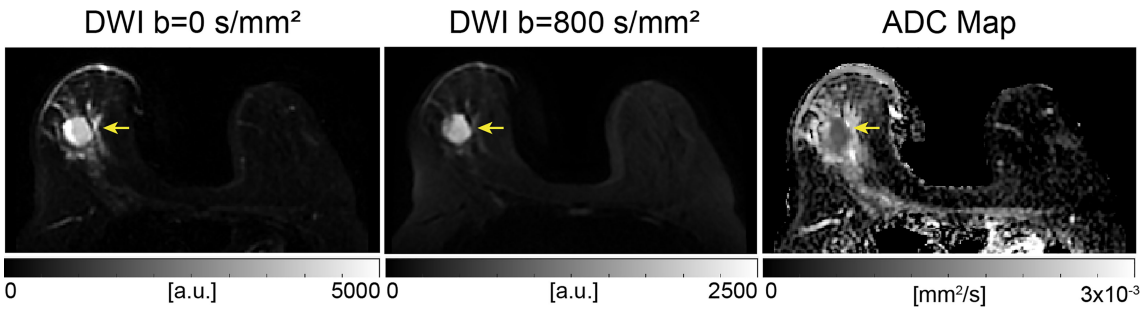

FIGURE 2 | Example of conventional breast DWI at 3T, shown at b-values 0 and 800 s/mm^2 and corresponding ADC map in a 49-year-old patient The lesion, indicated by the yellow arrow, has increased signal on b=800 s/mm^2 images and displays lower ADC values compared to surrounding tissue, indicating a finding suspicious for malignancy. This lesion was found to be an invasive ductal carcinoma from pathology.

time- and cost-effective adjunct to conventional screening protocols.

Lesion Detection and Characterization

Among the available breast imaging modalities, DCE-MRI has been established as the most sensitive in the detection of malignancy (23). Shared imaging features between benign and malignant lesions, however, limit specificity (23). The addition of DWI to DCE-MRI may offer a way of increasing diagnostic accuracy through improved specificity (24). A meta-analysis of 14 studies showed a pooled sensitivity and specificity of 91.6% and 85.5% for DCE-MRI with DWI, which was superior to DWI (86% and 75.6%) and DCE-MRI (93.2% and 71.1%) alone (25). These findings agree with other studies suggesting improved lesion characterization with multiparametric MRI (26–28). For example, a study by Pinker et al. evaluated the feasibility and diagnostic accuracy of multiparametric MRI (DCE imaging and DWI) at 7T and also found increased specificity compared to DCE-imaging alone, suggesting the addition of DWI as well as high resolution imaging may contribute to improved diagnostic accuracy (26). The added specificity from DWI holds potential to lower the false positive rate and decrease the number of unnecessary breast biopsies without missing malignancies (28).

Numerous studies have shown that DWI can be used to differentiate malignant from benign breast lesions, owing to the significantly hindered and restricted diffusion in breast cancers. A recent meta-analysis by Baxter et al. included 65 studies that evaluated the diagnostic performance of DWI and found a pooled sensitivity, specificity, and AUC of 89%, 82%, and 0.92 (29), respectively, which is comparable to results from multiple additional meta-analyses (30–32). Subgroup analysis showed that diagnostic performance was not significantly associated with the number or choice of b-values, field strength, or method of region of interest (ROI) segmentation (29).

Despite the comparable diagnostic performance of ADC across studies, threshold values varied. Small sample sizes with various proportions of lesion subtypes, differing field strengths, and selection of b-values have been suggested to contribute to this discrepancy. A recently published meta-analysis by Surov et al. aimed to provide clinically relevant information regarding use of ADC values in the differentiation of malignant and benign breast lesions (33). This analysis included 123 studies from across the world and a total of 13,847 breast lesions. The reported pooled mean ADC values for malignant versus benign breast lesions were 1.03×10^{-3} mm^2/s, 95% CI (1.01–1.05 $\times 10^{-3}$ mm^2/s) and 1.50×10^{-3} mm^2/s, 95% CI (1.45–1.55 $\times 10^{-3}$ mm^2/s), respectively (33). This study found that all benign lesions had ADC values above 1.0×10^{-3} mm^2/s, independent of field strength, choice of b-values, and ROI delineation technique (33). However, the study also demonstrated considerable overlap of malignant and benign lesions in the ADC range between 1 and 2×10^{-3} mm^2/s, which limits the clinical use of the proposed threshold value (33).

Diffusion-weighted imaging has also demonstrated potential in differentiating between invasive ductal carcinoma (IDC) and ductal carcinoma *in situ* (DCIS) (34–36). A meta-analysis of 15 studies showed a significantly higher ADC value in DCIS (0.92-1.56 $\times 10^{-3}$ mm^2/s) compared to IDC (0.89-1.31 $\times 10^{-3}$ mm^2/s) lesions, highlighting the microstructural differences between the two pathologies, potentially providing a noninvasive means of lesion characterization (34). Subgroup analysis stratified by ethnicity found lower ADC values in IDC compared to DCIS in the Asian population but not in Caucasians. Smaller sample size of Caucasian patients in this study (293 versus 858 Asians) may contribute to the differing results, as well as genetic and environmental differences (34).

Prognostic Factors

Prognostic factors for breast cancer are used to predict survival, guide treatments, and stratify patients into clinical trials. While some of these factors, such as stage or tumor size, can be provided by imaging, several others rely on pathologic diagnosis. The use of DWI has been explored as a potential non-invasive method of predicting prognostic factors. The driving hypothesis behind these studies is that malignant lesions demonstrate high proliferation, which causes the ADC values of tissues to decrease as a result of increased cellularity (37). Tumors with increased angiogenesis are suggested to display relatively higher ADC values from increased vascular permeability and increased extracellular fluid, although this hypothesis has not yet been validated (37). Several studies have evaluated the association of ADC values and prognostic factors in breast cancer, including tumor subtype, lymph node metastases, hormone receptor expression, and histologic grade, among others.

Lymph Node Metastasis

The identification of lymph node metastases is necessary for accurate staging of breast cancer, which in turn affects treatment planning and prognosis (38, 39). Tissue sampling remains the gold standard but is invasive and prone to sampling error (39). As a surrogate for underlying cellularity, DWI may provide a noninvasive way of evaluating the axilla. A meta-analysis of 10 studies and 2305 lymph nodes showed a significantly lower ADC for metastatic lymph nodes (benign: 0.75-1.77 $\times 10^{-3}$ mm^2/s vs. metastatic: 0.69-1.37 $\times 10^{-3}$ mm^2/s), with a pooled sensitivity and specificity of 89% and 83%, respectively (39), similar to results of a few other studies (40–42). A handful of studies, however, including a large multicenter analysis, found no correlation between ADC values and lymph node involvement (43–46).

Hormone Receptor Expression

The correlation between ADC and hormone receptor expression has also been explored, with varied results. A meta-analysis of 6 studies showed a negative correlation between ADC values and estrogen receptor (ER) and progesterone receptor (PR) expression (47), which is consistent with the results of a few additional studies (37, 44, 48). Other groups, however, found no association with ER or PR expression (40, 45, 49, 50). A positive correlation between ADC values and human epidermal growth factor receptor 2 (HER2) expression was shown by a few groups (40, 41, 45, 48, 51), whereas others found no association (43, 44, 46, 50, 52, 53). Conflicting results were also reported regarding histologic grade, with some studies demonstrating decreased ADC values with increasing grade (41, 42, 53, 54) and others

not finding a significant association (40, 52, 55, 56). Most studies found no significant association between ADC values and tumor size (42, 44, 46, 52, 53). Multiple factors may contribute to conflicting results, including differences in study design, technical parameters, and tumor types evaluated.

Histopathologic Subtype

The recommended treatment for breast cancer is highly dependent on biological subtype. For example, in terms of systemic treatment, Luminal A breast cancers generally only receive endocrine therapy, whereas the addition of cytotoxic therapy is indicated for most patients with Luminal B and triple negative breast cancer (57). Immunohistochemistry remains the gold standard for subtype classification but is costly and invasive. Multiple groups have investigated the potential for DWI to predict molecular subtype. A meta-analysis by Meyer et al. compared the ADC values between breast cancer subtypes and included 28 studies comprising 2990 lesions, of which 28.9% were classified as Luminal A, 30.1% Luminal B, 20% HER2 enriched, and 21% triple negative (58). Pooled data showed mean ADC values of 0.99×10^{-3} mm^2/s (95% CI 0.94–1.04×10^{-3} mm^2/s), 0.97×10^{-3} mm^2/s (95% CI 0.89–1.05×10^{-3} mm^2/s), 1.02×10^{-3} mm^2/s (95% CI 0.95–1.08×10^{-3} mm^2/s), and 0.99×10^{-3} mm^2/s (95% CI 0.91–1.07×10^{-3} mm^2/s) for these four subtypes, respectively (58). The large overlap in ADC values between subtypes is consistent with the results from a multicenter analysis by Surov et al., which found mean ADC values of $1.01 \pm 0.22 \times 10^{-3}$ mm^2/s, $0.95 \pm 0.23 \times 10^{-3}$ mm^2/s, $1.04 \pm 0.23 \times 10^{-3}$ mm^2/s, and $0.95 \pm 0.17 \times 10^{-3}$ mm^2/s for the four subtypes, respectively, suggesting that ADC values may not be a useful predictor of molecular subtype (43).

The proliferation index, Ki-67, is a component of the subtype classification differentiating Luminal A from Luminal B breast cancer, and therefore directly affects treatment strategy. A meta-analysis by Surov et al. found a weak negative correlation (ρ=-0.22) between ADC values and Ki-67 in breast cancers (59), consistent with the findings of multiple other studies (40, 41, 43, 46, 50, 54, 55). Comparison across studies is limited, however, due to different cutoff values in the classification of high proliferation, with some using 14% and others 20%. Although statistically significant, the association is considered too weak to be clinically useful as an imaging biomarker in this context.

Histogram analysis of ADC was performed by a few groups to capture tumor heterogeneity and to determine if additional metrics were associated with prognostic factors. A study by Horvat et al. showed that the maximum ADC value based on a two-dimensional (2D) ROI on the whole tumor differentiated luminal from non-luminal cancers with an AUC of 0.685 (37). Significant overlap in ADC values between subgroups was also shown in this study, but results suggest that whole tumor segmentation may better reflect tumor heterogeneity and the different underlying architecture among molecular subtypes. Another study evaluated the added value of the entropy of ADC values, a measure of the variation in the volumetric ADC histogram and a potential surrogate for underlying microstructure heterogeneity. Results showed that the ADC entropy values differed among Luminal A, Luminal B, and triple negative phenotypes (48).

Peritumoral edema associated with breast cancer has been reported to correlate with aggressiveness and portend a poor prognosis (60–62). It has been hypothesized that neovascularity and increased vascular permeability associated with aggressive malignancies are responsible for the peritumoral edema seen on MRI (62). Therefore, evaluation of the peritumoral region may contribute additional pathophysiologic information. A study by Okuma et al. investigated whether the peritumor/tumor ADC ratio correlated with prognostic factors and indexes (49). Results showed a positive correlation between the peritumoral/tumoral ratio and size, grade, proliferation index, lymph node involvement, and lymphovascular invasion (49). While the ratio correlation of peritumor/tumor ADC with the Nottingham Prognostic Index (NPI) (0.5) and PREDICT (0.44) was stronger than that of tumoral (-0.28 and –0.25, respectively) or peritumoral (0.27 and 0.19, respectively) ADC values alone, the correlation was still considered limited to moderate. Additional studies are needed to determine if the peritumoral/tumoral ADC ratio provides any value in the prognostication of breast cancer (49).

Predicting and Monitoring Treatment Response

Neoadjuvant chemotherapy (NAC) is commonly used in the treatment of locally advanced or large breast cancer to downstage the disease and potentially allow for breast-conserving therapy (63). The ability to non-invasively evaluate treatment response not only impacts clinical management, but also confers prognostic information, with improved outcomes seen in patients with complete pathologic response. DCE-MRI is the most commonly used modality to evaluate treatment response but is limited in the ability to differentiate residual tumor from treatment related changes, including scarring, necrosis, and reactive inflammation (64). DWI offers a potential alternative or complementary technique to overcome those limitations. The cytotoxic effects of chemotherapy disrupt cell membranes and decrease tumor cellularity, which theoretically should result in increased ADC values.

Multiple meta-analyses found that DWI could detect pathologic complete response (pCR) with a pooled sensitivity and specificity of 0.8-0.89 and 0.72-0.85, respectively (65–67). The criteria used to define complete pathologic response differed among the included studies, which partially limits comparison. The DWI metrics also varied, with some studies using the change in ADC (ΔADC) with treatment, pre-treatment ADC, post-treatment ADC, or a combination of all three to determine treatment response. Chu et al. compared the different metrics and found that the pooled specificity of the ΔADC was comparable to the post-treatment ADC, but significantly higher than that for the pre-treatment ADC group (67). This finding is partially supported by the mixed results from multiple smaller studies that investigated the ability of pre-treatment ADC to predict treatment response (68–73). While this suggests that pre-treatment ADC values may not represent as reliable a predictor of pCR compared to the ΔADC and post-

treatment ADC, multi-center trials with larger population sizes and standardized acquisition protocols would be needed to make this determination and validate the use of ADC for this clinical use.

The results from the American College of Radiology Imaging Network (ACRIN) 6698 trial further demonstrate the ability of DWI to predict pathologic response (74). In this clinical trial, 272 women with breast cancer underwent DW-MRI prior to NAC, 3 weeks into treatment, 12 weeks into treatment, and after completion of chemotherapy. The percent change in tumor ADC from baseline was measured at each time point. Results showed that the ΔADC was somewhat predictive of pCR at mid-treatment (12 weeks) (AUC 0.6; 95% CI: 0.52-0.68; P= 0.017) and after treatment (AUC 0.61; 95% CI: 0.52-0.69; P = 0.013). Significantly increased treatment related ΔADC values in patients with pCR supports the findings from multiple single center studies (68, 69, 72, 75–77).

A meta-analysis by Gu et al. evaluated the role of MRI in the detection of pCR after neoadjuvant treatment in patients with breast cancer and found that DCE-MRI demonstrated superior pooled specificity in terms of identifying residual tumor (0.92 versus 0.85) while DWI maintained higher sensitivity (0.93 versus 0.64) (65). The relatively low sensitivity of DCE-MRI may be secondary to nonspecific contrast enhancement from post-treatment changes, including reactive inflammation, necrosis, and perilesional edema, or from co-existing DCIS (65). The diagnostic accuracy of DCE-MRI was greater than ultrasonography and mammography (0.96 versus 0.66 and 0.53) but not significantly different than PET/CT (0.99), which demonstrated higher sensitivity of 0.9 (65). Results suggest that DCE-MRI combined with DWI or PET/CT in these patients may improve predictive accuracy (65).

VALIDATION AND TECHNICAL CONSIDERATIONS

Technical validation is necessary prior to translation of quantitative imaging biomarkers into community practice. This process involves standardization of acquisition protocols and demonstration of acceptable repeatability and reproducibility to ensure consistent results across practice settings.

Repeatability and Reproducibility

For implementation in clinical practice, a quantitative imaging biomarker should demonstrate high accuracy and precision, reflected in repeatability and reproducibility. Repeatability represents the precision of repeated measures taken under identical conditions in a short amount of time, while reproducibility represents the precision of repeated measures wherein some aspect of the procedure is changed (e.g. different field-strength scanners) (78). Understanding the factors which affect repeatability and reproducibility, such as image acquisition parameters and data analysis, is necessary for the development of a useful imaging biomarker.

Multiple small single center studies have shown good repeatability and reproducibility of ADC measurements in normal (79–82) and malignant breast tissue (80, 81, 83). The ACRIN 6698 trial evaluated the repeatability and reproducibility of ADC measurements in a multi-institution, multi-MRI platform clinical setting (84). Results demonstrated excellent repeatability [within-subject coefficient of variation = 4.8% (95% CI 4.0-5.7%)] and reproducibility [interreader intraclass correlation coefficient (ICC) = 0.92 (95% CI 0.80-0.97) and intrareader ICC = 0.91 (95% CI 0.78-0.96)] independent of field strength when using a standardized DWI protocol and quality assurance (QA) procedures (84). This study represents an important step in the validation of ADC as a quantitative imaging biomarker by showing high precision in a multi-institution setting.

The Quantitative Imaging Biomarkers Alliance (QIBA) previously excluded breast from the QIBA Profile for DWI in 2017 due to a lack of reproducibility data in the literature. In light of the increasing evidence, the QIBA added breast to the DWI Profile in 2019, providing guidance on protocol design (**Table 1**), quality assessment, and image analysis, with additional details provided in the following sections (85).

The European Society of Breast Radiology (EUSOBI), which works closely with the QIBA, created an international breast DWI working group consisting of MRI physicists, clinical breast MRI experts, and MRI vendor representatives from 16 countries (16). The group published the first consensus and mission statement in 2020, proposing acquisition parameters for DW sequences and ROI segmentation recommendations for clinical application with the goal of improving protocol standardization across institutions and attaining standardized ADC values. The group's future efforts will focus on addressing factors that alter precision and the development of quality control, with a goal of progressing towards widespread implementation of quantitative breast DWI (16).

Acquisition Techniques

The QIBA DWI profile currently recommends utilizing a single-shot echo planar imaging (ss-EPI) acquisition sequence for diffusion weighted breast imaging (85). In ss-EPI, the imaging data from all k-space is obtained with a single radio-frequency excitation, allowing for shorter acquisition time and decreased motion artifact (6, 86). However, ss-EPI is strongly affected by susceptibility artifacts and typically has low spatial resolution. These limitations can be mitigated by adequate fat suppression, use of parallel imaging, and shimming (6, 86).

Alternative acquisition techniques have emerged to address these limitations and have demonstrated potential for improved image quality in DWI breast imaging. In general, these techniques reduce the readout duration, thus shortening the time during which the signal is affected by field inhomogeneities that cause distortion artifacts.

Readout-segmented echo planar imaging (rs-EPI) is a multi-shot technique that divides k-space into multiple segments, allowing for decreased echo spacing, reduced geometric distortion, and improved resolution (87). Multiple

TABLE 1 | Protocol guidance for diffusion weighted imaging of the breast provided by the QIBA.

Field Strength	1.5 or 3 T
Acquisition sequence	Diffusion-weighted Single-Shot Echo Planar Imaging (ss-EPI)
Receive Coil type	Ideal/Target: 5-16 channel bilateral breast coil Acceptable: 4 channel bilateral breast coil
Fat Suppression	On
Number of b-values	Ideal: ≥ 4 Target/Acceptable: 3 (including one b=0-50, one 100, and one at highest b-value Acceptable: 2 (including one b=0-50 s/mm^2 and one at highest b-value)
Minimum highest b-value strength	Target/Ideal: b=600-800 s/mm^2 Acceptable: 600 s/mm^2
Diffusion directions	Target/Ideal: 3-orthogonal, combined gradient channels Acceptable: 3-orthogonal, single gradient channels
Slice Thickness	Ideal: 4 mm Acceptable: 5 mm
Gap thickness	Ideal: 0 mm Acceptable:1 mm
Field-of-view	Ideal/Target/Acceptable: 260-360 mm (complete bilateral coverage)
Acquisition matrix	Target/Ideal (128-192) x (128-192), or 2.8- 1.8 mm in-plane Acceptable: 128 x 128, or 2.8 mm in-plane resolution
Plane orientation	Transversal-axial
Half-scan factor	Acceptable/Target: >0.65
Phase-encode/frequency-encode direction	Anterior-Posterior/Right-Left or Right-Left/Anterior-Posterior
Number of averages	Ideal/Target: 3-5 Acceptable:2
Parallel imaging factor	Ideal: ≥ 2 Target/Acceptable: 2-3/2
TR	Ideal/Target/Acceptable ≥ 4000 ms
TE	Ideal/Target: minimum TE (50-100ms) Acceptable: < 114 ms
Receiver Bandwidth	Ideal/Target: maximum possible in frequency encoding direction (minimum echo spacing) Acceptable: > 1000 Hz/voxel

Definitions provided by the QIBA:
ACCEPTABLE: Actors that shall meet this specification to conform to this profile.
TARGET: Meeting this specification is achievable with reasonable effort and adequate equipment and is expected to provide better results than meeting the ACCEPTABLE specification.
IDEAL: Meeting this specification may require extra effort or non-standard hardware or software, but is expected to provide better results than meeting the TARGET.

studies have demonstrated superior breast lesion conspicuity and image quality with rs-EPI compared to ss-EPI (88–91). Inter-reader agreement of known mass and non-mass lesions was evaluated in two studies: DCE-MRI and rs-EPI collected with b-values of 0 and 850 s/mm^2 resulted in comparable morphologic lesion assessment and diagnostic performance (21, 92). These findings suggest rs-EPI as a potential alternative to DCE-MRI. However, improved image quality with rs-EPI is often at the expense of increased acquisition times, and lesion conspicuity remains inferior to DCE-MRI

Simultaneous multi-slice (SMS) rs-EPI was introduced to address the increased acquisition times required with rs-EPI. In SMS imaging, multiple slices are acquired simultaneously so that the number of excitations required for the same slice coverage is reduced (93). The spatial sensitivity of multichannel array coils is subsequently used to separate the slices acquired in parallel (93). Filli et al. first demonstrated the feasibility of SMS rs-EPI in 8 healthy volunteers, comparing conventional rs-EPI to two-fold and three-fold slice-accelerated rs-EPI (**Figure 3**) (94). They found that while scan time was significantly reduced and SNR was improved with additional acceleration, ghosting artifacts and shading in the prepectoral region were more distinct (94). A more recent study by Song et al. compared image quality, lesion conspicuity, and scan time between rs-EPI and SMS rs-EPI

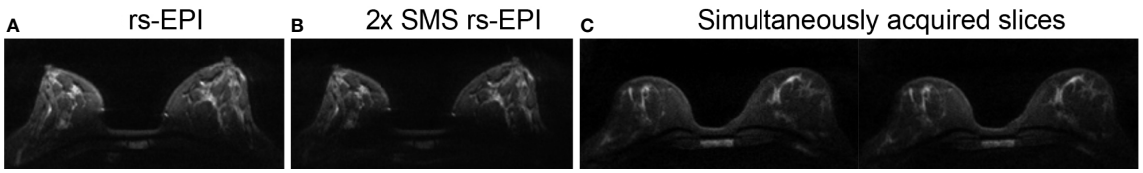

FIGURE 3 | Example of SMS rs-EPI acquisition at b=800 s/mm^2 in a 35-year-old healthy volunteer, wherein **(B)** two-fold (2×) SMS rs-EPI maintains comparable image quality as **(A)** conventional rs-EPI while reducing scan time in a 3T scanner. Panel **(C)** shows two simultaneously acquired slices used to generate a single-band equivalent image for the same patient at a different slice location (94). (Courtesy of Lukas Filli, MD, Zurich, Switzerland).

sequences in 134 women with invasive breast cancer (95). The study found a 44% reduction in scan times, improved image quality, and enhanced lesion conspicuity with SMS rs-EPI, similar to the results of a study by McKay et al. (95, 96). Compared to conventional rs-EPI, SMS rs-EPI produced comparable AUC and ADC values in multiple studies, suggestive a potential method of reducing scan time while preserving diagnostic accuracy (94, 95, 97, 98).

Reduced field of view (rFOV) improves spatial resolution and decreases artifacts by limiting the field of view and number of k-space lines in the phase-encoding direction (99, 100). Improved image quality with rFOV compared to standard DWI techniques has been shown to enhance lesion conspicuity and morphologic assessment in the breast (101–104). Significant differences in ADC values with rFOV compared to full FOV DWI, however, may limit the utility of proposed ADC cutoff values when employing rFOV techniques (**Figure 4**) (101, 102, 104, 105).

rFOV has been used in conjunction with other acquisition strategies to further improve image quality and reduce scan time. For instance, Taviani et al. developed a single-shot image-segmented technique that combines rFOV, 2D in-plane multiband radiofrequency pulses, and a generalized parallel imaging reconstruction method to generate images with high resolution and anatomical fidelity (106).

Diffusion weighted double-echo steady state (DW-DESS) imaging is an emerging technique that allows for rapid acquisition of high-resolution images by utilizing a short repetition time (TR) (107–110). The diffusion weighted DESS sequence acquires two echoes per radiofrequency pulse, during which a steady state of longitudinal and transverse magnetization is achieved. Multiple parameters affect the diffusion weighting in DW-DESS, such as the TE, TR, flip angle, spoiler gradient duration, and tissue relaxation and diffusion properties (107, 108, 110). A few studies have evaluated the use of DW-DESS imaging in the breast and found superior image quality and improved morphologic assessment when compared to conventional EPI DWI (108, 111). Benefits of this technique include rapid acquisition times and avoidance of EPI-associated distortions and blurring (107, 108). The DW-DESS sequence, however, is susceptible to motion artifacts, particularly with increased diffusion weighting (109). Moran et al. developed a DW-DESS-Cones method using a three-dimensional cones (non-cartesian) trajectory to address this limitation, and demonstrated significantly reduced motion artifacts (**Figure 5**) (109). At present, DW-DESS techniques do not provide a reliable quantitative measure of diffusion equivalent to ADC values, and will likely be the focus of future investigations (108, 109).

b-Value Selection

ADC values are typically displayed as a parametric ADC map. Regions of high cell density and hence highly hindered and restricted (including partially restricted) diffusion appear hypointense on the ADC map and hyperintense on high b-value diffusion weighted images.

According to the monoexponential mathematical model (Eqn. 1), b-value selection directly affects the ADC value, signal-to-noise ratio (SNR), and contrast-to-noise ratio (CNR). With increasing b-value, ADC values theoretically decrease due to the predominance of non-Gaussian diffusion. Additionally, increased CNR with increasing b-values may improve lesion detection at the expense of decreased SNR (10). Studies aiming to identify optimal b-value selection in DWI of breast demonstrate varied results (112–115). The QIBA requires a minimum of two b-values, b=0-50 s/mm^2 and b≥ 600 s/mm^2, but recommends ideally acquiring 4 or more b-values, including b=0-50 s/mm^2 (78). As more evidence emerges, particularly with advanced modeling techniques requiring multiple b-values, recommendations may become increasingly specific.

ROI Delineation

Typically, ADC values are extracted by placing a region of interest (ROI) on the restricting lesion. The most commonly employed methods of ROI placement are whole lesion

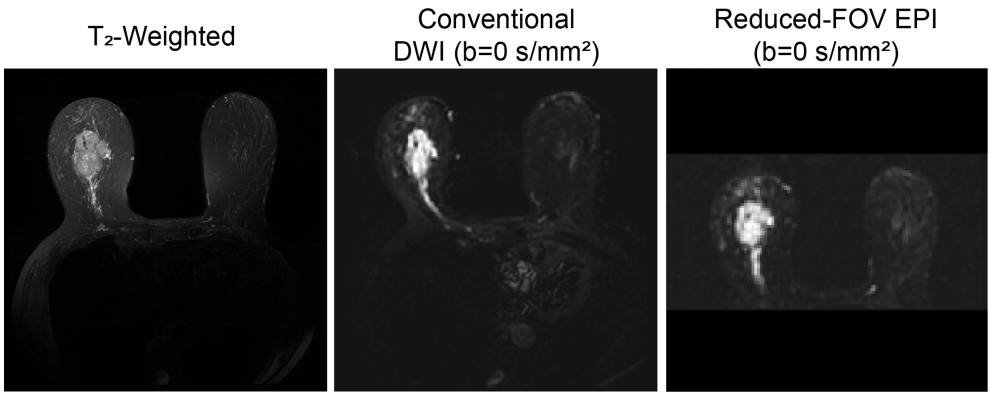

FIGURE 4 | Reduced FOV EPI in a 63-year-old patient with invasive ductal carcinoma. T_2-weighted, conventional DWI (b=0 s/mm^2), full FOV EPI (b=0 s/mm^2), and reduced FOV EPI (50% phase field of view) (b=0 s/mm^2 acquired at 3T) images are shown. Reduction of percent phase encoding direction to 50% reduces geometric distortions caused by B_0-inhomogeneity, especially in the nipple region (100).

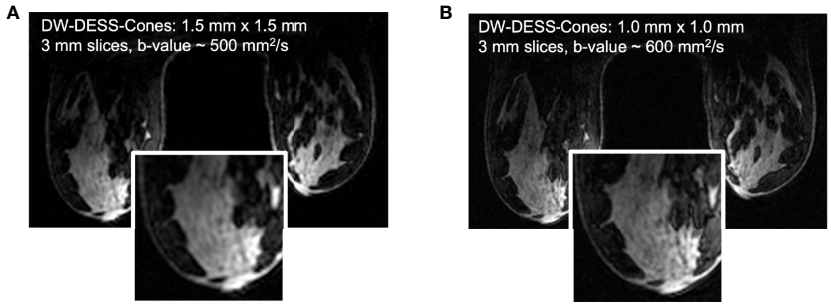

FIGURE 5 | Based on the results of the initial DW-DESS-Cones investigation in the breast at 3T **(A)**, the diffusion-weighting and resolution of the method can be further increased **(B)** to better match contrast and resolution expectations for breast MRI (109). (Courtesy of Catherine Moran, PhD, Department of Radiology, Stanford University, Stanford, California, USA).

segmentation and focused segmentation, where the ROI is applied to the most restricting portion of the lesion (highest signal on DWI corresponding to lowest ADC value on ADC maps) (116–119). ROI placement has been shown to significantly affect ADC measurements, limiting the use of proposed ADC cutoff values (116–119). Compared to whole lesion segmentation, focused ROI placement demonstrates superior diagnostic accuracy in the evaluation of breast lesions in a few studies, likely on the basis of emphasizing the most restricting and thereby most suspicious portion of the tumor (117, 119). Focused segmentation allows the exclusion of region of necrosis, non-enhancement, and artifacts, resulting in an ADC value that may better represent the underlying microstructure (16, 118). Additionally, semiautomated ROI delineation algorithms, such as that developed by Rahbar et al., can improve inter-reader reproducibility of ADC measures (120). While the QIBA has not provided ROI placement standards, the EUSOBI presently recommends using a focused segmentation method—while taking care to avoid regions of necrosis, non-enhancement, and artifacts—with the goal of improving consistency of DWI across institutions (16).

ADVANCED AND EMERGING TECHNIQUES

To address the shortcomings of the monoexponential ADC model in capturing the complex tissue micro-structure in the breast, several advanced diffusion models have been developed and will be explored in this section.

Diffusion Tensor Imaging

Diffusion tensor imaging (DTI) is a quantitative technique within DWI that measures the diffusion directionality (anisotropy) of water molecules by applying at least 6 directional diffusion gradients, providing a three-dimensional representation of diffusion (121–125). The diffusion tensor model is mathematically represented by a symmetric matrix of six parameters: three orthogonal eigenvectors (v_1, v_2, v_3), reflecting the direction of diffusion, and three corresponding eigenvalues (λ_1, λ_2, λ_3), reflecting the degree of diffusion in each orthogonal direction (121–125). From the eigenvalues, DTI metrics are derived (121, 125). The most common DTI metrics studied are fractional anisotropy (FA), or the fraction of diffusion that is anisotropic on a scale from 0 to 1, and mean diffusivity (MD), or the average of tensor's eigenvalues, also represented as the ADC (121, 125). Additional DTI parameters include maximal anisotropy (MA), relative anisotropy (RA), volume ratio, geodesic anisotropy, and radial diffusion. Maximal anisotropy represents the difference between the highest and lowest value of anisotropic water movement (λ_1 - λ_3) (126). Relative anisotropy is the ratio of the standard deviation to the mean of the three eigenvalues, ranging from 0 to $\sqrt{2}$, with 0 representing isotropic diffusion and the $\sqrt{2}$ representing diffusion in a single direction (126). The volume ratio is the ratio of the ellipsoid to spherical, ranging from 0 to 1, with 1 reflecting isotropic diffusion (127). Radial diffusivity is the average of the two smaller eigenvalues (λ_2 and λ_3) (128)

Normal breast architecture is comprised of multiple lobules with a complex ductal network with surrounding fibrous stroma and intervening fatty tissue. Within small ducts, it has been suggested that the diffusion of water molecules is anisotropic and DTI values may provide information regarding pathophysiologic changes in tissue microstructure (123, 129). A few studies have evaluated DTI parameters in women with normal breasts and found significant regional differences, with increased FA within the periphery and posterior aspects of the breast compared to the central breast, which is postulated to reflect anisotropic diffusion within smaller, collapsed ducts peripherally and posteriorly (123, 129, 130). A study by Plaza et al. showed no association between DTI parameters and fibroglandular tissue composition, but found a significantly lower λ_1 in normal breasts with moderate/marked background parenchymal enhancement (BPE) compared to those with minimal/mild BPE (131). Other studies have observed that DTI parameters are resistant to physiologic differences in breast tissue composition due to their unique ability to track underlying ductal microstructure (123, 132, 133). In comparison to DCE, certain DTI parameters have also shown superior tumor conspicuity in lactating patients with pregnancy-associated breast cancer (134). Background parenchymal enhancement is a challenge among this patient population. In a study by Nissan et al., CNR for lactating

patients with pronounced BPE were higher on λ_1, λ_2, λ_3, and MD (1.81 ± 0.67, 1.95 ± 0.87, 1.79 ± 0.83, respectively) maps as compared with those of DCE images (0.82 ± 0.49) ($p < 0.005$, for all) (134). These correspond to an increase in CNR of up to 138% by DTI-derived parameters, compared to DCE. DTI parameters, much like ADC (132, 135–137) have been shown to be resistant to changes in the breast parenchyma (131, 132, 134), unlike DCE (138, 139), which further demonstrates the utility of diffusion MRI as an effective adjunct to DCE.

Disruption of the breast architecture has been suggested to alter anisotropic indices, and which may therefore serve as potential imaging biomarkers of malignancy. A comprehensive meta-analysis by Wang et al. evaluated the diagnostic performance of DTI metrics in discriminating benign versus malignant breast lesions (140). This analysis included 16 studies with a total of 1636 patients and found significantly higher FA (0.15-0.55 versus 0.02-0.13), and lower MD (0.71-1.62 versus 1.08-1.91), λ_1 (0.97-1.62 versus 1.19-2.15), λ_2 (0.95-1.29 versus 1.50-1.68), and λ_3 (0.78-1.12 versus 1.20-1.56) in malignant lesions compared to benign lesions (140). Decreased diffusion coefficients may be in part secondary to increased cellularity within the malignancy, as well as ductal involvement of neoplastic cells (140). Pooled FA was increased in malignant lesions, but individual studies showed conflicting results (140). For example, Furman-Haran et al. found no difference in FA between malignant lesions and contralateral breast parenchyma, but did find that the absolute maximal anisotropy index (λ_1-λ_3) differentiated the tissues (lesion: 0.51 x 10−3, mm2/sec, versus normal: 0.84 x 10^{-3} mm^2/s, $p<0.001$) (126). Increased FA values in malignancy are postulated to reflect disorganized architecture with regional necrosis or hemorrhage, that results in increased diffusion along certain directions but hindered diffusion in others (126, 140). If regions of necrosis or hemorrhage are large enough, however, diffusion of water molecules may be uninhibited and result in reduced anisotropy, which may explain why some of the included studies concluded that FA could not distinguish malignant from benign lesions (140). Furthermore, normalized anisotropic indices such as FA are subject to the inherent mean diffusivity of the underlying tissue, which may differ by lesion subtype (126, 140). Subgroup analysis revealed a significantly lower MD value among invasive breast cancer lesions compared to DCIS (140). Overall, λ_1 demonstrated the highest diagnostic accuracy, with a pooled sensitivity of 93%, specificity of 92% and AUC of 97%. These findings suggest MD and λ_1 may be clinically useful markers of malignancy (123, 128, 140, 141).

An additional meta-analysis performed by Baxter et al. compared the diagnostic performance of DWI, DTI, and intravoxel incoherent motion (IVIM) in the characterization of breast lesions (29). In this analysis, λ_1 also demonstrated the highest diagnostic accuracy among DTI metrics, with a pooled sensitivity of 93%, specificity of 90% and AUC of 94% (29, 123, 128, 141). Overall, the diagnostic performance of DWI, DTI and IVIM was comparable but the conclusions were limited by the low number of included studies and thereby low statistical power (29).

The association of DTI parameters with prognostic factors has been investigated by a few studies with promising results (128, 142–144). Significantly low MD and FA values were found to correlate with larger tumor size (>2 cm), high histologic grade, and axillary nodal metastases/lymphovascular invasion (142–144). Other DTI parameters were also found to be significantly associated with ER, PR, CERB-B2, Ki-67 and intrinsic subtypes (128, 143).

A retrospective study by Furman-Haran et al. included 20 women undergoing NAC and compared DTI parameters with DCE-MRI in the ability to monitor treatment response (145). Results showed that the post NAC change in multiple DTI parameters, including MD, λ_1, λ_2, and maximal anisotropy (λ_1-λ_3) differentiated responders from non-responders after NAC, with the highest AUC seen with MD, λ_1 and λ_2 (145). The change in FA was not statistically significant (145). Pre-NAC DTI parameters however showed low diagnostic performance in the ability to predict NAC response (145). Tumor size changes following NAC measured by DTI were of comparable accuracy to that of DCE and found to also be a significant discriminator between responders and non-responders (145). Residual tumor diameter correlated well with the postoperative pathological tumor diameter (145).

At present, no standard DTI protocol exists, with varied selection of b-values and numbers of diffusion gradients seen across studies, which may affect the resultant DTI metrics. It has also been demonstrated that DTI is prone to artifacts at high b-values and high resolution, common to other EPI-based sequences, which affect interpretation of the DTI parameters (146). A study by Yamaguchi et al. found superior diagnostic performance of DTI based on rs-EPI compared to DWI based on ss-EPI, which was attributed to improved lesion conspicuity and diminished blurring artifact (144). Further studies are needed to establish a standardized protocol and threshold values for practical clinical use.

Intravoxel Incoherent Motion (IVIM)

Diffusion-weighted imaging and subsequent ADC measurement are influenced by both Gaussian and non-Gaussian diffusivity, which includes microcapillary perfusion. The intravoxel incoherent motion (IVIM) model, first introduced in 1986 by Le Bihan et al., provides a method to separate the contribution of micro-perfusion from tissue diffusivity to the diffusion-weighted signal (147). Using the following biexponential decay model,

$$S/S_0 = fe^{-b(D+D*)} + (1-f)e^{-bD} \quad [2]$$

and multiple b-values, the following parameters can be attained: water diffusion through tissue (D or D_t), pseudo-diffusion from perfusion (D^*, D_p or D_f) and the perfusion fraction (f, f_p, or f_{IVIM}). First applied to the breast in 2011 by Sigmund et al., the IVIM model has been increasingly studied and shown promise in the evaluation of breast lesions (148).

The IVIM parameters have been shown to aid in the discrimination of malignant from benign breast lesions. In multiple studies, malignant lesions showed significantly decreased tissue diffusivity (D_t) values and increased perfusion fraction (f_p) values compared to benign lesions and normal

breast parenchyma (36, 149–162). A recently published review of fifteen studies yielded sensitivity of 87 ± 10% and specificity of 79 ± 17% for D_t in malignant lesions, and a sensitivity of 81 ± 7% and specificity of 75 ± 3% for f_p (163). In terms of diagnostic performance, multiple studies found that at least one IVIM metric, most consistently D_t, outperforms ADC, with one study finding an increased AUC when D_t and f_p are combined (0.84 vs 0.75 for D_t alone, and 0.79 for f_p alone) (**Figure 6**) (36, 152–155, 157–159).

Direct comparison and correlation of IVIM parameters with standard DCE-MRI has been performed (155, 157, 165). In a few studies, D_t outperformed DCE-MRI derived parameters with an overall increased AUC when IVIM and DCE-MRI parameters were combined (AUC 0.99 with combination of D_t and time-signal intensity curve (157); AUC 0.93 with multivariate combination of IVIM and DCE parameters (155, 157, 165). Multiparametric approaches combining IVIM and other non-Gaussian DWI parameters also have shown increased diagnostic accuracy, with one study by Lima et al. demonstrating BI-RADS equivalent scores (150). These findings suggest that the addition of IVIM metrics to standard DCE-MRI may improve diagnostic accuracy, and that IVIM may represent a non-invasive alternative to DCE-MRI.

The role of IVIM in the non-invasive identification of prognostic factors in breast cancer has also been investigated. Multiple studies found a correlation between D_t and ER expression (36, 56, 161, 166). Zhao et al. also found that the D* and D_t significantly correlated with ER and PR expression and Luminal A subtypes (161). Luminal B subtypes in this study showed significantly decreased f_p, with significantly diminished peritumoral f_p values among HER2 positive lesions compared to HER2 negative lesions, a finding which may reflect diminished central perfusion secondary to intratumoral necrosis (161). The IVIM parameters D*, f_p and D_t correlated with TNBC status, with increased f_p values along the tumor edge compared to other subtypes and increased peritumoral D* values, which may suggest a high degree of invasiveness (161). The work by Zhao et al. showed that applying IVIM metrics to the peritumoral and tumor edge may shed light on the underlying pathophysiology.

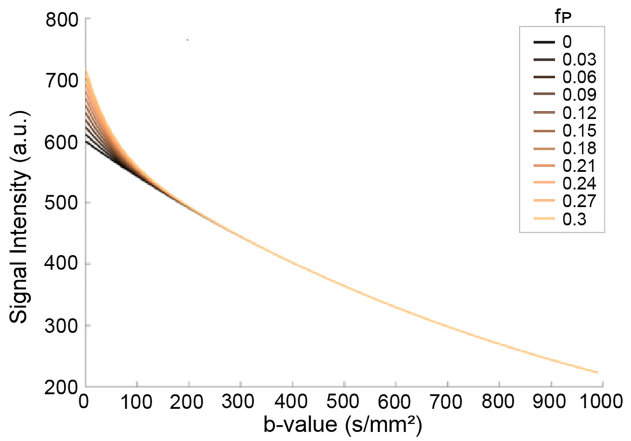

FIGURE 6 | Effects of pseudo-diffusion on DWI signal. Signal curves in the presence of increasing IVIM effects deviate from the simple mono-exponential curve (f_p=0, black line). The components have unique coefficients D_t = 0.001 s/mm^2 and D* = 0.02 s/mm^2 with relative proportions given by the pseudo-diffusion fraction f_p (164). (Courtesy of Igor Vidić, PhD, previously at the Department of Physics, Norwegian University of Science and Technology, Trondheim, Norway).

Multiple studies found a correlation between D_t values and Ki-67 expression (149, 161, 162, 167, 168), with two of these studies demonstrating a correlation with f_p values (161, 168). Evaluation of the association of IVIM metrics with lymph node metastases and histologic grade, however, have yielded conflicting results (56, 159, 161, 166, 168).

A study by Lee et al. investigated the association of IVIM parameters with two markers of tumor angiogenesis, microvascular density (MVD) and vascular endothelial growth factor (VEGF), in patients with breast cancer using 4 different curve fitting algorithms (169). The authors found significant associations between multiple perfusion related parameters and VEGF using a linear regression model to determine D_t and f_p at high b values, and linear regression to determine D* at low b values (≤50 s/mm^2) (169). However, no association was found between MVD and IVIM parameters obtained by the 4 different curve fitting algorithms, and additional studies are needed to determine if there is a correlation (169).

Histogram analysis of IVIM parameters performed by a few groups demonstrated the potential to distinguish breast cancer subtypes and additional prognostic factors (36, 166, 170). As opposed to the majority of studies where the average values for IVIM metrics are obtained, histogram analysis appears to provide additional information of the distribution of the metrics, including skewness and kurtosis, which better reflect tumor heterogeneity.

A few studies evaluating the ability of IVIM parameters to predict treatment response have shown conflicting results. Two studies reported increased D_t values following NAC in the responder (or pCR) group (171, 172), whereas two other studies did not find significant differences between groups (70, 173). The small sample sizes in these studies may account for the observed differences, warranting further investigation with larger cohorts.

Direct comparison across studies is limited due to the variability in the methods of image acquisition and data analysis, as the choice of curve fitting methods and b-values have been shown to affect IVIM metrics (174, 175).

The b-value selection significantly affects IVIM metrics. A threshold value of 200 s/mm^2 has been used, with perfusion effects predominating below 200 s/mm^2 and diffusion effects predominating above 200 s/mm^2 (150, 151, 153, 174). However, a variety of threshold b-values have been used in breast studies and there is currently no consensus on the optimal threshold or b-values choice. A study by Chen et al. aimed to determine the optimal threshold b-value and found an optimal cutoff value of 300 s/mm^2 discriminated diffusion from perfusion effects (176). Ongoing research efforts aim to determine the optimal b-values. For example, Cho et al. compared a free (conventional constrained least squares fit) versus a segmented (two step

constrained analysis) fitting method for both conventional or optimized b-values (174). This group found that the IVIM values differed significantly according to the sampling method, with a segmented method for optimized b-values showing the highest accuracy and precision (174).

Several studies have investigated different fitting and analysis methods for IVIM in order to increase accuracy and differentiation between lesion type. Suo et al. compared three frequently used calculation methods in women with biopsy proven IDC and found significantly higher precision when using either of the applied two step calculation methods compared to the conventional free fitting model (175). Most IVIM metrics differed significantly according to the calculation method, with a significantly larger f_p value with the free fitting model (175).

Bayesian fitting approaches have been investigated as an alternative to nonlinear least squares fitting (177, 178). The Bayesian model uses prior knowledge or assumptions of the system to provide estimates of IVIM parameters for pixels with a high degree of data fitting uncertainty, decreasing heterogeneity in the parameter maps (177). A study by While et al. compared the performance of multiple Bayesian modeling approaches with least squares-based approaches on simulated breast and liver tissue (177). In terms of relative error and estimator deviation, Bayesian approaches outperformed both full and segmented least squares-based methods (177). However, in areas of high parameter uncertainty, certain features disappeared, potentially masking important tissue characteristics and limiting interpretation (177). This study also showed that segmented least squares approach was superior to the full nonlinear approach in the breast (177).

Alternative methods of data analysis have been proposed. In one such method called the exhaustive approach, the parameters are derived from comparing the raw signal to an exhaustive database of simulated signals, comprised of a large set of parameter combinations (153). This method may provide a better estimation of IVIM metrics by eliminating the local minima issue seen in fitting models, but it requires high processing power (153). An additional method, termed the simplified approach, uses only three b-values to calculate the relative enhanced diffusivity (RED), a metric that pools the effects of ADC mapping and IVIM modeling (179, 180). A study by Teruel et al. found that the RED differentiated malignant from benign breast lesions with an overall accuracy of 90% using b-values of 0, 200 and 700 s/mm^2 (180).

Diffusion Kurtosis Imaging (DKI)

Diffusion kurtosis imaging (DKI) is an extension of DWI in which both Gaussian and non-Gaussian diffusion distributions are quantified, providing added insight into the tissue microstructure (181). DKI yields the parameters mean diffusivity (D), representing Gaussian diffusion, and mean kurtosis (MK, K), a unitless metric representing the degree of non-Gaussian diffusion. The DKI model is the following:

$$\ln \frac{S(b)}{S(0)} \approx -bD + \frac{1}{6} b^2 D^2 K \quad [3]$$

where S(b) is the DW signal with non-zero diffusion weighting, S (0) the signal without diffusion weighting, and b the diffusion weighting factor (181). As malignant lesions proliferate, increased cellularity results in decreased extracellular space and increased microstructural complexity (i.e. cell membranes and organelles), impairing Gaussian diffusion (182). The degree of deviation from Gaussian diffusion can be quantified by K, with increasing K value reflecting increasing deviation (**Figure 7**) (181).

The potential of DKI parameters in the characterization of breast lesions has been investigated. Multiple studies have found that malignant lesions demonstrate a significantly higher K (0.61-1.13) and lower D (1.01-1.52 × 10^{-3} mm^2/s) values compared to benign lesions (K of 0.37-0.69; D of 1.52-2.17 × 10^{-3} mm^2/s) (56, 150, 153, 182–188). Further, DKI studies have also shown promise in the K value for differentiating breast lesion types, as K was significantly higher in invasive cancers (0.93-0.94) compared to DCIS (0.78-0.81) (56, 188). Nogueira et al. found that K could differentiate a fibroadenoma from fibrocystic change (0.48 vs 0.25) (184).

Histogram analysis has been applied to the kurtosis model in two studies, in which it was found that histogram metrics within each individual group outperformed the mean values, which are typically used in standard diffusion kurtosis imaging (185, 189). Visualization of tumor heterogeneity *via* histogram analysis may result in identification of the most aggressive portions of the lesions and therefore increase diagnostic accuracy in the discrimination of benign and malignant lesions.

In terms of diagnostic performance, few reporting studies demonstrated a high AUC for both D and K in discriminating benign from malignant lesions (153, 182–184). Compared to ADC, kurtosis metrics in some studies demonstrate increased superior diagnostic performance (190), while in others, there was no significant difference (56, 187, 191).

The association of prognostic factors with kurtosis metrics has also been investigated, with studies yielding conflicting results. A few studies found a positive correlation between K and high histologic grade (186, 187, 190), while others showed no association (56, 191). Others also showed significantly increased K value with elevated Ki-67 expression (168, 186, 187, 190), while one found no significant association (108). Studies evaluating the correlation between kurtosis metrics and hormone receptor expression, HER2 status, and lymph node involvement also show varying results (56, 168, 186, 190).

The ability of DKI metrics to predict recurrence risk of breast cancer was evaluated by Wu et. al, and a significant difference was found among multiple histogram kurtosis metrics (D_{mean}, $D_{50\%}$, K_{mean}, $K_{30\%}$, $K_{50\%}$, $K_{70\%}$) and the low, intermediate and high RS groups (192). Specifically, the $K_{50\%}$ demonstrated the strongest correlation with risk scores and showed potential as a biomarker for the prediction of breast cancer recurrence.

Overall, the mixed performance of DKI in discriminating lesion malignancy and subtypes warrants critical evaluation into the sources of discrepancies prior to translation into clinical practice. For instance, Mlynarska-Bujny et al. found that residual fat signal from incompletely fat-suppressed DWI images significantly reduced the diagnostic performance of DKI measures

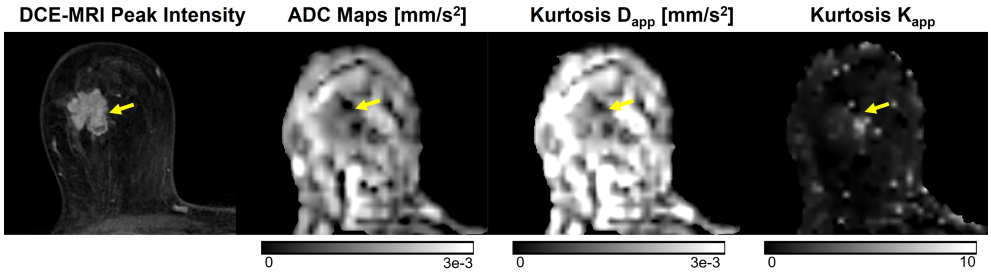

FIGURE 7 | Example of DKI analysis using b-values of 0, 500, 1000, and 2000 s/mm^2, compared to conventional ADC images using b-values of 0 and 1000 s/mm^2 and DCE-MRI peak intensity subtraction (1 min 30 s post-contrast). Invasive ductal carcinoma in a 67-year-old patient is indicated by the yellow arrow. The lesion displays higher mean kurtosis (K_{app}) than surrounding healthy tissue. Images were acquired using a wide-bore 3T scanner, and mean kurtosis and diffusivity (D_{app}) were calculated as previously demonstrated (181).

and proposed an additional fat correction term to account for fat-related signal contamination (193). Differences in experimental technique (e.g., diffusion time interval), analysis method, ROI selection, and subject variability seem to considerably influence DKI measures. Low SNR from high b-values and long scan times from an increased number of b-values needed for kurtosis modeling have also contributed to fewer clinical studies evaluating DKI (194). Future studies should aim to characterize the variation in DKI across acquisition parameters and provide recommendations for a standardized protocol.

Synthetic ADC (sADC)

There are several techniques where collecting multiple b-values is desired, however this process consumes scan time. Synthetic or shifted ADC (sADC), potentially addresses the issue of increased scan time by calculating the sADC at two shifted b-values, typically 200 s/mm^2 and 1500 s/mm^2, with the aim of capturing both Gaussian and non-Gaussian diffusion (150). A reader study conducted by Iima et al. compared sADC (using b-values=200 and 1500 s/mm^2) to two integrated diagnostic approaches (combined thresholds approach using IVIM and kurtosis parameters and a Bayesian approach) in the characterization of breast lesions (150). The "combined thresholds" approach calculated the K and ADC at b=0 s/mm^2 using the kurtosis model and combined them with f_{IVIM} to create a single metric comparable to the BI-RADS score. The Bayesian approach used the f_{IVIM}, ADC_0 and K within each individual lesion to create a probability for BI-RADS categories. The three approaches had high positive predictive value (for radiologists A and B, respectively: combined thresholds, 92.3% and 90.1%; Bayesian approach, 94.6% and 89.7%; and sADC approach, 92.3% and 93.2%), comparable with BI-RADS (93.8%) (150). Furthermore, sADC values differed significantly according to histologic subtypes (P = 0.006). While sADC did not demonstrate higher overall diagnostic performance compared to BI-RADS, the results of the study indicate the parameter's potential as a non-contrast diagnostic tool. Another study by Choi et al. compared synthetic DWI at b-values of 1000 and 1500 s/mm^2 with conventional DWI at b-values of 800 and 1500 s/mm^2 in a group of 50 individuals with breast cancer (195). $sDWI_{1500}$ showed increased lesion conspicuity compared to conventional DWI_{1500}, similar to the results of a study by Bickel et al. (196). Although $sDWI_{1500}$ demonstrated decreased overall image quality compared to conventional DWI_{1500}, the difference in cancer detection rate was not statistically significant (195). While sADC may demonstrate potential as a rapid alternative to DCE-MRI or conventional DWI, larger studies are needed to better evaluate its diagnostic performance in the breast. The limitation of the synthetic higher b-value is that although it may improve tumor conspicuity, it does not reflect true physiologic assessment associated with real higher b-value data.

Stretched Exponential Model

The stretched exponential model is another emerging non-Gaussian diffusion technique that provides added information about diffusion heterogeneity. Parameters include the distributed diffusion coefficient (DDC), which represents the mean intravoxel diffusion rate, and alpha (α), a value between 0 and 1 which quantifies the degree of deviation from monoexponential behavior. An alpha value of 1 represents pure Gaussian diffusion whereas lower values represent diffusion heterogeneity and represent a potential surrogate for tissue complexity (56). Significantly lower DDC and alpha values have been demonstrated in malignant lesions (DDC: 0.72-1.00 $\times$ 10^{-3} mm^2/s, α: 0.62-0.78) compared to benign lesions (DDC: 1.22-1.84 $\times$ 10^{-3} mm^2/s, α: 0.67-0.90) and normal breast tissue (DDC: 1.38-1.83 $\times$ 10^{-3} mm^2/s, α: 0.74-0.86) (**Figure 8**) (56, 197–200). A few studies have also demonstrated that DDC can discriminate invasive breast cancer from DCIS (56, 199) (56).

A study by Suo et al. compared the diagnostic utility of the monoexponential, biexponential, stretched exponential, and kurtosis models in the evaluation of breast lesions (56). The group found a negative correlation between alpha level and tumor size and Ki-67 expression, which is consistent with the hypotheses that larger tumors and those with higher Ki-67 expression (a marker of cellularity) demonstrate increased microperfusion and microstructural heterogeneity. The study also found significantly lower DDC values for ER positive tumors compared to ER negative tumors (0.68 versus 0.77) (56).

Regarding goodness-of-fit assessment, the kurtosis model best characterized benign voxels, while the stretched exponential model best characterized malignant voxels. Though multiple non-monoexponential parameters correlated significantly with malignancy, the diagnostic accuracy was not superior to conventional ADC, suggesting that these metrics may provide additional information for tissue characterization but that ADC may remain the standard for breast cancer diagnosis (56).

Signature Index

Another diffusion weighted technique which may mitigate the issue of complex post-processing and long acquisition times is the Signature index (s-index) proposed by Goto et al., which requires acquisitions at only 3 b-values (201). The S-index is a model free parameter derived from the difference in signal between the tissue in question and a library of reference DW signals for both malignant and benign lesions at two key b-values (201). Using this method, the authors reported comparable diagnostic performance of the S-index and sADC in the discrimination of malignant and benign breast lesions (201). The combination of the S-index with BI-RADS showed the highest diagnostic accuracy. The S-index was also found to correlate with HER2 status and PR expression. One potential drawback is that some of the specificity afforded by individual parameter values that reflect either microvascular or structural changes is lost with the S-index (201).

Restriction Spectrum Imaging (RSI)

Restriction spectrum imaging (RSI) is an emerging advanced DWI technique that aims to characterize tumor microenvironment based on the behavior of water molecules in different tissue-specific water pools (202–204). The RSI model requires multiple b-values (including b-values up to 4000 s/mm^2) and diffusion directions at a fixed diffusion time in order to produce maps that differentiate: [1] isotropic restricted (intracellular), [2] anisotropic hindered (extracellular), and [3] free water diffusion compartments (5). This distinction allows for the isolation of diffusion related changes secondary to peritumoral edema or necrosis, which often confounds standard ADC measurements, particularly in the evaluation of aggressive malignancies. In a small group of patients with high grade brain tumors, RSI improved lesion conspicuity and delineation compared to standard DWI (5). Additionally, in the evaluation of tumor response to antiangiogenic treatment in a group of patients with recurrent gliomas, RSI was less affected by medication-induced alterations in edema when compared to ADC, potentially addressing the issue of pseudoresponse and providing a method to identify true tumor response (5).

While initial oncologic applications were in the brain and prostate, the potential role of RSI in breast cancer is actively being explored. Rodríguez-Soto et al. found that a three-component (tri-exponential) RSI model better discriminates malignant lesions from healthy fibroglandular tissue compared to a bi-exponential model and conventional ADC, with similar tumor conspicuity as DCE-MRI (205). In the tri-exponential RSI breast-specific model, the main outputs are signal contribution maps of each compartment C_1, C_2 and C_3. The signal contributions from slow diffusion compartments (C_1 and C_2) were larger in malignant lesions than they were in healthy tissue (**Figure 9**) (205). In another study, Andreassen et al. utilized the three-component RSI model to characterize breast lesions in a group of 106 women with pathology-proven breast cancer (206). In this study, the RSI derived parameter C_1C_2, representing the product of the signal contributions of the slowest components C_1 and C_2, demonstrated comparable diagnostic accuracy to DCE-MRI, with an AUC of 0.984 (206). The false positive rate, given a sensitivity of 80% ($FPR_{80\%}$), of the C_1C_2 parameter (0.016) was significantly lower than that of conventional ADC (0.731) and K (0.684) (206). It is hypothesized that the higher discriminatory performance of C_1C_2 could be attributed to the ability of this parameter to suppress signal from both fibroglandular and fatty

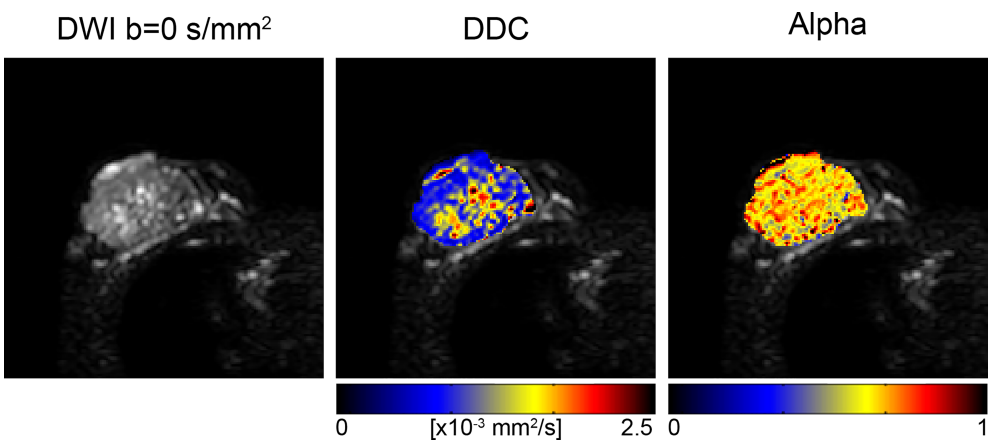

FIGURE 8 | Stretched exponential modeling with b-values of 0, 500, 1000, 1500 and 2000 s/mm^2 in a 73-year-old patient with invasive ductal carcinoma. Distributed diffusion coefficient (DDC) and alpha maps are overlaid on DWI b=0 s/mm^2 images, acquired at 3T (56). (Courtesy of Shiteng Suo, PhD, and Jia Hua, MD, Department of Radiology, Ren Ji Hospital, School of Medicine, Shanghai Jiao Tong University, Shanghai, China).

tissues, as well as maintain the signal contribution from T_2 that further differentiates these tissues (206). A case report by Rodríguez-Soto et al. demonstrated the ability of RSI to isolate different water pools in the breast by significantly increasing lesion conspicuity in a lactating woman (high BPE) with biopsy proven IDC compared to both DCE-MRI and conventional DWI (207). Thus, emphasizing the utility of the technique in identifying active disease separate from edema from a lactating breast. Studies of RSI in the breast have thus been performed in patients with known malignancy, and like other diffusion techniques may be challenged in evaluating small lesions. Next steps include adapting RSI to high resolution diffusion imaging, thus allowing the technique to be useful in a screening population (208)

Time Dependent Diffusion (TDD)

While ADC values obtained from conventional DWI reflect tissue cellularity, it cannot specifically differentiate underlying sub-cellular parameters such as cell size or density (209). Time dependent diffusion, sometimes called temporal diffusion spectroscopy, has shown potential as an emerging parameter to provide added information about the intracellular space, and thereby further characterize tissue biology (209).

Lima et al. demonstrated the time dependence of the ADC value in breast cancer xenografts, with increasing ADC values with increasing diffusion time (210). A few geometric models applied to the diffusion weighted signal, some of which utilize oscillating gradient spin echo (OGSE) acquisitions in addition to pulsed gradient spin echo (PGSE), quantified intracellular diffusion restriction and provided adequate estimates of cell size and intracellular volume (209, 211).

Teruel et al. applied a stimulated echo acquisition mode (STEAM) with multiple diffusion times to normal and pathologic breasts and used a DTI model to fit the data (**Figure 10**). Results showed differences in the estimation of the radial diameter and diffusion length scales for healthy fibroglandular tissue, a simple cyst, and malignant lesions. Complete fat suppression was also seen with longer diffusion times, allowing for more accurate T1 mapping (212).

A few groups have shown that TDD methods increase lesion contrast and may play a role in assessment of treatment response by detecting changes in cell size (211, 213–215). More research is needed to fully understand the application of TDD In breast cancer.

Radiomics

With the growth of precision medicine comes an opportunity for radiologists to add value by providing relevant information about the patient's underlying disease in a non-invasive manner. Radiomics is a method of extracting and analyzing large amounts of advanced quantitative data to create a mineable database (216, 217). This data is then used to create analytic and predictive models to correlate radiomic features with diagnostic and prognostic information. Ideally, these radiomic features or signatures would provide insight to the underlying tumor biology and contribute to individualized treatment (216). The standard radiomic process includes 1) image acquisition and reconstruction, 2) image segmentation 3) feature extraction and qualification, and 4) database creation (216, 217).

Ye et al. provided an in depth review of the application of radiomics in breast MRI (216). Although most of the studies were based on DCE modalities, a few were multiparametric and included DWI acquisitions, and even fewer utilized only DWI. For this review, only studies that included DW images will be discussed.

A few groups have evaluated the ability of radiomic models to characterize breast lesions.

Bickelhaupt et al. reported that a Radiomics model based on DKI in the evaluation of mammographic BI-RADS 4 and 5 lesions outperformed ADC and K alone, with improved specificity and a reduction in the number of false positive results by 70% (218). A few multiparametric studies have also demonstrated the ability of radiomic models to differentiate benign from malignant lesions (219–221). Zhang et al. demonstrated an AUC of 0.921 and accuracy of 0.833 in discriminating lesions when using a model based off of T2 weighted, DKI, and quantitative DCE-MRI parameter maps (221). Parekh and Jacobs presented a new radiomic feature mapping framework created from multiple MR

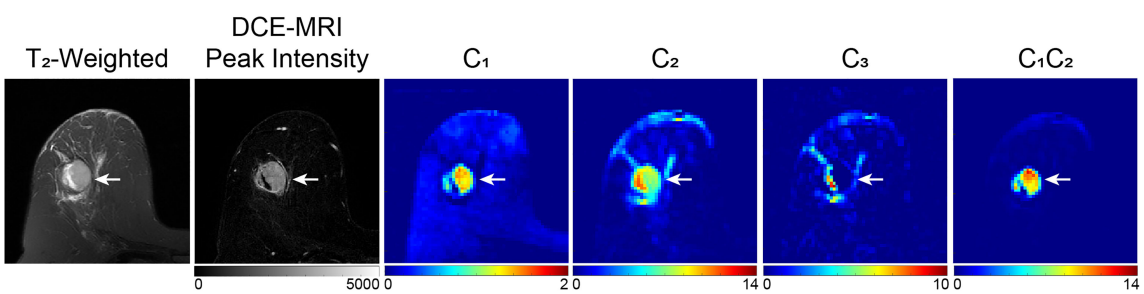

FIGURE 9 | Example of three-compartment RSI analysis in a 49-year-old patient with invasive ductal carcinoma. C_1, C_2, and C_3 maps correspond to the slowest, intermediary, and fastest diffusion compartments, respectively. The lesion, indicated by the white arrow, is hypointense on C_1 and C_2 maps compared to surrounding healthy tissue, whereas there is little difference in the C_3 compartment, which is suggested to correspond to vasculature. The product of C_1 and C_2 (C_1C_2) results in the greatest tumor conspicuity. DWI images were acquired at b = 0, 500, 1500, and 4000 s/mm^2 on a 3T scanner, with 50% reduced FOV and without parallel imaging (206).

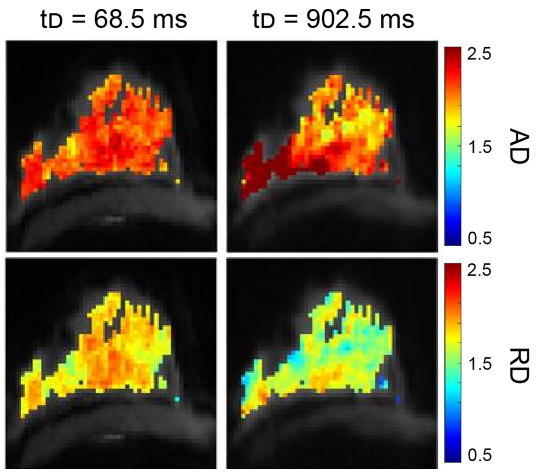

FIGURE 10 | Example of STEAM analysis in a healthy volunteer. The protocol collected a prototype STEAM-DTI sequence with two b-values (0, 500 s/mm^2) in six directions with parallel imaging in a 3T scanner. Axial diffusivity (AD, first row) and radial diffusivity (RD, second row) [μm^2/ms] parametric maps at the shortest and longest diffusion time for healthy fibroglandular tissue are shown (212). (Courtesy of Jose Teruel, PhD, Department of Radiation Oncology, NYU Langone Medical Center, New York, New York, USA).

sequences and evaluated the utility of this method in the characterization of breast lesions. Authors reported significant differences in textural features between malignant and benign lesions, with an overall sensitivity and specificity of 93% and 85%. Radiomic feature maps provide the added benefit of visual interpretation of feature values as well as lesion heterogeneity (222).

Recent studies have also evaluated the role of radiomics in the prediction of breast cancer subtypes and other prognostic factors. Holli-Helenius et al. reported that the texture features sum entropy and sum variance significantly differed between Luminal A and Luminal B subtypes, with a AUC of 0.876 for the combined radiomic model (223). Other studies have also demonstrated the potential of texture analysis to discriminate among different breast cancer subtypes (224–226). A study by Leithner et al. showed improved accuracy for breast cancer subtype classification when segmentation was performed on the ADC maps, with the highest discriminatory ability seen with Luminal B and HER2 enriched subtypes (227).

In a study by Dong et al., a radiomic model derived from a combination of T2-FS and DWI textural features demonstrated high performance in the prediction of axillary lymph node metastases, with an AUC of 0.863 in the training set and 0.805 in the validation set (228). Another group created predictive models from T1WI, T2WI, DWI and the second post-contrast phase of DCE sequences, and reported an AUC of 0.85 for DWI alone in the prediction of axillary lymph node metastases (229). The highest performance was reported for the model based off of CE2 images with kinetic features, with an AUC of 0.91 (229). No additional performance benefit was found when features from all four sequences were combined, suggesting that DWI radiomic signatures may not play as important a role in the preoperative prediction of axillary lymph node metastases (229).

A few groups have also shown good performance in the ability of radiomic models to predict Ki-67 expression (AUC 0.7 – 0.888) (230–232). A study by Fan et al. found that radiomic analysis of "super resolution" (SR) ADC images better predicted histologic grade and Ki-67 expression compared to features based on conventional ADC images, demonstrating the potential added diagnostic value of a SR technique (233).

The degree to which DWI-based radiomic analyses can predict response to NAC has been investigated by a few groups. Liu et al. found that a radiomics model derived from multiparametric MRI and clinical information better predicted pCR to NAC than individual clinical models and radiomic signatures (234). A model built from pretreatment texture and kinetic parameters significantly helped predict nonresponders with 84% sensitivity in another study (235). A study by Panzeri et al., however, reported no significant correlations between ADC texture radiomic signatures and response to NAC, but parameters derived from DCE-MRI showed utility in predicting response (236).

Comparison across studies is limited as the methods and population sizes used to develop radiomic signatures vary. The role of DWI in radiomics remains under active investigation, many groups demonstrated the potential to aid in the diagnosis, prognosis and surveillance of breast cancer.

Ultra-High Field Strength

Increasing the field strength is another method in which diffusion-weighted imaging may be improved. The increased CNR and SNR at higher field strengths lead to improved spatial and temporal resolution, which may increase lesion conspicuity and detection. A meta-analysis by Shi et al. included 61 studies comprising 5205 breast lesions and found no significant difference in the diagnostic performance of DWI in the differentiation of malignant and benign lesions at 1.5 T compared to 3 T (32).

Several technical limitations arise when increasing the field strength, particularly at ultra-high fields (7T and above). At 7T, DWI must overcome limitations due to the increased specific absorption rate (SAR) in addition to heterogeneous fat suppression and T2* blurring, which degrade image quality. A few groups have mitigated these issues through the use of bilateral coil designs and demonstrated the feasibility of DWI of the breast at 7T (**Figure 11**) (26, 237–240).

Bogner et al. showed that combination of rs-EPI DWI with parallel imaging at 7T significantly reduced artifacts and improved image quality, with submillimeter resolution and good diagnostic performance in the characterization of breast lesions (238). A study by Gruber et al. compared DWI of breast lesions at 7T versus 3T using rs-EPI and found increased sensitivity (100% compared to 94%) at 7T for the same ADC threshold and specificity, comparable SNR and CNR, and a 2.4 times higher spatial resolution. These findings suggest that 7T may aid in the detection of smaller lesions that otherwise are more difficult to visualize (239).

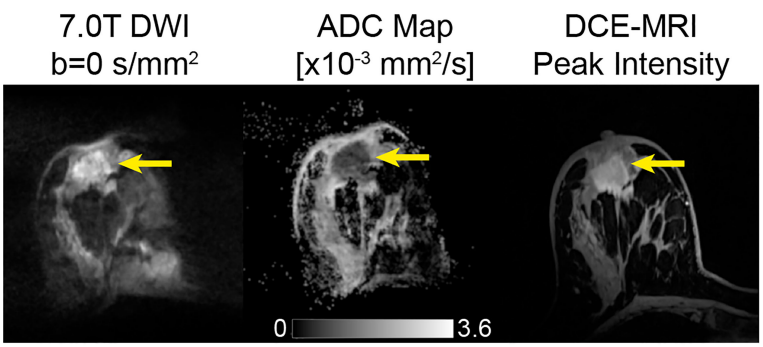

FIGURE 11 | 39-year-old female with invasive ductal carcinoma, imaged at 7T using a dedicated four-channel double-tuned $^{31}P/^{1}H$ breast coil. Images shown are b=0 s/mm^2, corresponding ADC map, and DCE-MRI peak intensity subtraction. The mean ADC of the tumor shown is 0.71 ± 0.18 × 10^{-3} mm^2/s. For DWI, a transverse DWI read-out segmented echo-planar imaging sequence was used. For DCE, patients were intravenously injected with a single dose of contrast agent (gadoterate meglumine) as a bolus, followed by a 20-mL saline flush after three of the 18 repetitions of the time-resolved angiographic imaging with stochastic trajectories sequence (26). (Courtesy of Katja Pinker-Domenig, MD, PhD, Department of Radiology, Memorial Sloan Kettering Cancer Center, New York, New York, USA).

Multiparametric MRI of the breast at 7T was also performed by a few groups (26, 237, 240). Of note, Pinker et al. generated excellent quality images and found that multiparametric MR eliminated false negative findings and decreased the number of false positive findings in 40 women (26). Clinically, this may translate into a reduced number of unnecessary biopsies and improved diagnostic accuracy.

Though most of the literature consists of a few studies with small sample sizes, the results are promising with the main limitation being the general lack of accessibility to 7T scanners for most patients (and breast imaging researchers).

DISCUSSION

An abundance of evidence has shown the utility of DWI as an imaging biomarker for breast cancer, with applications ranging from screening, lesion detection and characterization, and treatment response evaluation. The monoexponential ADC has shown promise in differentiating benign and malignant lesions; however, significant overlap in reported ADC ranges for these tissues limit the clinical utility of ADC cutoffs. Further, there have been conflicting results in the ability of ADC in discriminating lesion subtypes, likely owing to varying study design and protocol differences. Recently, the ACRIN 6698 trial showed high precision in a multi-institution and multi-platform setting, marking a milestone in the validation of DWI as a biomarker in breast imaging and highlighting the need for standardized protocols. As a result, a breast section was incorporated into the 2019 QIBA profile, providing guidance for implementation in community practice.

As described throughout this review, some advanced DWI models require data acquisition at high b-values, which increases susceptibility to B_0 inhomogeneity-induced artifacts and noise, especially for EPI-based sequences. Thus, several methods have been proposed to address this issue, but are beyond the scope of this review (241). An additional limitation of breast DWI is that due to the breast's underlying tissue complexity (e.g. intricate composition of fat, fibroglandular tissue and cancers), measurements of DWI-derived parameters in tissues different from fat tend to be underestimated unless adequate fat suppression is achieved (182). Moreover, the monoexponential ADC, which assumes Gaussian diffusion, may not completely capture the complex diffusivity properties of the breast, especially in lesions which display increased tissue heterogeneity. This may explain the conflicting results observed across multiple studies.

To circumvent the limitations of standard ADC, advanced diffusion modeling techniques such as DKI, DTI, IVIM, and RSI may provide added information on the underlying microenvironment by characterizing the non-Gaussian diffusion within tissues. Although promising, the advanced modeling techniques discussed in this paper require further validation through multi-institution studies, optimization of protocol parameters, and demonstration of repeatability and reproducibility prior to use in clinical practice.

With continued research on methods to improve standard DWI, such as increasing field strength and alternative acquisition techniques, advanced modelling techniques, and radiomics, DWI may play an increasingly important role in the evaluation of breast cancer.

AUTHOR CONTRIBUTIONS

AM: this author was responsible for interpreting the relevant literature and drafting the majority of the review. LF: this author was responsible for revising portions of the review and creating the figures. CM: this author was responsible for drafting and revising portions of the review. SB: this author was responsible for revising portions of the review. SL: this author was responsible for generating data and creating figures. AR-S: this author was responsible for critically revising the review and serving as an expert in the field. RR-P: this author was responsible for critically

revising the review, serving as an expert in the field, and approving the final draft. All authors contributed to the article and approved the submitted version.

FUNDING

This work was supported by the California Breast Cancer Research Program [24IB-0056 IDEA Award] and the Krueger v. Wyeth Research Award, and the National Cancer Institute R37 CA249659, and GE Research. The funder was not involved in the study design, collection, analysis, interpretation of data, the writing of this article or the decision to submit it for publication.

ACKNOWLEDGMENTS

We would like to thank our colleagues cited above who contributed images to our review and Alexandra Schlein, our lab manager, for her efforts on this project.

REFERENCES

1. Lehman CD, Schnall MD. Imaging in Breast Cancer: Magnetic Resonance Imaging. *Breast Cancer Res* (2005) 7(5):215. doi: 10.1186/bcr1309
2. Kaiser WA, Zeitler E. MR Imaging of the Breast: Fast Imaging Sequences With and Without Gd-DTPA. Preliminary Observations. *Radiology* (1989) 170(3 Pt 1):681–6. doi: 10.1148/radiology.170.3.2916021
3. Heywang SH, Fenzl G, Hahn D, Krischke I, Edmaier M, Eiermann W, et al. MR Imaging of the Breast: Comparison With Mammography and Ultrasound. *J Comput Assist Tomogr.* (1986) 10(4):615–20. doi: 10.1097/00004728-198607000-00014
4. Aminololama-Shakeri S, Lewin J, Appelton C, Lee CS, Giess CS, Ojeda-Fournier H, et al. *ACR Practice Parameter for the Performance of Contrast-Enhanced Magnetic Resonance Imaging (MRI) of the Breast*. American College of Radiology (2021). Available at: https://www.acr.org/-/media/ACR/Files/Practice-Parameters/mr-guided-breast.pdf?la=en.
5. White NS, McDonald C, Farid N, Kuperman J, Karow D, Schenker-Ahmed NM, et al. Diffusion-Weighted Imaging in Cancer: Physical Foundations and Applications of Restriction Spectrum Imaging. *Cancer Res* (2014) 74 (17):4638–52. doi: 10.1158/0008-5472.CAN-13-3534
6. Camps-Herrero J. Diffusion-Weighted Imaging of the Breast: Current Status as an Imaging Biomarker and Future Role. *BJR|Open* (2019) 1(1):20180049. doi: 10.1259/bjro.20180049
7. Basser PJ. Inferring Microstructural Features and the Physiological State of Tissues From Diffusion-Weighted Images. *NMR BioMed* (1995) 8(7–8):333–44. doi: 10.1002/nbm.1940080707
8. Basser PJ, Pierpaoli C. Microstructural and Physiological Features of Tissues Elucidated by Quantitative-Diffusion-Tensor MRI. *J Magn Reson B* (1996) 111(3):209–19. doi: 10.1006/jmrb.1996.0086
9. Partridge SC, McDonald ES. Diffusion Weighted MRI of the Breast: Protocol Optimization, Guidelines for Interpretation, and Potential Clinical Applications. *Magn Reson Imaging Clin N Am* (2013) 21(3):601–24. doi: 10.1016/j.mric.2013.04.007
10. Amornsiripanitch N, Bickelhaupt S, Shin HJ, Dang M, Rahbar H, Pinker K, et al. Diffusion-Weighted MRI for Unenhanced Breast Cancer Screening. *Radiology* (2019) 293(3):504–20. doi: 10.1148/radiol.2019182789
11. Monticciolo DL, Newell MS, Moy L, Niell B, Monsees B, Sickles EA. Breast Cancer Screening in Women at Higher-Than-Average Risk: Recommendations From the ACR. *J Am Coll Radiol* (2018) 15(3 Pt A):408–14. doi: 10.1016/j.jacr.2017.11.034
12. McDonald ES, Hammersley JA, Chou S-HS, Rahbar H, Scheel JR, Lee CI, et al. Performance of DWI as a Rapid Unenhanced Technique for Detecting Mammographically Occult Breast Cancer in Elevated-Risk Women With Dense Breasts. *Am J Roentgenol* (2016) 207(1):205–16. doi: 10.2214/AJR.15.15873
13. Yabuuchi H, Matsuo Y, Sunami S, Kamitani T, Kawanami S, Setoguchi T, et al. Detection of non-Palpable Breast Cancer in Asymptomatic Women by Using Unenhanced Diffusion-Weighted and T2-Weighted MR Imaging: Comparison With Mammography and Dynamic Contrast-Enhanced MR Imaging. *Eur Radiol* (2011) 21(1):11–7. doi: 10.1007/s00330-010-1890-8
14. Amornsiripanitch N, Rahbar H, Kitsch AE, Lam DL, Weitzel B, Partridge SC. Visibility of Mammographically Occult Breast Cancer on Diffusion-Weighted MRI Versus Ultrasound. *Clin Imaging* (2018) 49:37–43. doi: 10.1016/j.clinimag.2017.10.017
15. Pinker K, Moy L, Sutton EJ, Mann RM, Weber M, Thakur SB, et al. Diffusion-Weighted Imaging With Apparent Diffusion Coefficient Mapping for Breast Cancer Detection as a Stand-Alone-Parameter: Comparison With Dynamic Contrast-Enhanced and Multiparametric Magnetic Resonance Imaging. *Invest Radiol* (2018) 53(10):587–95. doi: 10.1097/RLI.0000000000000465
16. Baltzer P, Mann RM, Iima M, Sigmund EE, Clauser P, Gilbert FJ, et al. Diffusion-Weighted Imaging of the Breast-a Consensus and Mission Statement From the EUSOBI International Breast Diffusion-Weighted Imaging Working Group. *Eur Radiol* (2020) 30(3):1436–50. doi: 10.1007/s00330-019-06510-3
17. Geach R, Jones LI, Harding SA, Marshall A, Taylor-Phillips S, McKeown-Keegan S, et al. The Potential Utility of Abbreviated Breast MRI (FAST MRI) as a Tool for Breast Cancer Screening: A Systematic Review and Meta-Analysis. *Clin Radiol* (2021) 76(2):154.e11–154.e22. doi: 10.1016/j.crad.2020.08.032
18. Yamada T, Kanemaki Y, Okamoto S, Nakajima Y. Comparison of Detectability of Breast Cancer by Abbreviated Breast MRI Based on Diffusion-Weighted Images and Postcontrast MRI. *Jpn J Radiol* (2018) 36 (5):331–9. doi: 10.1007/s11604-018-0731-6
19. Baltzer PAT, Benndorf M, Dietzel M, Gajda M, Camara O, Kaiser WA. Sensitivity and Specificity of Unenhanced MR Mammography (DWI Combined With T2-Weighted TSE Imaging, ueMRM) for the Differentiation of Mass Lesions. *Eur Radiol* (2010) 20(5):1101–10. doi: 10.1007/s00330-009-1654-5
20. Bickelhaupt S, Laun FB, Tesdorff J, Lederer W, Daniel H, Stieber A, et al. Fast and Noninvasive Characterization of Suspicious Lesions Detected at Breast Cancer X-Ray Screening: Capability of Diffusion-Weighted MR Imaging With MIPs. *Radiology* (2015) 278(3):689–97. doi: 10.1148/radiol.2015150425
21. Baltzer PAT, Bickel H, Spick C, Wengert G, Woitek R, Kapetas P, et al. Potential of Noncontrast Magnetic Resonance Imaging With Diffusion-Weighted Imaging in Characterization of Breast Lesions: Intraindividual Comparison With Dynamic Contrast-Enhanced Magnetic Resonance Imaging. *Invest Radiol* (2018) 53(4):229–35. doi: 10.1097/RLI.0000000000000433
22. Kang JW, Shin HJ, Shin KC, Chae EY, Choi WJ, Cha JH, et al. Resonance Screening Using Fused Diffusion-Weighted Imaging and Maximum-Intensity Projection in Patients With a Personal History of Breast Cancer: Role of Fused DWI for Postoperative Screening. *Breast Cancer Res Treat* (2017) 165(17):119–28. doi: 10.1007/s10549-017-4322-5
23. Shahid H, Wiedenhoefer JF, Dornbluth C, Otto P, Kist KA. An Overview of Breast MRI. *Appl Radiol* (2016) 45(10):7–13. doi: 10.37549/AR2317
24. Rahbar H, Partridge SC. Multiparametric Breast MRI of Breast Cancer. *Magn Reson Imaging Clin N Am* (2016) 24(1):223–38. doi: 10.1016/j.mric.2015.08.012
25. Zhang L, Tang M, Min Z, Lu J, Lei X, Zhang X. Accuracy of Combined Dynamic Contrast-Enhanced Magnetic Resonance Imaging and Diffusion-Weighted Imaging for Breast Cancer Detection: A Meta-Analysis. *Acta Radiol* (2016) 57(6):651–60. doi: 10.1177/0284185115597265
26. Pinker K, Baltzer P, Bogner W, Leithner D, Trattnig S, Zaric O, et al. Multiparametric MR Imaging With High-Resolution Dynamic Contrast-Enhanced and Diffusion-Weighted Imaging at 7 T Improves the Assessment of Breast Tumors: A Feasibility Study. *Radiology* (2015) 276(2):360–70. doi: 10.1148/radiol.15141905

27. Partridge SC, WB D, BF K, PR E, SW W, Lehman CD. Quantitative Diffusion-Weighted Imaging as an Adjunct to Conventional Breast MRI for Improved Positive Predictive Value. *Am J Roentgenol* (2009) 193 (6):1716–22. doi: 10.2214/AJR.08.2139
28. Khouli RH EI, Jacobs MA, Mezban SD, Huang P, Kamel IR, Macura KJ, et al. Diffusion-Weighted Imaging Improves the Diagnostic Accuracy of Conventional 3.0-T Breast MR Imaging1. *Radiology* (2010) 256(1):64–73. doi: 10.1148/radiol.10091367
29. Baxter GC, Graves MJ, Gilbert FJ, Patterson AJ. A Meta-Analysis of the Diagnostic Performance of Diffusion MRI for Breast Lesion Characterization. *Radiology* (2019) 291(3):632–41. doi: 10.1148/radiol.2019182510
30. Chen X, Li W, Zhang Y, Wu Q, Guo Y, Bai Z. Meta-Analysis of Quantitative Diffusion-Weighted MR Imaging in the Differential Diagnosis of Breast Lesions. *BMC Cancer* (2010) 10(1):693. doi: 10.1186/1471-2407-10-693
31. Tsushima Y, Takahashi-Taketomi A, Endo K. Magnetic Resonance (MR) Differential Diagnosis of Breast Tumors Using Apparent Diffusion Coefficient (ADC) on 1.5-T. *J Magn Reson Imaging* (2009) 30(2):249–55. doi: 10.1002/jmri.21854
32. Shi R, Yao Q, Wu L, Xu J. Breast Lesions: Diagnosis Using Diffusion Weighted Imaging at 1.5T and 3.0T—Systematic Review and Meta-Analysis. *Clin Breast Cancer* (2018) 18(3):e305–20. doi: 10.1016/j.clbc.2017.06.011
33. Surov A, Meyer HJ, Wienke A. Can Apparent Diffusion Coefficient (ADC) Distinguish Breast Cancer From Benign Breast Findings? A Meta-Analysis Based on 13 847 Lesions. *BMC Cancer* (2019) 19(1):955. doi: 10.1186/s12885-019-6201-4
34. Ding J-R, Wang D-N, Pan J-L. Apparent Diffusion Coefficient Value of Diffusion-Weighted Imaging for Differential Diagnosis of Ductal Carcinoma *in Situ* and Infiltrating Ductal Carcinoma. *J Cancer Res Ther* (2016) 12 (2):744–50. doi: 10.4103/0973-1482.154093
35. Zhao S, Shao G, Chen P, Li L, Yang Y, Zhao X, et al. Diagnostic Performance of Minimum Apparent Diffusion Coefficient Value in Differentiating the Invasive Breast Cancer and Ductal Carcinoma *in Situ*. *J Cancer Res Ther* (2019) 15(4):871–5. doi: 10.4103/jcrt.JCRT_607_18
36. Cho GY, Moy L, Kim SG, Baete SH, Moccaldi M, Babb JS, et al. Evaluation of Breast Cancer Using Intravoxel Incoherent Motion (IVIM) Histogram Analysis: Comparison With Malignant Status, Histological Subtype, and Molecular Prognostic Factors. *Eur Radiol* (2016) 26(8):2547–58. doi: 10.1007/s00330-015-4087-3
37. Horvat JV, Bernard-Davila B, Helbich TH, Zhang M, Morris EA, Thakur SB, et al. Diffusion-Weighted Imaging (DWI) With Apparent Diffusion Coefficient (ADC) Mapping as a Quantitative Imaging Biomarker for Prediction of Immunohistochemical Receptor Status, Proliferation Rate, and Molecular Subtypes of Breast Cancer. *J Magn Reson Imaging* (2019) 50(3):836–46. doi: 10.1002/jmri.26697
38. Jatoi I, Hilsenbeck SG, Clark GM, Osborne CK. Significance of Axillary Lymph Node Metastasis in Primary Breast Cancer. *J Clin Oncol* (1999) 17 (8):2334–40. doi: 10.1200/JCO.1999.17.8.2334
39. Sui WF, Chen X, Peng ZK, Ye J, Wu JT. The Diagnosis of Metastatic Axillary Lymph Nodes of Breast Cancer By Diffusion Weighted Imaging: A Meta-Analysis and Systematic Review. *World J Surg Oncol* (2016) 14(1):155. doi: 10.1186/s12957-016-0906-5
40. Kim EJ, Kim SH, Park GE, Kang BJ, Song BJ, Kim YJ, et al. Histogram Analysis of Apparent Diffusion Coefficient at 3.0t: Correlation With Prognostic Factors and Subtypes of Invasive Ductal Carcinoma. *J Magn Reson Imaging* (2015) 42(6):1666–78. doi: 10.1002/jmri.24934
41. Ren C, Zou Y, Zhang X, Li K. Diagnostic Value of Diffusion-Weighted Imaging-Derived Apparent Diffusion Coefficient and its Association With Histological Prognostic Factors in Breast Cancer. *Oncol Lett* (2019) 18 (3):3295–303. doi: 10.3892/ol.2019.10651
42. Belli P, Costantini M, Bufi E, Giardina GG, Rinaldi P, Franceschini G, et al. Diffusion Magnetic Resonance Imaging in Breast Cancer Characterisation: Correlations Between the Apparent Diffusion Coefficient and Major Prognostic Factors. *Radiol Med* (2015) 120(3):268–76. doi: 10.1007/s11547-014-0442-8
43. Surov A, Chang Y-W, Li L, Martincich L, Partridge SC, Kim JY, et al. Apparent Diffusion Coefficient Cannot Predict Molecular Subtype and Lymph Node Metastases in Invasive Breast Cancer: A Multicenter Analysis. *BMC Cancer* (2019) 19(1):1043. doi: 10.1186/s12885-019-6298-5
44. Suo S, Cheng F, Cao M, Kang J, Wang M, Hua J, et al. Multiparametric Diffusion-Weighted Imaging in Breast Lesions: Association With Pathologic Diagnosis and Prognostic Factors. *J Magn Reson Imaging* (2017) 46(3):740–50. doi: 10.1002/jmri.25612
45. Park SH, Choi H-Y, Hahn SY. Correlations Between Apparent Diffusion Coefficient Values of Invasive Ductal Carcinoma and Pathologic Factors on Diffusion-Weighted MRI at 3.0 Tesla. *J Magn Reson Imaging* (2015) 41 (1):175–82. doi: 10.1002/jmri.24519
46. Choi SY, Chang Y-W, Park HJ, Kim HJ, Hong SS, Seo DY. Correlation of the Apparent Diffusion Coefficiency Values on Diffusion-Weighted Imaging With Prognostic Factors for Breast Cancer. *Br J Radiol* (2012) 85(1016): e474–9. doi: 10.1259/bjr/79381464
47. Meng L, Ma P. Apparent Diffusion Coefficient Value Measurements With Diffusion Magnetic Resonance Imaging Correlated With the Expression Levels of Estrogen and Progesterone Receptor in Breast Cancer: A Meta-Analysis. *J Cancer Res Ther* (2016) 12(1):36–42. doi: 10.4103/0973-1482.150418
48. Suo S, Zhang D, Cheng F, Cao M, Hua J, Lu J, et al. Added Value of Mean and Entropy of Apparent Diffusion Coefficient Values for Evaluating Histologic Phenotypes of Invasive Ductal Breast Cancer With MR Imaging. *Eur Radiol* (2019) 29(3):1425–34. doi: 10.1007/s00330-018-5667-9
49. Okuma H, Sudah M, Kettunen T, Niukkanen A, Sutela A, Masarwah A, et al. Peritumor to Tumor Apparent Diffusion Coefficient Ratio is Associated With Biologically More Aggressive Breast Cancer Features and Correlates With the Prognostication Tools. *PloS One* (2020) 15(6):e0235278. doi: 10.1371/journal.pone.0235278
50. Aydin H, Guner B, Esen Bostanci I, Bulut ZM, Aribas BK, Dogan L, et al. Is There Any Relationship Between Adc Values of Diffusion-Weighted Imaging and the Histopathological Prognostic Factors of Invasive Ductal Carcinoma? *Br J Radiol* (2018) 91(1084):20170705. doi: 10.1259/bjr.20170705
51. Martincich L, Deantoni V, Bertotto I, Redana S, Kubatzki F, Sarotto I, et al. Correlations Between Diffusion-Weighted Imaging and Breast Cancer Biomarkers. *Eur Radiol* (2012) 22(7):1519–28. doi: 10.1007/s00330-012-2403-8
52. Kamitani T, Matsuo Y, Yabuuchi H, Fujita N, Nagao M, Jinnouchi M, et al. Correlations Between Apparent Diffusion Coefficient Values and Prognostic Factors of Breast Cancer. *Magn Reson Med Sci* (2013) 12(3):193–9. doi: 10.2463/mrms.2012-0095
53. Tezcan Ş, Uslu N, Öztürk FU, Akçay EY, Tezcaner T. Diffusion-Weighted Imaging of Breast Cancer: Correlation of the Apparent Diffusion Coefficient Value With Pathologic Prognostic Factors. *Eur J Breast Health* (2019) 15 (4):262–7. doi: 10.5152/ejbh.2019.4860
54. Amornsiripanitch N, Nguyen VT, Rahbar H, Hippe D, Gadi VK, Rendi MH, et al. Diffusion-Weighted MRI Characteristics Associated With Prognostic Pathological Factors and Recurrence Risk in Invasive ER+/HER2– Breast Cancers. *J Magn Reson Imaging* (2018) 48(1):226–36. doi: 10.1002/jmri.25909
55. Surov A, Clauser P, Chang Y-W, Li L, Martincich L, Partridge SC, et al. Can Diffusion-Weighted Imaging Predict Tumor Grade and Expression of Ki-67 in Breast Cancer? A Multicenter Analysis. *Breast Cancer Res* (2018) 20(1):58. doi: 10.1186/s13058-018-0991-1
56. Suo S, Cheng F, Cao M, Kang J, Wang M, Hua J, et al. Multiparametric Diffusion-Weighted Imaging in Breast Lesions: Association With Pathologic Diagnosis and Prognostic Factors: DWI in Breast Lesions. *J Magn Reson Imaging* (2017) 46(3):740–50. doi: 10.1002/jmri.25612
57. Goldhirsch A, Wood WC, Coates AS, Gelber RD, Thürlimann B, Senn H-J, et al. Strategies for Subtypes–Dealing With the Diversity of Breast Cancer: Highlights of the St. Gallen International Expert Consensus on the Primary Therapy of Early Breast Cancer 2011. *Ann Oncol: Official J Euro Soc Med Oncol* (2011) 22(8):1736–47. doi: 10.1093/annonc/mdr304
58. Meyer H-J, Wienke A, Surov A. Diffusion Weighted Imaging of Different Breast Cancer Molecular Subtypes. A Systematic Review and Meta Analysis. *Breast Care (Basel)* (2022) 17(1):47–54. doi: 10.1159/000514407
59. Surov A, Meyer HJ, Wienke A. Associations Between Apparent Diffusion Coefficient (ADC) and KI 67 in Different Tumors: A Meta-Analysis. Part 1:

ADCmean. *Oncotarget* (2017) 8(43):75434–44. doi: 10.18632/oncotarget.20406
60. Cheon H, Kim HJ, Kim TH, Ryeom H-K, Lee J, Kim GC, et al. Invasive Breast Cancer: Prognostic Value of Peritumoral Edema Identified at Preoperative MR Imaging. *Radiology* (2018) 287(1):68–75. doi: 10.1148/radiol.2017171157
61. Kettunen T, Okuma H, Auvinen P, Sudah M, Tiainen S, Sutela A, et al. Peritumoral ADC Values in Breast Cancer: Region of Interest Selection, Associations With Hyaluronan Intensity, and Prognostic Significance. *Eur Radiol* (2020) 30(1):38–46. doi: 10.1007/s00330-019-06361-y
62. Panzironi G, Moffa G, Galati F, Marzocca F, Rizzo V, Pediconi F. Peritumoral Edema as a Biomarker of the Aggressiveness of Breast Cancer: Results of a Retrospective Study on a 3 T Scanner. *Breast Cancer Res Treat* (2020) 181(1):53–60. doi: 10.1007/s10549-020-05592-8
63. Thompson AM, Moulder-Thompson SL. Neoadjuvant Treatment of Breast Cancer. *Ann Oncol* (2012) 23:x231–6. doi: 10.1093/annonc/mds324
64. Yeh E, Slanetz P, Kopans DB, Rafferty E, Georgian-Smith D, Moy L, et al. Prospective Comparison of Mammography, Sonography, and MRI in Patients Undergoing Neoadjuvant Chemotherapy for Palpable Breast Cancer. *Am J Roentgenol* (2005) 184(3):868–77. doi: 10.2214/ajr.184.3.01840868
65. Gu Y-L, Pan S-M, Ren J, Yang Z-X, Jiang G-Q. Role of Magnetic Resonance Imaging in Detection of Pathologic Complete Remission in Breast Cancer Patients Treated With Neoadjuvant Chemotherapy: A Meta-Analysis. *Clin Breast Cancer* (2017) 17(4):245–55. doi: 10.1016/j.clbc.2016.12.010
66. Gao W, Guo N, Dong T. Diffusion-Weighted Imaging in Monitoring the Pathological Response to Neoadjuvant Chemotherapy in Patients With Breast Cancer: A Meta-Analysis. *World J Surg Oncol* (2018) 16(1):145. doi: 10.1186/s12957-018-1438-y
67. Chu W, Jin W, Liu D, Wang J, Geng C, Chen L, et al. Diffusion-Weighted Imaging in Identifying Breast Cancer Pathological Response to Neoadjuvant Chemotherapy: A Meta-Analysis. *Oncotarget* (2017) 9(6):7088–100. doi: 10.18632/oncotarget.23195
68. Shin HJ, Baek H-M, Ahn J-H, Baek S, Kim H, Cha JH, et al. Prediction of Pathologic Response to Neoadjuvant Chemotherapy in Patients With Breast Cancer Using Diffusion-Weighted Imaging and MRS. *NMR Biomed* (2012) 25(12):1349–59. doi: 10.1002/nbm.2807
69. Li X, Cheng L, Liu M, Zhang Y, Wang J, Zhang A, et al. DW-MRI ADC Values can Predict Treatment Response in Patients With Locally Advanced Breast Cancer Undergoing Neoadjuvant Chemotherapy. *Med Oncol* (2012) 29(2):425–31. doi: 10.1007/s12032-011-9842-y
70. Bedair R, Priest AN, Patterson AJ, McLean MA, Graves MJ, Manavaki R, et al. Assessment of Early Treatment Response to Neoadjuvant Chemotherapy in Breast Cancer Using non-Mono-Exponential Diffusion Models: A Feasibility Study Comparing the Baseline and Mid-Treatment MRI Examinations. *Eur Radiol* (2017) 27(7):2726–36. doi: 10.1007/s00330-016-4630-x
71. Woodhams R, Kakita S, Hata H, Iwabuchi K, Kuranami M, Gautam S, et al. Identification of Residual Breast Carcinoma Following Neoadjuvant Chemotherapy: Diffusion-Weighted Imaging—Comparison With Contrast-Enhanced MR Imaging and Pathologic Findings. *Radiology* (2010) 254(2):357–66. doi: 10.1148/radiol.2542090405
72. Fangberget A, Nilsen LB, Hole KH, Holmen MM, Engebraaten O, Naume B, et al. Neoadjuvant Chemotherapy in Breast Cancer-Response Evaluation and Prediction of Response to Treatment Using Dynamic Contrast-Enhanced and Diffusion-Weighted MR Imaging. *Eur Radiol* (2011) 21(6):1188–99. doi: 10.1007/s00330-010-2020-3
73. Bufi E, Belli P, Costantini M, Cipriani A, Di Matteo M, Bonatesta A, et al. Role of the Apparent Diffusion Coefficient in the Prediction of Response to Neoadjuvant Chemotherapy in Patients With Locally Advanced Breast Cancer. *Clin Breast Cancer* (2015) 15(5):370–80. doi: 10.1016/j.clbc.2015.02.002
74. Partridge SC, Zhang Z, Newitt DC, Gibbs JE, Chenevert TL, Rosen MA, et al. Diffusion-Weighted MRI Findings Predict Pathologic Response in Neoadjuvant Treatment of Breast Cancer: The ACRIN 6698 Multicenter Trial. *Radiology* (2018) 289(3):618–27. doi: 10.1148/radiol.2018180273
75. Richard R, Thomassin I, Chapellier M, Scemama A, de Cremoux P, Varna M, et al. Diffusion-Weighted MRI in Pretreatment Prediction of Response to Neoadjuvant Chemotherapy in Patients With Breast Cancer. *Eur Radiol* (2013) 23(9):2420–31. doi: 10.1007/s00330-013-2850-x
76. Agarwal K, Sharma U, Sah RG, Mathur S, Hari S, Seenu V, et al. Pre-Operative Assessment of Residual Disease in Locally Advanced Breast Cancer Patients: A Sequential Study by Quantitative Diffusion Weighted MRI as a Function of Therapy. *Magn Reson Imaging* (2017) 42:88–94. doi: 10.1016/j.mri.2017.06.002
77. Sharma U, Danishad KKA, Seenu V, Jagannathan NR. Longitudinal Study of the Assessment by MRI and Diffusion-Weighted Imaging of Tumor Response in Patients With Locally Advanced Breast Cancer Undergoing Neoadjuvant Chemotherapy. *NMR BioMed* (2009) 22(1):104–13. doi: 10.1002/nbm.1245
78. Shukla-Dave A, Obuchowski NA, Chenevert TL, Jambawalikar S, Schwartz LH, Malyarenko D, et al. Quantitative Imaging Biomarkers Alliance (QIBA) Recommendations for Improved Precision of DWI and DCE-MRI Derived Biomarkers in Multicenter Oncology Trials. *J Magn Reson Imaging* (2019) 49(7):e101–21. doi: 10.1002/jmri.26518
79. Sorace AG, Wu C, Barnes SL, Jarrett AM, Avery S, Patt D, et al. Repeatability, Reproducibility, and Accuracy of Quantitative MRI of the Breast in the Community Radiology Setting. *J Magn Reson Imaging* (2018) 48(3):695–707. doi: 10.1002/jmri.26011
80. Giannotti E, Waugh S, Priba L, Davis Z, Crowe E, Vinnicombe S. Assessment and Quantification of Sources of Variability in Breast Apparent Diffusion Coefficient (ADC) Measurements at Diffusion Weighted Imaging. *Eur J Radiol* (2015) 84(9):1729–36. doi: 10.1016/j.ejrad.2015.05.032
81. Jang M, Kim SM, Yun BL, Ahn HS, Kim SY, Kang E, et al. Reproducibility of Apparent Diffusion Coefficient Measurements in Malignant Breast Masses. *J Korean Med Sci* (2015) 30(11):1689–97. doi: 10.3346/jkms.2015.30.11.1689
82. O'Flynn EAM, Morgan VA, Giles SL, deSouza NM. Diffusion Weighted Imaging of the Normal Breast: Reproducibility of Apparent Diffusion Coefficient Measurements and Variation With Menstrual Cycle and Menopausal Status. *Eur Radiol* (2012) 22(7):1512–8. doi: 10.1007/s00330-012-2399-0
83. Spick C, Bickel H, Pinker K, Bernathova M, Kapetas P, Woitek R, et al. Diffusion-Weighted MRI of Breast Lesions: A Prospective Clinical Investigation of the Quantitative Imaging Biomarker Characteristics of Reproducibility, Repeatability, and Diagnostic Accuracy. *NMR BioMed* (2016) 29(10):1445–53. doi: 10.1002/nbm.3596
84. Newitt DC, Zhang Z, Gibbs JE, Partridge SC, Chenevert TL, Rosen MA, et al. Test-Retest Repeatability and Reproducibility of ADC Measures by Breast DWI: Results From the ACRIN 6698 Trial. *J Magn Reson Imaging* (2019) 49(6):1617–28. doi: 10.1002/jmri.26539
85. QIBA MR Biomarker Committee. MR Diffusion-Weighted Imaging (DWI). In: *Quantitative Imaging Biomarkers Alliance (RSNA)* (2019). Available at: http://qibawiki.rsna.org/images/6/63/QIBA_DWIProfile_Consensus_Dec2019_Final.pdf.
86. de Figueiredo EHMSG, Borgonovi AFNG, Doring TM. Basic Concepts of MR Imaging, Diffusion MR Imaging, and Diffusion Tensor Imaging. *Magn Reson Imaging Clin N Am* (2011) 19(1):1–22. doi: 10.1016/j.mric.2010.10.005
87. An YY, Kim SH, Kang BJ. Differentiation of Malignant and Benign Breast Lesions: Added Value of the Qualitative Analysis of Breast Lesions on Diffusion-Weighted Imaging (DWI) Using Readout-Segmented Echo-Planar Imaging at 3.0 T. *PloS One* (2017) 12(3):e0174681. doi: 10.1371/journal.pone.0174681
88. Wisner DJ, Rogers N, Deshpande VS, Newitt DN, Laub GA, Porter DA, et al. High-Resolution Diffusion-Weighted Imaging for the Separation of Benign From Malignant BI-RADS 4/5 Lesions Found on Breast MRI at 3T. *J Magn Reson Imaging* (2014) 40(3):674–81. doi: 10.1002/jmri.24416
89. Kim YJ, Kim SH, Kang BJ, Park CS, Kim HS, Son YH, et al. Readout-Segmented Echo-Planar Imaging in Diffusion-Weighted MR Imaging in Breast Cancer: Comparison With Single-Shot Echo-Planar Imaging in Image Quality. *Korean J Radiol* (2014) 15(4):403–10. doi: 10.3348/kjr.2014.15.4.403
90. Kanao S, Kataoka M, Iima M, Ohno A, Sakaguchi R, Ohashi A, et al. High-Resolution Diffusion-Weighted MRI of the Breast Using Readout-Segmented EPI and Single-Shot EPI. *Imaging Med* (2017) 9(6):185–90. doi: 10.1002/jmri.24416

91. Bogner W, Pinker-Domenig K, Bickel H, Chmelik M, Weber M, Helbich TH, et al. Readout-Segmented Echo-Planar Imaging Improves the Diagnostic Performance of Diffusion-Weighted MR Breast Examinations at 3.0 T. *Radiology* (2012) 263(1):64–76. doi: 10.1148/radiol.12111494
92. Kishimoto AO, Kataoka M, Iima M, Honda M, Miyake KK, Ohashi A, et al. The Comparison of High-Resolution Diffusion Weighted Imaging (DWI) With High-Resolution Contrast-Enhanced MRI in the Evaluation of Breast Cancers. *Magn Reson Imaging* (2020) 71:161–9. doi: 10.1016/j.mri.2020.03.007
93. Ohlmeyer S, Laun FB, Palm T, Janka R, Weiland E, Uder M, et al. Simultaneous Multislice Echo Planar Imaging for Accelerated Diffusion-Weighted Imaging of Malignant and Benign Breast Lesions. *Invest Radiol* (2019) 54(8):524–30. doi: 10.1097/RLI.0000000000000560
94. Filli L, Ghafoor S, Kenkel D, Liu W, Weiland E, Andreisek G, et al. Simultaneous Multi-Slice Readout-Segmented Echo Planar Imaging for Accelerated Diffusion-Weighted Imaging of the Breast. *Eur J Radiol* (2016) 85(1):274–8. doi: 10.1016/j.ejrad.2015.10.009
95. Song SE, Woo OH, Cho KR, Seo BK, Son YH, Grimm R, et al. Simultaneous Multislice Readout-Segmented Echo Planar Imaging for Diffusion-Weighted MRI in Patients With Invasive Breast Cancers. *J Magn Reson Imaging* (2021) 53(4):1108–15. doi: 10.1002/jmri.27433
96. McKay JA, Church AL, Rubin N, Emory TH, Hoven NF, Kuehn-Hajder JE, et al. A Comparison of Methods for High-Spatial-Resolution Diffusion-Weighted Imaging in Breast MRI. *Radiology* (2020) 297(2):304–12. doi: 10.1148/radiol.2020200221
97. Hu Y, Zhan C, Yang Z, Zhang X, Zhang H, Liu W, et al. Accelerating Acquisition of Readout-Segmented Echo Planar Imaging With a Simultaneous Multi-Slice (SMS) Technique for Diagnosing Breast Lesions. *Eur Radiol* (2021) 31(5):2667–76. doi: 10.1007/s00330-020-07393-5
98. Machida Y, Nomura K, Shimauchi A, Kato Y, Nagatsuka M, Fukuma E. Diffusion-Weighted Imaging With Simultaneous Multi-Slice Echo-Planar Technique for the Diagnosis of Breast Magnetic Resonance Imaging. *Jpn J Radiol* (2020) 38(4):358–64. doi: 10.1007/s11604-020-00919-3
99. Yuan J, Zhao T-C, Tang Y, Panych LP. Reduced Field-of-View Single-Shot Fast Spin Echo Imaging Using Two-Dimensional Spatially Selective Radiofrequency Pulses. *J Magn Reson Imaging* (2010) 32(1):242–8. doi: 10.1002/jmri.22204
100. Rodríguez-Soto AE, Fang LK, Holland D, Zou J, Park HH, Keenan KE, et al. Correction of Artifacts Induced by B0 Inhomogeneities in Breast MRI Using Reduced-Field-Of-View Echo-Planar Imaging and Enhanced Reversed Polarity Gradient Method. *J Magn Reson Imaging* (2021) 53(5):1581–91. doi: 10.1002/jmri.27566
101. Dong H, Li Y, Li H, Wang B, Hu B. Study of the Reduced Field-of-View Diffusion-Weighted Imaging of the Breast. *Clin Breast Cancer* (2014) 14 (4):265–71. doi: 10.1016/j.clbc.2013.12.001
102. Barentsz MW, Taviani V, Chang JM, Ikeda DM, Miyake KK, Banerjee S, et al. Assessment of Tumor Morphology on Diffusion-Weighted (DWI) Breast MRI: Diagnostic Value of Reduced Field of View DWI. *J Magn Reson Imaging* (2015) 42(6):1656–65. doi: 10.1002/jmri.24929
103. Dong H, Li Y, Yu K, Li H. Comparison of Image Quality and Application Values on Different Field-of-View Diffusion-Weighted Imaging of Breast Cancer. *Acta Radiol* (2016) 57(1):19–24. doi: 10.1177/0284185115569106
104. Singer L, Wilmes LJ, Saritas EU, Shankaranarayanan A, Proctor E, Wisner DJ, et al. High-Resolution Diffusion-Weighted Magnetic Resonance Imaging in Patients With Locally Advanced Breast Cancer. *Acad Radiol* (2012) 19 (5):526–34. doi: 10.1016/j.acra.2011.11.003
105. Lee SH, Shin HJ, Moon WK. Diffusion-Weighted Magnetic Resonance Imaging of the Breast: Standardization of Image Acquisition and Interpretation. *Korean J Radiol* (2021) 22(1):9–22. doi: 10.3348/kjr.2020.0093
106. Taviani V, Alley MT, Banerjee S, Nishimura DG, Daniel BL, Vasanawala SS, et al. High-Resolution Diffusion-Weighted Imaging of the Breast With Multiband 2D Radiofrequency Pulses and a Generalized Parallel Imaging Reconstruction. *Magn Reson Med* (2017) 77(1):209–20. doi: 10.1002/mrm.26110
107. McNab JA, Miller KL. Steady-State Diffusion-Weighted Imaging: Theory, Acquisition and Analysis. *NMR BioMed* (2010) 23(7):781–93. doi: 10.1002/nbm.1509
108. Granlund KL, Staroswiecki E, Alley MT, Daniel BL, Hargreaves BA. High-Resolution, Three-Dimensional Diffusion-Weighted Breast Imaging Using DESS. *Magn Reson Imaging* (2014) 32(4):330–41. doi: 10.1016/j.mri.2013.12.014
109. Moran CJ, Cheng JY, Sandino CM, Carl M, Alley MT, Rosenberg J, et al. Diffusion-Weighted Double-Echo Steady-State With a Three-Dimensional Cones Trajectory for non-Contrast-Enhanced Breast MRI. *J Magn Reson Imaging* (2021) 53(5):1594–605. doi: 10.1002/jmri.27492
110. Tendler BC, Foxley S, Cottaar M, Jbabdi S, Miller KL. Modeling an Equivalent B-Value in Diffusion-Weighted Steady-State Free Precession. *Magn Reson Med* (2020) 84(2):873–84. doi: 10.1002/mrm.28169
111. Daniel BL, Granlund KL, Moran CJ, Alley MT, Lipson J, Ikeda DM, et al. Breast MRI Without Gadolinium: Utility of 3D DESS, a New 3D Diffusion Weighted Gradient-Echo Sequence. *Eur J Radiol* (2012) 81 Suppl 1:S24–26. doi: 10.1016/S0720-048X(12)70010-4
112. Han X, Li J, Wang X. Comparison and Optimization of 3.0 T Breast Images Quality of Diffusion-Weighted Imaging With Multiple B-Values. *Acad Radiol* (2017) 24(4):418–25. doi: 10.1016/j.acra.2016.11.006
113. Peters NHGM, Vincken KL, van den Bosch MAAJ, Luijten PR, Mali WPTM, Bartels LW. Quantitative Diffusion Weighted Imaging for Differentiation of Benign and Malignant Breast Lesions: The Influence of the Choice of B-Values. *J Magn Reson Imaging* (2010) 31(5):1100–5. doi: 10.1002/jmri.22152
114. Pereira FPA, Martins G, Figueiredo E, Domingues MNA, Domingues RC, da Fonseca LMB, et al. Assessment of Breast Lesions With Diffusion-Weighted MRI: Comparing the Use of Different B Values. *AJR Am J Roentgenol* (2009) 193(4):1030–5. doi: 10.2214/AJR.09.2522
115. Bogner W, Gruber S, Pinker K, Grabner G, Stadlbauer A, Weber M, et al. Diffusion-Weighted MR for Differentiation of Breast Lesions at 3.0 T: How Does Selection of Diffusion Protocols Affect Diagnosis? *Radiology* (2009) 253 (2):341–51. doi: 10.1148/radiol.2532081718
116. Bickel H, Pinker K, Polanec S, Magometschnigg H, Wengert G, Spick C, et al. Diffusion-Weighted Imaging of Breast Lesions: Region-Of-Interest Placement and Different ADC Parameters Influence Apparent Diffusion Coefficient Values. *Eur Radiol* (2017) 27(5):1883–92. doi: 10.1007/s00330-016-4564-3
117. Gity M, Moradi B, Arami R, Arabkheradmand A, Kazemi MA. Two Different Methods of Region-Of-Interest Placement for Differentiation of Benign and Malignant Breast Lesions by Apparent Diffusion Coefficient Value. *Asian Pac J Cancer Prev* (2018) 19(10):2765–70. doi: 10.22034/APJCP.2018.19.10.2765
118. Nogueira L, Brandão S, Matos E, Nunes RG, Ferreira HA, Loureiro J, et al. Region of Interest Demarcation for Quantification of the Apparent Diffusion Coefficient in Breast Lesions and its Interobserver Variability. *Diagn Interv Radiol* (2015) 21(2):123–7. doi: 10.5152/dir.2014.14217
119. Arponen O, Arponent O, Sudah M, Masarwah A, Taina M, Rautiainen S, et al. Diffusion-Weighted Imaging in 3.0 Tesla Breast MRI: Diagnostic Performance and Tumor Characterization Using Small Subregions vs. Whole Tumor Regions of Interest. *PloS One* (2015) 10(10):e0138702. doi: 10.1371/journal.pone.0138702
120. Rahbar H, Kurland BF, Olson ML, Kitsch AE, Scheel JR, Chai X, et al. Diffusion Weighted Breast MRI: A Semi-Automated Voxel Selection Technique Improves Inter-Reader Reproducibility of Apparent Diffusion Coefficient Measurements. *J Comput Assist Tomogr* (2016) 40(3):428–35. doi: 10.1097/RCT.0000000000000372
121. O'Donnell LJ, Westin C-F. An Introduction to Diffusion Tensor Image Analysis. *Neurosurg Clin N Am* (2011) 22(2):185–viii. doi: 10.1016/j.nec.2010.12.004
122. Soares J, Marques P, Alves V, Sousa N. A Hitchhiker's Guide to Diffusion Tensor Imaging. *Front Neurosci* (2013) 7:31. doi: 10.3389/fnins.2013.00031
123. Eyal E, Shapiro-Feinberg M, Furman-Haran E, Grobgeld D, Golan T, Itzchak Y, et al. Parametric Diffusion Tensor Imaging of the Breast. *Invest Radiol* (2012) 47(5):284–91. doi: 10.1097/RLI.0b013e3182438e5d
124. Jones DK, Horsfield MA, Simmons A. Optimal Strategies for Measuring Diffusion in Anisotropic Systems by Magnetic Resonance Imaging. *Magn Reson Med* (1999) 42(3):515–25. doi: 10.1002/(SICI)1522-2594(199909)42:3<515::AID-MRM14>3.0.CO;2-Q
125. Le Bihan D, Mangin JF, Poupon C, Clark CA, Pappata S, Molko N, et al. Diffusion Tensor Imaging: Concepts and Applications. *J Magn Reson Imaging* (2001) 13(4):534–46. doi: 10.1002/jmri.1076

126. Furman-Haran E, Grobgeld D, Nissan N, Shapiro-Feinberg M, Degani H. Can Diffusion Tensor Anisotropy Indices Assist in Breast Cancer Detection? *J Magn Reson Imaging* (2016) 44(6):1624–32. doi: 10.1002/jmri.25292
127. Kubicki M, Westin C-F, Maier SE, Mamata H, Frumin M, Ersner-Hershfield H, et al. Diffusion Tensor Imaging and its Application to Neuropsychiatric Disorders. *Harv Rev Psychiatry* (2002) 10(6):324–36. doi: 10.1080/10673220216231
128. Onaygil C, Kaya H, Ugurlu MU, Aribal E. Diagnostic Performance of Diffusion Tensor Imaging Parameters in Breast Cancer and Correlation With the Prognostic Factors. *J Magn Reson Imaging* (2017) 45(3):660–72. doi: 10.1002/jmri.25481
129. Wiederer J, Pazahr S, Leo C, Nanz D, Boss A. Quantitative Breast MRI: 2D Histogram Analysis of Diffusion Tensor Parameters in Normal Tissue. *Magn Reson Mater Phy* (2014) 27(2):185–93. doi: 10.1007/s10334-013-0400-9
130. Partridge SC, Murthy RS, Ziadloo A, White SW, Allison KH, Lehman CD. Diffusion Tensor Magnetic Resonance Imaging of the Normal Breast. *Magn Reson Imaging* (2010) 28(3):320–8. doi: 10.1016/j.mri.2009.10.003
131. Plaza MJ, Morris EA, Thakur SB. Diffusion Tensor Imaging in the Normal Breast: Influences of Fibroglandular Tissue Composition and Background Parenchymal Enhancement. *Clin Imaging* (2016) 40(3):506–11. doi: 10.1016/j.clinimag.2015.12.001
132. Nissan N, Furman-Haran E, Shapiro-Feinberg M, Grobgeld D, Degani H. Diffusion-Tensor MR Imaging of the Breast: Hormonal Regulation. *Radiology* (2014) 271(3):672–80. doi: 10.1148/radiol.14132084
133. Shapiro-Feinberg M, Weisenberg N, Zehavi T, Furman-Haran E, Grobgeld D, Nissan N, et al. Clinical Results of DTI. *Eur J Radiol* (2012) 81:S151–2. doi: 10.1016/S0720-048X(12)70063-3
134. Nissan N, Allweis T, Menes T, Brodsky A, Paluch-Shimon S, Haas I, et al. Breast MRI During Lactation: Effects on Tumor Conspicuity Using Dynamic Contrast-Enhanced (DCE) in Comparison With Diffusion Tensor Imaging (DTI) Parametric Maps. *Eur Radiol* (2020) 30(2):767–77. doi: 10.1007/s00330-019-06435-x
135. Partridge SC, McKinnon GC, Henry RG, Hylton NM. Menstrual Cycle Variation of Apparent Diffusion Coefficients Measured in the Normal Breast Using MRI. *J Magn Reson Imaging* (2001) 14(4):433–8. doi: 10.1002/jmri.1204
136. McDonald ES, Schopp JG, Peacock S, DeMartini WB, DeMartini WD, Rahbar H, et al. Diffusion-Weighted MRI: Association Between Patient Characteristics and Apparent Diffusion Coefficients of Normal Breast Fibroglandular Tissue at 3 T. *AJR Am J Roentgenol* (2014) 202(5):W496–502. doi: 10.2214/AJR.13.11159
137. Kim JY, Suh HB, Kang HJ, Shin JK, Choo KS, Nam KJ, et al. Apparent Diffusion Coefficient of Breast Cancer and Normal Fibroglandular Tissue in Diffusion-Weighted Imaging: The Effects of Menstrual Cycle and Menopausal Status. *Breast Cancer Res Treat* (2016) 157(1):31–40. doi: 10.1007/s10549-016-3793-0
138. Kuhl CK, Bieling HB, Gieseke J, Kreft BP, Sommer T, Lutterbey G, et al. Healthy Premenopausal Breast Parenchyma in Dynamic Contrast-Enhanced MR Imaging of the Breast: Normal Contrast Medium Enhancement and Cyclical-Phase Dependency. *Radiology* (1997) 203(1):137–44. doi: 10.1148/radiology.203.1.9122382
139. Müller-Schimpfle M, Ohmenhaüser K, Stoll P, Dietz K, Claussen CD. Menstrual Cycle and Age: Influence on Parenchymal Contrast Medium Enhancement in MR Imaging of the Breast. *Radiology* (1997) 203(1):145–9. doi: 10.1148/radiology.203.1.9122383
140. Wang K, Li Z, Wu Z, Zheng Y, Zeng S, Linning E, et al. Diagnostic Performance of Diffusion Tensor Imaging for Characterizing Breast Tumors: A Comprehensive Meta-Analysis. *Front Oncol* (2019) 9:1229. doi: 10.3389/fonc.2019.01229
141. Jiang R, Zeng X, Sun S, Ma Z, Wang X. Assessing Detection, Discrimination, and Risk of Breast Cancer According to Anisotropy Parameters of Diffusion Tensor Imaging. *Med Sci Monit* (2016) 22:1318–28. doi: 10.12659/MSM.895755
142. Kim JY, Kim JJ, Kim S, Choo KS, Kim A, Kang T, et al. Diffusion Tensor Magnetic Resonance Imaging of Breast Cancer: Associations Between Diffusion Metrics and Histological Prognostic Factors. *Eur Radiol* (2018) 28(8):3185–93. doi: 10.1007/s00330-018-5429-8
143. Ozal ST, Inci E, Gemici AA, Turgut H, Cikot M, Karabulut M. Can 3.0 Tesla Diffusion Tensor Imaging Parameters be Prognostic Indicators in Breast Cancer? *Clin Imaging* (2018) 51:240–7. doi: 10.1016/j.clinimag.2018.03.022
144. Yamaguchi K, Nakazono T, Egashira R, Komori Y, Nakamura J, Noguchi T, et al. Diagnostic Performance of Diffusion Tensor Imaging With Readout-Segmented Echo-Planar Imaging for Invasive Breast Cancer: Correlation of ADC and FA With Pathological Prognostic Markers. *Magn Reson Med Sci* (2017) 16(3):245–52. doi: 10.2463/mrms.mp.2016-0037
145. Furman-Haran E, Nissan N, Ricart-Selma V, Martinez-Rubio C, Degani H, Camps-Herrero J. Quantitative Evaluation of Breast Cancer Response to Neoadjuvant Chemotherapy by Diffusion Tensor Imaging: Initial Results. *J Magn Reson Imaging* (2018) 47(4):1080–90. doi: 10.1002/jmri.25855
146. Laun FB, Schad LR, Klein J, Stieltjes B. How Background Noise Shifts Eigenvectors and Increases Eigenvalues in DTI. *Magn Reson Mater Phy* (2009) 22(3):151–8. doi: 10.1007/s10334-008-0159-6
147. Le Bihan D, Breton E, Lallemand D, Grenier P, Cabanis E, Laval-Jeantet M. MR Imaging of Intravoxel Incoherent Motions: Application to Diffusion and Perfusion in Neurologic Disorders. *Radiology* (1986) 161(2):401–7. doi: 10.1148/radiology.161.2.3763909
148. Sigmund EE, Cho GY, Kim S, Finn M, Moccaldi M, Jensen JH, et al. Intravoxel Incoherent Motion Imaging of Tumor Microenvironment in Locally Advanced Breast Cancer: IVIM Imaging in Locally Advanced Breast Cancer. *Magn Reson Med* (2011) 65(5):1437–47. doi: 10.1002/mrm.22740
149. Kim Y, Ko K, Kim D, Min C, Kim SG, Joo J, et al. Intravoxel Incoherent Motion Diffusion-Weighted MR Imaging of Breast Cancer: Association With Histopathological Features and Subtypes. *BJR* (2016) 89(1063):20160140. doi: 10.1259/bjr.20160140
150. Iima M, Kataoka M, Kanao S, Onishi N, Kawai M, Ohashi A, et al. Intravoxel Incoherent Motion and Quantitative Non-Gaussian Diffusion MR Imaging: Evaluation of the Diagnostic and Prognostic Value of Several Markers of Malignant and Benign Breast Lesions. *Radiology* (2018) 287(2):432–41. doi: 10.1148/radiol.2017162853
151. Sigmund EE, Cho GY, Kim S, Finn M, Moccaldi M, Jensen JH, et al. Intravoxel Incoherent Motion (IVIM) Imaging of Tumor Microenvironment in Locally Advanced Breast Cancer. *Magn Reson Med* (2011) 65(5):1437–47. doi: 10.1002/mrm.22740
152. Bokacheva L, Kaplan JB, Giri DD, Patil S, Gnanasigamani M, Nyman CG, et al. Intravoxel Incoherent Motion Diffusion-Weighted MRI at 3.0 T Differentiates Malignant Breast Lesions From Benign Lesions and Breast Parenchyma. *J Magn Reson Imaging* (2014) 40(4):813–23. doi: 10.1002/jmri.24462
153. Iima M, Yano K, Kataoka M, Umehana M, Murata K, Kanao S, et al. Quantitative Non-Gaussian Diffusion and Intravoxel Incoherent Motion Magnetic Resonance Imaging: Differentiation of Malignant and Benign Breast Lesions. *Invest Radiol* (2015) 50(4):205–11. doi: 10.1097/RLI.0000000000000094
154. Liu C, Liang C, Liu Z, Zhang S, Huang B. Intravoxel Incoherent Motion (IVIM) in Evaluation of Breast Lesions: Comparison With Conventional DWI. *Eur J Radiol* (2013) 82(12):e782–9. doi: 10.1016/j.ejrad.2013.08.006
155. Liu C, Wang K, Chan Q, Liu Z, Zhang J, He H, et al. Intravoxel Incoherent Motion MR Imaging for Breast Lesions: Comparison and Correlation With Pharmacokinetic Evaluation From Dynamic Contrast-Enhanced MR Imaging. *Eur Radiol* (2017) 26(11):3888–98. doi: 10.1007/s00330-016-4241-6
156. Ma D, Lu F, Zou X, Zhang H, Li Y, Zhang L, et al. Intravoxel Incoherent Motion Diffusion-Weighted Imaging as an Adjunct to Dynamic Contrast-Enhanced MRI to Improve Accuracy of the Differential Diagnosis of Benign and Malignant Breast Lesions. *Magn Reson Imaging* (2017) 36:175–9. doi: 10.1016/j.mri.2016.10.005
157. Wang Q, Guo Y, Zhang J, Wang Z, Huang M, Zhang Y. Contribution of IVIM to Conventional Dynamic Contrast-Enhanced and Diffusion-Weighted MRI in Differentiating Benign From Malignant Breast Masses. *Breast Care (Basel)* (2016) 11(4):254–8. doi: 10.1159/000447765
158. Dijkstra H, Dorrius MD, Wielema M, Jaspers K, Pijnappel RM, Oudkerk M, et al. Semi-Automated Quantitative Intravoxel Incoherent Motion Analysis and its Implementation in Breast Diffusion-Weighted Imaging. *J Magn Reson Imaging* (2016) 43(5):1122–31. doi: 10.1002/jmri.25086

159. Lin N, Chen J, Hua J, Zhao J, Zhao J, Lu J. Intravoxel Incoherent Motion MR Imaging in Breast Cancer: Quantitative Analysis for Characterizing Lesions. *Int J Clin Exp Med* (2017) 10(1):1705–14.
160. Chen F, Chen P, Hamid Muhammed H, Zhang J. Intravoxel Incoherent Motion Diffusion for Identification of Breast Malignant and Benign Tumors Using Chemometrics. *BioMed Res Int* (2017) 2017:3845409. doi: 10.1155/2017/3845409
161. Zhao M, Fu K, Zhang L, Guo W, Wu Q, Bai X, et al. Intravoxel Incoherent Motion Magnetic Resonance Imaging for Breast Cancer: A Comparison With Benign Lesions and Evaluation of Heterogeneity in Different Tumor Regions With Prognostic Factors and Molecular Classification. *Oncol Lett* (2018) 16(4):5100–12. doi: 10.3892/ol.2018.9312
162. Mao X, Zou X, Yu N, Jiang X, Du J. Quantitative Evaluation of Intravoxel Incoherent Motion Diffusion-Weighted Imaging (IVIM) for Differential Diagnosis and Grading Prediction of Benign and Malignant Breast Lesions. *Med (Baltimore)* (2018) 97(26):e11109. doi: 10.1097/MD.0000000000011109
163. Bihan DL, Iima M, Federau C, Sigmund EE, Iima M, Federau C, et al. *Intravoxel Incoherent Motion (IVIM) MRI : Principles and Applications*. New York, USA: Jenny Stanford Publishing (2018).
164. Vidić I. *Multi-Parametric Diffusion Weighted Magnetic Resonance Imaging and Analysis in Breast Cancer*. Trondheim, Norway: Norwegian University of Science and Technology (2019).
165. Li K, Machireddy A, Tudorica A, Moloney B, Oh KY, Jafarian N, et al. Discrimination of Malignant and Benign Breast Lesions Using Quantitative Multiparametric MRI: A Preliminary Study. *Tomography* (2020) 6(2):148–59. doi: 10.18383/j.tom.2019.00028
166. Lee YJ, Kim SH, Kang BJ, Kang YJ, Yoo H, Yoo J, et al. Intravoxel Incoherent Motion (IVIM)-Derived Parameters in Diffusion-Weighted MRI: Associations With Prognostic Factors in Invasive Ductal Carcinoma: IVIM Parameters of Breast Cancer. *J Magn Reson Imaging* (2017) 45(5):1394–406. doi: 10.1002/jmri.25514
167. Kawashima H, Miyati T, Ohno N, Ohno M, Inokuchi M, Ikeda H, et al. Differentiation Between Luminal-A and Luminal-B Breast Cancer Using Intravoxel Incoherent Motion and Dynamic Contrast-Enhanced Magnetic Resonance Imaging. *Acad Radiol* (2017) 24(12):1575–81. doi: 10.1016/j.acra.2017.06.016
168. You C, Li J, Zhi W, Chen Y, Yang W, Gu Y, et al. The Volumetric-Tumour Histogram-Based Analysis of Intravoxel Incoherent Motion and non-Gaussian Diffusion MRI: Association With Prognostic Factors in HER2-Positive Breast Cancer. *J Transl Med* (2019) 17(1):182. doi: 10.1186/s12967-019-1911-6
169. Lee YJ, Kim SH, Kang BJ, Son YH, Grimm R. Associations Between Angiogenic Factors and Intravoxel Incoherent Motion-Derived Parameters in Diffusion-Weighted Magnetic Resonance Imaging of Breast Cancer. *Medicine* (2021) 100(41):e27495. doi: 10.1097/MD.0000000000027495
170. Vidić I, Egnell L, Jerome NP, Teruel JR, Sjøbakk TE, Østlie A, et al. Support Vector Machine for Breast Cancer Classification Using Diffusion-Weighted MRI Histogram Features: Preliminary Study. *J Magn Reson Imaging* (2018) 47(5):1205–16. doi: 10.1002/jmri.25873
171. Che S, Zhao X, Ou Y, Li J, Wang M, Wu B, et al. Role of the Intravoxel Incoherent Motion Diffusion Weighted Imaging in the Pre-Treatment Prediction and Early Response Monitoring to Neoadjuvant Chemotherapy in Locally Advanced Breast Cancer. *Med (Baltimore)* (2016) 95(4):e2420. doi: 10.1097/MD.0000000000002420
172. Kim Y, Kim SH, Lee HW, Song BJ, Kang BJ, Lee A, et al. Intravoxel Incoherent Motion Diffusion-Weighted MRI for Predicting Response to Neoadjuvant Chemotherapy in Breast Cancer. *Magn Reson Imaging* (2018) 48:27–33. doi: 10.1016/j.mri.2017.12.018
173. Cho GY, Gennaro L, Sutton EJ, Zabor EC, Zhang Z, Giri D, et al. Intravoxel Incoherent Motion (IVIM) Histogram Biomarkers for Prediction of Neoadjuvant Treatment Response in Breast Cancer Patients. *Eur J Radiol Open* (2017) 4:101–7. doi: 10.1016/j.ejro.2017.07.002
174. Cho GY, Moy L, Zhang JL, Baete S, Lattanzi R, Moccaldi M, et al. Comparison of Fitting Methods and B-Value Sampling Strategies for Intravoxel Incoherent Motion in Breast Cancer. *Magn Reson Med* (2015) 74(4):1077–85. doi: 10.1002/mrm.25484
175. Suo S, Lin N, Wang H, Zhang L, Wang R, Zhang S, et al. Intravoxel Incoherent Motion Diffusion-Weighted MR Imaging of Breast Cancer at 3.0 Tesla: Comparison of Different Curve-Fitting Methods. *J Magn Reson Imaging* (2015) 42(2):362–70. doi: 10.1002/jmri.24799
176. Chen W, Zhang J, Long D, Wang Z, Zhu J. Optimization of Intra-Voxel Incoherent Motion Measurement in Diffusion-Weighted Imaging of Breast Cancer. *J Appl Clin Med Phys* (2017) 18(3):191–9. doi: 10.1002/acm2.12065
177. While PT. A Comparative Simulation Study of Bayesian Fitting Approaches to Intravoxel Incoherent Motion Modeling in Diffusion-Weighted MRI. *Magn Reson Med* (2017) 78(6):2373–87. doi: 10.1002/mrm.26598
178. Vidić I, Jerome NP, Bathen TF, Goa PE, While PT. Accuracy of Breast Cancer Lesion Classification Using Intravoxel Incoherent Motion Diffusion-Weighted Imaging is Improved by the Inclusion of Global or Local Prior Knowledge With Bayesian Methods. *J Magn Reson Imaging* (2019) 50(5):1478–88. doi: 10.1002/jmri.26772
179. While PT, Teruel JR, Vidić I, Bathen TF, Goa PE. Relative Enhanced Diffusivity: Noise Sensitivity, Protocol Optimization, and the Relation to Intravoxel Incoherent Motion. *Magn Reson Mater Phy* (2018) 31(3):425–38. doi: 10.1007/s10334-017-0660-x
180. Teruel JR, Goa PE, Sjøbakk TE, Østlie A, Fjøsne HE, Bathen TF. A Simplified Approach to Measure the Effect of the Microvasculature in Diffusion-Weighted MR Imaging Applied to Breast Tumors: Preliminary Results. *Radiology* (2016) 281(2):373–81. doi: 10.1148/radiol.2016151630
181. Jensen JH, Helpern JA, Ramani A, Lu H, Kaczynski K. Diffusional Kurtosis Imaging: The Quantification of non-Gaussian Water Diffusion by Means of Magnetic Resonance Imaging. *Magn Reson Med* (2005) 53(6):1432–40. doi: 10.1002/mrm.20508
182. Wu D, Li G, Zhang J, Chang S, Hu J, Dai Y. Characterization of Breast Tumors Using Diffusion Kurtosis Imaging (DKI). *PloS One* (2014) 9(11):e113240. doi: 10.1371/journal.pone.0113240
183. Christou A, Ghiatas A, Priovolos D, Veliou K, Bougias H. Accuracy of Diffusion Kurtosis Imaging in Characterization of Breast Lesions. *Br J Radiol* (2017) 90(1073):20160873. doi: 10.1259/bjr.20160873
184. Nogueira L, Brandão S, Matos E, Nunes RG, Loureiro J, Ramos I, et al. Application of the Diffusion Kurtosis Model for the Study of Breast Lesions. *Eur Radiol* (2014) 24(6):1197–203. doi: 10.1007/s00330-014-3146-5
185. Liu W, Wei C, Bai J, Gao X, Zhou L. Histogram Analysis of Diffusion Kurtosis Imaging in the Differentiation of Malignant From Benign Breast Lesions. *Eur J Radiol* (2019) 117:156–63. doi: 10.1016/j.ejrad.2019.06.008
186. Meng N, Wang X, Sun J, Han D, Bai Y, Wei W, et al. A Comparative Study of the Value of Amide Proton Transfer-Weighted Imaging and Diffusion Kurtosis Imaging in the Diagnosis and Evaluation of Breast Cancer. *Eur Radiol* (2021) 31(3):1707–17. doi: 10.1007/s00330-020-07169-x
187. Sun K, Chen X, Chai W, Fei X, Fu C, Yan X, et al. Breast Cancer: Diffusion Kurtosis MR Imaging—Diagnostic Accuracy and Correlation With Clinical-Pathologic Factors. *Radiology* (2015) 277(1):46–55. doi: 10.1148/radiol.15141625
188. Zhou W-P, Zan X-Y, Hu X-Y, Liu X, Sudarshan SKP, Yang S-D, et al. Characterization of Breast Lesions Using Diffusion Kurtosis Model-Based Imaging: An Initial Experience. *J Xray Sci Technol* (2020) 28(1):157–69. doi: 10.3233/XST-190590
189. Li T, Hong Y, Kong D, Li K. Histogram Analysis of Diffusion Kurtosis Imaging Based on Whole-Volume Images of Breast Lesions. *J Magn Reson Imaging* (2020) 51(2):627–34. doi: 10.1002/jmri.26884
190. Huang Y, Lin Y, Hu W, Ma C, Lin W, Wang Z, et al. Diffusion Kurtosis at 3.0T as an *In Vivo* Imaging Marker for Breast Cancer Characterization: Correlation With Prognostic Factors. *J Magn Reson Imaging* (2019) 49(3):845–56. doi: 10.1002/jmri.26249
191. Palm T, Wenkel E, Ohlmeyer S, Janka R, Uder M, Weiland E, et al. Diffusion Kurtosis Imaging Does Not Improve Differentiation Performance of Breast Lesions in a Short Clinical Protocol. *Magn Reson Imaging* (2019) 63:205–16. doi: 10.1016/j.mri.2019.08.007
192. Wu J, Yan F, Chai W, Fu C, Yan X, Zhan Y, et al. Breast Cancer Recurrence Risk Prediction Using Whole-Lesion Histogram Analysis With Diffusion Kurtosis Imaging. *Clin Radiol* (2020) 75(3):239.e1–8. doi: 10.1016/j.crad.2019.10.015
193. Mlynarska-Bujny A, Bickelhaupt S, Laun FB, König F, Lederer W, Daniel H, et al. Influence of Residual Fat Signal on Diffusion Kurtosis MRI of Suspicious Mammography Findings. *Sci Rep* (2020) 10(1):13286. doi: 10.1038/s41598-020-70154-3

194. Iima M, Honda M, Sigmund EE, Ohno Kishimoto A, Kataoka M, Togashi K. Diffusion MRI of the Breast: Current Status and Future Directions. *J Magn Reson Imaging* (2020) 52(1):70–90. doi: 10.1002/jmri.26908
195. Choi BH, Baek HJ, Ha JY, Ryu KH, Moon JI, Park SE, et al. Feasibility Study of Synthetic Diffusion-Weighted MRI in Patients With Breast Cancer in Comparison With Conventional Diffusion-Weighted MRI. *Korean J Radiol* (2020) 21(9):1036–44. doi: 10.3348/kjr.2019.0568
196. Bickel H, Polanec SH, Wengert G, Pinker K, Bogner W, Helbich TH, et al. Diffusion-Weighted MRI of Breast Cancer: Improved Lesion Visibility and Image Quality Using Synthetic B-Values. *J Magn Reson Imaging* (2019) 50 (6):1754–61. doi: 10.1002/jmri.26809
197. Jin Y-N, Zhang Y, Cheng J-L, Zheng D-D, Hu Y. Monoexponential, Biexponential, and Stretched-Exponential Models Using Diffusion-Weighted Imaging: A Quantitative Differentiation of Breast Lesions at 3.0T. *J Magn Reson Imaging* (2019) 50(5):1461–7. doi: 10.1002/jmri.26729
198. Ertas G, Onaygil C, Akin Y, Kaya H, Aribal E. Quantitative Differentiation of Breast Lesions at 3T Diffusion-Weighted Imaging (DWI) Using the Ratio of Distributed Diffusion Coefficient (DDC). *J Magn Reson Imaging* (2016) 44 (6):1633–41. doi: 10.1002/jmri.25327
199. Liu C, Wang K, Li X, Zhang J, Ding J, Spuhler K, et al. Breast Lesion Characterization Using Whole-Lesion Histogram Analysis With Stretched-Exponential Diffusion Model. *J Magn Reson Imaging* (2018) 47(6):1701–10. doi: 10.1002/jmri.25904
200. Chen B-Y, Xie Z, Nie P, Yang D, Hu Y-C, Liu S-T, et al. Multiple B-Value Diffusion-Weighted Imaging in Differentiating Benign From Malignant Breast Lesions: Comparison of Conventional Mono-, Bi- and Stretched Exponential Models. *Clin Radiol* (2020) 75(8):642.e1–8. doi: 10.1016/j.crad.2020.03.039
201. Goto M, Le Bihan D, Yoshida M, Sakai K, Yamada K. Adding a Model-Free Diffusion MRI Marker to BI-RADS Assessment Improves Specificity for Diagnosing Breast Lesions. *Radiology* (2019) 292(1):84–93. doi: 10.1148/radiol.2019181780
202. Brunsing RL, Schenker-Ahmed NM, White NS, Parsons JK, Kane C, Kuperman J, et al. Restriction Spectrum Imaging: An Evolving Imaging Biomarker in Prostate MRI. *J Magn Reson Imaging* (2017) 45(2):323–36. doi: 10.1002/jmri.25419
203. White NS, Leergaard TB, D'Arceuil H, Bjaalie JG, Dale AM. Probing Tissue Microstructure With Restriction Spectrum Imaging: Histological and Theoretical Validation. *Hum Brain Mapp* (2013) 34(2):327–46. doi: 10.1002/hbm.21454
204. White NS, Dale AM. Distinct Effects of Nuclear Volume Fraction and Cell Diameter on High B-Value Diffusion MRI Contrast in Tumors. *Magn Reson Med* (2014) 72(5):1435–43. doi: 10.1002/mrm.25039
205. Rodríguez-Soto AE, Andreassen MMS, Fang LK, Conlin CC, Park HH, Ahn GS, et al. Characterization of the Diffusion Signal of Breast Tissues Using Multi-Exponential Models. *Magn Reson Med* (2022) 87(4):1938–51. doi: 10.1101/2020.04.27.20082271
206. Andreassen MMS, Rodríguez-Soto AE, Conlin CC, Vidić I, Seibert TM, Wallace AM, et al. Discrimination of Breast Cancer From Healthy Breast Tissue Using a Three-Component Diffusion-Weighted MRI Model. *Clin Cancer Res* (2021) 27(4):1094–104. doi: 10.1158/1078-0432.CCR-20-2017
207. Rodríguez-Soto AE, Meriwether CH, Park AJ, Adams DWJR, Wallace A, Ojeda-Fournier H, et al. Noncontrast MRI With Advanced Diffusion Weighted Imaging for Breast Cancer Detection in a Lactating Woman. *Radiol Case Rep* (2020) 15(11):2358–61. doi: 10.1016/j.radcr.2020.08.058
208. Dialani V. *Comparing Restriction Spectrum Imaging (RSI) to Conventional and Abbreviated Breast MRI for Breast Cancer Screening* (2021). Available at: https://clinicaltrials.gov/ct2/show/NCT03495115.
209. Reynaud O. Time-Dependent Diffusion MRI in Cancer: Tissue Modeling and Applications. *Front Phys* (2017) 5. doi: 10.3389/fphy.2017.00058
210. Iima M, Nobashi T, Imai H, Koyasu S, Saga T, Nakamoto Y, et al. Effects of Diffusion Time on non-Gaussian Diffusion and Intravoxel Incoherent Motion (IVIM) MRI Parameters in Breast Cancer and Hepatocellular Carcinoma Xenograft Models. *Acta Radiol Open* (2018) 7(1):2058460117751565. doi: 10.1177/2058460117751565
211. Jiang X, Li H, Xie J, Zhao P, Gore JC, Xu J. Quantification of Cell Size Using Temporal Diffusion Spectroscopy. *Magn Reson Med* (2016) 75(3):1076–85. doi: 10.1002/mrm.25684
212. Teruel JR, Cho GY, Rt MM, Goa PE, Bathen TF, Feiweier T, et al. Stimulated Echo Diffusion Tensor Imaging (STEAM-DTI) With Varying Diffusion Times as a Probe of Breast Tissue. *J Magn Reson Imaging* (2017) 45(1):84–93. doi: 10.1002/jmri.25376
213. Colvin DC, Loveless ME, Does MD, Yue Z, Yankeelov TE, Gore JC. Earlier Detection of Tumor Treatment Response Using Magnetic Resonance Diffusion Imaging With Oscillating Gradients. *Magn Reson Imaging* (2011) 29(3):315–23. doi: 10.1016/j.mri.2010.10.003
214. Xu J, Jiang X, Li H, Arlinghaus LR, McKinley ET, Devan SP, et al. Magnetic Resonance Imaging of Mean Cell Size in Human Breast Tumors. *arXiv* (2020) 83(6):2002–14. doi: 10.1002/mrm.28056
215. Gore JC, Xu J, Colvin DC, Yankeelov TE, Parsons EC, Does MD. Characterization of Tissue Structure at Varying Length Scales Using Temporal Diffusion Spectroscopy. *NMR BioMed* (2010) 23(7):745–56. doi: 10.1002/nbm.1531
216. Ye D-M, Wang H-T, Yu T. The Application of Radiomics in Breast MRI: A Review. *Technol Cancer Res Treat* (2020) 19:1533033820916191. doi: 10.1177/1533033820916191
217. Kumar V, Gu Y, Basu S, Berglund A, Eschrich SA, Schabath MB, et al. Radiomics: The Process and the Challenges. *Magn Reson Imaging* (2012) 30 (9):1234–48. doi: 10.1016/j.mri.2012.06.010
218. Bickelhaupt S, Jaeger PF, Laun FB, Lederer W, Daniel H, Kuder TA, et al. Radiomics Based on Adapted Diffusion Kurtosis Imaging Helps to Clarify Most Mammographic Findings Suspicious for Cancer. *Radiology* (2018) 287 (3):761–70. doi: 10.1148/radiol.2017170273
219. Bickelhaupt S, Paech D, Kickingereder P, Steudle F, Lederer W, Daniel H, et al. Prediction of Malignancy by a Radiomic Signature From Contrast Agent-Free Diffusion MRI in Suspicious Breast Lesions Found on Screening Mammography. *J Magn Reson Imaging* (2017) 46(2):604–16. doi: 10.1002/jmri.25606
220. Jiang X, Xie F, Liu L, Peng Y, Cai H, Li L. Discrimination of Malignant and Benign Breast Masses Using Automatic Segmentation and Features Extracted From Dynamic Contrast-Enhanced and Diffusion-Weighted MRI. *Oncol Lett* (2018) 16(2):1521–8. doi: 10.3892/ol.2018.8805
221. Zhang Q, Peng Y, Liu W, Bai J, Zheng J, Yang X, et al. Radiomics Based on Multimodal MRI for the Differential Diagnosis of Benign and Malignant Breast Lesions. *J Magn Reson Imaging* (2020) 52(2):596–607. doi: 10.1002/jmri.27098
222. Parekh VS, Jacobs MA. Integrated Radiomic Framework for Breast Cancer and Tumor Biology Using Advanced Machine Learning and Multiparametric MRI. *NPJ Breast Cancer* (2017) 3:43. doi: 10.1038/s41523-017-0045-3
223. Holli-Helenius K, Salminen A, Rinta-Kiikka I, Koskivuo I, Brück N, Boström P, et al. MRI Texture Analysis in Differentiating Luminal A and Luminal B Breast Cancer Molecular Subtypes - a Feasibility Study. *BMC Med Imaging* (2017) 17(1):69. doi: 10.1186/s12880-017-0239-z
224. Sun X, He B, Luo X, Li Y, Cao J, Wang J, et al. Preliminary Study on Molecular Subtypes of Breast Cancer Based on Magnetic Resonance Imaging Texture Analysis. *J Comput Assisted Tomogr* (2018) 42(4):531–5. doi: 10.1097/RCT.0000000000000738
225. Xie T, Wang Z, Zhao Q, Bai Q, Zhou X, Gu Y, et al. Machine Learning-Based Analysis of MR Multiparametric Radiomics for the Subtype Classification of Breast Cancer. *Front Oncol* (2019) 9:505. doi: 10.3389/fonc.2019.00505
226. Xie T, Zhao Q, Fu C, Bai Q, Zhou X, Li L, et al. Differentiation of Triple-Negative Breast Cancer From Other Subtypes Through Whole-Tumor Histogram Analysis on Multiparametric MR Imaging. *Eur Radiol* (2019) 29(5):2535–44. doi: 10.1007/s00330-018-5804-5
227. Leithner D, Bernard-Davila B, Martinez DF, Horvat JV, Jochelson MS, Marino MA, et al. Radiomic Signatures Derived From Diffusion-Weighted Imaging for the Assessment of Breast Cancer Receptor Status and Molecular Subtypes. *Mol Imaging Biol* (2020) 22(2):453–61. doi: 10.1007/s11307-019-01383-w
228. Dong Y, Feng Q, Yang W, Lu Z, Deng C, Zhang L, et al. Preoperative Prediction of Sentinel Lymph Node Metastasis in Breast Cancer Based on Radiomics of T2-Weighted Fat-Suppression and Diffusion-Weighted MRI. *Eur Radiol* (2018) 28(2):582–91. doi: 10.1007/s00330-017-5005-7
229. Chai R, Ma H, Xu M, Arefan D, Cui X, Liu Y, et al. Differentiating Axillary Lymph Node Metastasis in Invasive Breast Cancer Patients: A Comparison

of Radiomic Signatures From Multiparametric Breast MR Sequences. *J Magn Reson Imaging* (2019) 50(4):1125–32. doi: 10.1002/jmri.26701
230. Liu W, Cheng Y, Liu Z, Liu C, Cattell R, Xie X, et al. Preoperative Prediction of Ki-67 Status in Breast Cancer With Multiparametric MRI Using Transfer Learning. *Acad Radiol* (2021) 28(2):e44–53. doi: 10.1016/j.acra.2020.02.006
231. Zhang Y, Zhu Y, Zhang K, Liu Y, Cui J, Tao J, et al. Invasive Ductal Breast Cancer: Preoperative Predict Ki-67 Index Based on Radiomics of ADC Maps. *La radiologia media* (2019) 125(2):109–16. doi: 10.1007/s11547-019-01100-1
232. Fan M, Yuan W, Zhao W, Xu M, Wang S, Gao X, et al. Joint Prediction of Breast Cancer Histological Grade and Ki-67 Expression Level Based on DCE-MRI and DWI Radiomics. *IEEE J Biomed Health Inf* (2020) 24 (6):1632–42. doi: 10.1109/JBHI.2019.2956351
233. Fan M, Liu Z, Xu M, Wang S, Zeng T, Gao X, et al. Generative Adversarial Network-Based Super-Resolution of Diffusion-Weighted Imaging: Application to Tumour Radiomics in Breast Cancer. *NMR Biomed* (2020) 33(8):e4345. doi: 10.1002/nbm.4345
234. Liu Z, Li Z, Qu J, Zhang R, Zhou X, Li L, et al. Radiomics of Multiparametric MRI for Pretreatment Prediction of Pathologic Complete Response to Neoadjuvant Chemotherapy in Breast Cancer: A Multicenter Study. *Clin Cancer Res* (2019) 25(12):3538–47. doi: 10.1158/1078-0432.CCR-18-3190
235. Michoux N, Van den Broeck S, Lacoste L, Fellah L, Galant C, Berlière M, et al. Texture Analysis on MR Images Helps Predicting non-Response to NAC in Breast Cancer. *BMC Cancer* (2015) 15:574. doi: 10.1186/s12885-015-1563-8
236. Panzeri MM, Losio C, Della Corte A, Venturini E, Ambrosi A, Panizza P, et al. Prediction of Chemoresistance in Women Undergoing Neo-Adjuvant Chemotherapy for Locally Advanced Breast Cancer: Volumetric Analysis of First-Order Textural Features Extracted From Multiparametric MRI. *Contrast Media Mol Imaging* (2018) 2018:1–7. doi: 10.1155/2018/8329041
237. Schmitz AMT, Veldhuis WB, Menke-Pluijmers MBE, van der Kemp WJM, van der Velden TA, Kock MCJM, et al. Multiparametric MRI With Dynamic Contrast Enhancement, Diffusion-Weighted Imaging, and 31-Phosphorus Spectroscopy at 7 T for Characterization of Breast Cancer. *Invest Radiol* (2015) 50(11):766–71. doi: 10.1097/RLI.0000000000000183
238. Bogner W, Pinker K, Zaric O, Baltzer P, Minarikova L, Porter D, et al. Bilateral Diffusion-Weighted MR Imaging of Breast Tumors With Submillimeter Resolution Using Readout-Segmented Echo-Planar Imaging at 7 T. *Radiology* (2014) 274(1):74–84. doi: 10.1148/radiol.14132340
239. Gruber S, Minarikova L, Pinker K, Zaric O, Chmelik M, Strasser B, et al. Diffusion-Weighted Imaging of Breast Tumours at 3 Tesla and 7 Tesla: A Comparison. *Eur Radiol* (2016) 26(5):1466–73. doi: 10.1007/s00330-015-3947-1
240. Korteweg MA, Veldhuis WB, Visser F, Luijten PR, Mali WPTM, van Diest PJ, et al. Feasibility of 7 Tesla Breast Magnetic Resonance Imaging Determination of Intrinsic Sensitivity and High-Resolution Magnetic Resonance Imaging, Diffusion-Weighted Imaging, and (1)H-Magnetic Resonance Spectroscopy of Breast Cancer Patients Receiving Neoadjuvant Therapy. *Invest Radiol* (2011) 46 (6):370–6. doi: 10.1097/RLI.0b013e31820df706
241. Iima M, Le Bihan D. Clinical Intravoxel Incoherent Motion and Diffusion MR Imaging: Past, Present, and Future. *Radiology* (2015) 278(1):13–32. doi: 10.1148/radiol.2015150244

Conflict of Interest: RR-P: Human Longevity Inc: Consultant, Cortech Labs: Stock options, Curemetrix: Stock options, consultant. and GE: research agreement.

The remaining authors declare that the research was conducted in the absence of any commercial or financial relationships that could be construed as a potential conflict of interest.

frontiers | Frontiers in Oncology

TYPE Original Research
PUBLISHED 22 August 2022
DOI 10.3389/fonc.2022.855519

OPEN ACCESS

EDITED BY
Marie-France Penet,
Johns Hopkins Medicine, United States

REVIEWED BY
Durgesh K. Dwivedi,
King George's Medical University, India
William Ian Duncombe Rae,
The University of Sydney, Australia

*CORRESPONDENCE
Michał Lis
lis.michal.md@gmail.com

†These authors have contributed equally to this work and share first authorship

‡These authors have contributed equally to this work and share last authorship

SPECIALTY SECTION
This article was submitted to Breast Cancer, a section of the journal Frontiers in Oncology

RECEIVED 15 January 2022
ACCEPTED 11 July 2022
PUBLISHED 22 August 2022

CITATION
Dołęga-Kozierowski B, Lis M, Marszalska-Jacak H, Koziej M, Celer M, Bandyk M, Kasprzak P, Szynglarewicz B and Matkowski R (2022) Multimodality imaging in lobular breast cancer: Differences in mammography, ultrasound, and MRI in the assessment of local tumor extent and correlation with molecular characteristics.
Front. Oncol. 12:855519.
doi: 10.3389/fonc.2022.855519

Multimodality imaging in lobular breast cancer: Differences in mammography, ultrasound, and MRI in the assessment of local tumor extent and correlation with molecular characteristics

Bartosz Dołęga-Kozierowski[1†], Michał Lis[2*†], Hanna Marszalska-Jacak[1], Mateusz Koziej[3], Marcin Celer[1], Małgorzata Bandyk[1], Piotr Kasprzak[1‡], Bartłomiej Szynglarewicz[4,5‡] and Rafał Matkowski[4,5‡]

[1]Breast Unit, Department of Breast Imaging, Lower Silesian Oncology, Pulmonology and Hematology Center, Wroclaw, Poland, [2]Burn and Plastic Surgery Department, Ludwik Rydygier Memorial Specialized Hospital in Krakow, Krakow, Poland, [3]Department of Anatomy, Jagiellonian University Medical College, Krakow, Poland, [4]Breast Unit, Department of Breast Surgery, Lower Silesian Oncology, Pulmonology and Hematology Center, Wroclaw, Poland, [5]Department of Oncology, Faculty of Medicine, Wroclaw Medical University, Wroclaw, Poland

Introduction: Invasive lobular breast cancer (ILC) is a diagnostic challenge due to the diversity of morphological features. The objective of the study was to investigate the presentation and local extent of ILC using various imaging techniques and to assess the correlation between imaging and molecular profile.

Materials and methods: We reviewed 162 consecutive patients with ILC found on vacuum-assisted biopsy, who underwent evaluation of the lesion morphology and extent using ultrasound (US), mammography (MMG), and magnetic resonance imaging (MRI). Radiographic features were compared with ILC intrinsic subtype based on the expression of Ki-67 and estrogen, progesterone, and HER2 receptors.

Results: A total of 113 mass lesions and 49 non-mass enhancements (NMEs) were found in MRI. Masses were typically irregular and spiculated, showing heterogeneous contrast enhancement, diffusion restriction, and type III enhancement curve. NMEs presented mainly as the area of focal or multiregional distribution with heterogeneous or clumped contrast enhancement, diffusion restriction, and type III enhancement curve. Lesion extent significantly varied between MRI and MMG/ultrasonography (USG) ($P < 0.001$) but did not differ between MGF and ultrasonography (USG). The larger the ILC, the higher the disproportion when lesion extent in MRI was compared with MMG ($P < 0.001$) and ultrasonography (USG) ($P < 0.001$). In the study group, there were 97 cases of luminal A subtype (59.9%), 54 cases of luminal B HER2– (33.3%), nine cases of luminal B HER2+ (5.5%), and two cases of triple

negative (1.2%). The HER2 type was not found in the study group. We did not observe any significant correlation between molecular profile and imaging.

Conclusion: MRI is the most effective technique for the assessment of ILC local extent, which is important for optimal treatment planning. Further studies are needed to investigate if the intrinsic subtype of ILC can be predicted by imaging features on MRI.

KEYWORDS

breast cancer, invasive lobular carcinoma (ILC), invasive lobular breast cancer, magnetic resonance imaging, multimodality imaging, lobular breast cancer

Background

Breast cancer imaging is constantly evolving and research protocols are continually being modified. The method of highest sensitivity (94% to 99%) for invasive lobular breast cancer (ILC) detection is magnetic resonance imaging (MRI) (1–3). Although ILC accounts for 5% to 15% of all breast cancers (4) due to its course and wide diversity of histopathological, clinical, and radiological images, ILC still presents significant challenge for clinicians specializing in breast oncology (2, 5, 6).

Biological diversity of ILC is reflected in molecular subtypes defined on the basis of standard biomarkers analyzed *via* immunohistochemistry: estrogen receptor (ER), progesterone receptor (PR), and human epidermal growth factor-2 receptor (HER2) as well as the estimation of tumor proliferation index Ki67 that allows risk stratification and implementation of personalized therapies. The modern classification of lobular breast cancer (LBC) includes five subtypes of different molecular profile: luminal A (ER+ and/or PR+, HER2−, Ki67<15%), luminal B (HER2− subtype: ER+ and/or PR+, HER2−, Ki67≥15%; HER2+ subtype: ER+ and/or PR+, HER2+), HER2 type (ER− and PR−, HER2+), and triple negative (TN) breast cancer (7).

Because of their radiological characteristics, lesions that cannot be seen in mammography (MMG) or in ultrasound (US) are revealed to be advanced when they are exhibited in MRI. Moreover, ILC is often multifocal, multicentric, or even bilateral, each of which influences choice of therapeutic procedure. That is why, for many years, MRI has been recognized as a diagnostic standard for ILC as it has the highest sensitivity among the available imaging methods (2, 8–10).

Abbreviations: BPE, background parenchymal enhancement; ER, estrogen receptor; FGT, fibroglandular tissue; HER2, Herceptin receptor; IDC, invasive ductal carcinoma; ILC, invasive lobular carcinoma; Lum A, luminal A; Lum B, luminal B; MMG, mammography; NME, non-mass enhancement; PGR, progesterone receptor; TN, triple negative.

Magnetic resonance imagining is often emphasized as the LBC diagnosis of choice because it can easily detect changes that other methods often cannot (11). One factor influencing MRI's popularity is that lobular carcinoma spreads along milk ducts and the loss of E-cadherins in terminal duct lobular units. This type of growth is characterized by much lower incidence of necrotic changes, hemorrhages, or microcalcifications when compared to ductal carcinoma *in situ* (2, 5, 12, 13).

The correlation between radiological features and molecular profile of the LBC is the subject of extensive research, the results of which do not allow clear conclusions to be drawn due to relatively small study groups (11, 14–17).

Study objectives

1. The assessment of morphology and local extent of ILC in three imaging techniques.
2. The assessment of the correlation between the results of three imaging methods (MMG, US, and MRI) and molecular profile of ILC.

Materials and methods

One hundred sixty-two patients with ILC diagnosis who were treated in the Breast Unit of Wrocław Comprehensive Cancer Centre, Wroclaw, Poland, between September 2016 and February 2020 were subjected to a retrospective analysis of their imaging (MRI, US, and MMG) and histological test results.

The diagnosis of ILC was made according to the following protocol: patients were referred to the Breast Unit of Wrocław Comprehensive Cancer Centre to check a lesion discovered during outpatient US examination. Shortly thereafter, US and MMG were performed in the Wroclaw breast unit. Results were

analyzed by two independent teams of specialists using American College of Radiology Breast Imaging Reporting and Data System, and patients were qualified for percutaneous core needle biopsy. Ultimately, the study included only patients with ILC confirmed in the histopathological examination.

The criteria for exclusion of patients from the study included neoadjuvant chemotherapy, allergy to gadolinium, and other medical contraindications to contrast-enhanced MRI. US and MMG scans were analyzed by three breast radiologists with at least 20 years of professional experience and one assistant with 4 years of professional experience, whereas the breast MRI scans were subjected to independent dual review by radiologists interpreting more than 600 breast MRI scans per year.

Ultrasound

Esaote My Lab Class C ultrasound devices and a 5- to 13-MHz linear probe were used to perform US examinations. The default "breast" preset was used for the analysis of images, which guaranteed repeatability of the tests. In addition, single focusing was used. The test result was prepared according to ACR BI-RADS.

Mammography

Mammographic examination was performed on the Hologic Selenia Dimension system (Hologic, Inc., Bedford, MA) in standard projections in the compression force range of 90N to 140N and then described on the Hologic console with Secure View software according to ACR BI-RADS lexicon. The measurement was performed as follows: round or oval tumor (main lesion – index mass), spiculated lesion (main lesion without projections), and area of high density (borders of the highest saturation area).

The description included isolated alterations of cell architecture and accompanying changes, as well as microcalcifications measured for greatest extent.

Magnetic resonance imaging

MRI of the breast was performed on the Magnetom Avanto Tim Dot 1.5T (Siemens Healthcare, Erlangen, Germany) with a compatible 18-channel diagnostic breast coil. Imaging was performed within 14 days of core needle biopsy and with the patient in the prone position. The tests were conducted according to the following protocol:

T1 HR—slice thickness, 0.7 mm [voxel size: 0.7 × 0.7 × 0.7 mm; SNR (signal-noise ratio), 1.00]; slices per slab, 208; TR, 5.64 ms/TE, 5.64 ms; FoV read, 250 mm; FoV phase, 169.3; bandwidth = 300 Hz; slice gap, 0.14 mm; flip angle, 15°; and a total acquisition time = 2 min 28 s.

T2—slice thickness, 2 mm (voxel size: 0.5 × 0.5 × 2.0 mm; SNR, 1.00); slices, 57; TR, 6,670 ms/TE, 100 ms; FoV read, 250 mm; FoV phase, 168.8; bandwidth = 326 Hz; slice gap, 0.4 mm; flip angle, 150°; and a total acquisition time = 2 min 53 s.

TIRM (Turbo Invertion Recovery Magnitude)—slice thickness, 2 mm (voxel size: 0.7 × 0.7 × 2.0 mm; SNR, 1.00); slices, 57; TR, 7,850 ms/TE, 63 ms; FoV read, 250 mm; FoV phase, 168.8; bandwidth = 334 Hz; slice gap, 0.4 mm; flip angle, 150°; and a total acquisition time = 3 min 24 s.

T1 3D dynamic—matrix, 389 × 256; slice thickness, 1 mm (voxel size: 1 × 1 × 1 mm; SNR, 1.00); slices per slab, 144; TR, 4.42 ms/TE, 1.7 ms; flip angle, 10°; acquisition time of each phase, approximately 55 s (one phase before contrast, six phases after contrast injection).

DWI—b-value, 50/400/800 s/mm^2; slice thickness, 3 mm (voxel size: 1.3 × 1.3 × 3.0 mm; SNR, 1.00); slice numbers, n = 45; TR, 6300 ms/TE, 70 ms; slice gap, 0.6 mm; and a total acquisition time = 3 min 22 s.

The dynamic test was performed with the administration of the contrast agent Dotarem (gadoterate meglumine) at the dose of 0.1 mmol/kg and the flow of 2 ml/s, followed by a rinse with 30 ml of NaCl.

The tests were analyzed by independent radiology specialists (double reading) using Siemens software tool (Brevis MRI), and all lesions were evaluated by the American College of Radiology – BIRADS breast MRI lexicon (Fifth Edition).

For all axial plane acquisitions, the phase encoding direction was from right to left to limit artifacts repeating cardiac and respiratory movement. Moreover, movement artifacts were eliminated by the "Motion Correction" function. "Color mapping" function allowed confirmation of the locations for determining the enhancement curves.

In first step, we placed Region of interest (ROI) on the aorta to confirm a typical washout pattern. Subsequently, the enhancement curve was assessed in the initial phase and next in the late phase. In the T1 3D dynamic, the first two phases are the sequences that were used to assess the morphology of the lesion and to determine the inflow of contrast in the initial phase (where we defined the inflow as slow <50%, medium 50%–100%, and fast > 100%). The remaining acquisitions were used to determine the type of washout curve: type 1, benign; type 2, intermediate with plateau; type 3, malignant, with secondary washout.

In the dynamic sequence, ROI (size, 3 × 3 pixels) was measured three times on hyperintense lesions in DCE-MRI, both within mass and non-mass enhancement (NME). Lesion size was measured on the DCE MRI images. An apparent diffusion coefficient (ADC) was calculated from DWI by using a monoexponential model in dedicated and clinically validated software syngo.MR BreVis (Siemens Helthineers Erlangen Germany) using standardized

DWI preprocessing pipeline that included all necessary steps in particular epi-distortion and motion correction.

To determine the ADC value, we looked for pathological contrast enhancement—tumor mass or NME, which correlated with the hyperintensive region in the DWI (b = 800 s/mm^2) and the low signal on the ADC maps. Afterward, ROI about 5 ± 2 mm^2 was placed two times on the most restricted area inside the solid part of the lesion on the ADC map. We were trying to avoid cystic, necrotic, fatty regions, or hematoma after biopsy inside the mass using T2-weighted images or TIRM.

Statistical analysis

Quantitative data were reported as mean ± standard deviation (SD) or median/interquartile range, according to a normal distribution. For the qualitative data, frequencies and percentages were calculated. Mean differences between the two groups were compared by the Student's t-test, whereas the Mann–Whitney U-test was applied for comparisons of median values. The qualitative variables were compared using the chi-squared ($\chi 2$) test of proportions for categorical variables. The receiver operating characteristic (ROC) curves were used to assess both MRI and MMG method to better discriminate nodal status (presence of metastases based on US, widely regarded as the gold standard for tumor detection). Area under the curve (AUC) with standard error (SE) was reported, as well as sensitivity and specificity. In addition, the Spearman correlation between parameters was performed. Bland–Altman method was used to compare two radiological methods in measuring lesion size. The data were analyzed using StatSoft Statistica 13.1 PL for Microsoft Windows 10. The results with $P < 0.05$ were considered as statistically significant. Correspondence analysis was performed to compare the relative frequencies of prevalence of selected features across different imaging methods.

Results

Mammography

In a study group of 162 patients, 54 cases of tumor and 20 cases of high density areas were found (Table 1). The sensitivity of MMG in the diagnosis of ILC in the study group was 113 of the 162 (69.8%). Areas of high density identified by MMG most often did not correspond to morphological changes of the NME identified by MRI. Moreover, the size of the lesions found in the two methods was different ($P = 0.007$).

Ultrasound

In US, a mass was found in 144 of the 162 patients (mean size, 22.6 mm; range, 9–84 mm), and an area of indefinite shape and borders were detected in 17 patients (mean size, 28.6 mm; range, 10–87 mm). The sensitivity of US in the diagnosis of ILC in the study group was 161 of 162 (99.4%). The vast majority of changes (93.8%) revealed poorly defined contours. It was also discovered that areas of concern revealed by US do not correspond accordingly to NME morphological changes isolated by MRI.

Magnetic resonance imaging

In a study group of 162 patients with ILC, there were 113 tumors (69.8%) and 49 (30.2%) NME-type changes found in MRI. The most common morphological type of ILC was an irregular, spiculated mass showing heterogeneous contrast enhancement, diffusion restriction of the mean ADC value of 0.74 × 10–3 mm^2/s, and type III enhancement curve. In NME changes, the types of distribution most often found were focal (36.7%) and multi-regional (34.7%), with heterogeneous and clumped contrast enhancement accounting for 44.9% and 30.6%, respectively, of all NME changes. In NME changes, the dominant type of enhancement was type III with the mean ADC value of 0.72 × 10^3 mm^2/s (Table 1; Figures 1, 2).

Histopathology

The dominant type of tumor identified in histopathology was of grade (G feature) 2 (88.3%) with no amplification of HER2 receptors (92%). The mean value of receptor expression in the study group was, respectively, ER – 93.9% and PR – 58.7%, whereas the mean Ki67 value was 13.37%, which is related to the higher incidence of luminal A subtype in the study group (n = 97, 59.9%). The data on the mass feature G, structure, and background parenchymal enhancement (BPE) show that G2 tumors with heterogeneous fibroglandular structure and slight enhancement in the stroma are more common (Table 2; Figure 3).

Imaging and assessment of local extent

It is interesting that, in the study group, microcalcifications were found in 34 of 162 (21%) patients in MMG. In the group of changes presenting as tumors in MRI, microcalcifications were found in 20 of 113 (17.7%) patients in MMG, whereas in the NME group, they were significantly more often, i.e., found in 14 of 49 (28.6%) patients ($P < 0.05$).

The size of the lesions described in MRI did not differ significantly from those described by US examination ($P = 0.056$).

It has also been observed that the bigger the lesion, the higher the disproportion between its size measured in different methods: MRI *vs.* MMG $R = 0.455$; $P < 0.001$ and MRI *vs.* US $R = 0.425$; $P < 0.001$). The Bland–Altman plot along with scatterplot

10.3389/fonc.2022.855519

TABLE 1 Imaging parameters and clinicopathological features of 162 patients with invasive lobular carcinoma.

Demographic data					
Patients count		**162**			
Patients age (min/max/average)		**32/94/65.5**			
MRI: mass		**MRI: non-mass enhancement (NME)**		**MRI: other**	
Shape	**113**	**Distribution**	**49**	**Architectural distortion**	**162**
Oval	8	Focal	18	None	159
Round	4	Linear	4	Present	3
Irregular	101	Segmental	6	**Lymph nodes**	**162**
Margin	**113**	Regional	4	Normal	146
Circumscribed	8	Multiple regions	17	Abnormal	16
Not circumscribed	105	Diffuse	0		
Enhancement	**113**	**Enhancement**	**49**		
Homogeneous	28	Homogeneous	8		
Heterogeneous	81	Heterogeneous	22		
Rim enhancement	4	Clumped	15		
Dark internal septations	0	Clustered ring	4		
Kinetic curve (delayed phase)	**113**	**Kinetic curve (delayed phase)**	**49**		
Persistent	18	Persistent	8		
Plateau	34	Plateau	8		
Washout	61	Washout	33		
Mammography (MMG)		**Ultrasound (US)**			
Lymph nodes	**162**	**Lymph nodes**	**162**		
Normal	154	Normal	142		
Abnormal	8	Abnormal	20		
Findings	**74**	**Findings**	**161**		
Mass	54	Mass	144		
Asymmetric density	20	Region	17		
Calcifications	**162**	**Margin**	**155**		
None	128	Circumscribed	3		
Present	34	Not circumscribed	152		
Architectural distortion	**162**				
None	129				
Present	33				
Histopathology and immunohistochemistry					
Molecular subtypes	**162**	**Grading (G)**	**162**		
Luminal A	97	G1	12		
Luminal B (HER2−)	54	G2	143		
Luminal B (HER2+)	9	G3	7		
HER2 type	0				
Triple negative	2				

Comparison of results between three imaging modalities

		Total cases	**Average**	**Median**	**Min**	**Max**	**Std Dev**
Mass (mm)	MRI	**113**	35	30	5	122	24
	US		24	22	3	65	13
	MMG		24	20	1	84	15
NME (mm)	MRI	**49**	59	60.5	15	96	24
	US		31	26	0.9	84	18
	MMG		31	20.5	8	84	23

(Continued)

TABLE 1 Continued

Demographic data								
Patients count	**162**							
Patients age (min/max/average)	**32/94/65.5**							
MRI: mass	**MRI: non-mass enhancement (NME)**					**MRI: other**		
Receptors and markers statistics								
Tested positive	**Total cases**	**Average**	**Median**	**Min**	**Max**	**Low**	**Up**	**Std Dev**
Estrogen receptor ER (%)	162	93.97	100	0	100	90	100	15.14
Progesterone receptor PR (%)	162	58.70	75	0	100	8	100	41.07
Ki-67 biomarker (%)	162	13.37	10	0	70	5	20	11.11

graph is presented in Figure 4. The limits of agreement for the lesion measured in MRI and MMG varied from −59.68 to 23.84 mm and for MRI and US varied from −67.14 to 29.97 mm (Figure 4)

In the studied patients with T1 tumor found *via* US (n = 57), MRI showed that the size of the lesion was underestimated and the T feature of the lesion increased to T2 in 23 cases (41%) and to T3 in two cases (3.6%). A similar situation occurred in patients who had T2 tumor found in US (n = 92), and the lesion was reassessed as T3 in 35 cases (38%).

In 50 (30.8%) cases, MMG did not reveal any pathological changes (tumors, high-density areas, microcalcifications, and/or architectural alterations).

In the analyzed material, NME lesions were characterized by a higher range of sizes and were not as homogeneous as tumors.

Comparison of the ADC value and the tumor's T feature according to the TNM classification showed statistically significant difference between the T1 and T3 group of tumors. The higher the tumor's T feature, the lower the ADC value, which corresponds to increased diffusion restriction.

Architectural alterations were found in 20.4% of patients in MMG. Molecular studies revealed association on the verge of statistical significance between architectural alterations and increased expression of progesterone receptors (P = 0.57). Other results of molecular studies do not correlate with architectural alterations (Table 4). Architectural alterations found in MMG were confirmed in MRI in two patients only.

Imaging and molecular profile

Apart from the results presented here, no findings proved correlation between ILC presentation on imaging and molecular profile of the tumor. Microcalcifications did not correlate with

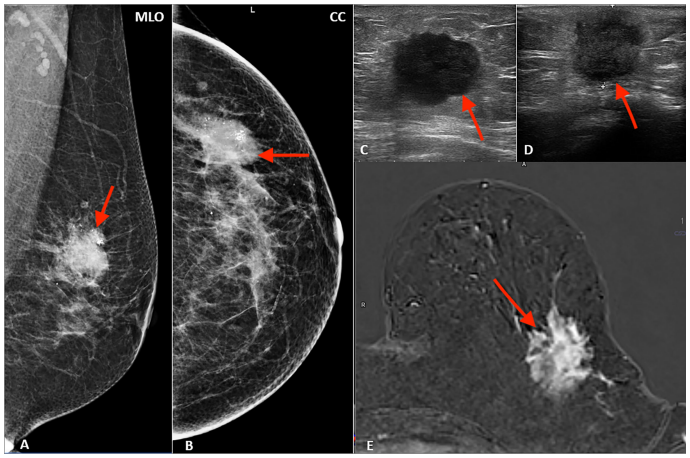

FIGURE 1
Multimodality presentation of lobular breast cancer; Patient 1 left breast: **(A, B)** mammography: MLO **(A)** and CC **(B)**—not circumscribed, spiculated mass with microcalcifications (red arrow); **(C, D)** ultrasound—not circumscribed, spiculated, hypoechoic mass (red arrow); **(E)** MRI T1 post contrast—not circumscribed, spiculated mass with heterogenous contrast enhancement (red arrow).

10.3389/fonc.2022.855519

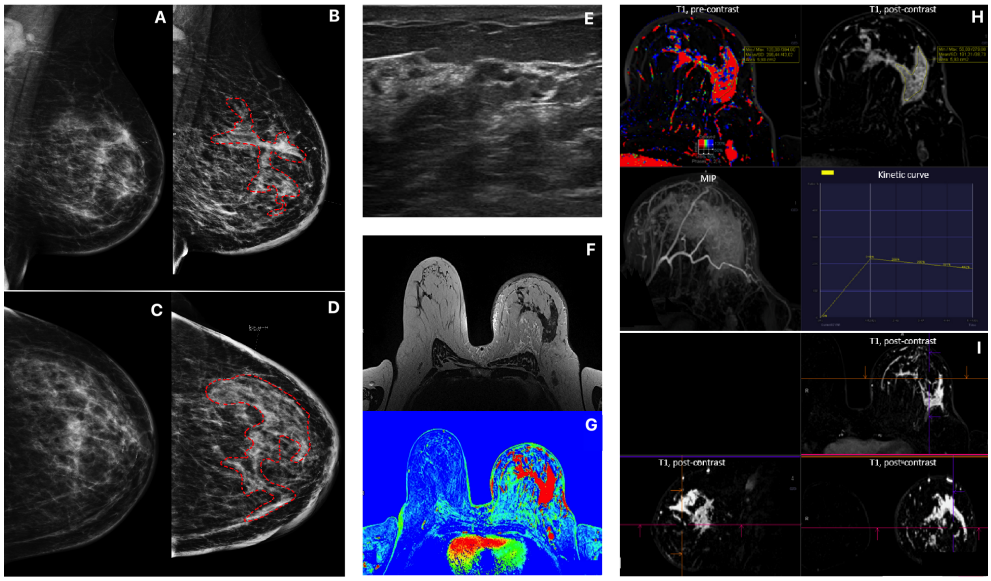

FIGURE 2
Patient 2, Multimodality presentation of Lobular Breast Cancer, left breast: **(A, B)** Mammography, [**(A)** MLO and **(B)** CC] asymetric density cancer, cancer marked with red dotted line. **(C, D)** Mammography, [**(C)** MLO and **(D)** CC] the same Patient after 4 months, cancer marked with red dotted line. **(E)** ultrasound- not circumscribed, hypoechoic region. **(F)** MRI T2 TSE - non-mass enhancement. **(G)** MRI T1 fl3d dynamic PEI. **(H, I)** MRI - diffused, non-mass enhancement with heterogenous enhancement [**(H)** T1 pre contrast; T1 post contrast; MIP and wash out kinetic curve; **(I)** 3D T1 post contrast].

the expression of HER2 receptors (P = 0.87), ER (P = 0.81), PR (P = 0.65), or Ki67 (P = 0.25). The same is true for architectural alterations that do not correlate with the expression of HER2 (P = 0.4), ER (P = 0.4), or Ki67 (P = 0.85). Similarly, morphological type of ILC revealed in MRI did not correlate with ADC value (P = 0.62) (Table 3).

Differences between luminal A and luminal B

In the study group consisting of 162 patients, there were 97 cases of luminal A subtype (59.9%), 54 cases of luminal B HER2– (33.3%), nine cases of luminal B HER2+ (5.5%), and two cases of

TABLE 2 Comparison between feature G *vs.* MRI and feature G *vs.* BPE.

Breast density	**G1**	**G2**	**G3**	**Total**
Almost entirely fat	2	19	0	21
Scattered fibrograndular tissue	4	77	4	85
Heterogenous fibrograndular tissue	4	36	2	42
Extreme fibrograndular tissue	2	11	1	14
Total	**12**	**143**	**7**	**162**
BPE	**G1**	**G2**	**G3**	**Total**
1. Minimal	6	68	4	78
2. Mild	1	37	1	39
3. Moderate	3	30	2	35
4. Marked	2	8	0	10
Total	**12**	**143**	**7**	**162**

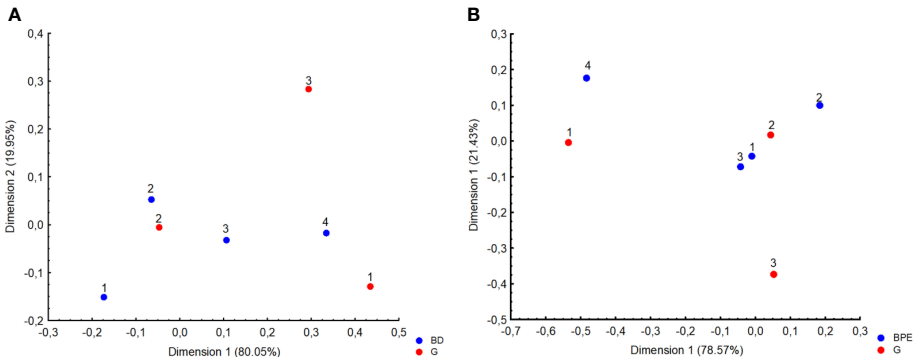

FIGURE 3
Correspondence analysis plot of the data which is a two-dimensional representation of grading (G) and **(A)** Breast Density (BD 1, almost entirely fat; 2, scattered fibrograndular tissue; 3, heterogenous fibrograndular tissue; 4, extreme fibrograndular tissue), as well as **(B)** background parenchymal enhancement (BPE).

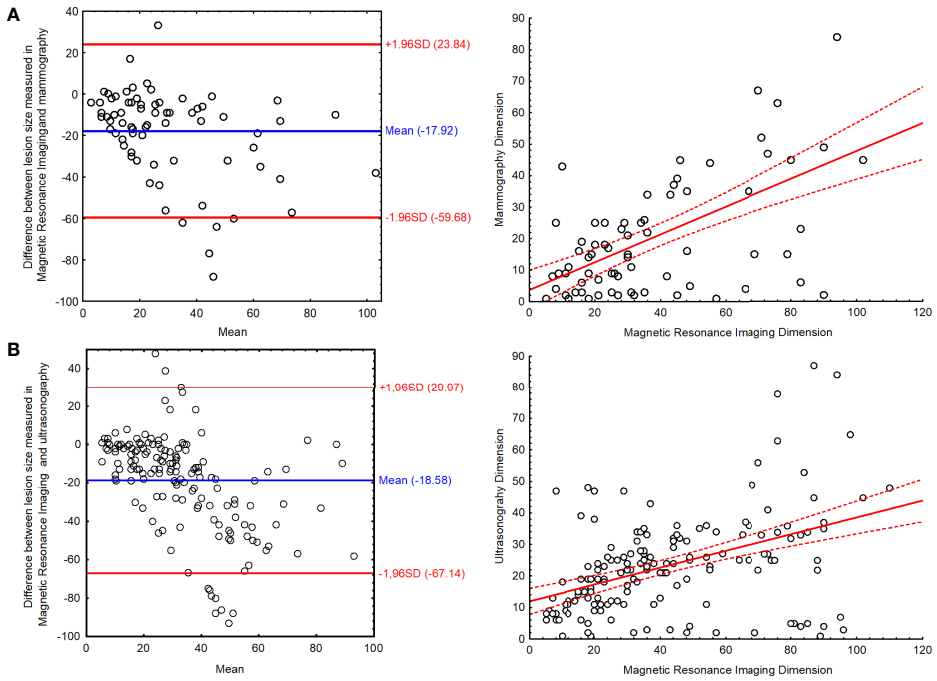

FIGURE 4
The Bland–Altman plot with scatter plot for the results of lesion size measured in magnetic resonance imaging and **(A)** mammography and **(B)** ultrasonography.

TABLE 3 Comparison between presence of microcalcifications and molecular tumor profile.

Variable	No Microcalcifications (n = 34)		Present Microcalcifications (n = 128)		
	Mean (SD)	Range	Mean (SD)	Range	p
ER	92.9	10–100	94.2	0–100	0.82
PR	55.1	0–100	59.6	10–100	0.66
KI67	14.6	1–60	13	5–19	0.26

triple negative (1.2%). The HER2 type was not found in the study group (Table 4).

Lymph nodes

In the study group, pathological lymph nodes were found in 20 patients (12.3%). US had the highest detection rate for pathological lymph nodes (US 12.3% vs. MRI 9.9% vs. MMG 4.9%) (MRI AUC 0.757 ± 0.071; MMG AUC 0.671 ± 0.076). MRI was shown to be more sensitive than MMG with similar specificity in imaging pathological nodes in patients with ILC when assessed using ROC curve (MRI sensitivity = 0.550; specificity = 0.965; MMG sensitivity = 0.350; specificity = 0.993) (Figure 5).

Discussion

Interestingly, this study confirms the findings of others regarding how MMG and US underestimate LBC size while MRI produces more accurate data. These findings suggest that MRI is the best choice during pre-operative management so as to customize the most appropriate therapeutic plan for the individual patient. (18–20) Some works suggest that ILC is often multifocal or even bilateral, but it is often not detected in methods other than MRI. Schelfout et al. demonstrated in their study that additional ILC foci, previously not shown by US or MMG, were detected in 50% of patients. (21) In addition to MRI's ability to most clearly define tumor parameters, this study also identified its ability to assess lesion size more accurately than other methods. This finding is important because

TABLE 4 Differences between luminal A and luminal B ILC type.

Demographic data

		Luminal A (Lum A)		Luminal B (Lum B)					
Patients count		97		63					
Patients age (min/max/average)		46/91/66		32/94/64.5					
General data									
Size distribution (feature T) in various methods		**T1size < 2 (cm)**	**T22 (cm) ≤ size < 5 (cm)**	**T3size ≥ 5 (cm)**	**Total cases**	**Grading (feature G)**	**Lum A**	**Lum B**	
Lum A	MRI	22	45	30	97	G1	6	6	
	MMG	78	16	3		G2	89	52	
	US	45	46	6		G3	2	5	
Lum B	MRI	14	28	21	63				
	MMG	40	19	4					
	US	25	35	3		Total cases	97	63	
MRI: mass			**MRI: non-mass enhancement (NME)**			**MRI: other**			
		Lum A	**Lum B**		**Lum A**	**Lum B**		**Lum A**	**Lum B**
Shape			**Distribution**				**Architectural distortion**		
Oval		6	2	Focal	11	7	None	89	55
Round		3	1	Linear	3	1	Present	8	8
Irregular		56	43	Segmental	4	2	**FGT**		
Margin				Regional	3	1	Fat	14	6
Circumscribed		6	2	Multiple regions	11	6	Scattered	49	35
Not circumscribed		58	43	Diffuse	0	0	Heterogeneous	26	16
Spicular		1	1	**Enhancement**			Extreme	8	6
Enhancement				Homogeneous	4	4	BPE		
Homogeneous		22	5	Heterogeneous	15	7	Minimal	49	28
Heterogeneous		43	41	Clumped	10	5	Mild	21	18
Kinetic curve (delayed phase)				Clustered ring	3	1	Moderate	19	15
Persistent		15	3	**Kinetic curve (delayed phase)**			Marked	8	2
Plateau		17	16	Persistent	6	2			
Washout		33	27	Plateau	6	2			
				Washout	18	13			

(Continued)

TABLE 4 Continued

Mammography (MMG)	Lum A	Lum B
Calcifications		
None	78	48
Present	19	15
Architectural distortion		
None	77	50
Present	20	13
Lymph nodes		
Normal	94	58
Abnormal	3	5
Findings		
Mass	29	25
Asymm. density	11	9

Ultrasonography (US)	Lum A	Lum B
Margin		
Circumscribed	1	2
Not circumscribed	88	57
Irregular	4	1
Spicular	0	0
Lymph nodes		
Normal	86	54
Abnormal	11	9
Findings		
Mass	85	57
Region	11	6

Size and diffusion statistics

Characteristic			Total cases	Average	Median	Min	Max	Low	Up	Std Dev
mass MRI	Mass size (cm)	Lum A	65	3.41	2.80	0.50	9.80	1.80	4.50	2.31
		Lum B	46	3.66	3.10	0.60	12.20	1.80	4.40	2.68
	Mass ADC[10^{-3} mm^2/s]	Lum A	65	0.73	0.70	0.30	1.20	0.60	0.80	0.17
		Lum B	46	0.76	0.75	0.40	2.00	0.60	0.90	0.28
NME MRI	NME size (cm)	Lum A	32	5.82	5.55	2.00	11.00	3.60	8.05	2.60
		Lum B	17	6.24	7.10	1.50	9.00	4.40	8.30	2.35
	NME ADC[10^{-3} mm^2/s]	Lum A	32	0.74	0.72	0.00	1.20	0.60	0.87	0.24
		Lum B	17	0.68	0.70	0.30	1.20	0.50	0.70	0.23
MMG	Mass size (cm)	Lum A	29	1.65	1.10	0.10	8.40	0.50	2.20	1.73
		Lum B	25	3.03	2.50	0.10	8.40	1.50	4.50	1.98
	asymmetric density size (cm)	Lum A	11	1.52	0.80	0.10	6.70	0.20	1.60	1.99
		Lum B	9	1.48	1.10	0.20	4.40	0.30	1.60	1.51
US	mass size (cm)	Lum A	85	2.13	2.10	0.10	8.40	1.10	2.70	1.51
		Lum B	57	2.46	2.30	0.20	6.40	1.20	3.30	1.53
	region size (cm)	Lum A	11	2.85	2.80	0.10	5.60	2.20	3.70	1.59
		Lum B	6	2.90	1.95	0.10	8.70	1.30	3.40	3.05

this information affects the T feature of TNM classification and consequently changes therapeutic management. (22)

In addition, the image of ILC in MRI was the same as described in the literature. According to the authors, ILC presents most often as an irregular, spiculated tumor showing a washout enhancement curve type. However, one should remember that this picture is not pathognomonic for ILC and may correspond to invasive ductal carcinoma (IDC). (4, 18, 23)

One of the diagnostic problems described in the available literature is the determination of ADC value for NME changes. (24) It should be noted, however, that although the T feature of the tumor correlates with the ADC value obtained in MRI, the literature, the same as the presented study, does not show any association between molecular profile of the tumor and ADC value.14 Therefore, ADC value is suitable only to indicate potential malignancy of the tumor, but it cannot be used to predict its molecular profile when standard examination protocol is followed.

An MRI may present LBC in two forms: as a mass or NME. The percentage distribution of these changes in the described database is consistent with the data from the literature: – 5% to 69% for NME and 31% to 95% for the tumor. (25–28) In the study group, LBC most often appeared as a mass in MMG. The second most frequent manifestation of LBC was architectural alteration. The obtained results regarding the morphology of LBC in imaging are consistent with the data from the literature. (13, 29)

Moreover, some data from the literature suggest a high rate of false negative results in MMG, as high as 29% of ILC cases. (30) This finding is probably due to the fact that the only presentation of ILC in MMG may be architectural alterations without the mass. (31) Approximately 50 cases (30.8%) of our study group had tumors that were impossible to identify, as were their associated pathological areas. In the described study, architectural alterations found in MMG were not visible in MRI. One of the reasons for this invisibility is the structure of

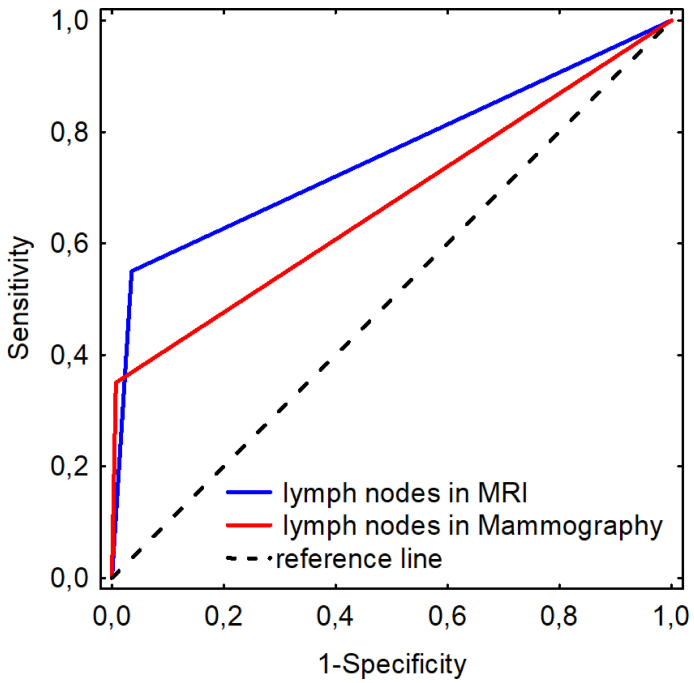

FIGURE 5
ROC curves for detecting lymph nodes in MRI and mammography.

breast tissue and it confirms that MRI is not a method of choice for the assessment of architectural alterations of the breast. (32)

Another factor that hinders the diagnosis of ILC in MMG is the relatively rare occurrence of microcalcifications. According to the literature, microcalcifications occur in only one to 25% of all ILC cases, which has a negative effect on the sensitivity of MMG in detecting this type of lesion (33–35). This finding is probably due to the fact that ILC does not invade milk ducts and, consequently, does not contribute to the formation of microcalcifications (13). At the same time, it should be noted that in the study group, microcalcifications were found in as many as in 42.85% of G3 tumors. It should be remembered, however, that there were too few patients with G3 tumor to consider these results statistically significant. The available literature indicates the much lower incidence of microcalcifications in ILC compared to IDC, which may be a predictive factor in the assessment of the tumor's G feature. This indication, however, requires further study on larger groups of patients (29).

In the study group, most LBC cases confirmed in MRI (99.38%) were also revealed in the US. Studies on the usefulness of US indicate its high sensitivity in the detection of LBC, defined by the authors at 68% to 95% (36–39). At the same time, the literature emphasizes the issue of accurate assessment of lesion size, an issue also highlighted in the presented work. The characteristics of LBC, particularly in this histological type of cancer, significantly complicate the assessment of the lesion borders and extent, which is often associated with underestimated size of the tumor (20, 40).

Literature mentions some attempts to find the association between radiological image and receptor profile of the tumor. Dilorenzo et al. reported attempts to demonstrate the relationship between BPE type and clinical tumor subtype. (41) This relationship, however, has not been found in the study group. Moreover, King et al. suggested in their work increased incidence of ILC in patients with high BPE. (42) Ko et al. found higher incidence of NME lesions in patients with the breast cancer (BC) HER2+ type (43).

Wen et al. correlated their findings with US images of the lesions. Interestingly, imaging did not reveal any differences between luminal A and luminal B morphologies, a finding consistent with ours. Wen et al. described the differences in the morphology between HER2-type tumors and the luminal type. Although the study by Wen et al. included a large number of study participants, none were experiencing HER2 tumors; therefore, data could not be compared between the study by Wen et al. and this one (44).

Despite the abovementioned limitations of US in the assessment of ILC size, it remains the gold standard in the diagnosis of changes in the lymph nodes. In the study group, US identified the largest number of pathological lymph nodes and was considered the gold standard in the evaluation of other methods (45, 46). The study is consistent with the literature data and it shows high sensitivity and specificity of MRI in the assessment of lymph nodes.

One limitation encountered during this study is the inability of MRI to correlate lesion size with its actual size as assessed *via* histopathology. This discrepancy was caused by retrospective methodology of the study and the fact that some patients received neoadjuvant chemotherapy that affected the size of the tumor before the surgery. As the result, objective determination of the lesion size in the histopathology was impossible. Historical evidence indicates that ILC is so rare and there is little archived data that describes it fully. Studies available for review are usually limited by any combination of these three elements: study limited to only one modality, group of study participants is small, or the histological type of BC is not taken into consideration (17, 47).

Conclusions

ILC poses a significant challenge to cancer diagnostics and management due to its histopathological and imaging complexity. This study strengthens the existing body of evidence, indicating that it is currently not possible to predict ILC molecular type when using imaging alone. Nevertheless, the large number of patients in this study made it possible to identify some radiological features that correlate to histopathology and part of the molecular panel. This study found MRI is still the preferred method for diagnosing ILC for multiple reasons that include how it enables detection of multifocal and bilateral neoplasms and allows for more reliable assessment of lesion size, both of which allow for improvements to therapeutic management plans based on TNM classification for ILC. Results obtained in the study group show, however, that there is no association between the studied parameters and proof that the morphology of ILC in imaging is independent of the cancer's histological type if luminal A and luminal B subtypes are considered. This study, like the study of Zhiqi Yang and Xiaofeng Chen (with others authors), suggests the importance of future study on larger groups of patients in multicenter settings as well as the value of developing radiogenetics, especially due to different results of studies (48).

Data availability statement

The original contributions presented in the study are included in the article/supplementary material. Further inquiries can be directed to the corresponding author/s.

Ethics statement

The study was conducted according to the Declaration of Helsinki. In each case an informed consent was obtained for all the procedures. All patients provided a written informed consent for the collection and publication of their medical data. Since the study was a retrospective analysis and did not involve any experimental interventions an independent ethics committee approval was abandoned. The Institutional Review Board reviewed and approved the study.

Author contributions

BD-K, ML, BS, and PK contributed to conception and design of the study. BD-K organized the database. MK performed the statistical analysis. BD-K and ML wrote the first draft of the manuscript. HM-J, MC, and MB wrote sections of the manuscript. All authors contributed to manuscript revision, read, and approved the submitted version.

Funding

This research was financed through statutory subsidies by the Minister of Science and Higher Education as part of the research grant SUBZ.C280.22.001 (record number in the Simple System).

Conflict of interest

The authors declare that the research was conducted in the absence of any commercial or financial relationships that could be construed as a potential conflict of interest.

Publisher's note

References

1. Montemezzi S, Camera L, Grazia M, Pozzetto A, Caliò A, Meliadò G, et al. Is there a correlation between 3T multiparametric MRI and molecular subtypes of breast cancer? *European Journal of Radiology* (2018) 108:120–7. doi: 10.1016/j.ejrad.2018.09.024

2. Derias M, Subramanian A, Allan S, Shah E, Teraifi HE, Howlett D. The role of magnetic resonance imaging in the investigation and management of invasive lobular carcinoma–a 3-year retrospective study in two district general hospitals. *Breast J* (2016) 22(4):384–9. doi: 10.1111/tbj.12594

3. Selvi V, Nori J, Meattini I, Francolini G, Morelli N, Di Benedetto D, et al. Role of magnetic resonance imaging in the preoperative staging and work-up of patients affected by invasive lobular carcinoma or invasive ductolobular carcinoma. *BioMed Res Int* (2018) 2018(Ilc):1–7. doi: 10.1155/2018/1569060

4. Lopez JK, Bassett LW. Invasive lobular carcinoma of the breast: Spectrum of mammographic, US, and MR imaging findings. *Radiographics* (2009) 29(1):165–76. doi: 10.1148/rg.291085100

5. Brem RF, Ioffe M, Rapelyea JA, Yost KG, Weigert JM, Bertrand ML, et al. Invasive lobular carcinoma: Detection with mammography, sonography, MRI, and breast-specific gamma imaging. *Am J Roentgenol* (2009) 192(2):379–83. doi: 10.2214/AJR.07.3827

6. Adachi Y, Ishiguro J, Kotani H, Hisada T, Ichikawa M, Gondo N, et al. Comparison of clinical outcomes between luminal invasive ductal carcinoma and luminal invasive lobular carcinoma. *BMC Cancer* (2016) 16(1):1–9. doi: 10.1186/s12885-016-2275-4

7. Ross JS, Slodkowska EA, Symmans WF, Pusztai L, Ravdin PM, Hortobagyi GN. The HER-2 receptor and breast cancer: Ten years of targeted anti–HER-2 therapy and personalized medicine. *Oncologist* (2009) 14(4):320–68. doi: 10.1634/theoncologist.2008-0230

8. Behjatnia B, Sim J, Apple SK. Does size matter? comparison study between MRI, gross , and microscopic tumor sizes in breast cancer in lumpectomy specimens. *Int J Clin Exp Pathol* (2010) 3(3):303–9.

9. Kuhl C, Kuhn W, Braun M, Schild H. Pre-operative staging of breast cancer with breast MRI: One step forward, two steps back? *Breast* (2007) 16(2 SUPPL.):34–44. doi: 10.1016/j.breast.2007.07.014

10. Barker SJ, Anderson E, Mullen R. Magnetic resonance imaging for invasive lobular carcinoma: is it worth it? *Gland Surgery* (2019) 8(3):237–41. doi: 10.21037/gs.2018.10.04

11. Cortadellas T, Argacha P, Acosta J, Rabasa J, Peiró R, Gomez M, et al. Estimation of tumor size in breast cancer comparing clinical examination, mammography, ultrasound and MRI-correlation with the pathological analysis of the surgical specimen. *Gland Surg* (2017) 6(4):330–5. doi: 10.21037/gs.2017.03.09

12. Arpino G, Bardou VJ, Clark GM, Elledge RM. Infiltrating lobular carcinoma of the breast: Tumor characteristics and clinical outcome. *Breast Cancer Res* (2004) 6(3):7–11. doi: 10.1186/bcr767

13. Hilleren DJ, Andersson IT, Lindholm K, Linnell FS. Invasive lobular carcinoma: Mammographic findings in a 10-year experience. *Radiology* (1991) 178(1):149–54. doi: 10.1148/radiology.178.1.1984294

14. Aydin H, Guner B, Bostanci IE, Bulut ZM, Aribas BK, Dogan L, et al. Is there any relationship between adc values of diffusion-weighted imaging and the histopathological prognostic factors of invasive ductal carcinoma? *Br J Radiol* (2018) 91(1084). doi: 10.1259/bjr.20170705

15. Horvat JV, Bernard-Davila B, Helbich TH, Zhang M, Morris EA, Thakur SB, et al. Diffusion-weighted imaging (DWI) with apparent diffusion coefficient (ADC) mapping as a quantitative imaging biomarker for prediction of immunohistochemical receptor status, proliferation rate, and molecular subtypes of breast cancer. *J Magn Reson Imag* (2019) 50(3):836–46. doi: 10.1002/jmri.26697

16. Jeh SK, Kim SH, Kim HS, Kang BJ, Jeong SH, Yim HW, et al. Correlation of the apparent diffusion coefficient value and dynamic magnetic resonance imaging findings with prognostic factors in invasive ductal carcinoma. *J Magn Reson Imag* (2011) 33(1):102–9. doi: 10.1002/jmri.22400

17. Navarro Vilar L, Alandete Germán SP, Medina García R, Blanc García E, Camarasa Lillo N, Vilar Samper J. MR imaging findings in molecular subtypes of breast cancer according to BIRADS system. *Breast J* (2017) 23(4):421–8. doi: 10.1111/tbj.12756

18. Mann RM, Hoogeveen YL, Blickman JG, Boetes C. MRI Compared to conventional diagnostic work-up in the detection and evaluation of invasive lobular carcinoma of the breast: A review of existing literature. *Breast Cancer Res Treat* (2008) 107(1):1–14. doi: 10.1007/s10549-007-9528-5

19. McGhan LJ, Wasif N, Gray RJ, Giurescu ME, Pizzitola VJ, Lorans R, et al. Use of preoperative magnetic resonance imaging for invasive lobular cancer: Good, better, but maybe not the best? *Ann Surg Oncol* (2010) 17(SUPPL.3):255–62. doi: 10.1245/s10434-010-1266-y

20. Boetes C, Veltman J, Van DL, Bult P, Wobbes T, Barentsz JO. The role of MRI in invasive lobular carcinoma. *Breast Cancer Res Treat* (2004) 86:31–37. doi: 10.1023/B:BREA.0000032921.10481.dc

21. Schelfout K, Van Goethem M, Kersschot E, Verslegers I, Biltjes I, Leyman P, et al. Preoperative breast MRI in patients with invasive lobular breast cancer. *Eur Radiol* (2004) 14(7):1209–16. doi: 10.1007/s00330-004-2275-7

22. Cuesta Cuesta AB, Martín Ríos MD, Noguero Meseguer MR, Velascod García JA, Martíneza MM, Sotillosa SB, et al. Accuracy of tumor size measurements performed by magnetic resonance, ultrasound and mammography, and their correlation with pathological size in primary breast cancer. *Cir Esp* (2019) 97 (7):391–396. doi: 10.1016/j.ciresp.2019.04.017

23. Dietzel M, Baltzer PA, Vag T, Tobias G, Mieczyslaw G, Kaiser CO, et al. Magnetic resonance mammography of invasive lobular versus ductal carcinoma: Systematic comparison of 811 patients reveals high diagnostic accuracy irrespective of typing. *J Comput Assist Tomogr* (2010) 34(4):587–95. doi: 10.1097/RCT.0b013e3181db9f0e

24. Avendano D, Marino MA, Leithner D, Thakur S, Davila BB, Martinez DF, et al. Limited role of DWI with apparent diffusion coefficient mapping in breast lesions presenting as non-mass enhancement on dynamic contrast-enhanced MRI. *Breast Cancer Res* (2019) 21(1):1–10. doi: 10.1186/s13058-019-1208-y

25. Demard NF, Boulet P, Prat X, Charra L, Lesnik A, Taourel P. Breast MRI in invasive lobular carcinoma: Diagnosis and staging. *J Radiol* (2005) 86(9):1027–34. doi: 10.1016/s0221-0363(05)81487-8

26. Qayyum A, Birdwell RL, Daniel BL, Nowels KW, Jeffrey SS, Agoston TA, et al. MR imaging features of infiltrating lobular carcinoma of the breast: Histopathologic correlation. *Am J Roentgenol* (2002) 178:1227–32. doi: 10.2214/ajr.178.5.1781227

27. Rodenko GN, Harms SE, Pruneda JM, Farrell RS Jr, Evans WP, Copit DS, et al. MR imaging in the management before surgery of lobular carcinoma of the breast: Correlation with pathology. *Am J Roentgenol* (1996) 167:1415–19. doi: 10.2214/ajr.167.6.8956569

28. Yeh ED, Slanetz PJ, Edmister WB, Talele A, Monticciolo D, Kopans DB. Invasive lobular carcinoma: Spectrum of enhancement and morphology on magnetic resonance imaging. *Breast J* (2003) 9(1):13–18. doi: 10.1046/j.1524-4741.2003.09104.x

29. Savaridas SL, Bristow GD, Cox J. Invasive lobular cancer of the breast: A pictorial essay of imaging findings on mammography, sonography, and magnetic resonance imaging. *Can Assoc Radiol J* (2016) 67(3):263–76. doi: 10.1016/j.carj.2015.09.007

30. Porter AJ, Evans EB, Foxcroft LM, Simpson PT, Lakhani SR. Mammographic and ultrasound features of invasive lobular carcinoma of the breast. *Journal of Medical Imaging and Radiation Oncology* (2014) 58:1–10. doi: 10.1111/1754-9485.12080

31. Johnson K, Sarma D, Hwang ES. Lobular breast cancer series: imaging. *Breast Cancer Res* (2015) 2015:1–8. doi: 10.1186/s13058-015-0605-0

32. Gaur S, Dialani V, Slanetz PJ, Eisenberg RL. Architectural distortion of the breast. *Am J Roentgenol* (2013) 201:W662–W670. doi: 10.2214/AJR.12.10153

33. Krecke KN, Gisvold JJ. Invasive lobular carcinoma of the breast: Mammographic findings and extent of disease at diagnosis in 184 patients. *Am J Roentgenol* (1993) 161(5):957–60. doi: 10.2214/ajr.161.5.8273634

34. Le Gal M, Ollivier L, Asselain B, Meunier M, Laurent M, Vielh P, et al. Mammographic features of 455 invasive lobular carcinomas. *Radiology* (1992) 185(3). doi: 10.1148/radiology.185.3.1438749

35. Mendelson EB, Harris KM, Doshi N, Tobon H. Infiltrating lobular carcinoma: Mammographic patterns with pathologic correlation. *Am J Roentgenol* (1989) 153:265–71. doi: 10.2214/ajr.153.2.265

36. Berg WA, Gutierrez L, NessAiver MS, Carter WB, Bhargavan M, Lewis RS, et al. Diagnostic accuracy of mammography, clinical examination, US, and MR imaging in preoperative assessment of breast cancer. *Radiology* (2004) 233(3):830–49. doi: 10.1148/radiol.2333031484

37. Butler RS, Venta LA, Wiley EL, Ellis RL, Dempsey PJ, Rubin E. Sonographic evaluation of infiltrating lobular carcinoma. *Am J Roentgenol* (1999) 172:325–30. doi: 10.2214/ajr.172.2.9930776

38. Chapellier C, Balu-Maestro C, Bleuse A, Ettore F, Bruneton JN. Ultrasonography of invasive lobular carcinoma of the breast: Sonographic patterns and diagnostic value. report of 102 cases. *Clin Imag* (2000) 24(6):333–36. doi: 10.1016/S0899-7071(00)00234-5

39. Paramagul CP, Helvie MA, Adler DD. Invasive lobular carcinoma: Sonographic appearance and role of sonography in improving diagnostic sensitivity. *Radiology* (1995) 195(1):231–4. doi: 10.1148/radiology.195.1.7892476

40. Watermann DO, Tempfer C, Hefler LA, Parat C, Stickeler E. Ultrasound morphology of invasive lobular breast cancer is different compared with other types of breast cancer. *Ultrasound Med Biol* (2005) 31(2):167–174. doi: 10.1016/j.ultrasmedbio.2004.11.005

41. Dilorenzo G, Telegrafo M, La Forgia D, Stabile Ianora AA, Moschetta M. Breast MRI background parenchymal enhancement as an imaging bridge to molecular cancer sub-type. *Eur J Radiol* (2019) 113:148–52. doi: 10.1016/j.ejrad.2019.02.018

42. King V, Brooks JD, Bernstein JL, Reiner AS, Pike MC, Morris EA. Background parenchymal enhancement at breast MR imaging and breast cancer risk. *Radiology* (2011) 260(1):50–60. doi: 10.1148/radiol.11102156

43. Ko ES, Lee BH, Kim HA, Noh WC, Kim MS, Lee SA. Triple-negative breast cancer: Correlation between imaging and pathological findings. *Eur Radiol* (2010) 20:1111–17. doi: 10.1007/s00330-009-1656-3

44. Azim HA, Malek RA, Azim HA. Pathological features and prognosis of lobular carcinoma in Egyptian breast cancer patients. *Women's Heal* (2014) 10 (5):511–8. doi: 10.2217/whe.14.48

45. Oliveira TMG, Elias J, Melo AF, Teixeira SR, Filho SC, Gonçalves LM, et al. Evolving concepts in breast lobular neoplasia and invasive lobular carcinoma, and their impact on imaging methods. *Insights Imag* (2014) 5(2):183–94. doi: 10.1007/s13244-014-0324-6

46. Adejolu M, Krishnamurthy S, Whitman GJ. Ultrasound of invasive lobular carcinoma. *Ultrasound Clin* (2011) 6(3):313–25. doi: 10.1016/j.cult.2011.04.002

47. Wen X, Yu Y, Yu X, Cheng W, Wang Z, Liu L, et al. Correlations between ultrasonographic findings of invasive lobular carcinoma of the breast and intrinsic subtypes. *Ultraschall Med* (2019) 40(06):764–70. Korrelation der sonografischen Befunde des invasiven lobulären Mammakarzinoms und der intrinsischen Subtypen Patients with ILC. doi: 10.1055/a-0715-1668

48. Zhiqi Y, Chen X, Zhang T, Cheng F, Liao X, Chen X, et al. Quantitative multiparametric MRI as an imaging biomarker for the prediction of breast cancer receptor status and molecular subtypes. *Front. Oncol* (2021). doi: 10.3389/fonc.2021.628824

Frontiers in Oncology

Advances knowledge of carcinogenesis and tumor progression for better treatment and management

The third most-cited oncology journal, which highlights research in carcinogenesis and tumor progression, bridging the gap between basic research and applications to imrpove diagnosis, therapeutics and management strategies.

Discover the latest Research Topics

See more →

Frontiers

Avenue du Tribunal-Fédéral 34
1005 Lausanne, Switzerland
frontiersin.org

Contact us

+41 (0)21 510 17 00
frontiersin.org/about/contact